THE UNIVERSITY *of* EDINBURGH

Broad Emission Line Variability in Active Galactic Nuclei on Long Timescales

David Homan

Doctor of Philosophy

The University of Edinburgh

July 2019

Lay Summary

All galaxies in the Universe are thought to have a black hole at their centre. A black hole is a region of space where so much mass has been gathered together that the gravity is strong enough to prevent even light from escaping. The black holes in galactic centres can contain up to a billion times as much mass as the Sun. In most galaxies this black hole interacts very little with the material around it, we call these black holes 'dormant'. Other black holes draw in a great amount of material from their surroundings, these objects are called Active Galactic Nuclei (AGN), as they lie at the cores of their host galaxy. We believe the infalling material forms a disc as it spirals towards the black hole. Due to friction in the disc the material can heat up to 10,000 K. This process makes the disc emit an enormous amount of light: the brightest AGN, known as quasars, can be a 100 times brighter than all stars in their galaxy put together. And most of this light is created in a region smaller than the distance between the sun and our nearest star, very small on the scale of galaxies.

The heating of gas and dust in the AGN is not a smooth process: all AGN are observed to vary in their brightness. Because AGN are so bright these changes in their emission are equivalent to millions of stars turning 'on' or 'off' in the time-span of decades to centuries. The variability of the emission from the disc has a significant effect on other material in the AGN. One of these surrounding regions absorbs a fraction of the light from the disc and re-emits it at specific wavelengths (forming lines in the spectrum). This region is called the Broad Line Region (BLR). The response of the BLR to the changing disc emission is the main topic of this thesis. I consider AGN in which the changes in brightness are both very large and very quick: the strong changes in the disc and in the BLR occur in just a few years.

Many aspects of the BLR are still unclear. It is likely that the region consists of clouds of gas, containing Hydrogen, Helium, and other elements such as Magnesium. These elements emit the lines in the spectrum, which is how we can observe their presence. When the disc emission varies, these emission lines vary too. By tracking how strong each line responds to the variations in the light from the disc, we can learn much about the distribution of the gas in the BLR and about the way the gas behaves when it exists in such an extreme environment.

In the research presented here I look at one particularly variable AGN, located in the spiral galaxy Mrk 110. I also consider one special emission line, associated with Magnesium, by looking at the spectra of multiple AGN and comparing the line's behaviour among the different objects. The Magnesium line has stood out in previous works due to its lack of response. In both studies the aim is to disentangle the many different factors that contribute to the response of a line, to better understand how and where in the BLR the lines are formed. The results of the studies paint a picture of a BLR that is constantly changing, not only because the light from the disc varies, but also because the structure of the region itself is altered.

Abstract

Active Galactic Nuclei are among the most powerful sources of radiation in the Universe and are known to show variability across the EM spectrum. This thesis will focus on the variability in the optical and UV range, which is dominated by emission from the central accretion disc and the Broad Line Region (BLR). All AGN are powered by the accretion of matter onto a supermassive black hole. The BLR reprocesses part of the continuum generated by the accretion disc, re-emitting the energy in atomic emission lines. Variations in the continuum lead to variations in the broad emission lines, however the manner in which the broad lines respond is complex. Neither the accretion disc nor the BLR are currently fully understood. Over the past years the availability of large data-sets from long term spectroscopic observations, such as the Sloan Digital Sky Survey (SDSS), has greatly improved our ability to study the variability of AGN, expanding the observed timescales to decades. These timescales match the dynamical timescales associated with the BLR, implying that we could be able to track structural changes in this region.

The research presented in this thesis will use the response of the broad lines to the continuum to investigate the properties of the BLR, with an emphasis on long timescales. The research is split over two independent, but closely linked studies. The first is a case study of the highly variable active galaxy Markarian 110. The second study focusses on one particular emission line: MgIIλ2798. Both studies rely on optical spectroscopic data. A pipeline was written to fit archival and new spectra included in the study.

Mrk 110 is a local Seyfert I, at z=0.035, with available spectroscopic data going back decades. Combining archival data with new observations from the William Herschel and Tillinghast Telescopes, it is possible to track Mrk 110 through dips and peaks in the continuum at a relatively high cadence. Of particular note is the behaviour of HeIIλ4686, which varies significantly more than the other emission lines. This line can be used as a proxy for the ionising (FUV) part of the continuum. Comparing Hα, Hβ, and HeIλ5876 with the FUV flux we note that the response of the line fluxes to continuum changes evolves considerably on the timescale of years. For the highest continuum fluxes it is possible to detect a saturation level of the line responses, correlated with the Reverberation Mapping lags associated with the lines. Analysing the line profiles, we can detect an offset between the narrow and broad components of the Hβ and HeIIλ4686 lines, likely associated with a radial flow in the BLR.

The Magnesium line at 2798Å is a prominent feature in most AGN spectra. Its response to continuum changes has been shown to be limited in previous studies. The study presented here will make use of two data-sets. The first is a sample of 43 extremely variable quasars. This sample combines SDSS spectra with new observations from the William Herschel, Magellan, and MTT Telescopes. The second data-set consists of approximately 16,000 SDSS quasars with repeat spectroscopy. The data from both samples indicate that there is in fact a broad range in MgII behaviour. We observe that the line tracks the continuum on average, but also note considerable scatter in this correlation.

Combining the results from the Mrk 110 and MgII studies we find that there is evidence in all samples for broad line responsivity that evolves over time. There is also considerable evidence to suggest that the dynamics of both the HeIIλ4686 and the MgII line are not only set by their positions in the gravitational potential.

Declaration

I confirm that this thesis for the degree of Doctor of Philosophy was written by myself, that the work herein is my own except where explicitly stated otherwise, and that this work has not been submitted for any other degree or professional qualification.

David Homan, December 2019

Acknowledgements

Over the past years I have had the good fortune to meet and work with many kind, intelligent, and generous people, both at the Royal Observatory and beyond. There are a few people that I would like to thank in particular.

First, my supervisor Andy Lawrence, for always providing guidance and insights at the right moment, and my second supervisor Chelsea MacLeod, for starting me off in the right direction and for all the help along the way.

From the other collaborators at the ROE, I would like to thank Nic Ross, for helpful discussions and a push for improvements, and Alastair Bruce, who was always ready to answer a question.

I would also like to thank Martin Ward, from Durham University, for a friendly and fruitful collaboration.

My gratitude goes out to all others at the ROE and from the wider University who made the past years such a pleasure.

Beyond the academic world, my thanks go out to my parents and brother, who have supported me throughout.

And finally, to Elizabeth, who helped me see this work through to the end.

Contents

List of Tables

List of Figures

1. Introduction

Active Galactic Nuclei (AGN) are among the most powerful sources of electromagnetic radiation in the Universe. The range in AGN luminosity spans from Seyfert galaxies, where the energy output of the galaxy's central region, on pc scales, can match the combined output of the rest of the galaxy, to quasars, where the central region can outshine its host by a factor of a hundred. Since the initial studies of AGN in the 1940s the study of nearby active galaxies and of the more distant quasars has progressed greatly. We have gained understanding of the processes underlying the emission, and the various features of the AGN spectrum have allowed us to construct a unified model for a 'typical' AGN. There are, however, challenges posed to this generic model, in particular by observations of strong variability. There is a number of textbooks that provide an overview of this material [Peterson, 1997; Krolik, 1999; Kembhavi & Narlikar, 1999; Netzer, 2013].

The research presented in this thesis concerns the variability of broad emission lines in the spectra of AGN. The broad lines are likely to be formed in inner regions of AGN and can provide insight into the dynamical processes of accretion, emission, absorption and re-emission that occur there. The focus of this work will be on spectroscopic analysis of a variety of sources: a case study of the Seyfert galaxy Markarian 110, a study of one particular emission line, MgIIλ2798, in a sample of highly variable quasars, and a comparative analysis of the same MgII line in the quasar population in general. The sample of highly variable quasars is the same as that presented in MacLeod et al. [2019], and the study is designed to be complementary to this work.

Their intrinsic power makes research into AGN relevant for other fields in astronomy as well. AGN can be detected over cosmic distances, making them very suitable to trace the largest cosmological scales, for example in the study of Baryon Acoustic Oscillations (see e.g.Bassett & Hlozek [2010]). The growth and evolution of AGN are of great importance to the evolution of their host galaxies, as feedback from the AGN to the host can impede star formation (see e.g. Fabian [2012]; Heckman & Best [2014]; Tadhunter [2016]). In these ways AGN play an important part in both cosmology and galaxy evolution. Most important, however, is that the complexity and diversity of AGN themselves make them a fascinating topic of study.

This chapter will start with a brief overview of the generic AGN model and the manner in which the different aspects of the AGN spectrum have been linked to the components of the AGN's physical structure. Section 1.2 will narrow down the focus to the inner region of the AGN, which is thought to be the source of both the optical continuum radiation and the emission lines. This section will be followed by a discussion of the observations of AGN variability (Section 1.3), photometric as well as spectroscopic, and the ways in which this variability has been interpreted. In Section 1.4 I will introduce some of the problems with the current models, which the research presented here will investigate further. Particular attention is paid to the importance of extremely variable objects, such as the so-called changing look AGN, as test cases for both our current models and our interpretation of AGN variability. This chapter will conclude with an outline of the rest of the thesis.

1.1. AGN: Observations and Structure

1.1.1 Discovery

The first person to classify a group of sources that belong to the category of Active Galaxies was Carl Seyfert [Seyfert, 1943], after whom this class of AGN is now named. Seyfert galaxies are relatively low luminosity (10^{9-10} $L_\odot$), local AGN, with a clearly resolved host galaxy. Seyfert noted the presence of strong, broad emission lines in six extragalactic sources, clearly distinct from stellar emission. Although unusual, it was not until the advent of radio astronomy during the next decade that it became clear that Seyferts belonged to a much broader class of objects.

The presence of extragalactic radio sources had been established during the 1950s, and optical counterparts had been found for some of these sources as well, as in the case of Cyg A. However it was the use of large radio surveys that led to the discovery of quasars: the Third Cambridge (3C) [Edge et al., 1959] catalogue contained two objects that proved key in the identification of these enigmatic sources The first was 3C 48, which was identified with what appeared to be a blue star [Matthews & Sandage, 1963]. The stellar spectrum showed broad emission lines at unexpected wavelengths, however. A similar identification was made for the radio source 3C 273, which appeared to be a strongly variable blue star-like object, with odd emission lines. It was Schmidt [1963] and Oke [1963] who realised that the odd emission line in 3C 273 was in fact greatly redshifted MgIIλ2798. The association of this redshift with a cosmological distance implied an extremely high luminosity, across the EM spectrum, for these objects.

These sources were labelled 'quasi stellar objects' or quasars. The similarity in the broad emission lines with the galaxies described by Seyfert were apparent, and indeed the detection of radio emission from a subset of Seyfert galaxies made the connection between the two even clearer. There is, however, a great range in the properties of active galaxies, from their bolometric luminosity to the strength of various emission lines, to the presence or absence of radio emission. A large fraction of the research into AGN over the following decades was devoted to developing a single model that could explain the various features exhibited by these sources. AGN unification is a topic of debate to this day. In the following sections I will give a brief overview of the properties that characterise a 'typical' AGN spectrum (Section 1.1.2), the considerations that led to the notion of accretion onto a supermassive black hole as the AGN power source (Section 1.1.3), and the manner in which we can construct a unified AGN model that matches these various characteristics (Section 1.1.4).

1.1.2 AGN Across the EM Spectrum

Although the initial discovery and classification of AGN was based on a combination of optical and radio data, AGN emit radiation over the full range of the EM spectrum. The continuum in the average AGN spectrum shows a typical triple hump structure: a peak in the infrared, a peak in the UV/optical, and a peak in X-rays. Not all AGN are radio sources, creating the sub-classes of radio loud and radio quiet AGN, where the classification is usually based on the ratio of the luminosities (L_ν) in the far infrared and in the radio [Condon, 1992; Heckman & Best, 2014]. Figure 1.1 shows a number of average Spectral Energy Distributions (SEDs) for radio quiet AGN. The grouping of the objects in Figure 1.1 is based on the Eddington ratio, a parameter describing the level of accretion occurring in the system (see Section 1.1.3).

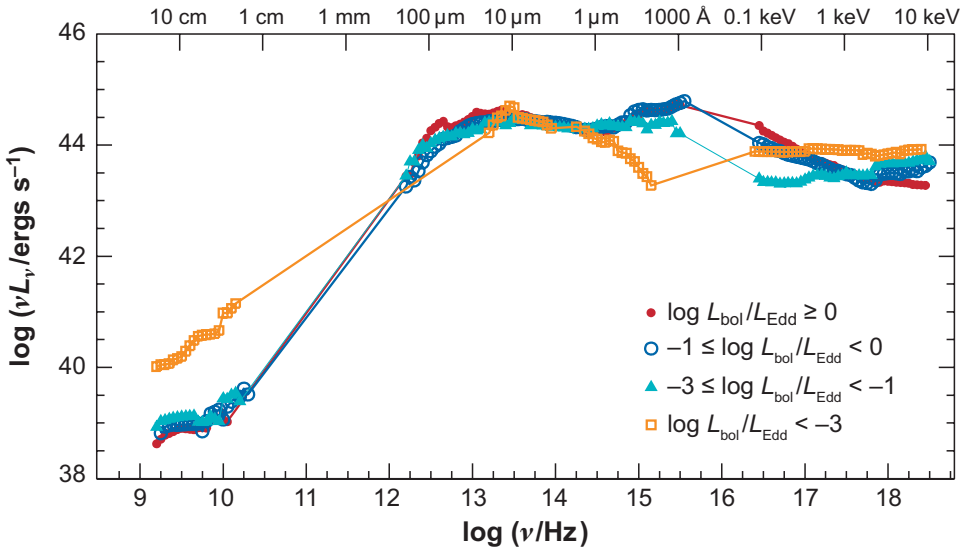

Figure 1.1: Average composite AGN SEDs for four groups of radio-quiet AGN. Note the triple hump structure, with distinct peaks in the infrared, UV/optical, and in X-rays. The subdivision between the four groups is based on the Eddington ratio, where a lower Eddington ratio corresponds to a lower accretion rate. The SEDs have been normalised at 1μm: AGN with a lower Eddington ratio are less luminous than their counterparts with higher Eddington rations. Figure from Ho [2008].

The triple hump structure of the SED is present in both radio loud and radio quiet AGN, as illustrated in Figure 1.2.

In addition to the emission in radio to X-ray, some AGN are strong gamma ray sources. A group of AGN that often shows prominent gamma ray and radio emission is referred to as blazars. Blazars form a very distinct subset of AGN that exhibit extremely rapid variability (on the timescale of seconds) and a distinctly non-thermal continuum (see e.g. Madejski & Sikora [2016]). The non-thermal continuum is thought to be associated with jetted emission from the nucleus. The AGN considered in this thesis do not fall in the category of blazars, and generally show very different behaviour from these objects. For this reason a discussion of blazars is beyond the topic of this text.

Radio Emission

Almost all AGN produce radio emission to some extent, however only approximately 10% of AGN are classified as radio loud [Netzer, 2013]. A significant part of the radio emission is nuclear, however for AGN in the local Universe radio emission can be used to trace extremely large structures ($\sim$ kiloparsecs), that extend from the nucleus. The SED of both the nuclear and the extended radio emission follow a power law, indicating a non thermal source of radiation. Based on the power law index, the unresolved nuclear emitting region is optically thick, whereas the extended region is optically thin [Peterson, 1997]. In both cases synchrotron emission matches the AGN spectrum.

As the radio emission can be resolved, it provides information about the structure of AGN. In a number of sources jet-like structures have been detected, which appear to connect to the radio lobes. This configuration suggests a system in which energy and matter are ejected from the central region, powering emission at scales comparable to the host galaxy. As with most aspects

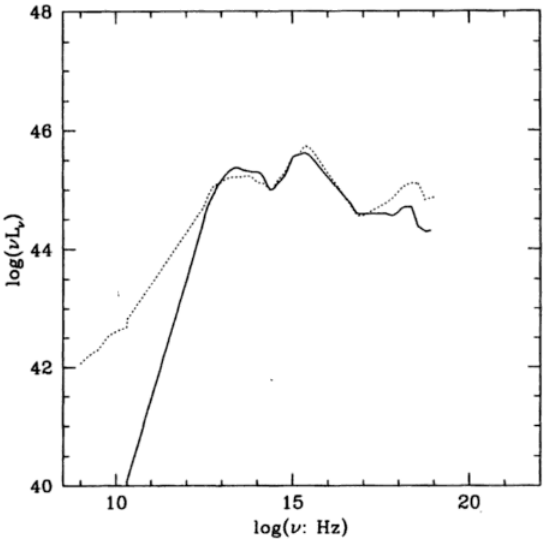

Figure 1.2: Composite AGN SEDs for radio quiet (solid line) and radio loud (dotted line) AGN. Although the difference is radio output is clearly distinct, both source classes show the triple hump structure noted in Figure 1.1. Figure from Krolik [1999], based on data by Elvis et al.

of AGN there is a great deal of diversity within the radio loud population. A phenomenological classification based on the distribution of emission in the radio lobes [Fanaroff & Riley, 1974] indicates that this distribution correlates with radio luminosity. In the more powerful FR-II objects, the radio emission in the lobes is edge-brightened, whereas in FR-I objects the radio luminosity is highest closer to the nucleus. The powering mechanism behind the extended emission can therefore produce different signatures

Infrared Emission

Infrared emission accounts for around 30% of the bolometric output of an average AGN [Richards et al., 2006; Elvis et al., 1994], although there is large range for this value [Roseboom et al., 2013]. Improvements in infrared observations, in particular the space based observations of Spitzer and WISE, have increased our understanding of the behaviour of AGN at these wavelengths. The emission associated with the AGN, after subtracting the contribution by the host galaxy in this spectral range, is constrained to a region with ∼parsec scale.

The bump in the AGN SED around 10μm is largely featureless, corresponding to greybody radiation with $T \sim 10^2$ K. The SED dips around 1μm, before rising into the optical/UV bump. Richards et al. [2006] give an IR spectral index $\alpha_\nu \sim 0.5$–1 ($f_\nu \propto \nu^{-\alpha_\nu}$), in the wavelength range 0.6–8μm, for type 1 AGN (see Section 1.1.4 for a discussion on the classification). Netzer [2015] indicates that there is likely a large scatter in this specral index for type 2 objects. The most prominent features visible in the infrared part of the spectrum are two broad bumps around 10 and 18μm [Netzer, 2013].

Optical and UV Emission

The peak in the optical range of the continuum SED, often referred to as the 'big blue bump', occurs around 1000Å. In a composite of ∼2200 quasar spectra Vanden Berk et al. [2001] report a spectral index ($f_\nu \propto \nu^{-\alpha_\nu}$) of -0.44 for the range 1300–5000Å , turning to -2.45 beyond 5000Å, towards the 1μm break.

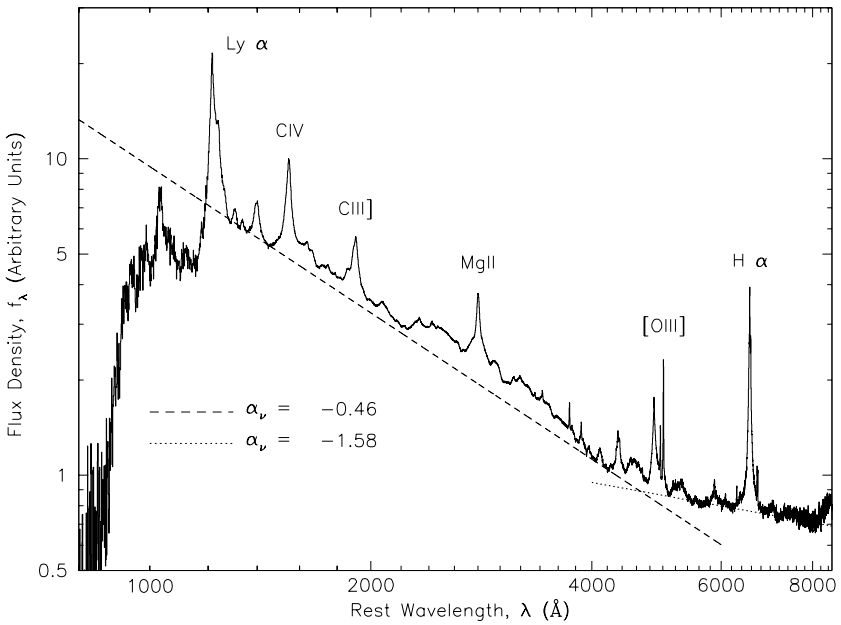

Figure 1.3: Composite median quasar spectrum in the wavelength range covering the Lyman break to the edge of the NIR. The most prominent emission lines are clearly visible on top of the thermal continuum. All lines are broad, except for the [OIII]$\lambda\lambda$4960,5007 lines, which are associated with forbidden transitions. Note that this representation of the optical part of the spectrum does not accurately display the continuum shape: the median composite was used to emphasize the emission lines. Figure from Vanden Berk et al. [2001].

Superimposed on the smooth thermal continuum is a complex of emission lines. The strongest lines are shown in Figure 1.3. The lines indicate the presence of various elements in the line emitting region of AGN. The most prominent lines are those of Hydrogen, but many metallic lines such as those of Carbon and Magnesium are also present. Remarkably the metallicity of quasars does not appear to evolve with redshift, and appears solar to super-solar even to redshifts $z \sim 6$ [Merloni, 2016].

AGN emission lines fall into two distinct categories: broad and narrow. The widths of the lines are such that Doppler broadening due to bulk motion is the most likely explanation. The broad lines correspond to permitted atomic transitions and have widths corresponding to $\Delta v \sim 10^4$ km/s. The narrow lines are associated with both permitted and forbidden transitions and usually show broadening corresponding to $\Delta v \sim 10^3$ km/s. All AGN show narrow line emission, but broad lines are not visible in all AGN spectra. All line species that are present as broad lines also have a narrow component, but not vice versa. The dichotomy between the two line classes implies two distinct line forming regions: a fast moving broad line emitting region where forbidden lines are collisionally suppressed (relative to the permitted lines), and a low density, slower moving narrow line emitting region. Observations of local AGN indicate that the narrow line region extends to kpc scale, whereas the broad line region cannot be optically resolved (see Section 1.2). The relative strengths of line species can be used as a further constraint on the physical conditions in the line forming regions.

AGN emission lines are the result of either recombination and subsequent de-excitation of the emitting atoms or collisional excitation. The existence and strength of reionisation lines

(such as those of Hydrogen) therefore suggests the presence of a strong ionising continuum. Both high (e.g. NV) and low (e.g. Lyα) ionisation lines are present in the AGN spectra. The ionising flux must therefore be hard enough to reach the required ionisation energies and high enough to cause the observed line strengths. This 'true' ionising continuum is obscured from us along the line of sight, by the material that forms the emission lines as well as by gas in the host and our own galaxy. The emission lines can be used as a measure of the underlying ionising continuum.

In the vicinity of the 2798Å MgII line, a complex of FeII emission lines blend together to form a feature referred to as the 'small blue bump'. This bump is of importance when trying to correctly measure the flux in the MgII line, as will be discussed in Chapter 3.

X-ray Emission

The high energy bump in the spectrum, in the X-rays around 10 keV, represents about 10% of the total radiated energy for a typical AGN. X-ray observations of AGN are usually not spatially resolved and show a well constrained photon power law index $\langle\Gamma\rangle = 1.8 \pm 0.2$ ($f \propto \nu^{-\Gamma+1}$) for 2–10 keV photons. The fact that this is a considerably softer spectrum than that of the cosmic X-ray background ($\langle\Gamma\rangle \approx 1.4$) indicates that a large fraction of the AGN population is likely obscured in some way [Merloni et al., 2014].

As was the case for the optical part of the spectrum, the X-ray continuum is combined with various emission lines, associated with either strongly ionised atoms or high energy transitions. The most prominent of these is the Fe Kα line, at 6.4 keV (e.g. Wu et al. [2009]). These function as indicators for various physical processes. In the case of X-rays, emission lines are often used as probes of obscuration along the line of sight.

A measure of the hardness of AGN SEDs is the spectral slope α_{OX}, which represents the ratio of luminosities (L_ν) at 2 keV and 2500Å. This slope has been shown to evolve with $L_\nu(2500)$, with the spectrum softening for larger values of the UV flux [Netzer, 2013; Merloni, 2016].

The study of AGN comprises the study of many physical components. The demarcation between the different components is assisted, or perhaps motivated, by the fact that the radiative signature of each is expected to dominate a different part of the EM spectrum. The combination of these various components is a single framework, AGN unification, is discussed in Section 1.1.4.

1.1.3 Energy Balance

The identification of quasars as extragalactic sources implied a very efficient process powering the emission, in order to explain the combination of enormous power and strong localisation. As the output from the central region can rival that of the combined stellar luminosity of the host galaxy, the process needs to be significantly more efficient than the nuclear fusion powering stars. The only known candidate for such a process is gravitational accretion onto a compact object. Efficiency for accretion is defined as $E/\dot{M}c^2$, i.e. the amount of energy released as a fraction of the rest-mass energy of the accreting matter. As it turns out, the only object compact and massive enough to attain the required efficiency is a black hole.

A simple energy consideration can illustrate this line of thought. Assuming a Newtonian

$1/r$ potential, the change in potential energy for a test mass m is

$$\Delta E_p = GMm\left(\frac{1}{R_{\text{in}}} - \frac{1}{R_{\text{out}}}\right) = \frac{mc^2}{2}\left(\frac{1}{R_{\text{S,in}}} - \frac{1}{R_{S,\text{out}}}\right), \tag{1.1}$$

where the radius has been expressed in terms of the Schwarzschild radius. This expression indicates that most of the potential energy is released close to the black hole. Assuming the test mass falls radially inward, all the way to the event horizon, the total amount of energy released is $\Delta E_p = \frac{mc^2}{2}$, or half of the rest mass energy. Note that this efficiency is independent of black hole mass.

A refinement of the estimate can be made by considering the form the accretion takes. As the black hole does not have a hard surface, the kinetic energy gained by the infalling matter needs to radiate away before the mass passes the event horizon; simple radial infall would not produce observable emission. Another consideration is the angular momentum: given that all galaxies exhibit rotation, it is highly likely the matter surrounding the black hole will need to lose angular momentum to be able to move inwards to the black hole. Finally, in the case of spherical accretion, in order to reach the energy output of AGN, the required infalling matter would likely form an optically thick shell, creating an advective system, thereby reducing the efficiency. These problems can all be addressed by assuming the infalling matter forms an accretion disc. This is observed in other accreting systems such as X-ray binaries. The fact that we can observe the UV/optical continuum is in agreement with the presence of such a disc.

Assuming Keplerian orbits for the material in the disk, the total energy for an orbiting test mass, and the associated change in energy ΔE over a change in radius Δr are

$$E_{\text{tot}} = E_p + E_k = -\frac{GMm}{r} + \frac{mv^2}{2} = -\frac{GMm}{2r}, \tag{1.2a}$$

$$\Delta E_{\text{tot}} = \frac{\partial E_{\text{tot}}}{\partial r}\Delta r = \frac{GMm}{2r^2}\Delta r. \tag{1.2b}$$

In this system a negative Δr, i.e. motion radially inward, decreases the total energy of the test mass. Half of the energy is spent on increasing the kinetic energy, leaving the other half available for radiation. Note that this transition is only possible by extracting energy and angular momentum from the system. We assume this extraction is facilitated by friction, without specifying what the exact physical mechanism involved should be (see Section 1.2). For a Schwarzschild black hole, the innermost stable circular orbit (ISCO) is 3 R_S. Equation 1.1 therefore gives $\Delta E_{p,max} = \frac{mc^2}{6}$. Combining the factor 1/2 for the disk system, and the factor 1/6 for the ISCO, the efficiency of gravitational accretion in this simplified approach becomes $\frac{\text{E}}{mc^2} = \frac{1}{12}$. For rotating black holes the ISCO can move closer to the black hole, increasing the efficiency, to a maximum of approximately 40% [Krolik, 1999].

An interesting question is what the required accretion rate would be to attain an AGN's luminosity. A relevant concept in this context is the Eddington luminosity. The Eddington luminosity is defined as the limiting luminosity for a spherically accreting object, where the emitted radiation exerts a pressure on the accreting material. The associated Eddington rate is defined as the bolometric luminosity divided by the Eddington luminosity. This approximation assumes the photons interact with free electrons, using the Thomson cross section σ_e, and that the electrons are bound, either as a plasma or in atomic form, to single protons (of mass m_p). An equal outward force to the radiation and inward force due to gravity are reached at the

Eddington luminosity L_{Edd}:

$$L_{Edd} = \frac{4\pi G c m_p}{\sigma_e} M. \tag{1.3}$$

Where M is the black hole mass. In SI units, $L_{Edd} \approx 6.37M$. For a 10^8 $M_\odot$ black hole (see Section 1.3 for a discussion of black holes mass estimates) and the estimated disc accretion efficiency this would correspond to an accretion rate of ~ 2 $M_\odot$ per year. Compared to the black hole mass, and the AGN's luminosity, this rate appears quite modest: an indication of the efficiency of gravitational accretion as a power source.

The final part to consider is the spectrum of the emitted radiation. Assuming that the friction in the disc causes heating and that the disc is optically thick, the emission powered by the accretion should be blackbody radiation. The spectrum is therefore determined by the temperature, which will be a function of radius. Dividing the disk into annuli, of width Δr, the luminosity of each ring is given by:

$$4\pi(r\Delta r)\sigma T^4 = L(r)\Delta r = \frac{GM\dot{m}}{2r^2}\Delta r. \tag{1.4}$$

Here σ is the Stefan-Boltzmann constant and $\dot{m}$ is the change in mass with time, i.e. the accretion rate. Solving for T we find:

$$T = \Big(\frac{GM\dot{m}}{8\pi\sigma r^3}\Big)^{1/4} \Rightarrow T \approx 4.53 \cdot 10^7 \Big(\frac{M}{M_\odot}\Big)^{-\frac{1}{4}} \Big(\frac{R}{R_S}\Big)^{-\frac{3}{4}} \mathrm{K}. \tag{1.5}$$

For the final step it was assumed that $\dot{m}$ is the accretion rate associated with the Eddington luminosity.

The highest temperature is found closest to the black hole, where the amount of energy released over a change Δr is the greatest. At $3R_S$ $T \approx 2 \cdot 10^5$K, implying peak emission at $\sim$150Å, in the extreme UV (EUV). This is clearly distinct from the observed big blue bump $\sim$ 1000Å. The full black body spectrum of the disc is found by integrating over the spectra of the annuli. As the disc and therefore the range in T is finite, there is a low and a high frequency cut-off. The high frequency cut-off is the exponential Wien tail, and at low frequencies $L_\nu \propto \nu^2$, in accordance with the Rayleigh-Jeans approximation. The profile of the spectrum for temperatures between the extremes should follow $\nu^{1/3}$. The resulting spectral signature of the accretion disc is therefore a bump in the UV with at its centre a power law, $L_\nu \propto \nu^{1/3}$.

1.1.4 From Spectrum to Structure

The observed characteristics and the energy considerations presented in the previous sections are the guidelines that shaped the current 'standard' model of AGN [Antonucci, 1993; Urry & Padovani, 1995]. This model comprises an accretion disc surrounding a central supermassive black hole, a sub-parsec-scale broad line emitting region (BLR), an parsec-scale obscuring region of dust, and a large narrow line emitting region (NLR) extending out to kiloparsecs. The different physical structures of the unified models are thought to dominate different parts of the spectrum, combining to form the characteristic triple-hump SED. Some AGNs also produce jets, channelling material away from the central black hole at relativistic velocities. A broad classification of AGN based on these properties is that of 'jet-mode' and 'radiative mode' AGN, where radiative mode AGN have a higher accretion rate and produce significantly more emission [Heckman & Best, 2014]. It should be noted that a small fraction of radiative mode AGN

also produce jets, which are among the most powerful. The presence/absence of jets is related to the radio loudness/quiescence of a source.

One of the central tenets of the standard AGN model is the black hole paradigm, which gained direct observational support through the observations of the shadow of the event horizon and the gravitationally lensed accretion disc of M87 [Event Horizon Telescope Collaboration et al., 2019]. The combination of black hole and accretion disc is often referred to as the 'central engine', as it is the gravitational accretion that generates the energy to power all radiative processes. The main way this energy is released is by frictional heating of the disc. A simple estimate of the efficiency of this process provides a temperature of $2 \cdot 10^5$ K at the $3R_S$ inner boundary of the disc. Assuming the radiation is thermalised, the hottest region is also the brightest, resulting in a peak emission at ∼150Å. The disc is therefore associated with the optical/UV continuum, and is the likely source of the ionising radiation that powers the line emission in this wavelength range.

The archetypal model for the accretion disc is the optically thick, geometrically thin disc model [Pringle & Rees, 1972; Shakura & Sunyaev, 1973]. Geometrically thin in this context means that the ratio of the disc scale height and radius is small ($D/R < 0.1$). Many unknowns about the dynamics of the system, including the mechanism of friction, are captured in the viscosity parameter α (for this reason this type of disc model is also referred to as an α-disc). The thin disc model has the general characteristics derived in Section 1.1.3, including the T$\sim r^{-3/4}$ scaling relation. The basic spectral properties associated with these temperature estimates should therefore also hold if this disc model is valid.

A key observational difficulty is that the high energy part of the spectrum, the EUV around 150Å, is obscured to any outside observer by a combination of neutral hydrogen within the BLR and material in the host galaxy and the Milky Way ISM. The shape of the ionising continuum can therefore only be deduced through indirect measurements. The study of the BLR in Mrk 110 (Chapter 4) will follow this line of investigation. The peak of the big blue bump, however, is not as blue as would be expected based on simple disc considerations. The observed maximum is around 1100Å (e.g. Shang et al. [2005]), corresponding to $T \sim 3 \cdot 10^4$ K.

Although a definitive resolution of this 'temperature problem' has not been reached, a possible solution is presented by Lawrence [2012]: rather than a true peak of the spectrum, the maximum around 1100Å could be formed by line emission from clouds in close proximity to the central engine ($\sim 30R_S$). Thermal emission in the accretion disc is reprocessed in these clouds into spectral lines. The broadening of the lines due to the rotational speeds of the clouds would be so great that the different lines are no longer individually detectable, but blur into one another, mimicking a continuum.

Another prediction of the disc accretion model is that the thermally produced spectrum follows a power law, $\nu^{1/3}$, from the optical into the NIR. This spectral shape is not observed, however, as the observed spectrum scales as $\nu^{(-0.2)-(-1)}$ [Vanden Berk et al., 2001]. However, Kishimoto et al. [2008] show that the $\nu^{1/3}$ dependency of the AGN continuum is in fact visible in the near infrared, but only in polarised light. The argument is that the observed, unfiltered, spectrum in the infrared is a combination of the continuum emission from the disc, and emission from the dusty obscuring region (described below). By filtering out the unpolarised light it is possible to observe the reflected light only. The polarised light is thought to consist of thermal emission from the disc, reflected on cloud like structures interior to the dusty obscurer. The fact that broad emission lines are greatly diminished in polarised light, indicates that the scattering

region lies inside the BLR as well. By considering the polarised light only, Kishimoto et al. [2008] therefore show that it is possible to have a clear view of the disc spectrum. Their estimate of the spectral index α (where $F_\nu \propto \nu^\alpha$) is $+0.44 \pm 0.11$. This result is in good agreement with the predictions of thermal emission from a simple thin disc model. Kokubo et al. [2014] find a slope of $\alpha \sim 1/3$ when considering the variable part of the optical emission, which the authors associate with the accretion disc (see Section 1.3).

The BLR has a clear observational signature, as discussed in Section 1.1.2, but much is still unclear about its geometry and kinematics. A helpful overview is provided in Peterson [2006]. From AGN with an unobscured view of the central region we know that the UV/Optical obscuration is extrinsic to the BLR, implying that the BLR gas is dust free. Atoms are ionised by the incident EUV continuum flux and recombine or are collisionally excited, subsequently they emit the line photons as a result of de-excitation. The BLR is stratified, with different lines forming at different radii from the central engine. For the observed temperatures of the emitting gas ($\sim 10^4$ K) the Doppler broadening of the emission lines would be equivalent to a motion of 10 km/s. The measured line widths, in the order of 10^4 km/s, therefore indicate a strong bulk motion of the broad line gas.

The size of the broad line region is $\sim$0.1 pc, and the outer boundary coincides with the inner boundary of the dusty obscurer [Landt et al., 2014]. Based on considerations of BLR size, a likely model for the gas distribution within the BLR is in clouds, although there are alternative models (see e.g. Devereux [2018]). The origin, kinematics and ionisation level of the clouds are still largely unclear, and there are various models that attempt to address this issue (e.g. Goad et al. [2012]; Baskin et al. [2014a]; Elvis [2017]). The line profiles, formed as a combination of the profiles from the individual clouds, are smooth, indicating that the number of clouds is relatively large or that there is a significant contribution from a more dispersed medium.

The BLR and its relation to continuum emission are the central topic of this thesis, and for that reason I will discuss its properties in more detail in Section 1.2. For the purpose of discussing AGN unification, however, it is important to mention the classification of type 1 and type 2 AGN [Khachikian & Weedman, 1971; Osterbrock, 1981]. The distinction is based on the presence of the broad Hβ line in the spectrum, with subtypes like type 1.9 indicating the relative strength of the line. The essence of the AGN unification scheme is that type 1 and type 2 objects are separated only by orientation: in type 1 objects we have an unobscured line of sight to the BLR, whereas for type 2s the BLR is obscured by dust, which has a vertical distribution around the equatorial plane. This obscuring dust is associated with the central obscurer. Intermediate AGN types would correspond to intermediate inclinations of the AGN with respect to our line of sight. The fraction of type 2 AGN is approximately 55% [Lawrence & Elvis, 2010; Merloni et al., 2014].

The origin of the X-ray bump is the least certain among the three spectral peaks. Approximately 10% of the total energy output of the AGN falls in this spectral range. Obscuration effects and the timescale of X-ray fluctuations both indicate that the X-ray emitting region is close to the centre, internal to the BLR [Maiolino et al., 2010; Merloni et al., 2014]. A popular model for the emission region is the so-called X-ray corona [Haardt & Maraschi, 1991], which is thought to be formed of an optically thin plasma above the central part of the disc. The coronal X-rays are the result of inverse Compton scattering of accretion disc photons in the hot plasma. Part of the emission from the corona is likely reprocessed and reflected by the disc [Merloni, 2016; Heckman & Best, 2014]. The X-ray emission is therefore formed very close to the black

hole. However, an observed correlation between infrared and X-ray luminosities [Gandhi et al., 2009], indicates that the two emission regions are indeed powered by the same source.

As follows from the brief overview presented above, the central obscuring region plays a key role in AGN unification. The model is also referred to as 'unification by orientation': it is our viewing angle of the AGN that largely determines its observational characteristics, whereas the AGN all have similar physical components. As the central obscurer is of importance to the distinction between type 1 and type 2 AGN, I will discuss its current standing in some detail. The role of the central obscurer and the status of the unified model are reviewed in Netzer [2015]. The author identifies the main observational signatures for the obscuring region as: the anisotropy of UV/optical and X-ray emission, the shape of the NLR, which resembles two ionisation cones extending from the central disc, infrared emission, and a transition region between the BLR and the obscurer.

Observations of emission from central regions of AGN in polarised light have long indicated the presence of a central obscurer. An otherwise strongly dimmed nucleus can be seen in reflected light coming from within the dusty region (e.g. Hines & Wills [1993]; Kishimoto et al. [2008]). Not only the continuum but also broad line emission has been detected in this manner (a recent example is Ramos Almeida et al. [2016]), supporting the unification by orientation notion that type 1 and type 2 AGN only differ in line-of-sight extinction to the BLR. Not all type 2 AGN have polarised type 1 signatures, however [Tran, 2003]. This could indicate that some AGN intrinsically lack broad emission lines. These objects can be referred to as *true* type 2 AGN, in contrast to obscured type 1s. The existence of true type 2 AGN and the relation to changing look objects will be discussed in Section 1.4.

The basic model for the obscurer is of a geometrically thick region, sometimes referred to as a torus, with an inner radius of $\sim$pc. This region is filled with both gas and dust which absorbs the incident optical, UV, and X-ray radiation from the disc and BLR, heating the dust. This process explains the infrared emission, corresponding to a T$\sim 10^2$ K blackbody, as well as the shape of the ionisation cones, as these are thought to correspond to the solid angle (as seen from the central engine) left unobscured by the dust. An important concept in this discussion is that of the sublimation radius. The infrared emission is associated with dust grains that are destroyed by the disc's radiation within a certain radius. This implies a direct correlation between source luminosity and the inner radius of the obscurer: more luminous sources will destroy dust grains further out, and will therefore push the inner radius of the obscurer outward. A complicating factor is that the temperature at which grains are destroyed depends on their chemical composition. Graphite grains can withstand temperatures up to 1800 K, whereas silicate grains are destroyed by temperatures above 1500 K.

As discussed in Netzer [2015], the theoretical modelling of the torus has so far met with mixed results. Phenomenological models focus on fitting the IR SED. The distribution of dust can be modelled as continuous, clumpy or a mix of the two. The inclusion of clumps of dust in the model allows for more complex SEDs to be formed, as the temperature difference between the fronts and backs of clumps creates a mix of blackbody spectra, and the space between clumps can leave a relatively clear line of sight to the central engine and BLR. Roseboom et al. [2013] note that clumpy models more closely match the observed distribution between NIR and MIR radiation, and Netzer [2015] concludes that mixed models show the most promise.

A defining characteristic for the obscuring region is the amount of sky it covers, as seen from the central engine. This fraction is referred to as the covering factor. The covering factor

corresponds directly to the fraction of X-ray, UV, and optical emission that is reprocessed into IR. A study by Roseboom et al. [2013] based on type 1 AGN IR SED fitting finds an average covering factor of approximately 40%, but indicates that there is a large range among AGN. There is also evidence that the covering factor decreases with luminosity [Netzer, 2015]. For continuous torus models the covering factor describes the opening angle that sets the angular size of the NLR as seen from the SMBH. For clumpy models the relation between these two parameters is not as clear.

The covering factor is closely related to the discussion about the obscuration fraction among AGN. This is the fraction of AGN that show evidence of obscuration. If one assumes random orientations of AGN with respect to our line of sight, the average value of the obscuration fraction should correspond to the average covering factor. The hard spectrum of the Cosmic X-ray Background in comparison to the softer slope found in AGN, suggests that most AGN need to be obscured to prevent them from dominating the background spectrum [Gilli et al., 2007]. Estimates of the obscured fraction range between 50 and 60 percent. However, the question is complicated by the fact that the measurement of 'obscuration' is dependent on the choice of bandwidth [Lawrence & Elvis, 2010; Merloni et al., 2014]. Selection effects are also discussed in Netzer [2015]. The author appears to disagree with Lawrence & Elvis [2010] and Mayo & Lawrence [2013] about the size of the discrepancy between infrared/optical and X-ray obscuration levels.

Interestingly, there is an apparent evolutionary trend in obscuration, with X-ray luminosity (L_X) showing a significantly reduced obscured fraction among X-ray bright AGN. Lawrence & Elvis [2010] note that the presence of this effect is less clear in samples based on observations in other wavebands and suggest this trend could partially be explained by selection effects. The authors argue optically obscured objects could be more obscured in X-rays than modelled for, because they are partially covered by Compton thick material (a column density $N_H \geq 10^{24}\mathrm{cm}^{-2}$). In that case an insufficient X-ray correction would lead to an underestimation of L_X. An improvement to the X-ray correction would increase the number of obscured AGN with high L_X, thereby reducing the trend. This could affect 50-60% of the AGN population [Mayo & Lawrence, 2013]. However, a study of AGN from the XMM-COSMOS survey also finds an evolutionary trend with L_X, and the authors present evidence to exclude obscuration by Compton-thick material as a cause [Merloni et al., 2014]. This discussion is further complicated by the fact that Merloni et al. [2014] show that X-ray defined obscuration does not appear to have the same evolutionary effect.

A problem for the modelling of the central obscurer is the difficulty in maintaining a relatively cold and geometrically thick structure. Without the strong turbulence associated with high temperatures such as in the disc, the structure is liable to collapse to the equatorial plane under its own gravity. A possible solution to this problem is suggested by Gaskell et al. [2008], who present an AGN model that lacks the clear physical distinction between components presented in the 'unified' model. The disc, BLR and torus are all part of the same inflow, where self-shielding of clouds in the BLR prevents the clouds being driven outward except along the edges of the opening angle.

Another alternative to the dominant disc and 'torus' model for the central region is presented in Lawrence & Elvis [2010]. The suggested mechanism is a misalignment of the central accretion disc with the inflowing material from the surrounding galaxy. Because the inflow of material into the central region of the galaxy could very well be random, and separated into

discrete events due the clumpiness of the material, there will be a warp in the disc. The warp would span the region where the disc connects to the newly infalling material. In this manner the obscuring region is not a torus formed in a ring around the disc, but rather part of the disc itself. This possibility is briefly discussed in Netzer [2015] and the author notes that it is difficult to compare the theory with observations, as there is no prediction of the SED or dust sublimation radius. An additional problem is that there is currently no simulation of the physical conditions of a system of this type. The covering factor for this model varies according to the misalignment of the disc. Roseboom et al. [2013] note that their results are in approximate agreement with expectations for the warped disc model.

The features of the AGN spectrum have been described as static up to this point. However, one of the most important characteristics of AGN is their variability. Indeed, quasars were first discovered as radio sources with a highly variable optical flux. Variability is so inherent to AGN, that perhaps the best way to view them, as suggested by Richards et al. [2011], is "not as *things* so much as *processes*". All parts of the spectrum fluctuate over time and these fluctuations are of particular relevance to the research presented in this thesis. AGN variability will be discussed separately in Section 1.3.

1.2. The Inner Region: Accretion Disc and Broad Line Region

1.2.1 Disc Models

The inner region of an AGN, also referred to as the central engine, is where the power for AGN emission is generated through gravitational accretion. As discussed in the previous section, there are convincing arguments that this accretion should take the form of a disc. The precise geometric shape of this disc is unclear, however. The form the accretion process takes is of great influence on the AGN's spectral features: both for the continuum emission and for the reprocessing that takes place in the broad line region. There are various types of models for accretion onto black holes. These models account for the different spectral shapes observed in both AGN and other accreting compact systems, such as black hole binaries. It is likely that different modes of accretion occur in nature, and can be associated with AGN with different luminosities and different SEDs. This section will provide a brief overview of the most relevant disc models, and the connection they have to observed types of AGN.

The basic model for the accretion disc is the geometrically thin, optically thick disc introduced by Pringle & Rees [1972] and Shakura & Sunyaev [1973], with a relativistic treatment first considered by Novikov & Thorne [1973] (the relativistic approach is particularly relevant for X-ray emission). The basic principle of this accretion system is that energy is released locally and emitted locally, in a viscous process that transports angular momentum outward. The disc has a $T \propto r^{-3/4}$ temperature profile. This model is also referred to as the 'α disc' and the 'thin disc' model, to differentiate it from accretion flows with other geometries. The α parameter was introduced as a method to solve the fluid dynamic equations for the disc: it encapsulates the unknown viscocity physics by parameterising the turbulence in terms of the sound speed. The outer radius of the α disc can be defined as the point where the inward gravitational force of the black hole is balanced by turbulent forces in the disc, which is estimated to be in the order of $10^3 R_S$ [Netzer, 2013]. However, as pointed out by Czerny & Naddaf [2018] the precise point of transition between disc and BLR is still ambiguous. The efficiency of the accretion process

is defined a $\eta = L_{bol}/\dot{M}c^2$ (Section 1.1.3). A comparison of the black hole mass function and AGN luminosity function indicates that the average efficiency is around 10% [Heckman & Best, 2014]. This is in reasonable agreement with the estimate of $\eta = \frac{1}{12}$ derived for the simple disc model.

The viscosity parameter does not specify the mechanism that causes the friction. Friction allows angular momentum to be transported outward and allows for a fraction of the orbiting matter to move toward the black hole. The nature of the friction mechanism is a topic of ongoing debate. In a review of black hole accretion modelling Blaes [2014] lists three possible processes that can extract angular momentum: external large scale magnetic fields (associated with outflows), magneto-rotational instabilities, and shock waves in the disc. Of these processes magneto-rotational instability (MRI; Balbus & Hawley [1991]) is deemed the most likely candidate [Yuan & Narayan, 2014]. MRI is based on the idea that thermal ionisation of material in the accretion disc creates a rotating ring of charged material around the black hole, which amplifies and possibly locks in any external magnetic field. The stresses this induces as the disc rotates form the basis for turbulence that creates friction between different parts of the disc. The details of the MRI process, however, are beyond the scope of this text.

The modelling of accretion discs is limited by the computational complexity of solving MHD equations, as well as by the theoretical uncertainties in the viscosity and turbulence processes. Blaes [2014] notes that producing MRI-based models that can be falsified by observations has remained illusive. However, models are able to broadly reproduce the continuum SED features observed in AGN [Capellupo et al., 2015; Gardner & Done, 2017]. A model presented in Proga et al. [2008] consists of a rotating disc illuminated by a hot X-ray corona. The results show both an accreting inflow in the equatorial plane and a polar outflow close to the black hole. The authors note that the addition of rotation to the model, in combination with X-ray irradiation and UV line driving, led to a greater fragmentation of the outflow. This could tentatively be associated with the formation of BLR clouds. The solution provided by the model is not stable, however. Inclusion of vertical stratification in models has led to the notion that ionised gas can be made buoyant by MRI in the inner disc, which could be associated with the central X-ray corona [Jiang et al., 2014; Blaes, 2014].

A key factor in the comparison of various models in the literature is the timescale on which changes can occur in a system. Timescales provide a way to make direct comparisons between models and observations: if an AGN is observed to fluctuate on a timescale that is characteristic of a particular process, this is an indication of the relevance of this process in AGN emission. Timescale arguments are also of great importance to the discussion of extreme variability in the BLR and will be referred to in the discussion of both Mrk 110 and the MgII samples. The most relevant timescales are listed in Figure 1.1, with a numerical estimate for the thin disc model based on a $\sim 10^8 M_\odot$ black hole.

Although the thin disc model has proven successful in replicating the basic thermal origin of the continuum radiation, it falls short in several key aspects (see e.g. Lawrence [2012]; Dexter & Begelman [2019]). Several of these problems relate to the ability to reproduce AGN variability, as will be discussed in Section 1.4. There are also issues with matching the time-averaged SED. To attempt to address these issues, various alterations and additions for the thin disc model have been suggested.

One of the problems is related to the accretion disc size: a continuum reverberation mapping study of NGC 5548 shows a significantly larger accretion disc than could be expected based on

Table 1.1: An overview of estimated timescales for various physical processes in the accretion disc. Estimates can differ considerably based on the models (see e.g. Blaes [2014]; Dexter & Begelman [2019]). Here I use values from Netzer [2013] for $\tau_{viscous}$ and $\tau_{thermal}$, and from Lawrence [2016] for the other three. Values are based on a $10^8 M_\odot$ BH, and $R_{BLR} = 100 r_g$. $\tau_{viscous}$ represents the time it would take for information to travel through the disc via viscous transport (such as angular momentum is expected to be); $\tau_{thermal}$ is associated with cooling or heating; $\tau_{dynamical}$ corresponds to the rotational speed and is the shortest timescale at which physical changes can occur in the system (it of the same order as the free-fall timescale); τ_{sound} is the sound crossing time, and τ_{light} is the light crossing time. With regard to the symbols: Ω is the angular speed, ρ the gas density, P the gas pressure, and α the viscosity parameter.

$\tau_{viscous}$	$\sim \frac{1}{\alpha\Omega}\left(\frac{H}{R}\right)^{-2}$	$\sim 10^4$ years
$\tau_{thermal}$	$\sim \frac{1}{\alpha\Omega}$	$\sim 10^2$ years
τ_{sound}	$\sim \sqrt{\frac{\rho R^2}{P}}$	~ 10 years
$\tau_{dynamical}$	$\sim \frac{1}{\Omega}$	$\sim$ days
τ_{light}	$\sim \frac{R}{c}$	~ 10 hours

the thin disc model [McHardy et al., 2014; Cackett et al., 2018], and results from microlensed quasars show the same [Morgan et al., 2010]. An observational explanation for this effect could be that AGN are in fact more luminous than is usually assumed, because there is significantly more reddening than is accounted for [Gaskell, 2017]. An attempt to address this issue through modelling is presented in Dexter & Agol [2011]. The authors suggest a stochastic variation of disc temperature across the disc, rather than the radial temperature profile of the thin disc model. This type of disc would therefore lack a clear annular structure.

A possible physical realisation of such an inhomogeneous disc is geometrically thick and supported by magnetic pressure resulting from MRI [Dexter & Begelman, 2019]. Extra vertical support for the disc is suggested to come from a non-zero torque at the ISCO. In the traditional thin disc model the torque at the disc's inner edge is set to zero. Relinquishing this boundary condition allows for a thicker and hotter inner disc (see also Ross et al. [2018]). In the magnetically elevated disc model, the disc is geometrically thick at all radii and the temperature and luminosity are decoupled from the physical structure. This allows for a more rapid inflow of material, as well as a more stochastic energy distribution. The authors argue this model solves several other problems with the thin disc model as well, in particular with respect to extreme variability (see Section 1.4).

A different problem with the current understanding of black hole accretion is that the peak temperature of the modelled disc is too high. This is the temperature problem discussed in Section 1.1.4. Rather than changes to the disc itself, the solution suggested in Lawrence [2012] is based on reprocessing radiation from the inner disc in central clouds. The viability of this model depends strongly on the possibility of clouds to exist this close to the central source. The key argument here is that these clouds do not have to be long lived: in a dynamic atmosphere around the disc clouds can form and dissipate on a timescale of around 50 days, comparable to the dynamical timescale at their expected rotational distances [Lawrence, 2012].

The origin of X-ray emission is another issue not addressed directly by the thin disc approach. Gardner & Done [2017] point out there are in fact two X-ray components that any full SED model would need to fit: a hard (> 10 keV) and a soft (2-10 keV) X-ray excess. A helpful

measure in discussing the relative strength of X-ray emission is the ratio of X-ray to optical emission, α_{OX}. This parameter is based on the ratio of the 2500Å to 2 keV fluxes: harder spectra have lower values of α_{OX}. Observational constraints on the X-ray emitting region indicate a highly centralised emitter of hard X-rays, within $10R_S$ of the black hole [Czerny & Naddaf, 2018]. One of the options for this emitter is the X-ray corona discussed above, possibly lifted by magnetic buoyancy.

A second option for a hard X-ray emitter is a hot inner accretion flow (see reviews by Yuan & Narayan [2014] and Ho [2008] for an in-depth discussion). Thin disc accretion can be be considered 'cold' in comparison to the virial temperature close to the black hole, which is $\sim 10^{11}$ K. Based on the initial work in Shapiro et al. [1976], theoretical work on hot inflows shows that these accretion solutions are distinct from cold inflows in both emission and geometrical structure. The most important difference between hot and cold accretion flows is that hot flows are optically thin. Inefficient cooling of the ionised nuclei causes the average temperature to approach the virial temperature. This type of flow is associated with a low accretion rate, to allow the opacity of the accreting matter to be low enough to become optically thin.

The emission processes in a hot flow are dominated by synchrotron emission, bremsstrahlung, and Compton scattering of the created photons. X-rays are produced through Compton scattering on the electrons, which are assumed not to be in thermal equilibrium with the nuclei. The increased thermal pressure makes the disc puff up, forming a geometrically thick structure. Hot gases are less likely to provide stable solutions in accreting systems, however a decreased accretion time scale can prevent thermal instabilities from disrupting the disc. Most hot accretion flow models are said to be advection dominated, implying that timescale for radiation to escape the disc can exceed the accretion timescale. These flow models are referred to as Advection Dominated Accretion Flows (ADAFs). Note that ADAFs and hot accretion are not identical concepts: although hot inflows are likely to be advective, cold ADAFs could also exist. For very high accretion rates (approaching the Eddington rate) a cold inflow can become sufficiently optically thick for some photons no to have enough time to escape the disc before passing the event horizon. The latter type of solution is referred to as a 'slim disc' [Yuan & Narayan, 2014].

Many current models combine elements from the different accretion types: using a hot ADAF in the central region, and a classic thin disc further outward. This approach is related to the concept of truncated discs, where the thin disc does not form all the way down to the ISCO [Blaes, 2014]. The presence or absence of different disc components is associated with 'hard' and 'soft' emission states, where hard states have a lower value of α_{OX}. Like many aspects of accretion disc modelling, this terminology is an analogy to accretion in black hole binaries. A combination of different accretion processes, as well as switching between states, are prominent among explanations for extreme quasar variability (e.g. Ruan et al. [2019]; Ross et al. [2018]; Noda & Done [2018]). The applicability of the 'hard' and 'soft states' to AGN accretion is still debated. An illustration of different accretion model components and their possible association with AGN accretion states is show in Figure 1.4.

The high temperature of hot central flows implies that the matter is not as strongly gravitationally bound to the black hole as the matter in cold accretion flows. This makes thermally and radiatively driven outflows probable. Some of this outflow is thought to take the form of a jet, whereas the rest will be a polar outflow in the form of a disc 'wind'. Although the precise jet formation mechanism remains unclear, it is likely associated with the magnetic field and

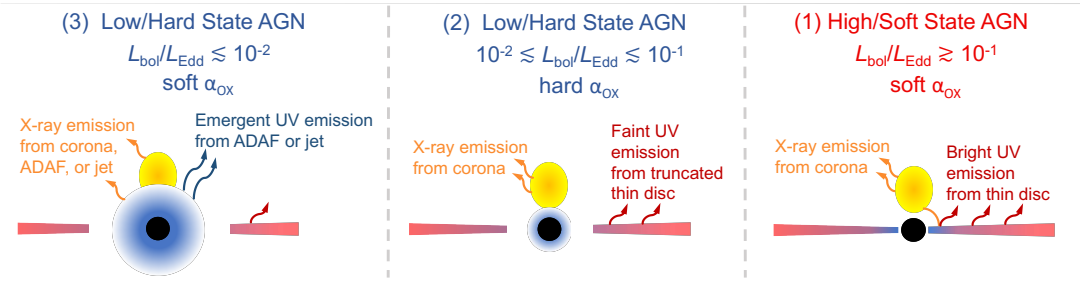

Figure 1.4: An overview of various AGN states as depicted in Ruan et al. [2019]. The states, marked by different values of α_{OX}, are associated with different model components and disc truncations. The components are a thin accretion disc (*red*), a hot inner accretion flow (*blue*), and an X-ray corona (*yellow*), the possible jet component in the lowest accretion state is not drawn. The phenomenological model illustrated here was developed to explain the extreme variability seen in a subset of AGN (see Section 1.4). The different accretion states are labelled by their Eddington ratio (L_{bol}/L_{Edd}). The figure on the right also illustrates the concept of X-ray reprocessing by the disc: coronal X-rays heat the thin disc, which increases its UV emission as a result.

rotational energy of the black hole and/or the inner accretion disc [Yuan & Narayan, 2014]. The propensity for jet formation in ADAF systems allows the theoretical accretion flow to be linked to observational parameters. Jet-mode AGN are more likely to found in 10^8 $M_\odot$ than in 10^7 $M_\odot$ black hole systems [Heckman & Best, 2014]. There is also an established connection between low luminosity AGN, low mass ($< 10^6$ $M_\odot$) AGN and jet formation [Ho, 2008]. These are indications that ADAFs and their associated jets can preferentially be found around very high mass and low mass black holes.

A modification of the thin disc model is illumination of the disc by a central X-ray source and reprocessing of these X-rays into UV radiation. This is illustrated in the right panel of Figure 1.4. The main motivation for the addition of X-ray reprocessing is to address the problem of simultaneous variability of the AGN continuum across optical and UV wavelengths (see Section 1.4). The geometry of this process requires that there is in fact a lag in response between different wavelengths, but that this lag is dictated by the light travel time from the central X-ray source to different regions of the disc. The light travel time is much smaller than e.g. the viscous time-scale associated with the disc.

Observations of NGC 5548 in X-rays and UV show such lags, although they appear too long for a standard thin disc size by a factor ~ 4 [McHardy et al., 2014]. It is possible that the disc is simply larger than expected [Dexter & Begelman, 2019], however Gardner & Done [2017] suggest that in the case of NGC 5548 reprocessing alone cannot reproduce the observed time-lags and X-ray SEDs. The model proposed by Gardner & Done [2017] consists of multiple components: a central corona produces hard X-rays, a puffed up inner disc produces soft X-rays and the edge of the geometrically thick inner disc irradiates the thin outer disc. Changes in the central region travel outward on a thermal timescale, heating the inner disc, resulting in stronger irradiation of the UV producing thin disc. This interpretation is refuted by Goad et al. [2019] however, who stress the importance to the UV of BLR continuum emission. This is based on an observed decoherence of the EUV and FUV continuum in NGC 5548 during an anomalous drop in luminosity in 2014. The presence of BLR continuum emission and its contribution to UV lags is also shown to exist in NGC 4593 [Cackett et al., 2018].

There are, in conclusion, many forms the accretion process can take and these can be linked to different classes of AGN (e.g. Blaes [2014]; Heckman & Best [2014]). The thin and slim disc accretion types are likely associated with quasars and luminous Seyfert galaxies. These objects accrete matter efficiently, with an Eddington ratio greater than $\sim 1\%$ and form the same category as the radiative mode objects. Similarly, objects with an optically thin ADAF in the inner region of the disc can be associated with jet-mode AGN. In these objects the efficiency of accretion is lower on average, and the jets can carry away a significant portion of the generated energy in bulk kinetic form.

1.2.2 Emission Lines

The emission formed in the accretion process is partially reprocessed in the Broad Line and Narrow Line Regions. Estimates of the covering factor of broad line forming material (as seen by the continuum) range from 0.1 [Netzer, 2013] to 0.3 [Stern & Laor, 2012]. In order to model the BLR it is necessary to understand the processes that govern how the lines are formed. The observed response of broad line emission to variations in the continuum (Section 1.3) indicates most line formation is driven by photoionisation. This section will briefly describe the line forming mechanism and some observational characteristics of AGN broad lines.

The lines seen in the spectra of AGN (Figure 1.3) are formed by a process of ionisation, recombination, and a subsequent cascading de-excitation in the case of recombination lines, or by collisional excitation and de-excitation. Most of the broad emission lines are recombination lines, for which the strength of the line is an indicator of the amount of incident photons with sufficient energy to ionise the emitting atom. Figure 1.5 shows an overview of the associated energies for some of the most prominent elements for line emission. Table 1.2 lists the minimum ionisation energies for the elements that are central to the discussion in this thesis. Note that due to the difference in their ionisation energies H and the higher ionisation state of He respond to very different parts of the continuum SED.

In addition to the ionising flux, an important factor in the line formation process is the electron density (n_e). The fact that we can observe emission lines implies that the density in the line emitting regions is low enough to prevent establishing a thermal equilibrium, otherwise the collisional deexcitation-rate would be too high for the emission to form. Photoionisation heats the gas, and the gas cools through line emission, even though a fraction of the line photons are reabsorbed within the BLR. At the same time, n_e should be such that the recombination timescale is short enough to allow broad lines to respond to continuum changes on the light travelling timescale in the BLR. The electron density clearly distinguishes the BLR and NLR. Typical values of n_e (in cm^{-3}) are 10^9 for the BLR and 10^4 for the NLR, based on the limits set by the observed suppression of forbidden line emission, as well as by the presence or absence of density sensitive emission lines (e.g. CIII]λ1909). The sensivity to density comes from colisional suppresion of the line formation mechanism: if the pressure is too high, the lines cannot form. [Krolik, 1999; Peterson, 1997]. The difference between the regions in suppression of forbidden lines is observed as the presence of narrow lines associated with forbidden transitions (e.g. [OIII]λ5007), which are not seen as broad lines. The timescales associated with forbidden transitions are so long that collisional de-excitations prevent these transitions from occurring in the BLR. This observation sets a lower limit on n_e in the BLR [Netzer, 2013]. The relatively

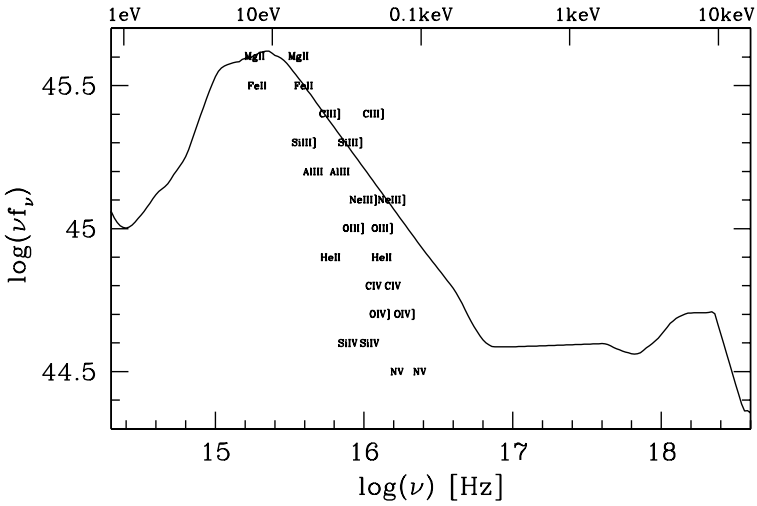

Figure 1.5: Ionisation potentials for common quasar elements. For each element the left marker is for the creation energy and the right marker the destruction energy. The latter represents the required energy to create the higher ionisation level necessary to form recombination lines. Vertical stratification correlates with the wavelength at which the most prominent lines resulting from recombination are emitted. The horizontal offsets show a clear stratification of ionisation energies from low ionisation lines (which also include those of Hydrogen at 13.6 eV) to high ionisation lines like NVλ1240. The included SED (*black line*) is an average for a radio-quiet AGN sample. Figure from Richards et al. [2011].

high values of n_e suggest that the material in the BLR is likely concentrated in condensations, or 'clouds' (see the discussion in the next section).

The profiles of the lines provide additional information about the physical condition in the BLR. The width of the broad lines is associated with motions of $\sim 10^3 - 10^4$ km/s, which far exceeds thermal broadening, which would be $\sim$10 km/s for the expected BLR temperatures. Similarly the observed widths exceed those expected for pressure broadening. In pressure broadening the high probability of collisional de-excitation (such as in the BLR gas) reduces the average time atoms in an excited state have to reduce their energy by emitting a photon, thereby increasing the spread in the emitted photon energies.

Peterson [1997] shows how a spherical, rotating distribution of clouds can form the observed Lorentzian line profiles. The smoothness of the broad lines indicates that if the lines are formed in clouds, the number of clouds is large. This constraint on the number of clouds can be reduced if turbulence adds to the smoothness [Goad et al., 2012] or if there is a strong contribution from gas among the clouds [Goad et al., 2019]. An alternative geometry to BLR clouds, such a filamentary structure, cannot be excluded, however.

The most prominent lines in AGN spectra are those associated with Hydrogen and Helium. The spectrum for a cloud of ionised H can be approximated by the simple Case A and Case B emission [Baker & Menzel, 1938]. In Case A the gas is modelled as optically thin to all lines, and in case B it is optically thin to all lines except the Lyman lines and the Lyman continuum. The line ratios predicted by Case B are is good agreement with observations from low density Galactic nebula. AGN spectra deviate significantly from these predictions however, such as for the Hα/Hβ ratio (the 'Balmer decrement'). Reddening could be a factor in this discrepancy too [Gaskell, 2017]. The optical depth of clouds is of significant influence on the emergent spectrum:

Table 1.2: Minimum ionisation energies and associated wavelengths for several ions relevant to the observations discussed in this thesis.

Ion	Energy (eV)	Wavelength (Å)
HII	13.6	911.6
HeII	24.6	504.0
HeIII	54.4	227.9
MgII	7.6	1631.4
MgIII	15.0	826.6

Netzer [2013] notes that for the inner regions of the BLR, the HeII Lyα line is one of the most prominent *emitted* lines, however many of the line photons do not escape the cloud.

Beyond the H and He lines, the emission processes for metals can also be modelled, where Magnesium is of particular importance for the discussion here. The most prominent spectral feature of Mg in the UV/optical range is the MgIIλ2798 doublet ($\lambda\lambda$2798,2803). Limits in spectroscopic resolution and a spatially extended, heterogeneous emission region mean that the doublet is almost always observed as a blend. Photoionisation modelling indicates that the MgII doublet is caused by collisional excitation and that the recombination of MgIII is of negligible importance [MacAlpine, 1972; Guo et al., 2019]. Neutral Mg is photoionised, after which a collisional energy of 4.4 eV (2798Å) is required to bring the atom into its excited state. The similarity of the ionisation energies of H and MgII (Table 1.2) implies that MgII emission is suppressed in HII regions of the clouds through photoionisation of MgII into MgIII. On the other hands, the dependence on free electrons for collisional excitation reduces MgII emission in HI regions. For these reasons the MgII emitting region is likely formed in the transition region between HI and HII, where the Balmer opacity is high [MacAlpine, 1972; Netzer, 1980; Collin-Souffrin et al., 1986; Krolik, 1999; Guo et al., 2019].

The dependence of the atomic transitions on the prevalent conditions in the gas, makes the emission lines in AGN useful diagnostic tools. Various ratios of the H spectrum can be used to determine reddening and approximate the ionising flux. The ratios with other lines of H can be used to establish the gas metallicity [Netzer, 2013]. Many other line combinations can be used to similar ends, for example: the ratio of [OIII]λ5007/[OIII]λ4959 can be used to calibrate observational data, as it should always be 3:1, and the ratio [OIII]λ4363/[OIII]λ5007 is an indicator of temperature due to its dependence on collisional excitation. The strength of particular line ratios ([NII]λ6584/Hα and [OIII]λ5007/Hβ) can be used to distinguish AGN from other galaxies, as AGN form a specific subset in this parameter space [Baldwin et al., 1981].

An important classification based on the emission lines is that of type 1 and type 2. The distinction is made on the presence or absence of the broad Hβ line in the spectrum. Intermediate types, such as 1.9 and 1.5 also exist, showing increasing strength of broad Hβ [Khachikian & Weedman, 1971; Osterbrock, 1977; Osterbrock, 1981]. As discussed in Section 1.1 this classification is closely tied to the concept of AGN unification: the presence or absence of broad lines can be associated with the viewing angle and obscuration of the BLR by the dusty region. The observed changing of spectral type for some AGN, as well as the possible existence of 'true' or 'pure' type 2 AGN challenge this view, however (Section 1.4).

An interesting correlation, or rather a number of correlations, among emission lines, first described by Boroson & Green [1992], is usually referred to as Eigenvector 1. This concept

connects an increasing FeII emission strength (in a wide complex of lines), with a decreasing Hβ FWHM, and an increasing [OIII]λ5007 peak intensity. The change in the Hβ line profile can further be linked to the classification of AGN into population A and B sources (e.g. Sulentic et al. [2016]). This classification scheme, based primarily on the width of Hβ, makes a coarse match to the distinction between radiative mode and jet mode AGN, as radio loud sources primarily belong to population B. A link between Eigenvector I and the Eddington ratio, which separates jet and radiative mode sources, is claimed by Shen & Ho [2014]. The authors show that the [OIII] strength anti-correlates strongly with the FeII strength, even for a subset of data with the same L_{bol}, implying both characteristics rely on the SED shape, which is set by the accretion rate.

A trend that is observed for the high ionisation CIVλ1549 line is a blueshift with respect to the quasar restframe. The restframe is usually defined by the MgII redshift, which has been found to be approximately systemic, although with large uncertainties [Shen et al., 2016c]. The shift in the CIV line centre has been associated with a motion of the line emitting material relative to the rest of the AGN. This has led to the association of the CIV line with a BLR outflow (see Section 1.2.3: the discussion on Gaskell [2009] for an alternative interpretation). In a study based on SDSS DR7 data, Richards et al. [2011] show an anti-correlation between luminosity and blueshift, and an anti-correlation with radio loudness. The authors argue that the underlying cause is also responsible for the Baldwin Effect.

The Baldwin Effect is one of the most prominent correlations in AGN spectra, and relates the equivalent width (EW) of various emission lines to the luminosity, or continuum strength [Baldwin, 1977; Baldwin et al., 1978]. In general the EW of a line goes down as the luminosity goes up. This anti-correlation was first detected for MgIIλ2798 and CIVλ1549, and soon established for most other lines (see the reviews by Osmer & Shields [1999] and Dietrich et al. [2002]). The effect is defined as the slope $\Delta\log(\mathrm{EW})/\Delta\log(L_{continuum})$. The Baldwin Effect is dependent on the ionisation level of the line: the EWs of high ionisation lines show a stronger anti-correlation with the continuum. A notable exception to this trend is the EW of NVλ1240, which shows almost no correlation. The BE appears to be independent of redshift, which indicates it is not strongly related to AGN evolution [Richards et al., 2011]. The original hope was to use this effect as an independent estimate of L_{bol}, allowing AGN to be used as cosmological standard candles. There is, however, considerable scatter in the correlation.

The scatter in the Baldwin Effect can partially be explained by AGN variability, as single epoch observations of an individual AGN may catch the object as it is transitioning between different luminosity states. This would observe the BLR before having fully adjusted to the new luminosity level. However, there is an additional trend in the correlation which shows a steeper slope for more luminous objects, indicating that an intrinsic difference among AGN plays a role [Osmer & Shields, 1999]. The Baldwin Effect can be seen when comparing single epoch observations for multiple objects (the ensemble Baldwin Effect, eBE), as well as when comparing multiple epochs for a single object (the intrinsic Baldwin Effect, iBE). The slopes of the iBE are considerably steeper than those of the ensemble effect. For example, the ensemble BE of CIV shows logarithmic slopes of -0.1 to -0.3, whereas for the intrinsic BE these values are -0.3 to -0.9 [Osmer & Shields, 1999]. Examples of the eBE can be seen in Figure 1.6. The left hand plot shows the effect for CIV, the right hand plot for MgII, with slopes of -0.19 and -0.16 respectively. The CIV eBE has been shown to correlate not just with the UV continuum, but also with α_{OX} [Richards et al., 2011].

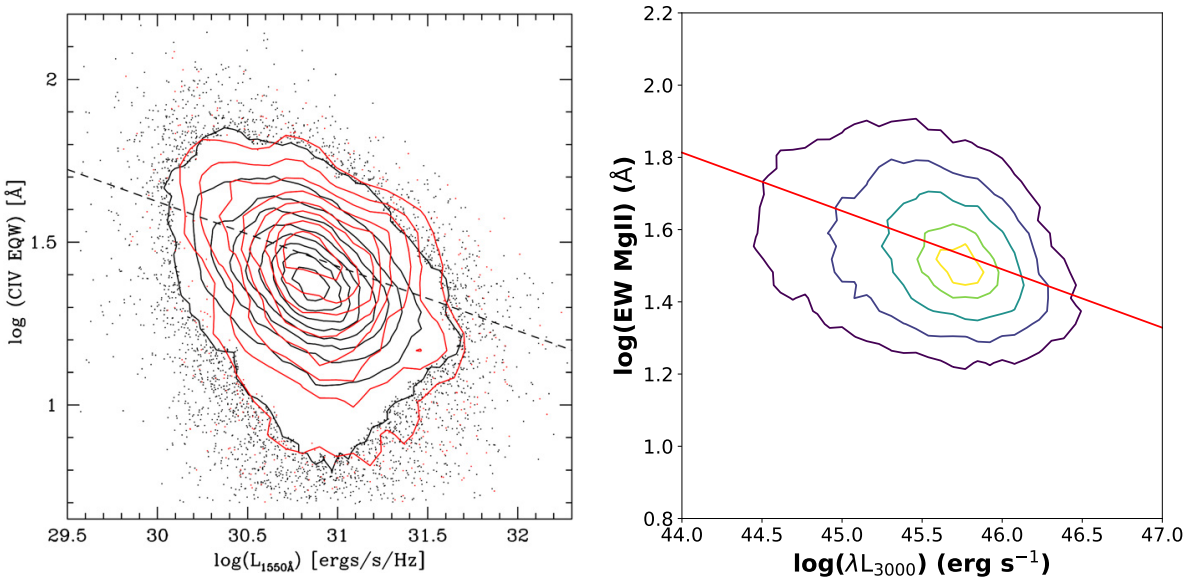

Figure 1.6: The ensemble Baldwin Effect for the CIVλ1549 and MgIIλ2798 lines, the correlation between the two quantities is clearly visible for both lines. The slope is steeper for the high ionisation line CIV. The vertical axes represent the EW of the lines, and the horizontal axes are a measure of the continuum luminosity. Both plots are based on SDSS DR7 quasars. $left$: CIV; the AGN sample is split into radio loud (red) and radio quiet (black) sources. The dashed line is the average BE calculated by of -0.20 Wu et al. [2009] (Figure from Richards et al. [2011]). $right$: MgII; I have made this plot using data presented in Shen et al. [2011]. The slope of the linear fit to these data (red) is -0.16.

The connection between eBE slope, as well as with the hardness of the spectrum has led to increased confidence in the theory that the ensemble Baldwin Effect is caused by a changing SED. In this interpretation brighter objects tend to have softer spectra: the UV output increases, but the FUV spectrum actually goes down. As a result the ionising flux that powers the line emission decreases, whereas the continuum in the spectral range of the emission line increases. We observe this as a decrease in the EW. In the argument put forth by Richards et al. [2011] this is connected to the blueshift of CIV through the impact of the ionising flux on the disc wind. The outflow rate of this wind can have a negative response to an increase in ionising flux (see the discussion in Section 1.2.3).

1.2.3 Modelling the BLR

The Broad Line Region provides some of the most important diagnostic information about the inner workings of AGN. The emission lines represent reprocessed energy from the ionising part of the spectral continuum. This part of the continuum is obscured from us, but quite likely contains the peak output of the SED. Second, the motion of gas in the BLR is dominated by the gravitational potential of the central SMBH. Therefore information about gas kinematics can be used to estimate the black hole mass. Although the BLR has been a topic of study for decades, many aspects of BLR kinematics and the ionisation structure of the BLR gas are still debated (see e.g. Peterson [2006]; Netzer [2013]; Lawrence [2016]; Czerny & Naddaf [2018]). In this section I will list the basic parameters of the BLR, introduce the fundamental concepts of

AGN modelling, and discuss the most relevant models of BLR physics.

The diversity in BLR models is so extensive that it can be difficult to find any part on which they agree. There are various observational characteristics of the BLR that need to be explained. Key features that any model needs to cover are that high ionisation lines (e.g. CIVλ1549, HeIIλ4686) are broader than low ionisation lines (e.g. the Balmer lines), that some lines, in particular CIVλ1549, show a clear blueshift with respect to the other lines, and that high ionisation lines respond on shorter timescales (Section 1.3; the stratification of the BLR is evident in Figure 1.5). Theoretical approaches differ considerably. Material in the BLR is modelled as an inflow, an outflow, or as a mixture of the two, and usually with a rotational component to its motion as well. The geometric distribution of the gas is depicted as either spherical or disc-like, and the location of the line emission differs among models as well. Most models do agree on two things: the BLR is located in the region between the central engine and the dusty obscurer and the material in the BLR is distributed in clouds.

The evidence for the BLR location inside the inner radius of the dusty region is mostly based on the fact that the broad lines are obscured by dust in some AGN, evidenced by their absence in type 2 AGN (although there are possibly other effects involved there as well, see Section 1.4). This is supported by observations of broad lines in polarised light in some type 2 AGN, where the broad line photons have been scattered inside the dusty regionor the NLR (e.g. Ramos Almeida et al. [2016]). Conversely: the fact that we are able to observe the broad lines implies that they are formed in a dust free region, arguably inside the dust sublimation radius, otherwise broad line emission would have been suppressed and absorbed by the dust [Netzer & Laor, 1993]. The BLR must lie outwith the continuum emitting region, as the incident ionising flux needs to be low enough to allow the recombinations and atomic de-excitations that form the lines. The precise location of the inner and outer radii of the BLR differ strongly from model to model, however.

Observations of the size of the BLR are based on Reverberation Mapping (Section 1.3.2). Results from RM campaigns based on Hβ in 70 AGN are shown in Figure 1.7. This study confirms previous results that showed that the size of the BLR scales with luminosity to the power 1/2. Another key finding of reverberation mapping studies is that the radius of the BLR (R_{BLR}) depends on the line used for the measurement: high ionisation lines such as CIVλ1549 are found at smaller radii than e.g. Hβ. This is a stratification of the BLR. If the BLR gas is in approximately Keplerian motion around the black hole, the smaller radii would explain the broader line width found for higher ionisation lines.

The motivation for a cloud-like distribution of the line emitting gas consists of a number of observations. First is the presence of condensations in other regions of ionised gas, such as galactic HII regions: if clouds are likely to form there, they could also form inside the BLR [Peterson, 1997]. Second, the speeds associated with the broadening of the lines, $\sim 10^4$ km/s, are likely to be supersonic in the thermal conditions associated with the BLR gas, where $c_s \sim 10$ km/s [Krolik, 1999]. Bulk motion of clumps of gas, possibly through a lower density medium, would not require a large supersonic flow. Finally, X-ray obscurations in nearby AGN have been observed on time-scales that put the localised obscurer within the BLR radius [Maiolino et al., 2010]. BLR clouds would fit this observation well.

An additional argument for a cloud-like, or at least non-uniform, distribution of gas in the BLR can be made by calculating the filling factor. The filling factor is the total volume of line emitting gas and is found by integrating a profile of line emissivity (for a particular emission

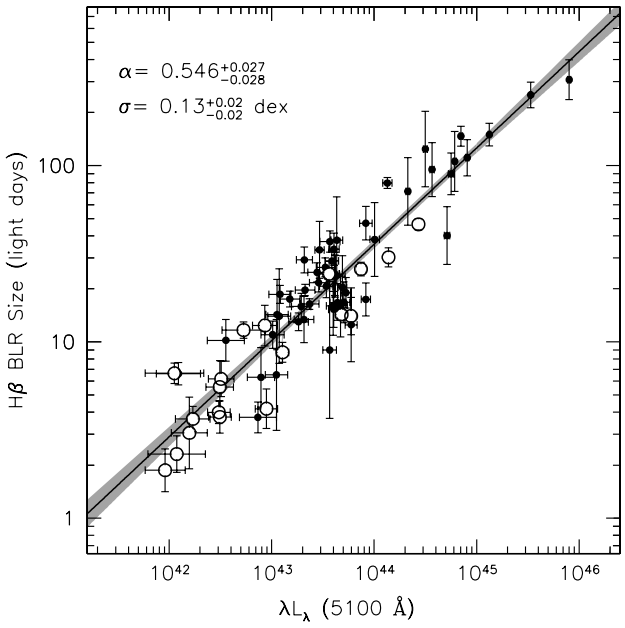

Figure 1.7: Size of the BLR in light days based on Hβ RM, versus the spectrophotometric luminosity at 5100Å. The measurements are based on a total of 70 AGN. The grey band indicates uncertainties in the model fit, α represents the power law index (equation 1.7), and σ the scatter in the data around the fit. Following correction for contamination from the host galaxy these data indicate an $R_{BLR} \propto L^{1/2}$ relation, which extends into the low luminosity regime (Figure from Bentz et al. [2013]).

line) over the volume of the BLR. The volume of the BLR is set by Reverberation Mapping results for the line in question. Reverberation Mapping is an observational technique that tracks the response of different line forming regions to the central engine to fluctuations of the continuum, in order to estimate the radial distances to the central engine. This technique will be discussed in more detail in Section 1.3.2. The filling factor is found to be quite low, $\sim 10^{-6}$, if one assumes electron densities appropriate for the BLR [Peterson, 1997]. This indicates that most of the BLR emission comes from small condensations inside the BLR volume.

The general characteristics of the broad line emitting gas can be deduced from the emission line spectrum [Peterson, 1997; Krolik, 1999; Netzer, 2013]. The relative suppression of forbidden transitions in the BLR indicates a high density, with an estimated electron density $n_e \sim 10^9$ cm^{-3}. The BLR temperature is $\sim 10^4$ K, although a clumpy gas distribution will inevitably lead to a more complex temperature structure. The BLR gas is also thought to have solar or even super-solar metallicity, which is evidenced by the prominence of strong C, N, O, and Mg emission lines. Based on the equivalent width of the emission lines, it is possible to estimate the total amount of energy reprocessed by the BLR and the covering factor. Most models find a BLR covering factor of approximately 10%, although this estimate becomes more complicated if one considers a mix of optically thin and optically thick gas [Stern et al., 2014]. What is most remarkable about these conditions is that they appear to be quite universal: regardless of size and luminosity, the BLR looks similar in all AGN. Stellar-mass accreting black hole binaries lack a BLR equivalent: this feature appears intrinsic to AGN alone.

Table 1.3: Estimates of the size, density n_e, and ionisation parameter U across the AGN population. The size is given in gravitational radii, $r_g = \mathrm{GM}/c^2$. Adapted from Netzer [2013].

Component	Size (r_g)	Density (cm^{-3})	U
Accretion disc	10^2	$\sim 10^{15}$	–
BLR	10^4–10^5	$\sim 10^{10}$	10^{-2}
Dusty Obscurer	10^5–10^6	10^3–10^6	–
NLR	10^7–10^8	10^3–10^5	10^{-2}

One of the most important parameters in the modelling of photoionisation in the BLR is the incident ionising flux. Using the ionisation energy of H as the limit, the ionising flux is usually combined with n_e to define the ionisation parameter, which is the ratio of the number of ionising photons to the number of hydrogen atoms in a given volume:

$$U = \frac{\mathrm{N}_{ion}}{4\pi R^2 c \cdot n_H}. \tag{1.6}$$

Here N_{ion} is the total number of ionising photons emitted by the source, assumed to be emitted isotropically. This value depends strongly on the shape of the SED. The ionisation parameter is a meausre of the fraction of atoms that can be expected to be ionised. U can be defined for individual BLR clouds, and could have a complex dependence on the BLR geometry. However, the similarity in BLR appearance across much of the AGN population implies that the distribution of U over BLR clouds is remarkably universal, over several orders of magnitude in luminosity. An overview of values of U for different parts of an AGN is given in Figure 1.3.

An often used distinction between two limiting cases of ionisation is 'radiation bounded' and 'matter bounded'. The first case refers to partially ionised clouds, where a higher incident flux will lead to a larger number of ionisations and recombinations. The second case describes a fully ionised cloud, where an increase in ionising flux can only suppress recombinations and de-excitations. Clouds closer to the central engine are more likely to be matter bounded (fully ionised). The limited capability of forming H (and He) lines in these innermost clouds implies their contribution to the observed line profile is small [Korista & Goad, 2004]. A BLR cloud with a larger contribution will consist of an ionised part, facing the source, and a radiation bound (partially ionised) part on the opposite side [Peterson, 1997]. This immediately introduces a geometric complexity in this model, as the non-ionised gas functions as an obscurer, making the clouds' emission anisotropic. In the LOC ionisation models discussed below, the visibility of cloud emission along our line of sight is modelled as similar to the phases of the moon [O'Brien et al., 1995].

Based on simple photoionisation arguments it is possible to make an estimate of the size of the BLR. If one ignores self-shielding of BLR clouds, the ionising flux has an inverse square dependence on the radius. A further assumption to make is that the outer edge of the BLR is at the largest radius where the flux is still sufficiently high to ionise enough atoms for a detectable contribution to the emission line. Note that this outer radius is likely to be different for different lines. Under these assumptions the size of the BLR is expected to scale according to the power law

$$\mathrm{R}_{\mathrm{BLR}} \propto \mathrm{L}^{\alpha}. \tag{1.7}$$

Here L is assumed to be the bolometric luminosity, although the scaling relation is tighter if the ionising luminosity alone is considered (see below). Netzer [2013] cites a value of $\alpha = 0.6 \pm 0.1$. A study by Bentz et al. [2013] that corrects for host galaxy contamination, which is of particular concern for low luminosity AGN, finds $\alpha \approx 0.53 \pm 0.03$. Bentz et al. [2013] also cite NGC 5548 as a potential outlier to this relation: measurements of the R_{BLR} for this AGN at different epochs yield different scaling laws between L and R_{BLR}. A possible solution to this issue is presented in Peterson [2006], who argues that when the luminosity dependent relation between the UV and optical part of the SED is taking into account, one again finds a value $\alpha = 0.5$. In other words: R_{BLR} always scales with L_{UV} even if a changing SED distorts the scaling with L_{opt}. The assumption underlying this correction is that the size of the line emitting region is controlled by photons with E>13.6 eV.

If a relation between BLR size and luminosity could be firmly established for all AGN, luminosity-independent measurements of the BLR size could be used to find luminosity distances for AGN. This would turn them into cosmological standard candles. The universality of the $L^{1/2}$ scaling relation is not entirely clear, however. Results from spectroscopic interferometry of the Paschen α line in 3C 273 show that the size of the BLR is at the very low end of size estimates based on other methods, in particular on Reverberation Mapping [Gravity Collaboration et al., 2018]. The authors of this study also note this difference agrees with results that indicate a flattening off in the R∝L relation for high luminosity objects.

A final important model parameter is the Hydrogen column density, N_H. This parameter indicates the optical depth for ionising radiation along our line of sight, and is estimated to be at least 10^{22} cm^{-2} for the BLR. In cloud-based models the line emitting regions consist of high n_e, high U, and high N_H material. For a full description of the BLR it is therefore necessary to understand how these dense regions are formed *and* stay around long enough to contribute to the line emission. The cloud formation mechanism is not properly understood, but it is clear some form of containment is required. The first cloud models (e.g. Goad et al. [1993]) considered a balance in gas pressure between the cloud and intercloud medium, however Peterson [1997] points out that this would require too high a temperature for the intercloud gas. Currently viable models are thermal, magnetic, and radiation pressure confinement. Cloud confinement determines both the formation mechanism and the lifetime of BLR clouds. It is unlikely that these clouds will last many dynamical timescales (see Figure 1.4), and therefore the BLR cloud population needs to be constantly replenished. Not just the kinematics, but also the very presence of broad line emitting gas is therefore subject to change.

Below I will discuss models of the broad line region, which fall into two broad categories. The first attempts to recreate the BLR spectral features through full radiative transfer modelling of the line emitting regions. The second class of models focusses on the kinematics of the BLR and attempts to understand key spectral features by modelling the cloud formation and distribution. One of the main problems in modelling the line formation process is the uniformity of the BLR signature. To create similar broad line emission over a large range of luminosities and black holes masses would appear to require an uncomfortable amount of fine-tuning. One of the most promising solutions to this problem is the concept of Locally Optimally emitting Clouds (LOC, Baldwin et al. [1995]). Rather than placing the right clouds at the right U in every BLR, this approach assumes there are clouds with a distribution in N_H and n_e at every radius and only those clouds whose conditions meet the right line-forming criteria under U at their location will contribute to a given line profile.

The LOC approach has inspired a series of studies that explore the effects of illuminating such a distribution of clouds with a quasar continuum SED. These papers generally rely on the CLOUDY photoionisation and radiative transfer models [Ferland et al., 2013]. In the seminal model presented in Korista & Goad [2000] the authors attempt to match the observed BLR spectrum from the well monitored Seyfert I NGC 5548. The BLR is modelled as a spherical volume within which both the number density of clouds as well as n_e of each cloud drops off according to a power law. All clouds are bound in gravitationally determined orbits. This BLR therefore lacks significant inflow or outflow. The authors note that both the ionising flux and collisional (de-)excitations are relevant factors in calculating the occupancy of various atomic energy levels. The main success of the model is that it is able to reproduce the observed BLR stratification by following the LOC assumption. Different lines will form most efficiently at different radial distances, which approximately match the RM time lags. Figure 1.8 shows an example of radial emissivity profiles for different line species. A drawback of the LOC modelling approach is a degeneracy with regard to the cloud distributions and densities: it is always possible to select the specific cloud configuration that will produce the correct spectrum and line emissivity, as the cloud distribution is observationally poorly constrained.

The response of emission lines to a changing continuum, of particular relevance to the topic discussed here, is explored by Korista & Goad [2004]. The focus of the study is on the H and He lines. An important concept for this type of modelling is the responsivity: the efficiency of the BLR gas to convert a change in the number of incoming ionising photons into line photons that escape the cloud. Note that this is an *instantaneous* measure, it corresponds to atomic de-excitation timescales for permitted lines ($\ll$1 second). Following Korista & Goad [2004], the responsivity of a line is defined as:

$$\eta(r) = \frac{\Delta \log F(r)_{line}}{\Delta \log \Phi(r)_{\rm H}}, \tag{1.8}$$

where $F(r)_{line}$ and $\Phi_{\rm H}$ are the emitted line flux and incident ionising flux respectively. For very high levels of incident flux and high densities (both more prominent in clouds at small radii), the authors find that the responsivity becomes negative. This is explained as an increase in the optical depth for line photons emitted inside the cloud, as the number density of H and He atoms occupying higher energy states increases. The optical depth effect is strongest for the Balmer lines. This effect shifts the flux-response of the BLR to clouds at larger radii. For even higher ionising fluxes the clouds could become fully ionised, and line formation thermally suppressed. This is referred to as over-ionisation. The flux dependence of η implies that the responsivity is highest for objects that are in a state of relatively low luminosity. The results from ionisation modelling indicate that HeIIλ4686 should be among the most responsive lines, although the responsivity flattens off to approximately 1:1 at larger radii. The response of the Balmer lines increases at larger radii.

The dependence of the line responsivity on the initial continuum level also provides an explanation for the so-called 'AGN breathing'. This is the observed change in the lag of the line response to continuum fluctuations, under a changing luminosity (see Section 1.3.2 for further discussion). Breathing has been observed in RM studies (e.g. De Rosa et al. [2015]; Barth et al. [2015]). In LOC terms, breathing implies that the optimally emitting region moves radially outward as the luminosity increases and the responsivity changes with luminosity. If the responsivity were constant with initial luminosity the lag time would depend on a fixed

radial emissivity profile. The authors stress the importance of the continuum history for a full understanding of line responsivity, as it is the historical continuum that has set current BLR conditions. Note that AGN breathing does not require a physical change in the BLR itself: different pre-existing BLR regions are lit up by the continuum as the luminosity changes.

A more detailed model, which relies on the two papers discussed above, is presented in Goad et al. [2012]. This model investigates the implications of a non-spherical geometry. The motivation for this break in symmetry is a number of studies which purportedly show a flattened geometry for CIV, and a more spherical geometry for Hβ clouds. This is partially in contrast with results from Shen & Ho [2014], who claim a flattened BLR geometry is indicated for Hβ as well. The study by Shen & Ho [2014] is based on a comparison of the FWHM of Hβ in a sample of radio-loud quasars, which reveals a strong dependence on orientation. To account for the difference in distributions between the line forming regions Goad et al. [2012] model the BLR clouds as spread over a bowl shape. High ionisation lines are in the relatively flat inner regions, whereas e.g. Hβ clouds are located in a region with a considerably larger scale height. The clouds form the upper layer of this bowl, and underneath is a thick layer of shielded gas, which also allows dust grains to exist well within the sublimation radius. This is similar to a geometry suggested in Gaskell [2009] (discussed below). The vertical pressure required to sustain this shape is supplied by turbulence. Another effect of the turbulence is that lines that form further outward (such as Hβ and MgII) are less susceptible to inclination effects.

Although orientation and turbulence do play a role in line responsivity, Goad et al. [2012] find that the ionisation stratification and the associated radial responsivity profile are the dominant factor in determining line response. The radial profiles calculated for the bowl-shaped model are shown in Figure 1.8. The importance of the radial emission profile is further emphasised in Goad & Korista [2014]. The authors argue the emission profile is dominant over all other factors in determining both the responsivity and the emergent line profile.

The physics that form the radial emission profile and responsivity in more complicated photoionisation models still resemble those of the far more simplistic single cloud models (e.g. Goad et al. [1993]; O'Brien et al. [1995]). From these older models it is possible to understand the behaviour of the H and He lines as follows: when U increases, the H emissivity goes up until the H gas becomes fully ionised. The emissivity will drop once U is so high that the gas temperature suppresses recombination. Helium follows H in this pattern, but at higher values of U. A difficulty in modelling is that the responsivity is inherently non-linear, as changing continuum conditions (on timescales greater than τ_{lt}) can produce *structural changes* in the BLR, whereas the responsivity (equation 1.8) is defined as instantaneous. One expected feature is that responsivity functions will be shifted downward by an increasing U, as the line emission saturates, and turn negative for higher values of U due to overionisation and high temperatures.

With respect to MgIIλ2798 the LOC papers note that it is expected to have a similar responsivity to the Balmer lines. For these line species optical depth effects reduce the responsivity at small radii. In a non-spherical BLR a vertical force is required to maintain a thick geometry, and as argued in Goad et al. [2012] this is most likely to be turbulence. This is in turn implies that lines that form further out, such as MgII, are most susceptible to any effects turbulence induces, such as a smoothing of the line profile. Korista & Goad [2000] note that MgII is the most difficult to model among their chosen emission lines, as it is affected by both Balmer line transmission and continuum changes. A complex pattern of behaviour can therefore be expected for the MgII emission line.

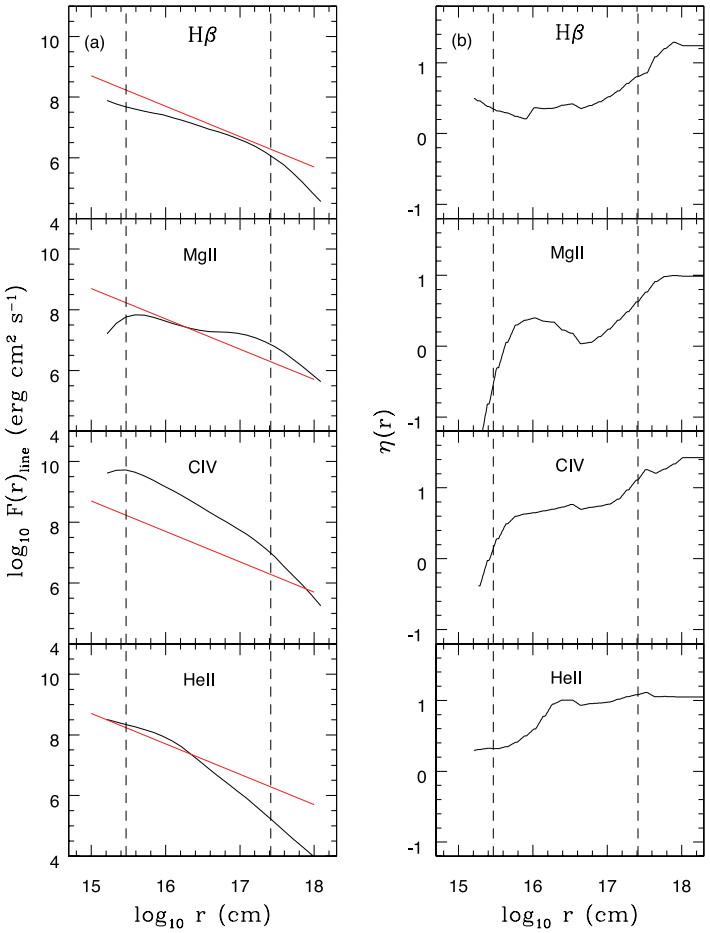

Figure 1.8: The radial emissivity ($left$) and responsivity ($right$) profiles for the 'bowl shaped' BLR model. The red line in the plots of the emissivity profile is a reference emissivity distribution which scales as r^{-1}. The dashed lines indicate the approximate inner and outher radius of the BLR. The emissivity profile shows the relative contributions of clouds at different radii to the profile of a given line. The responsivity profile show the propensity of the line emission to change if the incoming ionising flux were to increase. The steep gradient of the HeII emissivity indicates that the line profile is dominated by emission from clouds at small radii. Note the negative responsivity for MgII at small radii, which would be the result of overionisation. Figure from Goad et al. [2012].

The demarcation between different AGN components is not clear (e.g. Czerny & Naddaf [2018]), and indeed several authors depict the inner radii of the AGN as a continuous region, where disc, BLR and dusty torus are all part of the same structure (see e.g. Gaskell [2009]; Elitzur & Ho [2009]; Goad et al. [2012]). In this view the BLR-torus boundary is simply set by the sublimation radius. The connection between the accretion disc and BLR is less clear, but as pointed out by Netzer [2013] and discussed in Section 1.2.1, disc outflows are a natural part of several accretion models. Any gas lifted above the accretion disc could be accelerated by the pressure from the continuum flux, enhanced by line driving. This idea created the class of models that describe a 'disc wind' [Elvis, 2000]. The outflow associated with this wind could explain the observed blueshift of the CIVλ1549 line [Richards et al., 2011], as well as asymmetries in CIV and other high ionisation lines [Peterson, 2006].

Once some gas has been lifted above the disc, and has an unobstructed line of sight to the continuum source, the speed the line can achieve will depend on the incident flux and N_H. Modelling the effect of radiation pressure in AGN, Netzer & Marziani [2010] show that, under the assumption of a radially dependent cloud confinement mechanism, a disc wind (or any system that lifts material from the disc) will produce clouds with a wide range of N_H across the BLR. This appears in agreement with the basic assumptions of the LOC approach. A sudden increase in L_{bol} will knock a large fraction of clouds out of a virialised state, which in the model proposed by Netzer & Marziani [2010], leads to a precessing elliptical orbit. Elliptical orbits are found by Pancoast et al. [2014] in the Lick AGN data-set.

Clouds that contribute to the broad line emission are those that are not driven out of the BLR on timescales smaller than τ_{dyn}. Conversely, the cloud formation mechanism can stop when the accretion flow is too low. Based on mass conservation arguments, the replenishment of BLR clouds can falter for objects where the Eddington ratio is too low. This has also been suggested as an arguments for the existence of 'true' type 2 AGN [Elitzur & Ho, 2009; Elitzur & Netzer, 2016]. The correlation between the existence of a disc wind and a minimum accretion rate for BLR formation is also stressed by Giustini & Proga [2019].

The radiation pressure of the UV continuum forms a good candidate to power a radiatively driven outflow in the central region. The radius at which such an outflow would occur ($\sim$100 r_g) does not match that of the observed BLR, however. It could be linked to the very central X-ray obscuring clouds described in Maiolino et al. [2010]. A possible way in which a disc wind can be formed is through radiation pressure on dusty gas, as proposed by Czerny & Hryniewicz [2011]. The required disc surface temperature for dusty gas to be lifted is significantly lower than for dust free gas, allowing disc wind formation at larger disc radii (cf. equation 1.5) [Czerny & Naddaf, 2018]. This idea is further explored by Baskin & Laor [2018]. In the more detailed model presented by these authors, the disc wind forms an inflated clumpy disc, whose scale height increases with radius. The BLR is formed by clouds on the outer layer of the disc, akin to the geometry presented in Goad et al. [2012]. This type of BLR would be prone to structural changes in its vertical stratification, on a timescale of decades.

A more generic discussion of the disc wind model was discussed in Richards et al. [2011]. The authors relate this concept to both the eBE and the CIVλ1549 blueshift. The 'disc' referred to in this case is the flattened BLR geometry suggested by Chiang & Murray [1996]. The correlation described by the authors shows that an increase in luminosity produces a decrease in EW and an increase in line blueshift. A changing SED is used to explain both effects. In the case of the wind, an increase in L_{bol} implies a lower soft X-ray flux. This reduces the degree of

Table 1.4: Estimated timescales relevant to the BLR (see Figure 1.1 for the definitions). Estimates based on Lawrence [2016] and Elvis [2017], for a 10^8 $M_\odot$ black hole and a 10^3 r_g BLR.

τ_{dyn}	$\sim \frac{1}{\Omega}$	$\sim$ 10 years
τ_{sound}	$\sim \sqrt{\frac{\rho R^2}{P}}$	$\sim$ 800 years
τ_{light}	$\sim \frac{R}{c}$	$\sim$ 10 days

ionisation in the BLR gas, increasing the efficiency of momentum transfer by the UV flux. An anti-correlation of the blueshift with radio loudness also agrees with this interpretation. The population of radio loud AGN includes jet mode AGN, which are thought to have inefficient accretion flows, associated with a higher X-ray flux [Heckman & Best, 2014, Section 1.2.1].

A possible formation mechanism for clouds in the disc wind scenario is the 'quasar rain' model [Elvis, 2017] in which relatively cool clouds (T$\sim 10^4$ K) form within a hot (T$\sim 10^6$ K) wind. The high temperature of the surrounding gas will keep the clouds pressure confined. This is in contrast with the rejection of gas pressure confinement by Peterson [1997]. Elvis [2017] argues that a two-phase medium can be created as a result of the rapidly varying X-ray continuum. Stochastic X-ray variability rapidly changes the pressure and temperature of initial condensations in the wind, which alter the radiation pressure the gas is subjected to. Based on ionisation modelling, certain p,T-combinations are less susceptible to this effect, creating stable regions in phase-space where clouds congregate. This results in a multiphase medium and clouds with a uniform density. Within the accelerating wind the dense clouds are relatively slow, and cannot reach escape velocity, falling back towards the equatorial plane, on an elliptical orbit, before being destroyed in the high speed wind.

The quasar rain model produces a flattened BLR geometry, in agreement with observations (e.g. Shen & Ho [2014]; Pancoast et al. [2014]), and matching the geometry of Chiang & Murray [1996]. Note that the intercloud gas in this model differs from the tenuous BLR component of the UV continuum that was observed in in NGC 5548 [Goad et al., 2019], as the the temperature (T$\sim 10^6$ K) is too high for broad line emission. It is possible the broad line emitting gas is located at larger radii. The clouds formed in the quasar rain model could plausibly form the gas distribution required for the LOC description. In similarity to models for the accretion disc, the quasar rain model relies strongly on arguments based on timescales. BLR clouds are expected to have a limited lifetime, therefore both their formation and expulsion from the central region need to occur before the clouds are destroyed again. BLR timescales also play an important role in the discussion of extremely variable AGN. An overview of the most important timescales is given in Figure 1.4.

The Radiation Pressure Confinement (RPC) model [Stern et al., 2014; Baskin et al., 2014a,b] is another cloud formation model, which attempts to explain the uniformity of the BLR among the AGN population, through a formation mechanism that produces $U \sim 0.1$ for all BLR clouds. This U is a factor 10 larger than the value cited by Netzer [2013] (Figure 1.3), however the authors cite convincing observational evidence to support this value. The main notion underlying the RPC model is that the continuum radiation will inevitably transfer momentum to the BLR gas. Unlike Netzer & Marziani [2010] the authors model all gas as gravitationally bound and assume that the radiation pressure balances the gas pressure of the

cloud. In this manner the radiation forms the cloud confinement mechanism. The value of U is calculated through photoionisation modelling of the conditions inside the cloud. The possibility of a UV driven outflow from these clouds is discussed in Baskin & Laor [2018]. The authors note that the ionised layer of the clouds can be sheared off under the UV pressure, forming an outflow in addition to a dust driven wind.

RPC results in a strong T and n_e gradient within the clouds. High T, low n_e, and highly ionised layers exist on the continuum side of the cloud, and a low T, high n_e layer exists at the back of the cloud, where low ionisation lines are formed. Results from photoionisation modelling are that $U{\sim}0.1$ for the inner regions of all clouds in the BLR. The temperature and pressure gradients per cloud change with distance from the continuum source, such that the local conditions result in $U \sim 0.1$. As is the case in the LOC model, each cloud contributes to all lines. Radiation pressure compresses the gas from the 'continuum' side and gas pressure from the cooler high n_e layers compress the cloud from the back. An example of the ionisation stratification inside an RPC cloud is shown in Figure 1.9. The 'cloud' is modelled as a single thick slab, which ionisation forms into a superposition of transparent layers covering a radiation bound back layer. In the traditional LOC model [Baldwin et al., 1995] there is a wide range of U and other parameters, that average out to a particular emission profile at every radius. Baskin et al. [2014a] point out that a dominance of $U \sim 0.1$ clouds is in agreement with observations and argue that this would require a fine-tuned cloud distribution. RPC, on the contrary, forms clouds which are structured by the balance of pressures to form an ionisation stratification per cloud that results in a $U \sim 0.1$ at every radius.

The radiative transfer modelling (performed with CLOUDY) on which these results are based, provides the resulting BLR stratification in the RPC model. Although the authors have not calculated the responsivity to continuum changes for this model, the stratification shown in Figure 1.9 does provide an indication. The first thing to note is that any increase in L_{bol} will not result in a change in the appearance of the BLR, as the gas and radiation pressure will again find a $U \sim 0.1$ equilibrium and the BLR will expand. The timescales on which this re-adjustment will occur are unclear, however. Any change in the BLR spectrum on long timescales (∼years) will need to be the result of a change in the SED. The authors state that a change in the spectral slope will affect different lines differently.

With respect to the ionisation regions in Figure 1.9, the sharpness of the edges to the HeIII and HII ionisation front are remarkable, as are their relative locations. It is possible to imagine a rapid increase in ionising flux, which would drive the HeIII front deeper into the cloud and would reduce the size of the HII region. This reduces the emitting volume for the H lines. Indeed, in the equilibrium state this is the case for clouds that lie at smaller radii in the BLR. The reservoir of neutral Helium explains the relative strength of response of HeII on shorter timescales (see Table 1.5). Under a rapid flux change this could alter the ratio of He and H recombination lines. Equally interesting is the very broad region of the cloud where MgII is present. Even under a sudden ionisation of a larger portion of the cloud, there is still a considerable fraction of the cloud available to produce MgII emission lines. Note also that the MgII region lies in the relatively low T region of the gas: the collisional excitation depends temperature, which means for a large part of the MgII region no 2700Å is produced [MacAlpine, 1972; Guo et al., 2019]. The MgII emitting region is therefore expected to be more geometrically confined [Collin-Souffrin et al., 1986; Krolik, 1999].

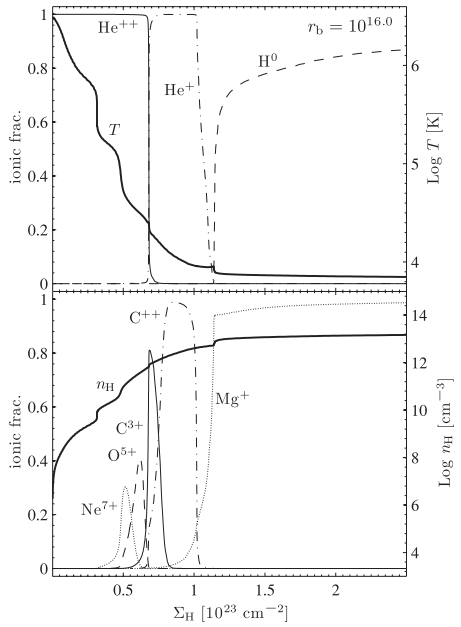

Figure 1.9: Example of the ionisation structure in a modelled RPC gas slab. The value r_b is the distance (in cm) of the back of the cloud to the SMBH and Σ_H is the hydrogen column density, measured from the front of the cloud. *top*: The radial temperature profile (with respect to Σ_H) and the ionisation fraction of H and He. *bottom*: The radial density profile and the ionisation fraction of various metals in the cloud. Of particular interest are the steep drop-off in the HeII population and the extended spatial region in which MgII is present. Figure from Baskin et al. [2014a], it is part of Figure 3 there.

The disc wind and LOC models have gained favour over recent years, and have proven relatively successful in meeting the requirements set by observations such as BLR stratification and emission line blueshifts. There are, however, alternative models that present a different interpretation of these observables. One of the most prominent of these models represents the BLR as part of the same continuous structure as the dusty torus and the disc [Gaskell et al., 2008; Gaskell, 2009, 2017]. An important assumption underlying this model is that the outflow from AGN is minimal, and disc, BLR, and torus are all in inflow. In this interpretation the blueshift of high ionisation lines can be explained through scattering of emission line photons off inflowing material.

A small outflow could be driven from the central region which is shaped like a flaring disc. This cone shaped geometry is quite similar to the bowl shape suggested in Goad et al. [2012]. The stratification of the BLR in this model follows from self-shielding by BLR clouds within the inflow. In the LOC models all clouds produce some of the emission for each line, their contribution depending on the degree of ionisation within the cloud. In the model presented in Gaskell [2009] the ionisation stratification is among the clouds: inner clouds have a higher degree of ionisation, and produce lines such as CIVλ1548 and clouds at larger radii produce low ionisation lines such as MgIIλ2798.

The relative suppression of the Hα/Hβ ratio (the 'Balmer decrement', see e.g. Berman [1936]), which is produced in LOC modelling, is explained in Gaskell [2017] as the result of reddening. The stratification based on cloud self-shielding would result in classic Case B emission [Baker & Menzel, 1938], which differs from observed AGN spectra. This case B emission ratio

can be reproduced if a specific extinction correction is applied to the AGN spectrum. Gaskell [2017] argues for the presence of dust inside the traditional sublimation radius (similar to Goad et al. [2012]), as the dust could be shielded by the surrounding gas. The further argument is that this inner AGN dust follows a different extinction law than interstellar dust, resulting in a correction that reproduces the expected Case B ratios. Based on the modelled ratio of Hα/Hβ, Korista & Goad [2004] note that case B emission for hydrogen recombination does not apply in their BLR approach.

As a final consideration, it is possible to do away with BLR clouds altogether, as suggested in Devereux [2018]. Instead of clouds reprocessing the continuum, the BLR is modelled as a large (up to 7 pc) sphere of ionised, low density gas. Most metal lines are formed outside this sphere. All gas in this BLR is in radial free-fall, creating another inflow dominated model. Possible evidence for a BLR component in free-fall is discussed in Richards et al. [2011]. The main strength of the model is the accurate reproduction of the line profiles of the Balmer lines, from such a small set of assumptions. A drawback of this model is that it fails to account for e.g. broad MgII emission. Predictions with regard to the responsivity of the lines to continuum changes are needed to prove whether this model is indeed a viable representation of the BLR.

1.3. AGN Variability

1.3.1 The Changing Continuum

Variability is inherent to AGN emission, occurs on many timescales, and affects all parts of the spectrum. The timescale and amplitude of fluctuations differ across the spectral range. The discussion here is limited to the UV/optical, where continuum variability can reach as high as a factor of two in flux for most AGN [MacLeod et al., 2010]. The UV and optical continua have been observed to fluctuate on a timecale of days to weeks. Larger changes occur on timescales of years. An important development in variability studies over the last decade has been continued AGN observations in large surveys. The Sloan Digital Sky Survey (SDSS) observations used for this thesis are an example of data-sets that include at least two observations for many AGN [Schneider et al., 2010; Abolfathi et al., 2018]. Surveys allow for the investigation of variability on a much more complete sample of the AGN population than case studies. They provide information on AGN behaviour on longer timescales and allow for the possible discovery of extreme or unique objects [Lawrence, 2016].

The correlation of the amplitude of continuum fluctuations with wavelength is clear in the difference between the UV and optical continuum: on the timescale of weeks, changes in the rms of the UV flux can be $\sim$30%, whereas the rms of the optical flux changes $\sim$3%. On the timescale of years, however, the optical flux can reach a similar amplitude of variability, indicating it may need some time to 'catch up' with UV fluctuations [Lawrence, 2016].

Another prominent wavelength dependent effect for individual AGN is a change in shape of the SED. This effect, referred to as 'bluer when brighter', represents a hardening of the optical spectrum, as the big blue bump becomes more prominent. It was first established by Paltani & Courvoisier [1994], and has since been confirmed in various samples [Vanden Berk et al., 2001; Schmidt et al., 2012; Kokubo et al., 2014; Lawrence et al., 2016]. The study by Kokubo et al. [2014] indicates that the hardening of the optical continuum is associated with the accretion disc. The authors find that the flux difference spectrum (the difference between two spectra) in

the optical range is constant on a timescale of years, and follows the $\nu^{1/3}$ relation expected for the thin disc model. This relation has previously been established in the NIR [Kishimoto et al., 2008], and its discovery in the optical difference spectra indicates that optical AGN emission is usually mixed with a constant component, likely associated with the host. Interestingly, a redder-when-brighter trend was reported in the NIR, associated with increased dust reprocessing [Yang et al., 2018]. However, Graham et al. [2019] argue this effect likely does not hold for the full AGN population, after searching for the same effect in a sample extending to higher luminosities.

The fluctuations in the UV and optical continuum are aperiodic. However, they are clearly correlated across wavelengths [Lawrence, 2012; Dexter & Begelman, 2019]. Crosscorrelation studies of different continuum bands show a coherent response in the UV/optical to the FUV with a relative delay of ∼hours (e.g. McHardy et al. [2014]). The coordination across wavelengths presents a problem for the α-disc model, as it implies a causal link on a shorter timescale than the viscous timescale in the disc (Figure 1.1). This has been explained as X-ray reprocessing, where the response time is set by the speed of light. Support for this interpretation is presented in Shappee et al. [2014], who report on high cadence observations of a strong brightening of the nucleus of NGC 2617. The authors show that increases in UV, optical, and NIR continuum flux all follow the rise in X-rays on the light travel time. Interestingly, this follows on a large change in the BLR for this object, changing from a type 1.8 to a type 1 Seyfert. As discussed in Section 1.2.1, observations from NGC 5548 challenge the X-ray reprocessing interpretation. The issue therefore remains unsolved.

A useful phenomenological description of AGN photometric variability in the optical range is the Damped Random Walk (DRW) model [Kelly et al., 2009; Kozłowski et al., 2010]. The basic assumption of this description is that AGN variability is a stochastic process: it is modelled as a random walk in magnitude space, with a driving amplitude (SF_∞) and a damping timescale (τ). Physically, this model provides a description of a changing accretion rate over time. The damping of the fluctuations brings the brightness back to the mean. At large timescales, the rms of the variability will tend to the driving amplitude. This method was applied by MacLeod et al. [2010] to describe the light curves of quasars in Stripe 82, which is a particularly well sampled area of the sky in SDSS. The results from this publication were expanded upon in a study that used the same technique to analyse ∼80.000 SDSS quasars [MacLeod et al., 2012].

The DRW model is fitted to the structure function (SF) of the light curve. The SF defines the rms of the change in magnitude (Δm) as a function of elapsed time (Δt). This provides best-fit values for τ and SF_∞. MacLeod et al. [2010] show that this model provides a good match to the Stripe 82 observations. The average value of τ is 200 days and the mode of SF_∞ is ∼0.2 mag. The SF depends on the frequency ($f = 1/\Delta t$) as f^{-2} for high frequencies, showing an increase in Δm with larger Δt. The results therefore indicate that the largest changes in flux are significantly more likely to occur over longer time intervals. The authors also find that there is a natural maximum to the amplitude of fluctuations and that variability is correlated with rest frame wavelength. If the data are split into their respective photometric bands, the bluer bands are more variable.

The DRW damping timescale τ provides a natural timescale on which to expect large changes in AGN flux, as it represents a knee in the SF. It is ∼200 days in the UV [Welsh et al., 2011] and if it indeed exists in the optical range, it is ∼years. MacLeod et al. [2010] show that the timescale and amplitude of the AGN DRW correlate negatively with luminosity and BH mass.

However the scaling with mass is surprisingly weak if the variability is driven by effects caused in a disc matching the thin disc model. The weak luminosity correlation of the variability timescale matches results by Vanden Berk et al. [2004]. MacLeod et al. [2010] and MacLeod et al. [2012] further show that τ and SF_∞ appear to be uncorrelated with redshift, suggesting that the parameters are intrinsic quasar properties. How this relates to AGN evolution is unclear. Is is relevant to note that there is considerable scatter in the fitting values, in particular for the damping time scale. Whereas all AGN show the same DRW behaviour, the light curves of individual objects can therefore differ considerably.

In addition to variability intrinsic to AGN, it almost certain that a fraction of variable objects in surveys is due to gravitational microlensing [Lawrence et al., 2016]. This occurs when a stellar mass object passes our line of sight to a more distant AGN. Microlensing can produce flux level changes of all amplitudes. Additionally, although the lensing is itself achromatic, temporarily resolving the BLR or even the disc could produce wavelength dependent effects as well [Bruce et al., 2017]. Microlensed objects will be part of any large survey, but most AGN variability will not be the result of these transient events [Lawrence et al., 2016]. The discussion in this thesis will focus on changes occurring within the AGN.

1.3.2 Response of the BLR

The broad emission lines also vary over time. The broad lines appear to respond to a changing continuum flux. One of the most important conclusions to draw from the BLR response is that photoionisation by the continuum drives most broad line emission. This is the assumption that underpins all of the modelling discussed in Section 1.2.3. As both the optical disc and the BLR are almost always below resolution limits (see, however, Gravity Collaboration et al. [2018]) time-resolved spectroscopy affords the most promising insights into the structure of these inner regions. Reverberation Mapping (RM) has been the most successful effort in this line of investigation.

Guided by the initial mathematical formulation by Blandford & McKee [1982], RM is based on three assumptions about the inner structure of AGN: emission lines respond rapidly to changes in the continuum flux, the size of the continuum emitting region is small enough to be considered a point source illuminating the BLR, and the ionising continuum has a scaling relation to the observed continuum. A change in the ionising flux, observed by a UV or optical continuum change, can be tracked through the BLR as different emission lines respond to the change in U. An example of this response is shown in Figure 1.10. The principle of RM comes down to the reconstruction of the transfer function, which describes the response of the line to a δ-function continuum outburst. The transfer function depends on the lag (τ) and the line of sight velocity, which is indicated by its relative Doppler shift. RM should enable a full representation of BLR kinematics, as it potentially reveals both the radius and velocity of different emitting regions. Observational requirements, in particular the necessity of high cadence, high S/N spectra, have meant that most studies have focussed on observing the mean lag of various emission lines [Peterson, 2006; Peterson, 2014].

The main results of RM studies have been a determination of the size of the BLR (Figure 1.7) and revealing the ionisation structure of the BLR. These results have been consistent across many RM studies. Table 1.5 shows results from UV and optical RM in NGC 5548. The L-R_{BLR} relation (equation 1.7) has also been found to hold across the AGN population. This

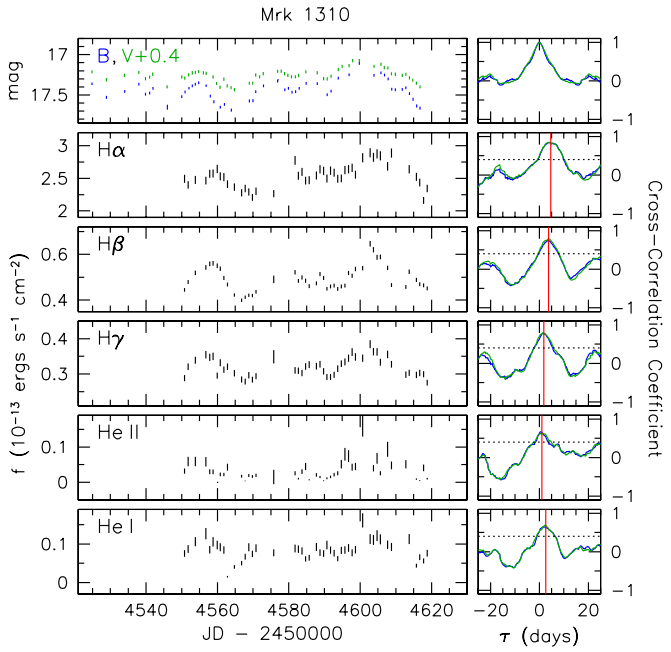

Figure 1.10: This RM study from the Lick AGN Monitoring Programme shows high cadence observations of continuum and lines in Mrk 1310. The upper panel shows the continuum levels, in the Johnson B and V filters. The relative lag of each line is identified in the cross correlation function displayed in the panel on the right. The lags indicate a stratified BLR. The difference in lag time between the Balmer lines is likely due to a changing line opacity with radius. Figure from Bentz et al. [2010].

is a clear indication that the photoionisation assumptions that underlie RM are indeed correct [Peterson, 2014]. There is significant scatter in lags for different lines: some studies find no lag or even a lead for the HeIIλ4686 line [De Rosa et al., 2015], and the differences between Balmer line lags can be almost negligible [Grier et al., 2017]. Both optical and UV lines are observed to reverberate. Recent large optical campaigns include the Lick AGN monitoring programmes (e.g. Bentz et al. [2010, 2013]) and the SDSS-RM programme, part of SDSS IV (e.g. Grier et al. [2017]; Shen et al. [2016b]).

The relationship between L and R_{BLR} has been found to depend on the luminosity, in agreement with predictions from photoionisation models, in which the inner clouds become fully ionised as the ionising flux increases. This effect is referred to as AGN breathing. Breathing has been detected in two different ways. De Rosa et al. [2015] present results for NGC 5548 in which the observed τ emission lines increased during the RM campaign, coinciding with an overall increase in continuum. This result also indicates that the expansion of the BLR can occur on a timescale of days to weeks. An LOC interpretation of the BLR, in which an existing cloud structure is lit up by a changing continuum agrees with this timescale. The second method of registering AGN breathing is presented in Barth et al. [2015], who show an anti-correlation between line width (σ) and luminosity in a sample of low z Seyfert 1 galaxies.

In addition to differences in lag, RM has revealed differences in the relative variability of emission lines, as well as changes in the line profiles. A large fraction of type 1 AGN, $\sim$66%, show variability in the profile of Hβ line as indicated by the line width [Runco et al., 2016]. HeIIλ4686 has the largest flux variations and the level of variability decreases with ionisation

Table 1.5: Results from a reverberation mapping campaign of NGC 5548. The lags scale with ionisation energy (see Figure 1.5), evidence for a stratified ionisation structure of the BLR. Data from Peterson [2008].

Emission line	lag (days)
HeIIλ1640	$3.8^{+1.7}_{-1.8}$
NVλ1240	$4.6^{+3.2}_{-2.7}$
HeIIλ4686	$7.8^{+3.2}_{-3.0}$
CIVλ1549	$9.8^{+1.9}_{-1.5}$
Ly$\alpha\lambda$1216	$10.5^{+2.1}_{-1.9}$
H$\beta\lambda$4861	$19.7^{+1.5}_{-1.5}$
CIII]λ1909	$27.9^{+5.5}_{-5.3}$

potential (e.g. Bentz et al. [2010]). The variability of emission lines can be assessed by calculating the rms of a collection of spectra. The benefit of this method is that it works for relatively low S/N data-sets. The rms profiles of higher ionisation lines are found to be broader than those of low ionisation lines, indicating that the wings of the high ionisation lines are more variable [Peterson, 2014]. This agrees with the stratification indicated by the lags: high ionisation lines form at smaller radii, where rotational speeds are higher. A time differentiated response of the wings is also detected for CIVλ1549, where the wings lead the line core [De Rosa et al., 2015]. The relative responsivity of components of the line profile indicates that the origin of any broad line is geometrically extended.

A more recent development, based on the availability of high quality spectra, has been the reconstruction of velocity delay maps, thereby utilising the full potential of RM. In this approach the response of the lines is divided into small wavelength bins, so that a velocity resolved response of the line can be established. Results of velocity delay mapping show a thick BLR geometry and signs of inflow in both the Balmer and higher ionisation lines [Grier et al., 2013; Pancoast et al., 2014]. Pancoast et al. [2014] also note that the observed response agrees best with a BLR model in which cloud self-shielding is present, such that most of the Hβ line emission we observe comes from the 'far side' of the BLR.

Another development over the past decades has been the extension of RM studies to higher redshift, $z \gtrsim 0.3$. The results of RM studies are based on around 50 relatively nearby sources. This small sample size could introduce a bias. Richards et al. [2011] note that the CIVλ1549 blueshift that has been observed across the quasar population has not been detected in any of the RM objects. Studies of variability at higher redshift are complicated by the necessity for high S/N spectra and by the fact that the detected sources will on average be more luminous, which is anti-correlated with their variability. Results presented in Lira et al. [2018] show AGN breathing for a high z sample, as well as the same L-R$_{BLR}$ relation found at lower z. The results of Bentz et al. [2010] and Lira et al. [2018] together indicate that the L-R$_{BLR}$ relation holds for AGN across at least five orders of magnitude in luminosity.

A lot of the focus of RM studies has been on the Hβ line, due to its prominence in type 1 spectra and its location near the outer boundary of the BLR. In order to use optical detection for high redshift objects, the MgIIλ2798 line is considered as a substitute, as Hβ will be shifted

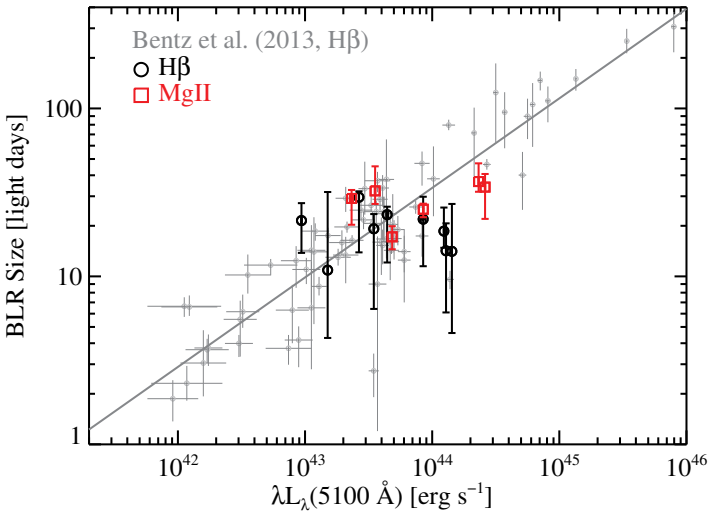

Figure 1.11: Estimates of the R_{BLR} based on RM time lags found for the Hβ line (black circles) and the MgII (red squares) line. New measurements for the $z \gtrsim 0.3$ SDSS-RM subsample are compared with other measurements for low redshift objects (grey). The horizontal axis represents the luminosity at 5100Å, used as an indicator for the bolometric luminosity. The correlation between continuum luminosity and R_{BLR} is clear. The values for the higher redshift sample show the same correlation as the other data, although the scatter is significant. Figure from Shen et al. [2016b].

out of the optical range. Sun et al. [2018] show that MgII does indeed vary with the continuum, although the flux variability is smaller than for Hβ. The authors conclude that MgII is suitable for RM studies. An initial study of RM using on Hβ and MgII measurements in objects at high z is presented in Shen et al. [2016b]. A comparison of R_{BLR} for these objects with those of the lower z objects of Bentz et al. [2013] is shown in Figure 1.11.

The efforts to include MgIIλ2798 in RM studies have met with mixed results. A detection of the MgII lag in NGC 4151 was claimed by Metzroth et al. [2006], but an RM campaign of NGC 5548 by Cackett et al. [2015] detected no correlation between continuum and the MgII line. However, the results from Shen et al. [2016b] and Sun et al. [2018] indicate that MgII *does* respond to UV continuum changes. The overall responsiveness of MgII on RM timescales has been found to be quite small compared to e.g. the Balmer lines, which have a comparable ionisation energy [Lawrence, 2016]. As discussed in Section 1.2.3 this is likely related to the different physical conditions in the line emitting regions. The case of MgII responsivity will be discussed in more detail in Section 1.4, and new analysis of SDSS data and new observations will be presented in Chapter 5.

The variability and complexity of the line response is also encountered when considering the intrinsic Baldwin Effect (iBE). The slopes of the iBE are considerably steeper than those of the eBE [Osmer & Shields, 1999] and this difference is difficult to explain based on the eBE interpretation of a luminosity dependent SED shape. Results presented by Rakić et al. [2017] suggest that the iBE is perhaps more closely connected to AGN breathing. Observations of Hβ in several different classes of AGN show no difference in the iBE, indicating that the Eddington ratio plays a limited role. Rakić et al. [2017] argue that the effect is caused by a changing R_{BLR}(Hβ). An AGN in a low luminosity state can more easily fully ionise the

Hβ forming region if L_{ion} rapidly increases, as the cloud is closer in and the flux scales with R^{-2}. This approach does not appear to take into account that BLR breathing can occur on very short timescales, however, as it relies on a single cloud model. The difficulty in finding a photoionisation model that explains the iBE indicates that the formation mechanism is rather complex.

One of the main applications of RM results has been the estimation of the black hole mass. The method is based on the assumption that the motion of the line forming gas is dominated by the gravitational potential. A review of black hole mass estimation methods and results can be found in Peterson [2014]. The distance to the black hole can be calculated from the line lag, and the velocity of the gas from the line width. The black hole mass can subsequently be estimated as:

$$M_{BH} = f\left(\frac{\Delta V^2 R}{G}\right), \tag{1.9}$$

where ΔV and R are the velocity of the line and the its radial distance. ΔV is measured as the broad line width. Both R and ΔV can be found using RM studies. f is referred to as the virial factor, which is estimated to be $\sim$5. The virial factor can be found by calibrating RM M_{BH} estimates with masses found through other methods. Examples of other methods of mass estimation are those based on the stellar velocity in the galactic bulge (M-σ_*) [Ferrarese & Merritt, 2000] and the relationship between bulge luminosity and M_{BH} [Kormendy & Freeman, 1998]. RM measurements are by definition taken from type 1 AGN. These objects are preferentially observed 'face on' [Lagos et al., 2011]. The relatively small value of f therefore implies that there is a significant vertical component to rotational velocities in the BLR, further evidence for a thick geometry [Peterson, 2014].

To compensate for the fact that the RM and M-σ_* methods are viable for only a relatively small number of objects in the local Universe, a method has been developed to estimate black hole mass based on a single spectroscopic epoch [McLure & Jarvis, 2002; McLure & Dunlop, 2004]. This method relies on the constancy of the L-R_{BLR} relationship across the quasar population, extrapolating results for the RM sample. A measure of the luminosity can be used to estimate the size of the BLR. In combination with a line width measurement and an estimate of f this yields all the required input for equation 1.9.

The strength of the single epoch mass estimate lies in its wide applicability (e.g. Shen et al. [2011]), however the method is susceptible to several uncertainties: an estimation of M_{BH} requires the constraint of f, a scaling relation between the observed L and R_{BLR}, and a relation between line width and orbital velocity. These factors are found by linear regression on a sample of AGN with known black holes masses. Different combinations of emission line and reference continuum yield different uncertainties on the factors [Shen & Liu, 2012]. Peterson [2014] notes that changes to the line profile are so common it is important to use the Gaussian width σ rather than the FWHM to define line width estimates using RM results, as the ratio FWHM/σ is a function of flux. Wang et al. [2019] find that the FWHM is more sensitive to changes in inclination, but do not find evidence that either σ or FWHM provide a better estimate of M_{BH}. Correlations between spectrophotometric luminosities at different wavelengths and between luminosity and emission line profile are therefore of key importance for accurate M_{BH} estimates.

1.4. Extreme Variables and the Limits of Current Models

Our image of the structure of the inner regions of AGN has been developed over the past decades to match observed AGN characteristics, as described in the previous sections. However several unknowns have persisted in our understanding of AGN for decades. These unknowns include the nature of viscosity in the accretion disc and the geometric structure of the BLR. Observational evidence gathered in recent years, in many cases as the result of a combination of continuous monitoring in large surveys and repeat spectroscopy, has put increasing strain on our current models. A particularly interesting case is that of the extremely variable quasars (EVQs). These AGN show large photometric changes in optical or IR flux (more than a magnitude). Closely related to EVQs is the set of changing look AGN or changing look quasars (CLQs). These are highly variable AGN that show dramatic changes in their broad emission lines. Observed changes occur on a time-scale of years, challenging the expected timescales for such dramatic flux variations, based on results of fitting DRW models and from the model timescales shown in Figures 1.1 and 1.4.

The tensions that extreme AGN variability creates between models and observations, are also an opportunity for improvement and new discoveries. These are the motivation for the research in this thesis. The strong variability of Mrk 110 and the behaviour of the supposedly marginally variable MgIIλ2798 emission line provide good test cases for the limits of our current understanding of AGN. In the research presented here I will focus on the response of the BLR to a variable continuum. Mrk 110 is a case study of a particularly well observed AGN, allowing for a comparison on a long timescale. For the study of MgII I will make use of both an EVQ sample, based on the sample presented in MacLeod et al. [2019], and a general AGN sample, to evaluate the possible range in MgII line response. In this section I will describe the current observational status of the changing look phenomenon, discuss the challenges this poses to our models of AGN, and discuss results on MgIIλ2798 variability found to date, providing the context for the new work presented here.

1.4.1 Changing Look Objects

Large changes in flux are possible in the DRW variability scenario, but they are expected to be rare or take place over longer timescales (e.g. MacLeod et al. [2010]). Recent studies show a different pattern of AGN behaviour, however. In a study of 102 local Seyferts, Runco et al. [2016] find no correlation between change in continuum flux and the elapsed time in the AGN restframe, in contrast with results from DRW studies. A study of ∼8,500 quasars with data from SDSS and the Dark Energy Survey found approximately 1,000 EVQs [Rumbaugh et al., 2018]. In the latter study EVQs were defined as objects showing an absolute change in g-band magnitude greater than one ($|\Delta g| > 1$) over the duration of the ∼15 year long lightcurves. Accounting for selection effects in their sample, the authors argue for a 30-50% EVQ fraction among the AGN population in general. Additionally, Rumbaugh et al. [2018] found several interesting correlations, that will be relevant in the discussion of CLQs: extremely variable objects were found, on average, to have stronger broad UV lines (as indicated by their equivalent width), to have stronger narrow [OIII] lines, to be overall more variable (i.e. on *all* timescales), and on average to have a lower Eddington ratio than the general AGN population.

Large amplitude brightening ($\Delta m > 1.5$) also defines a set of 50 blue 'hypervariable' AGN

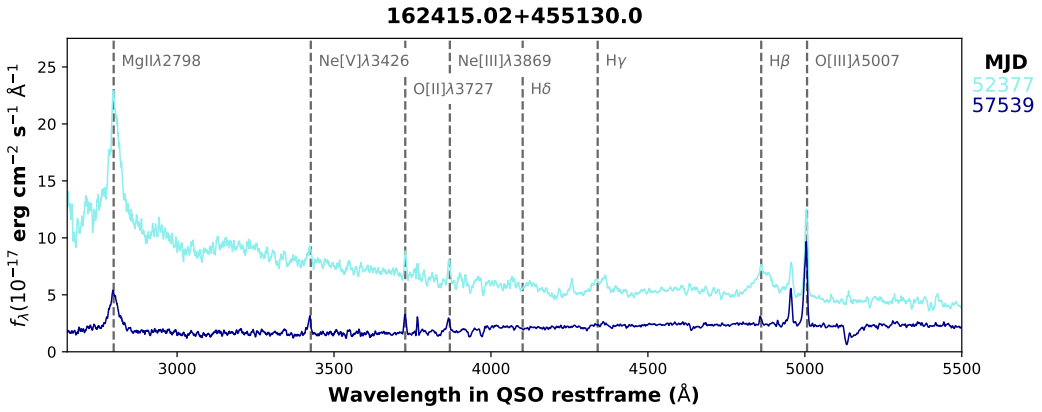

Figure 1.12: The SDSS quasar 162415.02+455130.0 shows the significant dimming, especially noticeable by the loss of blue continuum flux, and the loss of broad Hβ (4861Å) typical of a changing look object. Flux levels represent an absolute flux calibration. This object is part of the 'supervariable sample' in the MgIIλ2798 study, as defined in Chapter 2. The older spectrum is from SDSS and the newer spectrum was taken with the William Herschel Telescope.

[Lawrence et al., 2016]. These objects were identified by comparison of SDSS and PanSTARSS-I photometry and are characterised by a blue continuum evolving on a ∼10 year timescale. The AGN all appear to follow the bluer-when-brighter scenario. Based on selection effects Lawrence et al. [2016] estimate the fraction of hypervariable AGN as 1 in 10^5. This is considerably lower than the estimate by Rumbaugh et al. [2018], however the amplitude criteria are more stringent for the hypervariable category.

Abrupt and large amplitude changes in AGN continua were also reported by Guo et al. [2016] and Goad et al. [2019]. Guo et al. [2016] present observations of an SDSS quasar (z=0.32) showing a rapid decline in the UV continuum, over a period of days, after which X-ray observations indicate the ionising continuum recovered. A similar turnoff, on a timescale of weeks, was reported by Goad et al. [2019] for the EUV continuum in NGC 5548. The EUV emission was determined using the Lyα and HeIIλ1640 lines as a proxy. Remarkably, the UV continuum remained approximately stable. The change in line flux is in contrast to the Guo et al. [2016] results, which showed no changes in the BLR. The variability in these sources indicates that the UV and FUV continua can vary independently of one another.

Closely related to EVQs are changing look objects. The term 'changing look' originates in X-ray studies of AGN [Matt et al., 2003], referring to objects that appeared to switch from Compton thick (N_H ∼10^{24}cm^{-2}) to Compton thin (N_H ∼10 ^{22}cm^{-2}), or vice versa. As these X-ray changes occur on a timescale of years, they are likely associated with a change in the emission source, rather than in the absorbing or obscuring medium [Matt et al., 2003] (N_H, in this case, is a measure of spectral hardness, not neccesarily absorption). When applied to changes in the optical range of the AGN spectrum, the term changing look is used to refer to transitions between type 1 and type 2 AGN, that is: to objects with strongly appearing or disappearing broad Balmer lines. An example of changing look behaviour is shown in Figure 1.12.

Optical changing look AGN have been known for decades, although the number of objects was small (see e.g. Tohline & Osterbrock [1976]; Cohen et al. [1986]; Storchi-Bergmann et al. [1993]; Goodrich [1995]; Aretxaga et al. [1999]). These objects are all Seyfert galaxies, some of which switched 'on', changing from a type 2 to a type 1, with an associated increase in

luminosity, and some of which switched 'off', showing the reverse transition. The following is a brief overview of the most prominent sources in the recent literature.

Mrk 1018 notably changed from a type 1.9 Seyfert to a type 1 and back to a type 1.9 over the course of three decades [Cohen et al., 1986; McElroy et al., 2016]. The turn-off of the continuum and the drop in the broad Balmer lines occurred over a period of six years, after thirty years in a high type 1 state. NGC 2617 transitioned from type 1.8 to a type 1 AGN within a period of 28 years [Shappee et al., 2014]. Subsequent high cadence multiwavelength follow-up observations showed an outburst in X-rays ($\Delta m > 1$) followed by a UV continuum rise. Shappee et al. [2014] speculate this outburst is related to the spectral type change. Mrk 590 changed from a Seyfert 1 to a Seyfert 1.8 within a period of 7 years, and to a type 2 within another 10. The AGN decreased significantly in X-ray flux and lost virtually all broad Hα and Hβ [Denney et al., 2014].

The sample of changing look AGN has been expanded with the detection of objects at higher redshift, and with a higher luminosity. The first of these changing look *quasars* (CLQ) was reported by LaMassa et al. [2015]. It concerns an SDSS quasar (z=0.31) that shows significant dimming and loss of broad Hβ, over a period of $\sim$7 years in the QSO restframe. Contemporaneous X-ray observations also show a large drop in the 2-10 keV flux. This discovery was followed by that of another dimming quasar, found in TDSS [Runnoe et al., 2016], and three more original SDSS quasars, also showing a turn-off [Ruan et al., 2016]. The latter four objects displayed their change on a timescale of $\sim$10 years. A particularly rapid turning on of an AGN continuum was reported in Gezari et al. [2017a]. Coinciding UV and X-ray observations reveal a flux change of approximately a factor 10, taking place within a period of $\sim$500 days. The associated change in spectral type was from 1.8 to type 1. Gezari et al. [2017a] also note that that the continuum shows continued variability on smaller scales, in both the low and the high state, in agreement with the trend observed by Rumbaugh et al. [2018].

These reports on individual sources show some interesting common traits. Several studies report the typical signs of AGN breathing in Hα: as the line luminosity decreases, the line width increases, indicating the line is formed at a smaller radius. This is turn means that the black hole mass estimates, based on the individual epochs, remain consistent [LaMassa et al., 2015; Runnoe et al., 2016]. For several objects, X-ray observations show a dimming of the hard ionising continuum, approximately contemporaneous with the diminishing broad line flux [Denney et al., 2014; LaMassa et al., 2015; Gezari et al., 2017a]. Finally, all of the objects appear to have relatively low Eddington ratios ($\sim$0.05) and the change of state appears to be associated with a large fractional change in Eddington ratio. This change can reasonably be associated with a large change in accretion rate [LaMassa et al., 2015; Ruan et al., 2016; Runnoe et al., 2016]. It is possible this change in rate also corresponces to a change in the nature of the accretion flow.

A systematic search for CLQs in the SDSS data was conducted in MacLeod et al. [2016]. This study looked for a large change in photometric magnitude $|\Delta g| > 1$ among SDSS DR7 quasars [Schneider et al., 2010] and visually compared SDSS I/II with SDSS III-BOSS spectra. The result was 11 new CLQs: 5 with appearing broad lines, 5 with disappearing broad lines, and one object that appeared to go through a cycle of appearing and disappearing lines (MgIIλ2798 for this object is shown in Figure 1.15). A similar ratio of 'on' and 'off' transitions was found by Yang et al. [2018], who report the detection of 21 new CLQs, found through a combination of archival searches and new observations. Identification of changing look objects using mid-infrared variability, searching data from the WISE survey, resulted in the detection

of two new CLQs [Ross et al., 2018; Stern et al., 2018].

Using new follow up spectroscopy on photometrically identified targets, MacLeod et al. [2019] (MCL19) report the discovery of 17 new CLQs. The sample of the MCL19 paper forms an important part of this thesis. I have made some of the observations for this study (at the William Herschel Telescope) and am one of the co-authors. MCL19 follows up on the successful archival identification of changing look objects, based on photometric variability, published in MacLeod et al. [2016]. The target selection is discussed in detail in Section 2.3 and the follow-up spectroscopic observations in Section 2.1. The candidate sample for the follow-up observations consists of EVQs. The objects show turn-on, turn-off, and flickering light curves: the sample covers a range of extreme variability. Beyond the discovery of 17 new CLQs, the study also confirms the average low Eddington ratio for changing look objects (see Figure 1.13 and the results discussed in Chapter 5). The confirmation rate of CLQs among the EVQ sample increases strongly with amplitude of variability. This correlation appears to indicate that CLQs can form the high variability tail of 'regular' quasar variability. This is in contrast to an interpretation of CLQ behaviour as a change in state (see the discussion in the next section).

The potential of high cadence photometric surveys, as well as the necessity of spectroscopic follow-up, is perhaps best demonstrated by results from the Catalina Real-time Transient Survey (CRTS) [Drake et al., 2009], containing 71 new changing look objects [Graham et al., 2019]. The authors use a different definition for the level of Hβ fluctuation than MCL19, measuring the flux strength as the ratio Hβ/[OIII]λ5007 and assuming a constant narrow [OIII] flux. The changing AGN are referred to as 'Changing State Quasars' (CSQs), marking the (slight) distinction from the MCL19 CLQs. This difference in definitions also illustrates that the key point about highly variable AGN is that they show various kinds of fluctuations: changing broad lines, changing SEDs and differences in these changes from object to object. The Hβ based definition for CLQ is not as important as this broader class of behaviour.

The large sample introduced by Graham et al. [2019] provides some interesting results with respect to EVQs and the changing look population. The first is that the authors do not find that EVQs have lower Eddington ratios than the general AGN population, in contrast to Rumbaugh et al. [2018] and MCL19. However they do find that this relationship holds for CLQs/CSQs, with the amplitude of variability showing an anti-correlation with the Eddington ratio. Second, the authors find that large changes in continuum do not necessarily correspond with a change in spectral state. This is in agreement with results from MCL19, who find that the probability of a large change in broad line flux ranges from 10% to 50%, with the probability rising as the relative change in the 3420Å continuum increases from a factor 1.5 to 6. Third, in agreement with Yang et al. [2018]; Ross et al. [2018] and Stern et al. [2018], the authors of Graham et al. [2019] find that the CSQs are variable in the MIR as well as the optical. They do not find a correlation between the MIR variability amplitude and changing look behaviour. This lack of correlation is possibly due to light travel time effects, and the correlation could manifest on longer timescales.

The observations of large continuum and spectral changes occurring on a restframe timescale of years logically lead to the question of what is causing them. Several possibilities have been considered and the merits of each strongly depend on whether they can match the timescales on which changes occur in changing look objects.

The first possibility is variable obscuration: an optically thick medium crosses the line of

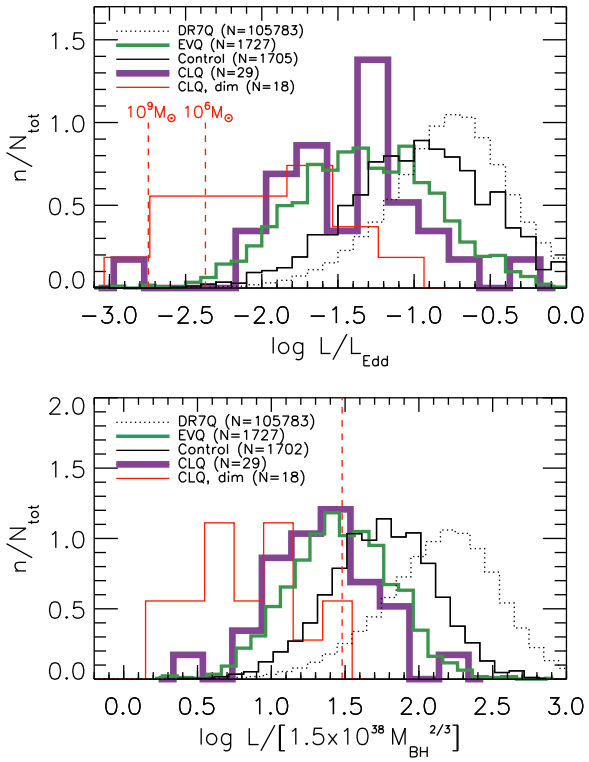

Figure 1.13: *top*: The distribution of the Eddington ratio for the samples defined in MCL19. 'DR7Q' is the full sample from Schneider et al. [2010], 'EVQ' the parent sample from which CLQ candidates were selected (also see Section 2.3), and 'Control' a sample of less variable quasars selected to match the EVQ sample in z and L_{bol}. The red dotted lines indicate possible cut-off Eddington ratios for BLR formation. It is clear from this figure that the EVQs and CLQs form a distinct subset of the AGN population. *bottom*: the same distributions as in the top plot, compared to the parameter $L_{bol}/M_{BH}^{-2/3}$, which describes a possible cut-off level of BLR formation in the disc wind scenario [Elitzur & Ho, 2009]. The red dashed line indicates the theoretical lower limit for the formation of BLR clouds. Figure from MCL19.

sight to the active galaxy, temporarily blocking our view of the central engine. The most likely object to produce strong obscuration is a cloud containing dust, which implies a cloud orbiting outside the dust sublimation radius. Under the assumption that the obscurer is outwith the BLR, at 3 R_{BLR}, LaMassa et al. [2015] find that the cloud crossing timescale is ∼20 years. This is at least twice as long as the observed dimming timescale for the CLQ in question. All studies of CLQs listed in the discussion above find that the timescales do not match predictions of the dust obscuration timescale. Similarly, Ross et al. [2018] consider a cloud in free-fall and, neglecting possible effects that might destroy the cloud on its way in, find that this would correspond to a timescale of decades. MacLeod et al. [2016] do note that the timescale to block the UV continuum source (but not the BLR) is ∼160 days. The authors add that the physical extent of the UV emitting region makes it unlikely the continuum can be blocked effectively. In all plausible cases obscuration would take too long to cause the observed change in spectral type and the EVQ variability.

In addition to the timescale, several authors note other problems with obscuration as the cause for CLQs. The first is the required spectral shape of the reddening effect. Both McElroy et al. [2016] and Guo et al. [2016] note that the observed continuum change would require an unusual extinction curve. MacLeod et al. [2016] simulate reddening with both a Milky Way and an SMC-like reddening curve, and are unable to reproduce the changes in lines or continuum. Ruan et al. [2016] find that the observed change in the ratio Hα/Hβ is unlikely to be explained with dust extinction. In a follow-up study of the switching off in Mrk 1018, Hutsemékers et al. [2017] find no increase in the degree of polarisation, as could be expected in the case of scattering of continuum light off dust in an obscurer. It should be noted, however, that detection of polarised raduiation would depend on the specifics of Mrk 1018's geometry. Finally, both Stern et al. [2018] and Graham et al. [2019] note that the response of the MIR continuum rules out obscuration along the line of sight, as obscuration is unlikely to affect the response of the dusty region. This is in agreement with a study of a source that undergoes strong dimming followed by a full recovery by Kynoch et al. [2019]. The changes in optical flux for this object are clearly tracked by the IR emission.

A second possible explanation is the disruption and rapid accretion of a star in the inner accretion disc, in a Tidal Disruption Event (TDE). The strength of this argument in terms of timescale is that it allows for a very rapid turn-on as well as a relatively quick turn-off. Examples of likely observed TDEs are Gezari et al. [2017b]; Blanchard et al. [2017] and Mattila et al. [2018]. An argument was put forth by Merloni et al. [2015] that the CLQ reported by LaMassa et al. [2015] was a TDE, as the decline in observed X-ray flux approximately matches the expected $t^{-5/3}$ decay. However, the lightcurve lacks the clear peak that should precede this decay. Runnoe et al. [2016] and McElroy et al. [2016] both reject the TDE hypothesis for their respective objects, considering the relative stability of the continuum in the time leading up to the spectral change. Based on the analysis of relative line strengths in a BPT diagram Ruan et al. [2016] and Runnoe et al. [2016] also find cause to believe something other than a TDE is causing the changes in luminosity.

Lawrence et al. [2016] state that microlensing is a reasonable explanation for a fraction of hypervariable objects, as it is statistically likely that it will occur for at least some AGN. The probability of such an occurrence is strongly correlated with redshift. Microlensing can have various effects on the appearance of the BLR, as discussed in Bruce et al. [2017]. Similarly there is a large range of lightcurves than can be matched to lensing effects, although the erratic

nature of many light curves makes finding a right match more difficult (MCL19). It is unlikely, however, that all reported CLQs are the result of microlensing. Although microlensing cannot be excluded as a possibility, a cause intrinsic to variable AGN is necessary to explain the number of occurrences.

After excluding the other options, intrinsic large amplitude brightening and dimming of the ionising continuum, followed by a strong response of the BLR, appears to be the most likely remaining option. LaMassa et al. [2015] and MacLeod et al. [2016] argue that the timescale that best matches that of changing look behaviour is the inflow timescale (τ_{inf}) in a thin α disc. This timescale can also plausibly be associated with a change in accretion rate, to account for the correlation with Eddington ratio. LaMassa et al. [2015] estimate this timescale as:

$$\tau_{inf} = 31 \left(\frac{\alpha}{0.1}\right)^{-1} \left(\frac{\lambda_{Edd}}{0.03}\right)^{-2} \left(\frac{\eta}{0.1}\right)^{2} \left(\frac{r}{10 r_g}\right)^{7/2} \left(\frac{M_{BH}}{1.7 \cdot 10^8 \mathrm{M}_\odot}\right) \text{years}, \tag{1.10}$$

where λ_{Edd} is the Eddington ratio and η is the accretion efficiency. The authors note that this timescale is also a poor match with observations, although it is possible the timescale is smaller if more effective processes of angular momentum transport through the disc are at work. Husemann et al. [2016], Stern et al. [2018], and Graham et al. [2019] argue that a disc thermal timescale is more appropriate, although a comparison with the value in Figure 1.1 shows this requires some modification of estimates about the structure of the accretion disc. The conclusion that the variability is indeed intrinsic to the AGN is therefore at odds with assumptions about the working of the accretion disc and with assumptions about the possible timescales on which variability can occur. The observations of changing look objects therefore raise questions concerning the workings of the inner region of AGN, both the accretion disc itself and the relation between the BLR and the ionising continuum.

1.4.2 Problems and Unknowns

Large amplitude variability in the UV and optical continuum of AGN presents a problem for the Shakura-Sunyaev thin disc, which forms the basis for most 'radiative-mode' AGN models. The variability timescale problem is perhaps the most pressing issue in a longer list of challenges to the this model. An overview of these challenges is presented in Lawrence [2012] and Lawrence [2018]. In summary the issues are: the temperature problem, the ionisation problem, the coordination problem, the size problem, and the timescale problem. Most of these issues are interrelated.

The temperature and ionisation problems refer to the offset of the apparent peak of the UV continuum, which is found to be around 1000Å rather than at 150Å (see Section 1.1.3). This in turn implies a lack of ionising photons available to create the broad emission lines. The coordination problem refers to the near-synchronicity of fluctuations across multiple wavebands, inconsistent with viscous propagation of fluctuations in the disc. The size problem comes down to a discrepancy between the observed size of the disc (e.g. in microlensing events) and size estimates based on variability. The timescale problem, finally, concerns the speed at which UV and optical changes occur. This problem has been emphasised by EVQ observations.

Many of these observational challenges to the standard accretion disc theory have been known for a long time (e.g. Clavel et al. [1991]). The coordination and size problem were

addressed by the concept of X-ray reprocessing. In fact, the inflow timescale proposed as a possibly appropriate timescale for CLQ transitions also requires X-ray reprocessing to work [LaMassa et al., 2015]. The validity of X-ray reprocessing in explaining the timing of the UV variability is also under discussion, however (Section 1.2.1). Additionally, the variability in EVQs concerns the optical wavelengths as well as the UV, increasing the problem by extending the physical range over which variability occurs. The timescales associated with alterations in the disc (Figure 1.1) are either too long or too short (with the exception of τ_{sound}, which could indeed be linked to extreme variability, as discussed below). Solutions to the variability problem are therefore sought in changing the way in which we model the inner accretion flow in AGN.

To address the variability problem several studies propose modifications to the viscosity dominated α disc. Most of these studies focus on the possibility of faster accretion, in combination with rapid changes in accretion rate. Dexter & Begelman [2019] suggest it is possible to significantly shorten accretion timescales if the scale height of the disc is increased through magnetic pressure. Another proposed solution is a combination of a stable outer thin accretion disc and an inner ADAF, which can be triggered due to a radiation pressure instability in the disc on a thermal timescale [Śniegowska & Czerny, 2019]. Ross et al. [2018] reject the ADAF explanation for the changing look behaviour in the two EVQs discovered in WISE data, based on the shape of the SED after dimming. Instead the authors propose a solution comprised of several modifications to the thin disc model: the high state of the quasar is described as an α disc that is geometrically thicker than a classic thin disc due to a torque at the inner boundary. The torque inflated disc is necessary to explain the high UV intensity. The transition is then modelled as a loss of the torque, settling the disc to the standard thin disc, in combination with the creation of a cold or scattering phase in the gas. The front of this phase can travel radially outward through the disc. Stern et al. [2018] note that the propagation of this front occurs at $\sim\alpha c_s$, where c_s is the sound speed. The variability of the EVQ sample presented in Graham et al. [2019] matches the thermal and front timescales proposed by Ross et al. [2018] and Stern et al. [2018].

Another possibility under discussion is that the changing look objects are undergoing a change of state akin to that observed in stellar mass BH binaries. In these objects a decrease in accretion rate has been observed to result in a rapid turnover from a luminous thin disc to a radiatively inefficient thick accretion flow. This transition is associated with a hardening of the X-ray spectrum. Based on the dimming of Mrk 1018, Noda & Done [2018] suggest that a change of state can manifest itself in low Eddington rate AGN and can also explain the response of the BLR. This interpretation assumes that a small drop in accretion rate can trigger an ADAF in the inner disc. The formation of an ADAF could then lead to a collapse of the soft X-ray emission, reducing the ionising flux powering the BLR.

Possible observational evidence for this theory was reported by Ruan et al. [2019]. Evaluating α_{OX} for faded AGN down to very low Eddington ratios ($\sim 10^{-4}$), the authors find that the spectrum hardens with diminishing Eddington ratio, moving from a luminous soft state to a dimmer hard state (see Figure 1.4). Unlike Noda & Done [2018] however, the authors remark that the timescales for these changes to take effect likely do not match those seen in EVQs.

The speculation about the nature of extreme variability in the continuum is closely linked with the discussion of extreme variability of the broad emission lines, the changing look phenomenon.

This discussion touches on unknowns in our understanding of the BLR, as well as problems with the current model of AGN unification. The unification scheme [Antonucci, 1993; Urry & Padovani, 1995] is based on orientation and obscuration. In this view the spectral type of an AGN should be constant. As variable obscuration has definitively been ruled out as an explanation for CLQs, the appearance and disappearance of broad lines are difficult to explain in this framework.

The detection of scattered broad line emission in several type 2 AGN [Antonucci & Miller, 1985; Ramos Almeida et al., 2016] confirmed that at least a fraction of type 2 objects are indeed obscured type 1s. This notion is also supported by the observation that type 1 Seyferts are preferentially observed face-on, compared to higher spectral types [Lagos et al., 2011]. However spectropolarimetric studies do not always recover a broad line signature for type 2 AGN, leading to speculation on the existence of 'pure' or 'true' type 2 AGN, which intrinsically lack broad line emission, if not a BLR [Tran, 2003]. Changing look objects further complicate this issue: the BLR can apparently be switched on and off, even reversing the transition in the same object (e.g. MacLeod et al. [2016]), which is possibly associated with a type of duty cycle.

The existence of true type 2 AGN is a subject of ongoing debate. The absence of a broad line is difficult to positively establish observationally. Antonucci [2012] argues that reports of true type 2's are largely erroneous, as they are based on insecure (or absent) upper limits on broad emission line detections, and that any population study showing distinct properties of type 2s is likely dominated by selection bias. The argument about insecure upper limits is supported by Stern & Laor [2012]. However, the latter study does find that AGN of an intermediate spectral type (e.g 1.7, 1.8) are 'real' and not caused by obscuration. Using measurements of Hα in a sample of SDSS AGN, the authors find that the fraction of intermediate type objects compared to type 1 increases with decreasing L_{bol}.

True type 2 objects have been argued for on theoretical grounds [Elitzur & Ho, 2009; Elitzur & Netzer, 2016]. This interpretation assumes a disc-wind scenario, in which there is a minimum accretion rate associated with wind formation. Should accretion in an AGN drop below this rate there will be no radiation driven outflow in which BLR condensations can form, thereby creating a true type 2. MCL19 found that scaling of the accretion rate predicted by this theory provided an apt metric to separate CLQs from other AGN, as well as turn-off CLQs from other EVQs (Figure 1.13).

As can be seen from this discussion, the debate on the nature of CLQs involves many uncertainties about the nature of the BLR. Does the geometry of the BLR change with changes in the continuum? Is the BLR in CLQs depleted, or is the line emission simply dimmed? Can all AGN potentially display such dramatic transitions? AGN variability not only raises these questions, but can also help answer them. The study of the highly variable Seyfert 1 Mrk 110 presented in this thesis will address the relative response of the BLR to changes in the continuum, when measured over a long period. Using a proxy for the FUV ionising continuum, it is possible to identify changing responsivities of broad emission lines. The change in response over time implies that we are not just observing a change in luminosity lighting up different parts of a pre-existing cloud distribution, but also structural changes in the BLR itself. The case of MgIIλ2798 provides another line of insight into the BLR, due to its apparently anomalous variability.

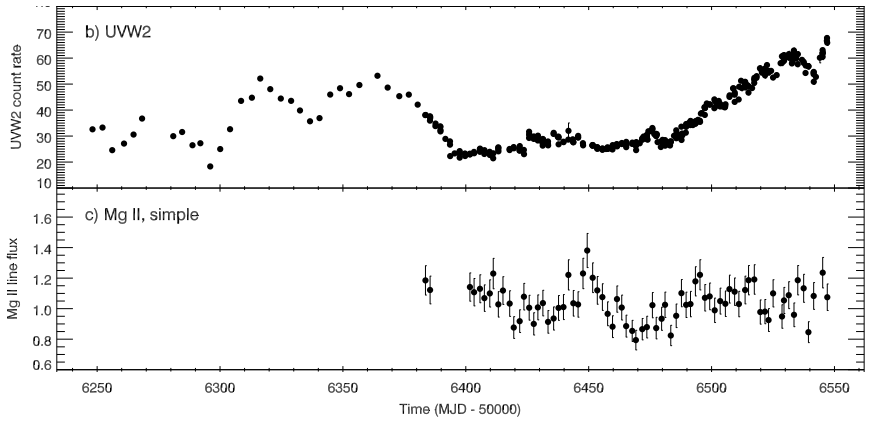

Figure 1.14: Results from a UV RM campaign of NGC 5548. The data presented is from Swift: 'UVW2' is the Swift filter used for the lightcurve photometry and 'MgII simple' refers to the method used to calculate the line flux (it is based on subtracting a pseudo-continuum). The lack of correlation between the UV continuum and the line flux is evident on all timescales. Figure from Cackett et al. [2015], it is part of Figure 2 in this publication.

1.4.3 The Responsiveness of MgIIλ2798

In studies on short timescales, notably RM campaigns, MgII stands out because it has been claimed that it does not respond with the same amplitude as other prominent spectral lines. It not only differs from the high ionisation lines such as CIVλ1549, but also from the low ionisation Balmer lines. Results from RM studies with regard to MgII have been mixed. Some studies have found a response [Clavel et al., 1991; Reichert et al., 1994; Metzroth et al., 2006; Hryniewicz et al., 2014], although the variable fraction of the flux is usually only a few percent. An exception to this is the quasar studied by Hryniewicz et al. [2014], which shows a fluctuation in the EW of $\sim$25% over several hundred days. A similar number of studies finds no correlation between continuum changes and the variability of MgII [Trevese et al., 2007; Cackett et al., 2015].

The studies listed above cover timescales of months. A UV RM campaign of NGC 5548 [Cackett et al., 2015] is one of the studies that found no correlation. The lack of response of the MgII line in this study can be seen in Figure 1.14. In comparison with Figure 1.10 the contrast between the behaviour of the MgII and H lines is clearly visible. The authors of the study note that the LOC-based photoionisation models presented by Korista & Goad [2000] predict an intrinsically low responsivity for MgII (see Section 1.2.3) and find that the result for NGC 5548 is consistent with this prediction. The results from other MgII studies, however, indicate that even on short timescales the behaviour of MgII changes from object to object. Concisely, the MgII line can respond to the continuum, but does not always do so and is often quite stable, but it can also show large flux changes.

This complex behaviour has also been studied using larger samples, consisting of survey data. As discussed in Section 1.3.2, MgII could be a promising candidate for RM studies at high z and has been studied in the SDSS-IV RM programme. Early results of this study found a credible MgII lag in six quasars ($0.3 < z < 0.8$) out of a sample of $\sim$100 objects, where the detection level was set by S/N [Shen et al., 2016a]. For reverberation mapping of MgII to be successful, especially at higher redshift, the response of MgII needs to be both coherent and significant. Both of these attributes are unclear for MgII: the coherent response appears to vary

from object to object and studies into the level of MgII variability find mixed results.

Woo [2008] finds peak-to-peak changes up to 25% on a timescale of approximately a year, indicating the potential for large scale changes. In a study of ∼9,000 Stripe 82 quasars Kokubo et al. [2014] find that both MgII and the complex of FeII lines in the same wavelength range vary only slightly, when compared to the Balmer lines. The authors argue that this cannot be due to a lack of change in the ionising continuum and also discard the notion that the line response is too slow to have been observed. The latter argument is based on the time period covered by the SDSS observations. They therefore also find that the detected low variability of MgII is the result of an intrinsic lack of line responsivity.

A study based on SDSS-RM data finds that MgII is only slightly less variable than Hβ [Sun et al., 2015]. The authors of the study present some other interesting findings as well. First, the level of variability of the MgII line and that of the 3000Å continuum are anti-correlated with L_{bol}, in agreement with DRW studies [MacLeod et al., 2010]. When comparing the level of variability of the MgII flux with that of the UV continuum the authors find a positive correlation. Additionally the authors find that this correlation scales up with L_{bol}. In other words: in brighter objects the MgII variability level tracks that of the UV continuum more closely. Even at high luminosities the scatter is still considerable, however.

The second finding is that the structure functions of the UV continuum and MgII both increase with Δt and decrease with L_{bol}. This similarity between the two could indicate that the MgII variability is driven by that of the continuum. The lags reported in Shen et al. [2016a], as well as the correlation between the level of variability of MgII and continuum indicate that there is a pattern in which MgII responds to the continuum. It should be noted that the effects described above hold for an *ensemble*, and do not represent a correlation that should hold for every object. The large scatter found by Sun et al. [2015] is consistent with the range of variability levels found in MgII RM studies.

Ensemble studies provide hints about the behaviour of MgII in comparison to the other lines, but the interpretation is not always clear. The line flux of MgII is found to correlate strongly with the optical continuum (5100Å) [Shen & Liu, 2012] and the width of MgII is found to correlate strongly with that of Hα and Hβ [Shen & Liu, 2012; Wang et al., 2019]. These correlations suggest that MgII and the Balmer lines are formed in the same, or a similar, region in the BLR. This would broadly agree with photoionisation models [Korista & Goad, 2004; Baskin et al., 2014a]. Among emission lines, the centre of the MgII line is found to best match the redshift of the host galaxy [Shen et al., 2016a], indicating a lack of inflow or outflow. This is perhaps related to the observation that in sources with high CIVλ1549 blueshift the MgII flux is stable compared to that of CIV [Sun et al., 2018].

Dong et al. [2009] find that the EW of MgII is strongly anti-correlated with the Eddington ratio, but not with with the continuum luminosity at 3000Å. The authors argue that this is the physical correlation underlying the MgII eBE. An investigation into epoch to epoch MgII variability in SDSS quasars is presented in Zhu et al. [2017]. The study presents two important results. The first is that the MgII line tracks the continuum, as changes in MgII flux correlate with changes in the flux at 3000Å. This would agree with the ensemble result based on the line and continuum structure functions [Sun et al., 2015]. Second, the authors find that the responsivity of the line decreases with a higher initial continuum state and with a higher Eddington ratio. The latter conclusion is supported by the results by Sun et al. [2015].

An initial study of MgII in EVQs is presented in Yang et al. [2019]. The authors report a

weak correlation between the change in the 3000Å continuum and the change in MgII luminosity, based on spectroscopic follow up of 16 objects. The variability of MgII is of smaller amplitude than that of the continuum, but does appear to track it. A suggested explanation for the reduced flux response of MgII is that only part of the line is due to photoionisation (cf. Korista & Goad [2004]). In contrast to the flux changes, the FWHM of MgII does not change with the fluctuating continuum. The lack of profile change in the line suggests that the R-L relationship (on which the single epoch BH mass estimates are based) does not hold for MgII. This marks a particular difference with broad Hβ. Interestingly, Roig et al. [2014] found a class of quasars using SDSS-III data that are characterised by a strongly suppressed broad Hα and Hβ emission and a very prominent MgII line, without other signs of reddening. Although the nature of these AGN is unclear, it does suggest that the MgII line emission is either powered differently from other emission lines, or at least that changes in the MgII line can occur asynchronously with the Balmer lines.

The connection between MgII and the ionising continuum is clearly complex, however the combined results from the various studies discussed above do indicate that a connection exists. MgII *should* track the continuum, the question is whether the line is always an outlier in its responsivity, and if so: why? As the amplitude of MgII variability is on average lower than that of other emission lines, EVQs form a good target sample to study the response of the line. Any response of the lines should arguably be larger in these objects. The changing look objects form a particularly interesting subset of this sample: the variability of the Balmer lines indicates dramatic changes occurring in the BLR, will MgII be subject to these changes as well? A first indication is an object included in MacLeod et al. [2016]: a CLQ that shows a disappearing and reappearing MgII line, almost certainly responding to changes in the continuum. Yang et al. [2018] also report a dimming CLQ losing a significant fraction of its MgII flux. The MgII variable quasar from MacLeod et al. [2016] is part of the analysis presented in this thesis. The change in MgII is shown in detail and in combination with additional light curve information in Figure 1.15. Multi-epoch spectroscopy of EVQs on a timescale of years can reveal behaviour of MgII that studies on shorter timescales or of less variable objects cannot.

1.5. Outline of Thesis

In this thesis I will present research into the variability of broad emission lines on long timescales and the manner in which the broad line emission is linked to the continuum. The investigation is split between the case study of Mrk 110 and the ensemble study of the MgIIλ2798 line. By evaluating the behaviour of the broad lines on the time scale of years, it is possible to consider changes beyond the flickering of the luminosity used in RM campaigns and to study the possibility of longer evolutionary trends in the BLR.

The outline of the rest of the thesis is as follows: Chapter 2 describes the construction of the data-sets for the two studies. Both studies contain archival spectra and new spectra from observations. For the new observations the instrumental setup as well as the reduction pipeline is explained. To extract the required information from the spectra I fit them with a model AGN profile. This process is described in Chapter 3. The chapter will cover both the process of fitting the individual spectra for Mrk 110 and pipeline I have written to fit the large amount of SDSS spectra.

The study of Mrk 110 will be presented in Chapter 4. This investigation focusses on four

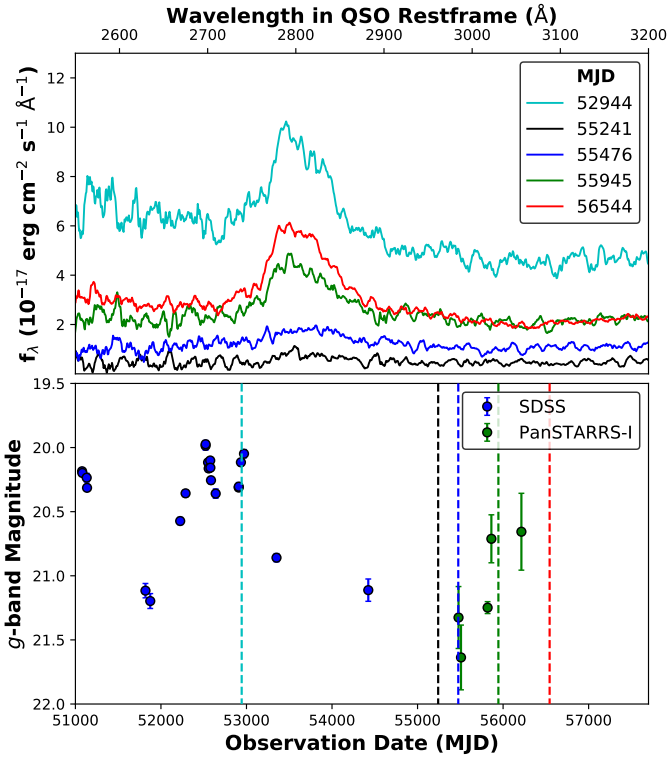

Figure 1.15: The SDSS spectra showing MgIIλ2798 (*top*) and the lightcurve (*bottom*) for the CLQ J022556+003026.7. Coinciding with a $\sim$1.5 magnitude dimming, the spectra show a complete disappearance and reappearance of the MgII line. The dashed lines in the bottom plot indicate the observation dates of the spectra. Data from SDSS DR14 [Abolfathi et al., 2018] with additional photometry from PanSTARRS-I [Kaiser et al., 2010]. This object was identified as a CLQ in MacLeod et al. [2016], and is also in the sample discussed in this thesis. The figure and combination with PanSTARRS data are part of new analysis.

emission lines: HeIIλ4686, Hβ, HeIλ5876, and Hα. The first part of the study considers the relative flux levels of the lines, using the HeII line as a proxy for the FUV ionising flux (Section 4.3). In the second part I will consider the evolution of the line profiles of HeIIλ4686 and Hβ and kinematics of Mrk 110's BLR (Section 4.4).

The MgIIλ2798 study is described in Chapter 5. The chapter starts with an overview of the observed behaviour in the spectra of the EVQ sample based on that published by MCL19. Various statistical methods to analyse the ensemble are defined in Section 5.2. The results for the analysis for the supervariable EVQ sample and the full population SDSS sample are presented separately in Sections 5.3 and 5.4 respectively, followed by a comparison of the two samples.

The results and conclusions for the Mrk 110 and MgII studies are presented at the end of their respective chapters. A summary of this discussion forms the concluding chapter of this thesis (Chapter 6). An overview of the available spectra of the supervariable MgII sample is provided in appendix A.

2. Constructing the AGN Samples

For the research in this thesis I have made use of both new and archival spectroscopic observations of AGN. The archival observations consist of SDSS spectra, using the 14th data release [Abolfathi et al., 2018], and of observations made with the FAST spectrograph on the Tillinghast Telescope [Fabricant et al., 1998]. The new observations were made using the William Herschel Telescope (WHT) on La Palma, the MMT on Mt. Hopkins, Arizona, the Magellan Clay Telescope at Las Campanas, and theb FAST spectrograph. For the new observations I have been part of the observing team for three runs with the WHT (February, May 2016 and February 2017), and was the lead observer for the final two. The spectroscopic reduction for the WHT observations was done by me, as were the spectrophotometric calibrations of the FAST spectra. For the Magellan and MMT data I have used the reductions performed by C. MacLeod, as presented in MacLeod et al. [2019] (MCL19).

This chapter covers the sample selection for the Mrk 110 and MgII projects, the instruments and setup used in the required observations, and the process of data reduction (with an emphasis on the WHT spectra). For the archival spectra the observations and reductions are also briefly described for completeness. The aim of both research projects is to compare spectra from different observations. Therefore understanding the flux calibration is of particular importance. The samples introduced for the MgIIλ2798 variability study are (1) a sample of optically highly variable quasars which is derived from the CLQ candidate set from MCL19, and (2) a full population sample covering as large a range of quasar variability as possible. These two samples will be referred to throughout as the **supervariable** and the **full population** samples.

2.1. Observations

An overview of the most important parameters of the spectroscopic observations, such as slit width and resolution, for all observations used in this thesis, is provided in Table 2.1.

2.1.1 Archival Spectra

SDSS

SDSS spectra are part of both the Mrk 110 and the MgII samples. All SDSS observations were made using the 2.5m wide field telescope described in Gunn et al. [2006], located at Apache Point Observatory. For the initial imaging, during SDSS-I (2000-05), the camera consisted of thirty 2000x2000 pixel CCDs, and data were collected in the five *ugriz*-filters [Fukugita et al., 1996]. A quasar target sample was constructed based on imaged objects' distribution in colour-colour space [Richards et al., 2002], after which follow up spectroscopy was conducted to positively identify the targets. During SDSS I/II (2000-2008) spectroscopic observations were made using double spectrographs covering a wavelength range of 3800-9200 Å, with a dichroic at 6150 Å. The light was transported to the spectrographs using optical fibres, which were connected to a pre-drilled plate in the telescope's focal plane. The CCD data were reduced using the SDSS

spectroscopic pipeline described in Stoughton et al. [2002]. The reduction process follows the standard steps of flat-fielding, sky subtraction, and wavelength calibration and is largely similar to that described in Section 2.2.1. The SDSS spectrographs were rebuilt for SDSS-III/BOSS (2008-2014). Focussing on higher redshift objects the spectrographs now jointly covered a wavelength range of 3600-10000Å. Although continually improved, the reduction pipeline for BOSS remained similar to the original SDSS pipeline [Bolton et al., 2012]. An overview of the basic paramters of the observations used for this thesis is provided in Table 2.1.

The most important part of the reduction for this discussion is the flux calibration. For the SDSS calibration the spectra of pre-selected standards in the field are matched to a synthetic F-class sub-dwarf spectrum, after which the spectrophotometric r-band magnitude is matched to SDSS photometry. For SDSS-III (BOSS) a change in the instrumentation led to an inaccurate spectrophotometric pipeline calibration for quasars. This has resulted in an artificial difference between fluxes belonging to observations made during SDSS-I/II and those of SDSS-III (see e.g. Harris et al. [2016]). These calibration issues were addressed in DR14, and the instrumental effect causing the calibration error was removed for SDSS-IV. Given the relevance of this problem to the research presented in this thesis, I will briefly discuss its origin, as well as the solution applied to the DR14 spectra, following the recipe in Margala et al. [2016] (MAR16).

The calibration issue stems from the difference in scientific goals between BOSS-III and the previous iterations: as the new survey was to focus on higher redshift objects, with one of the main science goals to investigate BAOs, the throughput of the fibre-holes for quasar targets was optimised for a different wavelength than for other target objects. In all SDSS iterations the fibres for the spectrograph are fixed to plates with pre-drilled holes, matching each target's position on the sky (for an assumed observing time). The holes matching quasar targets have a maximum throughput of flux at $\lambda_{max} = 4000$Å, designed to match the Lyα forest in high z quasar spectra. Non-quasar targets, however, *which include the photometric calibration stars in every plate*, have $\lambda_{max} = 5400$Å.

The optimisation of the flux throughput is established by their position in the plate. The position and angle of the fibre is selected such that the atmospheric refraction brings the optimal wavelength to the centre of the 2" fibre opening, when the plate is in the focal plane. There is therefore a λ-dependent difference in flux throughput between the quasar targets and the calibration targets. Even more problematically: as the wavelength dependence is a result of atmospheric refraction, the resulting effect is also a function of airmass at the time of observation and of the position of the fibre-hole on the plate. This implies that the resulting offset in fluxes differs from target to target, without a correlation to the target properties.

The original BOSS pipeline did not account for the difference in λ_{opt} between the quasar target spectra and those of the calibration spectra. The stellar calibration spectra are compared with the model F-type SED and the ratio of measured flux to modelled flux is used to calibrate the science spectra. The discussed offset therefore introduces a λ-dependent miscalibration of the quasar spectra. Estimates by MAR16 are that this results, on average, in an overestimation of ∼19% of the flux at 3600 Å and ∼24% underestimation at 10,000 Å. The correction algorithm presented in MAR16 takes the various contributing factors (airmass, fibre position, atmospheric refraction) into account, to adjust each individual exposure.

The result of the correction function can be seen in Figure 2.1, where the median flux ratio (SDSS-I/II to BOSS) of reobserved SDSS-I/II quasars is presented. The size of the correction blueward of 4500 Å indicates that any comparison between SDSS-I/II and BOSS spectra is

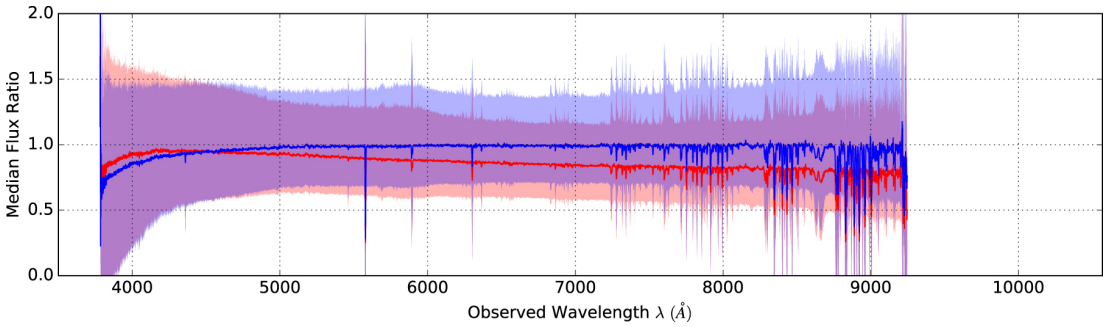

Figure 2.1: Median flux ratios of quasars observed with the old as well as the new SDSS spectrographs: the ratio is between the fluxes of the BOSS and SDSS-I spectra for each object. The ratio for the uncorrected spectra is in red, for the corrected spectra in blue. The shaded region regions contain 68% of the flux distribution, calculated for each wavelength bin. The figure is from Margala et al. [2016].

strongly influenced by this. It is likely this is one of the main contributions to the offset in ΔEW between the derived quasar properties for the DR7 and DR12 catalogues, as discussed in Chapter 5.

In the SDSS 14th data release the correction proposed in MAR19 has been implemented in the reduction pipeline on an exposure by exposure basis. This accounts for the changing atmospheric refraction as a result of chagning airmass between the exposures. The individually corrected spectra are coadded into the final spectrum, which is the data product used in the studies presented here. The reduced SDSS spectra were downloaded in bulk from the SDSS website[1]. As can be seen in Figure 2.1, there is still a residual difference in the calibration of the blue end of the spectrum. It is suggested by Harris et al. [2016] that this is possibly due to a mismatch between the synthetic stellar spectra and the population of flux standard stars used in both BOSS and SDSS. In order to use as large a data-set as possible, I have made no further corrections to the SDSS-III/IV spectra included in the sample, as I deem the corrections applied in DR14 to be sufficient to allow for a reliable comparison of spectral fluxes between epochs.

Tillinghast

The data collected with the Tillinghast telescope are used in the Mrk 110 sample. The 1.5m Tillinghast reflector is located on Mt Hopkins, Arizona. Observations were made with the slit at parallactic angle. In total I use 59 spectra, which were all taken with FAst Spectrograph for the Tillinghast telescope (FAST, Fabricant et al. [1998]). 50 of these spectra are archival. These spectra are part of several different observation campaigns, which spanned the period 2002-2009. Three of the spectra were used in a study published by Landt et al. [2008]. For these spectra I used the fully reduced spectra provided by H. Landt. The remaining spectra were part of two Reverberation Mapping campaigns conducted by B. Peterson, for which the results were not published. These spectra are publicly available on the FAST website[2]. The spectra in the FAST archive have been partially reduced, including wavelength calibration, but have not been flux calibrated. This issue is addressed in Section 2.2.

[1] data.sdss.org
[2] http://tdc-www.harvard.edu/cgi-bin/arc/fsearch

2.1.2 New Observations

William Herschel Telescope

Observations with the WHT provided spectra for both the MgII and the Mrk 110 studies. The WHT is a 4.2m optical–infrared telescope located at Roque de Los Muchachos Observatory on La Palma and is part of the Isaac Newton group of telescopes. All observations were made using the telescope's Intermediate-dispersion Spectrograph and Imaging System (ISIS). The data were collected as part of several programmes, but using the same instrumental set-up for every run. The runs which provided spectra included in this study were carried out 6–8 February 2016, 30–31 May 2016, and 17–18 February 2017. Additionally, spectra for J081916 were taken during runs in 2013, 2014, and 2015 [Bruce, 2018].

The instrumental set-up was selected to observe several broad emission lines, focussing on the Hβ line. The light was split into the red and blue arms using a 5300 Å dichroic. The gratings for the red and blue arms (R158R and R300B respectively), with an additional order sorting filter in the red arm (GG495), and a slit width of 1" resulted in a resolution R$\sim$1500 at 5200Å in the blue and R$\sim$1000 at 7200Å in the red. To speed up the read-out process, the binning during the readout was 1:1 in the λ direction, but 2:1 in the spatial direction. Additionally the readout was limited to a narrow spatial window over the CCD.

During the observing nights, dome flats, sky flats, and CuNe and CuAr arc-lamp images were taken. In order to flux-calibrate the science observations, spectra were taken of photometric standards immediately before or after each science observation, averaging to 2 standards per hour. The standard stars were selected to match the science targets as closely as possible in airmass. The length of the science exposures was 15 minutes to 2 hours, where the initial estimate of the duration was based on the latest photometry. This photometry was either from PanSTARRS I or from the Liverpool Telescope observation programme associated with the WHT observations [Lawrence et al., 2016]. The exposures were broken down into 15–30 minute segments, to reduce the risk of cosmic rays disrupting a detection.

Breaking up the longer exposures also allowed for intermediate checks on progress. As all targets are variable, it was important to ensure that the estimated exposure times suited the requirements for the current state of the AGN. The measure used to determine the number of exposures required is an estimate of the signal to noise ratio. This estimate is based on the 2D spectroscopic image, by fitting a Gaussian to the profile of signal along one column along the spatial axis. This approximation works best for high peak values of the Gaussian, as it assumes a triangular profile for the distribution. The ratio is calculated as:

$$\frac{S}{N} = \sqrt{\mathrm{FWHM} \times C_{\mathrm{peak}} \times \mathrm{Gain}}. \tag{2.1}$$

Here FWHM is the full width at half maximum for the fitted Gaussian, C_{peak} is the peak number of counts and the Gain is a constant specific to the CCD, $\sim$1 but different for the red and the blue arm. This check can be repeated at several different points along the λ axis to find an average S/N. As a rule of thumb a S/N of 20 was required for the red arm, and 10 for the blue. Checks on the CCD image also allowed to watch out for overexposure fir the brightest objects in the target sample, such as Mrk 110, and for the calibration stars.

Table 2.1: An overview of all observations included in this thesis. The columns list, from left to right: the telescope or observing programme, the epoch of the included observations, the resolution, the range of slit widths or fibre diameters for the included observations, and a summary of the average observing conditions on the nights the observations were made. For large data-sets, such as those of SDSS, the conditions vary strongly across the sample. The observing conditions for these data-sets are set to 'mixed'.

Telescope	Observation Epoch	Resolution	Slit/Fibre	Conditions
SDSS I/II	2000-2008	1500 (at 3800Å)	3"	mixed
SDSS III/IV	2008-2014	1500 (at 3800Å)	2"	mixed
Tillinghast	2002-2019	1600 (at 4800Å)	3"	mixed
WHT	2013-2017	1500 (at 5200Å)	1–1.5"	mixed
Magellan	July 26-29 2016	860 (at 6500Å)	1"	clear (non-photometric)
MMT	2016-2018	740 (at 4800Å)	1.5"	clear (non-photometric)

MMT and Magellan

Further observations for the sample used in the MgII study were conducted by C. MacLeod, using the MMT and Magellan telescopes. The objects observed with these larger telescopes were fainter than those observed with the WHT, usually with a g-band magnitude in the latest photometry greater than 20.5 ($g > 20.5$). The 6.5m MMT was used in combination with the Blue Channel Spectrograph [Angel et al., 1979], on several dates over 2016-2018 (see Table 2.6). The instrument was set up with a 300 mm^{-1} grating and 2× spatial binning. Observations with the MMT were done remotely.

The observations with the Magellan Clay 6.5m telescope were carried out on 26-29 July 2016. The instrument used was the Low Dispersion Survey Spectrograph 3 (LDSS3)-C, with the VPH-All grism. This provided a wavelength range of 4250–10000 Å.

Tillinghast

Follow-up observations of Mrk 110 were made using the FAST instrument in the period 2018–2019. The data used from the Tillinghast are therefore spread out over two decades, with archival observations from 2002–2009 and new observations starting almost ten years later. These observations were specifically made to contribute to this study, and the observing campaign is ongoing. 9 new FAST spectra were included in the research presented here.

2.2. Reduction of Spectroscopic Observations

2.2.1 WHT: Spectroscopic Pipeline

The spectra obtained with the WHT were reduced using the method developed by A. Bruce (AB), and presented in Bruce [2018]. The method is built on IRAF routines [Tody, 1986], and the L.A.–Cosmic cosmic ray extraction method [van Dokkum et al., 2012] These routines are combined into a pipeline of python scripts using the `pyraf` wrapper for IRAF. For the observing runs I have participated in, I have performed the data reductions myself, and compared the results with AB, who reduced the spectra in parallel. The methods used were identical, and are discussed in full in Bruce [2018]. A brief overview is given below. Apart from the cosmic ray extraction all functions referred to are IRAF functions.

The first two steps in extracting the spectra from the CCD images are bias and flatfield

corrections. Note that these steps are done twice per observation: once for the red, and once for the blue arm. A masterbias file is made by combining the images of the non exposed CCD, taken at the start and end of the night. This bias is then used to correct the dome flat exposures by subtracting spurious signal. The flats are combined in a masterflat file. This masterflat represents the response per pixel in the CCD and is used to adjust the science images fir the CCd's pixel sensitivity, using the `response` and `ccdproc` functions. This is followed by the cosmic ray removal. The L.A.–Cosmic algorithm searches for strong outliers in flux, and interpolates the values for affected pixels based on a fit of the spectrum.

Following the corrections of the 2D image, the image of the spectrum is extracted, by defining an aperture and the trace of the image across the CCD, using the functions available in `apall`. The aperture is set to be ∼3 FWHM (in pixels) of a Gaussian fit to the cross section of the slit's image. This step is repeated at different wavelengths. A range of columns (parallel to the spectrum, in the λ direction) is selected to measure the sky background, which is subtracted from the extracted spectrum. The spectrum is then wavelength calibrated using the arc-lamp images.

This brings us to the final correction: the flux calibration, using the standard star spectra. After masking telluric absorption features, `sensfunc` is used to create a sensitivity function which converts pixel counts to flux. This is done by scaling the masked spectrum of the standard star to the known spectral flux values for this object. The known spectral flux values are provided on the ING website[3]. The standard star selected for calibration is the one closest in airmass and observation time to the science observation. `sensfunc` takes atmospheric correction into account, adjusting the spectrum for the standard star using the average airmass and an atmospheric correction curve. The atmospheric correction curve (in units of magnitude per airmass) is an annual average, and is provided on the ING website as well. The sensitivity function is used to calculate the flux for the science spectrum. Telluric absorption features are not corrected, as these features were masked out when creating the sensitivity function.

Finally, the blue and red side of the spectrum are combined using `scombine`, and the spectra from the different 15–30 minute segments of the observations are averaged together. The IRAF script also calculates errors on the flux values, from the original Poissonian noise in the CCD. When combining the different epochs through addition, these errors are propagated in the standard way.

Spectra from MMT and Magellan observations were extracted in a similar manner, as detailed in MCL19. These reductions provided all the necessary spectra for the new observations used in the MgII study, as well as two spectra of Mrk 110. For several of the MMT spectra no error was available for the flux measurements, and a uniform error was set for all bins, using the standard deviation of the flux distribution as the error. This method will have overestimated the uncertainties, but as their main purpose is to guide the spectral fitting process (see Section 3.2), this will have a relatively minor effect on the final results.

2.2.2 Tillinghast Spectra of Mrk 110

Flux Corrections

As the data-set for the Mrk 110 project contains spectra from various telescopes and instruments, particular care was taken in the flux calibration. In addition to the WHT and SDSS

[3]http//catserver.ing.iac.es/landscape/tn065-100/workflux.php

reductions, discussed in the previous sections, I have made use of observation with the Tillinghast telescope (2.1.1 and 2.1.2). The spectra from the FAST archive still required flux calibration. To perform this calibration, I wrote a script based on the pipeline developed by AB, to find a sensitivity function using standard star observations.

The first step in the process was to identify the relevant standard stars, by searching through the scanned (handwritten) observation logs[4] for the nights Mrk 110 observations were made. Flux data for the standards are available via the ING website, which also provided the data for the WHT calibration. Standards are selected to be as close as possible in observation time and airmass to the science exposures. The spectra for the standards are also available via the FAST data archive. Both the cadence of standard exposures and the match in airmass to the science observations is considerably worse then for the WHT observations.

The larger difference in airmass between standard and science observations, compared to the observations running through the WHT pipeline, increases the importance of atmospheric corrections. Without it, the science spectrum is simply scaled by IRAF using the ratio of the standard spectrum to the established standard flux values. An issue for the FAST observations is the lack of availability of an atmospheric extinction curve for Mt. Hopkins. The nearest geographical locations with mean extinction curves available are Kitt Peak Observatory, Arizona (KPO), and Apache Point Observatory, New Mexico (APO), both available in IRAF. To explore the effect of the different extinction curves I reduced the FAST spectra using each curve, and compared the reduced spectra. The results are displayed in Figure 2.2.

After calculating the spectral fluxes for the two extinction curves, I calculated the ratio of the extinction corrected flux to the flux values of the same spectrum reduced without atmospheric correction, to quantify the impact of the correction on the sample. The median of this ratio, calculated over the FAST sample, is displayed in the top panel of Figure 2.2. The bottom panel shows the median ratio of the spectral flux of spectra reduced with the two different corrections. Although it is clear from the comparison to spectra without correction that extinction correction is necessary, the difference between the two curves is quite small, $< 1\%$. The altitude of the Tillinghast telescope is approximately midway between those of the APO and the KPO. As the KPO is closer in geographical proximity, I have selected the KPO extinction curve for the spectral reduction.

The spectra for the best available standards were scaled to the flux data using `sensfunc`, and the Mrk 110 spectra can be converted to the corrected flux. The calibrated spectra were checked by eye, after which one spectrum was rejected, as the observation was most likely not on target (or the spectrum file was mislabelled in the FAST archive). An overview of the Mrk 110 data is given in Table 2.2.

To further reduce the impact of any instrumental or possible calibration differences, another correction was applied to the Tillinghast spectra, as well as to the two Mrk 110 WHT spectra. The spectra were re-scaled so that the [OIII]λ4959 and [OIII]λ5007 fluxes match those in the single SDSS spectrum for Mrk 110, from 2001. This is based on the assumption that for the time-span during which the various observations took place, the narrow line flux is constant. The other spectra are rescaled to match the SDSS calibration. The fits to the lines are made using `lmfit` (see Chapter 3), after which the ratio of the measured line fluxes was calculated for each spectrum. The spectra are adjusted by multiplying them with a grey rescaling factor, which is the average of the two narrow [OIII] line flux ratios. The average scaling factor is 0.98,

[4] http://tdc-www.harvard.edu/instruments/fast/logs/

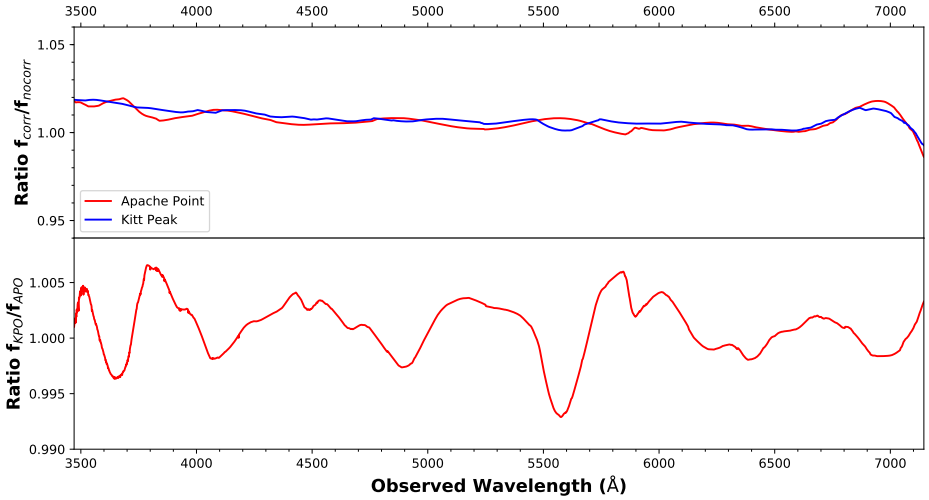

Figure 2.2: Comparison of the effects of two different atmospheric extinction curves, one for Kitt Peak Observatory (KPO) and one for Apache Point Observatory (APO), on the reduction of FAST spectra. *top*: medians of the flux ratio between corrected and uncorrected spectra for KPO and APO. *bottom*: median of the ratio between KPO and APO extinction curve corrected spectra. The medians have been calculated over the sample of archival Mrk 110 FAST spectra.

and the standard deviation of the distribution of the factors is 0.16.

The rescaling of the spectra using the [OIII] narrow lines rests on the assumption that none of the [OIII] emission from Mrk 110 is optically resolved. However, for objects in the nearby Universe the physical extent of the narrow line region as well as a host contribution can mean that part of the emission is resolved (see e.g. Tadhunter et al. [2018]). In objects where some of the narrow line emission is partially resolved, calibrating to the narrow line can be problematic, as changes in slit width and seeing can alter the fraction of narrow line flux that reaches the CCD. In the case of Mrk 110, with $z = 0.035$, the comoving distance in approximately 156 Mpc. This implies that a 1" slit width represents a transverse distance of 43 kpc. I therefore assume that the probability of mixing resolved and unresolved [OIII] is negligible. B99 also conclude that the narrow line region of Mrk 110 is not resolved, in their discussion of the [OIII] rescaling technique. However, the absence of a resolved [OIII] component, does not negate the possibility that any non-AGN narrow line contribution is not entirely constant over the range of observational epochs. The possible impact of this error on the Mrk 110 analysis will be discussed in Chapter 4.

Finally, as an additional check on a possible colour dependent calibration error during the WHT calibration, I compared the line fluxes of OIIλ3727 and OIλ6300 with those from SDSS. As the two lines are located far apart in terms of wavelength, any difference in the flux ratios between these two lines is an indication of a colour change. No such effect appeared to be present, and the narrow [OIII] grey scaling was deemed sufficient to guarantee a reliable epoch to epoch flux comparison.

For the newest FAST observations (2018–2019) the steps in the reduction are identical: all steps up to the spectrophotometric calibration have been performed by the FAST pipeline. Some of the observing nights have multiple exposures of Mrk 110, separated to reduce the risk of cosmic ray contamination. To create a single spectrum for each epoch, spectra taken on

the same night are combined to find the average. The spectra are first fully reduced and flux calibrated, after which I calculate the weighted mean of the flux for each bin. As the binning is identical for each spectrum, this calculation is slightly more straightforward than the one described in the next section. The weighting of the mean is simply by the inverse variance. The expression below shows the calculation of $\hat{f}_\lambda$, the average flux in a given bin, and of $\sigma^2(\hat{f}_\lambda)$, the associated variance:

$$\hat{f}_\lambda = \frac{\sum_i^N f_i/\sigma_i^2}{\sum_i^N 1/\sigma_i^2} \qquad \sigma^2(\hat{f}_\lambda) = \frac{1}{\sum_i^N 1/\sigma_i^2} \tag{2.2}$$

Increasing Signal to Noise: Spectral Stacking

For some of the Tillinghast spectra it was not possible to perform a more precise fitting of the HeIIλ4686 and Hβ lines than a simple pseudo-continuum method (see Chapters 3 and 4 for details). This is because the HeII flux was so low any signal in the individual spectra was lost in the noise. In order to nonetheless extract some useful information from this data-set, I wrote a script to stack these spectra. The spectra concerned are those observed between MJD 52252 and 52798, and between MJD 52940 and 53140.

The script for the stacking was written to incorporate spectra with different wavelength ranges and binnings, and takes these differences into account when calculating the error on the resulting flux bins. The bin size of the first spectrum is kept for the stacked spectrum. If a bin from the spectra to be added does not match the precise wavelength range of the bin of the original spectrum, the overlapping fraction is calculated and the same fraction of the flux and error is added, in quadrature for the errors. As the aim of the stacking is to create an average of the combined spectra, which have different levels of flux, the spectra are all normalised by dividing by the maximum flux (bin with the highest flux) in the wavelength range for the line under consideration. This prevents the spectra with relatively high line fluxes from dominating the stacked average.

2.3. Sample Construction

2.3.1 The Mrk 110 Sample: New Observations & Literature Values

The data for Mrk 110 come from a variety of sources, combining new spectral fits with flux data from the literature. The initial data for the project come from two papers by Bischoff and Kollatschny: Bischoff & Kollatschny [1999] (B99) and Kollatschny et al. [2001] (K01). In these papers the authors use combined data from the Calar Alto and McDonald observatories (located in Spain and Texas, respectively) for Reverberation Mapping studies of Mrk 110. The data-set for the first paper is spread out over eight years, but the spectra for the 2001 paper were taken at a much higher cadence, in a single observing season. The authors published the results of their spectral fitting, listing several line and continuum fluxes for all epochs. The relevant data for this study are those for the Hα, Hβ, HeIIλ4686, and HeIλ5876 lines, as well as for the 5100 Å continuum.

The literature data are expanded with line fluxes provided by B. Peterson, for the 5100Å continuum, Hβ and HeIIλ4686. The fluxes for Hβ were published in Peterson et al. [1998], but

Table 2.2: Overview of the data for Mrk 110. The first three columns in turn list the source of the data, the period over which the data were collected, and the number of spectra taken. The fourth and fifth columns concern the availability of the data: the 'spectra' column indicates whether the full spectra were available for analysis in this thesis. For those publications without the spectra available, I have made use of the published flux data (for the line as well as the continuum). The final column lists the shorthand notation for each data-set, as it will be used in Chapter 4.

Data	Epoch	N_{spec}	Spectra	Fluxes	Abbreviation
Peterson et al. (1998)	1992–1996	95	✗	✓	P98
Bischoff & Kollatschny (1999)	1987–1995	24	✗	✓	B99
Kollatschny & Bischoff (2001)	1999–2000	26	✗	✓	K01
SDSS	2001	1	✓	✓	SDSS
Tillinghast	2002–2019	59	✓	✓	FAST
WHT	2016–2017	2	✓	✓	WHT

Table 2.3: An overview of the parameters for the observations pertaining to Mrk 110, including for archival data and data from literature where available. The columns list, from left to right: the data-set (as labelled in Table 2.2), the resolution of the instrument, the range of slit widths or fibre diameters for the included observations, and a summary of the average observing conditions on the nights the observations were made.

Telescope	Resolution	Slit/Fibre	Conditions
P98	1600 (at 4800Å)	–	–
B99	1300 (at 4000Å)	2–2.5"	non-photometric
K01	650 (at 4000Å)	2"	–
SDSS	1500 (at 3800Å)	2"	photometric
FAST	1600 (at 4800Å)	3"	mixed
WHT	1500 (at 5200Å)	1−1.5"	photometric (2016)/cloudy (2017)

the HeII fluxes were not. The observations were made using the Perkins Telescope in Arizona, as part of an extended monitoring campaign of variable AGN.

The observations of Mrk 110 for which the spectra themselves are available are from SDSS, the Tillinghast telescope, and the WHT, as described in Section 2.1. The benefit of this data-set is that we can extract more information, specifically about the line profile, as will be discussed in Chapter 4. An overview of the data that make up the Mrk 110 sample is given in Table 2.2. In total the sample consists of 207 spectral epochs, and for 62 of these the spectrum itself was used for the analysis.

2.3.2 Defining the Samples for the MgII Study

The study into the long term variability of the MgII emission line is based on two samples: a set of 43 highly variable objects, 40 of which have new observations (the **supervariable sample**), and the set of suitable SDSS DR14 quasars (the **full population sample**). The basis of both samples is the quasar catalogues for DR7 [Schneider et al., 2010] and DR14 [Pâris et al., 2014], referred to here as DR7Q and DR14Q respectively. As these catalogues underlie the two samples, I will give a brief overview of their composition.

Since the first SDSS data release, every new release is accompanied by a catalogue of the SDSS quasars, which are those targets that were selected as QSO targets, and confirmed as QSOs by spectroscopic follow up. As discussed in Richards et al. [2002] the target selection of

quasars for SDSS I/II was largely based on the initial photometry: quasars occupy a specific region of the colour-space spanned by the *ugriz* colours. Additional QSO targets were added by matching object positions with the FIRST radio catalogue. Inclusion in the DR7 catalogue was limited to objects with an absolute magnitude in the i-band, $M_i < -22$, after correction for Galactic extinction. The selection for the DR14 targets was based on a wider range: colour-colour selection using both SDSS and WISE data, photometric variability in data from the Palomar Transient Factory, as well as FIRST cross-matches.

The main track of identifying quasars spectroscopically was the SDSS reduction pipeline. The core principle of this pipeline, with regard to identification, is to fit multiple spectral templates (e.g. quasar, galaxy, star) to the reduced spectrum and to use the fit with the lowest χ^2 as the identification. For DR7Q the results of this pipeline were verified by eye, resulting in a total of 105,783 quasars. For DR14Q the initial inspection by eye was performed for the BOSS spectra, but for SDSS IV was replaced with a second automated identification, which weights the automated fitting results to make a positive identification, leaving only a relatively small number of quasars candidates for classification by eye. The full set of DR7Q objects is included in DR14Q. Clearly great care has been taken in verifying the quasar identifications, making the SDSS catalogues reliable databases for quasars.

A final point about the quasar catalogues concerns previously derived measurements of line fluxes and spectral fits. An often cited paper based on DR7Q is Shen et al. [2011], which derived a multitude of spectral and physical qualities about the quasars in the catalogue. This was done through spectral fitting, as well as inferring parameters such as black hole mass (using the single epoch virial mass relationship). Some of the same parameters were re-derived in the quasar catalogue for DR12 [Pâris et al., 2014], covering both the DR7 quasars and the new observations. This would make a good basis for comparing MgII flux changes, and in fact this was the initial intention of the MgII full population study. Unfortunately a combination of instrumental difficulties (see Section 2.1.1) and differences in spectral fitting techniques make a good comparison impossible. A comparison will require a single fitting method for all spectra, providing a uniform metric of comparison, as well as the BOSS flux calibration corrections that were included in DR14. The nature of the problematic comparison between DR7Q and the DR12 catalogue is discussed in more detail in Chapter 5. The rest of this Chapter focusses on the selection of the two samples used in the MgII study from these two quasar catalogues.

The Supervariable Sample

The supervariable sample is a combination of two subsets from papers by C. MacLeod: one is a subset of the confirmed SDSS CLQs presented in MacLeod et al. [2016] (MCL16) and the other is subset of the CLQ candidate sample presented in MCL19. In both cases the objects in the sample with sufficiently high redshift to have MgII in their optical spectrum are included. The CLQs discussed in MCL16 were found by comparing BOSS and SDSS I/II spectra in the SDSS archival data, selecting candidates based on photometric variability in the g and r band.

For the project of identifying new quasars (MCL19) I was involved in the observations. The study of new spectra presented here was largely designed as a complimentary study to the work presented in MCL19. The main purpose of the observing campaign was to identify new CLQs. Following the SDSS archival searches presented in MCL16, we intended to expand the sample of known CLQs with follow-up observations on objects that showed strong photometric variability in PanSTARRS-I (PS-I) and SDSS-I data, but lacked recent (BOSS) spectroscopy. The aim

Table 2.4: Overview of the selection of CLQ candidates for observations, as presented in MCL19. This table is based on Table 1 in MCL19. g and r are filters in the SDSS $ugriz$ system.

Criterion	N_{obj}
DR7 catalogue	105,783
No BOSS spectrum	79,838
max $\|\Delta g\| > 1$, $\|\Delta r\| > .5$ & $z < 0.83$	1,727
No radio detection	1,403
Recent $\|\Delta g\| > 1$	262
Observed	130
MgII in range	**40**

was therefore to use spectroscopic follow-up to investigate whether the strong optical (g band) continuum fluctuations were accompanied, or followed, by changes in broad line emission. The characterisation of a highly optically variable source was made through the requirement that the difference in at least one pair of photometric epochs showed $|\Delta g| > 1$ and $|\Delta r| > 0.5$. This behaviour was verified with additional photometric data from CRTS [Drake et al., 2009] where available.

The starting point for the search for new CLQ targets was the DR7Q sample of confirmed quasars. The selection criteria for new CLQs are set out below. The target properties for the CLQ candidate selection were laid out in the telescope proposals as well as in MCL19. The precise list of conditions for an object to be considered a CLQ candidate is:

1. Included in the DR7 quasar catalogue (Schneider et al. [2010]; DR7Q)
2. There is no BOSS spectrum following the initital SDSS observation
3. A large magnitude change in PS-1 and SDSS photometry: max $|\Delta g| > 1$ and $|\Delta r| > 0.5$
4. $z < 0.83$, so that Hβ is in the spectral range (for WHT, MMT and Magellan)
5. There is no associated radio source: this excludes blazars.
6. The most recent photometry (2013) indicates a change in g of at least 1 mag compared to the SDSS epoch

The final condition, on the most recent photometry, is to ensure that at the time of observing the object is likely still in a period of change, rather than having returned to a more stable state. The selection is summarised in Table 2.4. The resulting sample of 262 objects was targeted with the follow up observations described in Section 2.1.2. Not all objects on this list were observed, with observation depending on allocated observing time, a by eye selection of the most interesting candidates (largely based on the photometric light curve), and conditions during the observing nights. A total of 130 of the candidates were observed. Of the observed targets with MgII in the spectral range, three objects were excluded because the new spectra did not allow for a good fit to the line. From the QSO candidate sample 40 objects finally met the criteria. In combination with the three MCL16 objects, this gives a *total of 43 objects* that were included in the study. The supervariable sample therefore consists of both confirmed CLQs and observed CLQ *candidates*. All objects are characterised by strong variation in the optical flux and can be considered EVQs. The full sample is listed in Table 2.6.

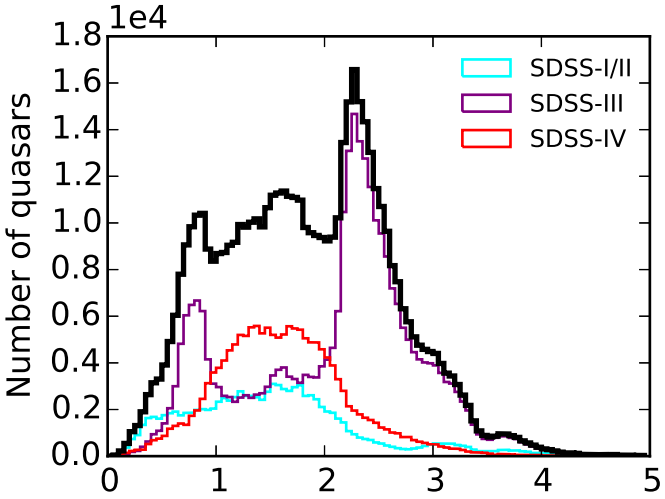

Figure 2.3: The redshift distribution of DR14Q (*black*), with number of quasars on the vertical axis and z on the horizontal axis. The decomposition of the sample into the main iterations of SDSS is also shown. There are many more high-z quasars available in DR14, due in particular to the strong peak at $z = 2$–3 of the SDSS-III/BOSS survey. Figure from DR14Q.

The Full Population Sample

The full population sample is derived from the DR14 quasar catalogue [Pâris et al., 2018]. DR7Q is the basis of both MCL16 and MCL19, and therefore of the supervariable sample, however DR14 provides a much larger sample of quasars. DR7Q has a total of ∼105,000 quasars, whereas DR14Q comprises about 523,000 objects. Additionally, a significantly larger fraction of the catalogue sample is at a redshift suitable for detecting MgII in the optical range. As can be seen in Figure 2.3, the number of quasars at higher redshifts is much larger in the DR14 sample, mainly due to the focus on BAO mapping in the BOSS survey. When focussing on MgII, DR14Q therefore allows for a better sampling of the population.

The sample is selected to include as wide a range of quasars as possible, to represent the 'general' quasar population. I have therefore made some simple requirements in terms of data quality, but put no further restrictions on the objects with repeat spectroscopy of MgII available. The first step in the selection among the 500,000+ quasars in DR14Q was to find objects with repeat spectroscopy, and with sufficient time between the observational epochs. For each object with more then one spectrum available, the pair with the largest difference between observation dates was selected. If this difference was less than 30 days, the object was excluded for the sample. For the included objects, the pair of spectra with the largest time difference is used from here on. The final sample therefore consists of two spectra for every included quasar. The motivation for selecting the objects with the largest temporal baseline is that, under the assumption that large continuum changes are more likely the longer we observe a quasar, this pair of spectra is most likely to represent the largest change in continuum flux.

The next step in the selection process is to exclude any Broad Absorption Line (BAL) quasars. These objects present a serious difficulty in the spectral fitting process, especially in the case of an automated pipeline. In addition, the presence of BALs in the spectrum is likely to indicate a physical process not detected in the other quasars, including those of the supervariable sample. This makes BAL quasars less suitable for purposes of comparing quasar

Table 2.5: The selection criteria for the full population sample, where the number in bold is the total number of quasars included in this sample. The table also shows the number of objects in a subsample of objects with high quality spectra available.

Criterion	N_{obj}
DR14 catalogue	523,356
$N_{spec} \geq 2$	72,747
$\Delta t > 30$days	61,147
not BALQ	56,724
z-warning/exposure/coordinates	55,028
MgII in range	**15,824**
S/N≥20	1,438

spectral behaviour.

The requirements on the data quality follow the advice from the SDSS archive website, using the `z_warning` flag in the spectral fits files as a quality indicator. Any spectrum with an active `z_warning` has presented difficulty to the SDSS fitting pipeline, likely due to poor S/N, and is excluded from the sample. A second check is on the exposure times for the individual observations that contribute to the coadded spectrum: if the exposure times listed in one of the spectral fits files sum to zero, the object is excluded as well. This step also excludes eleven objects for which one of the spectra could not be found in the SDSS archive (interestingly, all missing spectra belong to plate 2516).

Following these general requirements, the only other cut to the sample is in redshift: the MgIIλ2798 line needs to be in the spectral range for both the SDSS I/II and BOSS spectrographs. Assuming that for a proper fit of the MgII line it is necessary to have flux data at $\pm$100 Å from the line centre, and using the smaller λ-range available to the SDSS spectrograph (3800–9200 Å), the requirements on the quasar redshift are $0.41 < z < 2.17$. For this criterion I used the z value in the SDSS fits file.

This defines the full population sample, consisting of 15,824 pairs of quasar spectra. Finally, I also define a high quality subset of the sample (discussed in Section 5.2) based on the median signal-to-noise per pixel for the full coadded spectrum. For this selection, the limiting value is set to S/N = 20. An overview of the selection process is given in Table 2.5.

Table 2.6: (Next Page) Overview of the supervariable sample. From left to right, the columns list: the SDSS name, whether the AGN is listed in the DR7 quasar catalogue, the RA and Dec, the bolometric luminosity, the fiducial black hole mass estimate, the Eddington ratio, whether the object is identified as a CLQ, the largest total change in g-band magnitude, the number of spectra in the sample for the given object, the observation date of the most recent spectrum, and the telescope used to take the most recent spectrum.

	SDSS name	DR7	RA	Dec	z	log L_{Bol}	log M_{BH}	log $\frac{L_{bol}}{L_{Edd}}$	CLQ	max $\|\Delta g\|$	A_V	N_{spec}	Last spectrum	Telescope
1	001113.46−110023.5	✓	2.806	−11.007	0.495	45.2	8.2	−1.1	✗	1.2	0.11	2	57989	MMT
2	001206.25−094536.3	✓	3.026	−9.76	0.566	45.5	8.5	−1.1	✓	2.0	0.09	2	57597	Magellan
3	002311.06+003517.5	✓	5.796	0.588	0.422	45.5	9.2	−1.8	✓	1.0	0.07	4	58037	MMT
4	002450.50+003447.7	✓	6.21	0.58	0.524	45.5	8.7	−1.3	✗	1.1	0.06	2	57989	MMT
5	002714.21+001203.7	✓	6.809	0.201	0.454	45.5	8.2	−0.8	✗	0.5	0.06	2	57726	MMT
6	010529.61−001104.0	✓	16.373	−0.184	0.738	45.2	8.3	−1.2	✗	0.8	0.1	3	58037	MMT
7	013458.36−091435.4	✓	23.743	−9.243	0.443	45.6	8.5	−1.0	✓	1.4	0.09	3	57989	MMT
8	022556.07+003026.7	✓	36.484	0.507	0.504	45.4	8.4	−1.1	✓	1.7	0.1	15	56596	SDSS
9	022652.24−003916.5	✓	36.718	−0.655	0.625	45.3	7.5	−0.3	✗	1.4	0.08	5	56577	SDSS
10	034144.72−002854.3	✓	55.436	−0.482	0.623	45.4	9.9	−2.6	✓	1.2	0.18	2	57726	MMT
11	034330.48−073703.1	✓	55.877	−7.618	0.742	45.5	8.7	−1.3	✗	1.0	0.17	3	57597	Magellan
12	074502.90+374947.0	✓	116.262	37.83	0.593	45.3	8.4	−1.2	✗	1.3	0.13	2	58081	MMT
13	074719.65+215245.9	✓	116.832	21.879	0.462	45.2	8.7	−1.6	✗	1.2	0.15	2	58081	MMT
14	075228.65+405931.7	✓	118.119	40.992	0.423	45.4	8.2	−0.9	✗	1.3	0.15	3	58081	MMT
15	081916.15+345050.3	✓	124.817	34.847	1.5	45.9	9.3	−1.4	✗	2.1	0.14	4	57425	WHT
16	090104.75+345524.2	✓	135.27	34.923	0.564	45.7	9.2	−1.6	✓	1.8	0.08	2	57430	MMT
17	092223.17+444629.0	✓	140.597	44.775	0.536	45.5	8.9	−1.5	✗	1.4	0.06	2	57430	MMT
18	094132.89+000731.1	✓	145.387	0.125	0.489	45.5	8.0	−0.7	✗	1.2	0.19	2	57430	MMT
19	102016.04+014231.7	✓	155.067	1.709	0.448	45.3	8.1	−0.9	✗	1.4	0.14	2	57430	MMT
20	111348.64+494522.4	✓	168.453	49.756	0.659	45.7	9.2	−1.6	✗	1.5	0.04	2	57539	WHT
21	123228.08+141558.7	✓	188.117	14.266	0.427	45.3	8.6	−1.4	✗	1.2	0.1	2	57845	MMT
22	132815.50+223823.8	✓	202.065	22.64	0.486	45.4	8.8	−1.5	✓	1.4	0.06	2	57426	WHT
23	145519.88+364800.4	✓	223.833	36.8	0.525	45.5	8.6	−1.1	✗	1.3	0.04	2	57425	WHT
24	152044.63+394930.3	✓	230.186	39.825	0.439	45.2	8.5	−1.4	✗	1.2	0.05	2	57895	MMT
25	153734.06+461358.9	✓	234.392	46.233	0.378	45.3	8.5	−1.3	✓	1.4	0.05	2	57894	MMT
26	153912.76+524540.2	✓	234.803	52.761	0.415	45.3	8.3	−1.2	✓	1.1	0.04	2	57894	MMT
27	154341.64+385319.3	✓	235.924	38.889	0.432	45.4	9.1	−1.8	✗	1.2	0.05	2	57818	MMT
28	160226.01+323019.1	✓	240.608	32.505	0.557	45.7	8.8	−1.1	✗	1.1	0.07	2	58037	MMT
29	162415.02+455130.0	✓	246.063	45.858	0.481	45.4	8.5	−1.2	✓	1.2	0.02	2	57539	WHT
30	163031.47+410145.8	✓	247.631	41.029	0.531	45.5	8.8	−1.4	✗	1.3	0.02	2	57894	MMT
31	164053.05+451033.7	✓	250.221	45.176	0.422	45.4	8.9	−1.6	✓	2.6	0.03	2	57430	MMT
32	212436.64−065722.1	✓	321.153	−6.956	0.43	45.4	8.3	−1.0	✗	2.1	0.42	2	57543	MMT
33	214613.31+000930.8	✓	326.555	0.159	0.621	45.2	8.9	−1.8	✗	0.5	0.21	2	55478	SDSS
34	223133.89+003312.7	✓	337.891	0.554	0.476	45.4	8.6	−1.3	✓	1.2	0.19	2	57989	MMT
35	223500.50−004940.7	✓	338.752	−0.828	0.642	45.1	8.5	−1.5	✗	0.5	0.13	2	58037	MMT
36	224017.28−011442.8	✓	340.072	−1.245	0.502	45.1	8.3	−1.3	✗	1.2	0.14	2	57726	MMT
37	224829.47+144418.0	✓	342.123	14.738	0.424	45.5	8.9	−1.5	✓	1.5	0.18	2	57430	MMT
38	225240.37+010958.7	✓	343.168	1.166	0.534	45.3	8.9	−1.7	✓	1.7	0.22	3	57599	MMT
39	230427.86−000803.2	✓	346.116	−0.134	0.526	45.2	8.7	−1.6	✓	1.1	0.12	2	57726	MMT
40	231552.95+011406.1	✓	348.971	1.235	0.521	45.1	8.5	−1.6	✗	1.1	0.11	2	57726	MMT
41	231742.68+011425.2	✓	349.428	1.24	0.518	45.3	9.0	−1.8	✓	1.6	0.12	2	57726	MMT
42	233317.38−002303.4	✓	353.322	−0.384	0.513	45.3	10.2	−3.0	✓	1.7	0.09	4	57989	Magellan
43	234623.42+010918.1	✓	356.598	1.155	0.509	45.3	8.9	−1.7	✓	2.0	0.08	2	57989	MMT

3. Spectral Fitting

This chapter concerns the fitting techniques used in analysing the spectra from the various samples described in Chapter 2. For both the Mrk 110 and the MgII studies the key point is to accurately measure line fluxes, in order to quantify flux changes over time. The calculation of the line flux differs between the studies, to account both for the difference in line species to be fit and for the literature values with which the fitting results need to be compared. The relevant fitting methods for the two studies are discussed separately, starting with those for the Mrk 110 spectra.

3.1. Mrk 110: Individual Spectra

3.1.1 Fluxes: Pseudo-Continuum

As discussed in Section 2.3, the data for Mrk 110 consist of both literature values and new spectra. In order to make the comparison of line fluxes across epochs as reliable as possible, I have used the same method to calculate the flux as used in B99 and K01. This calculation is applied to the SDSS, Tillinghast and WHT spectra. The basic idea of the method is to calculate a linear pseudo-continuum in the region of the line, and then subtract this from the spectral flux. The remaining flux is counted as the line flux. The pseudo-continuum is simply a linear interpolation between two points on either side of the line. The most important parameters for this calculation are therefore the wavelengths chosen as anchor points for the pseudo-continuum and the wavelengths that set the width of the window in which the line flux is calculated. Continuum flux values in B99 and K01 are calculated as the average over a set range.

The wavelengths and ranges are taken from K01. An overview of the values is given in Table 3.1. The fluxes are calculated for Hα, Hβ, HeIλ5876, HeIIλ4686, and the continuum at 5100Å. To prevent outlying bins from skewing the pseudo-continuum, the two flux points at either end are not the values of the single bin at that wavelength, but rather the median of the fluxes in 20 bins around the central value. For the example of Hα, the lower flux value is calculated by finding the bin that contains 6260Å (in the redshifted spectrum), and taking the median of the range spanned by going 10 bins up and 10 bins down. The same is done with the bins around 6780Å for the higher point. The pseudo-continuum is then simply the line connecting these two points. The value of the continuum is calculated at the central value for the flux bins in the line window, 6400-6700Å in the case of Hα, and subtracted from the flux values. Finally, the flux values of the bins in the window, multiplied with the bin widths in Ångstrom, are summed to find the line flux.

There is a small discrepancy in the choice of parameters between B99 and K01, with slight changes in the wavelength windows and ranges. The shift in the windows between the calculations is of the order of a few Å. As in both cases the broad lines are still well contained by the window, and as median values are used for the pseudo continuum calculation, the effect of this

Table 3.1: Overview of the wavelengths and spectral ranges used to calculate continuum and line flux values, using the pseudo-continuum method. This table follows Table 2 in Kollatschny et al. [2001].

Region of interest	Line Window	Pseudo-Continuum Range
Hα	6400–6700Å	6260–6780Å
He I λ5876	5785–6025Å	5650–6120Å
Hβ	4790–4940Å	4600–5130Å
He II λ4686	4600-4790Å	4600–5130Å
5100Å continuum	–	5130–5140Å

change can reasonably be expected to be negligible.

3.1.2 Profile changes: Full Fit

In addition to the line flux calculation, the results of which are used for comparison with the literature data, I perform a more detailed fit to the available spectra. This is in order to extract more information from this data-set. Specifically, the aim is to find information about changes in line profiles, using line widths and the centres of the line components. As the subset of Mrk 110 spectra consists of 62 observations, the fitting was done on an individual basis: I adjusted the fitting parameters to optimise the fits, checking the result for every spectrum by eye. As discussed in the following section, this method was not feasible for the much larger MgII full population sample.

The software used for this fitting process is `lmfit`[1]. This method uses χ^2 minimisation, in the form of the Levenberg-Marquardt method, to perform spectral fitting. At its core `lmfit` functions as a wrapper for the scientific python (SciPy) minimisation libraries, and the package provides an easy way to construct fitting models and tune or fix the model parameters. For each model parameter the user can set an initial value, from which the parameter space is explored.

This more detailed fitting focusses on the Hβ and HeIIλ4686 lines, as discussed in Section 4.2. The fitting was applied to the spectra with sufficient HeIIλ4686 flux for a successful fit, as well as to the stacked spectra discussed in Section 2.2.2. In order to find the optimal method, I constructed several fitting models, and tried multiple spectral windows to apply the fit. The possible components of the models are Gaussian and Lorentzian line profiles for the HeII, Hβ, [OIII]λ4959, and [OIII]λ5007, with additional narrow line components for HeII and Hβ, a power law continuum, and an optical FeII emission template.

The power law, which should capture the continuum emission, has the simple form of $A\nu^{-\alpha}$, where the amplitude A and index α are the fitted parameters. The line components have three free parameters: the line centre, line width (σ in the case of the Gaussian profile) and the amplitude. The FeII template also has three fitted parameters: amplitude, redshift with respect to the observer, and a smoothing parameter. The latter is designed to capture line broadening by dynamic processes in the FeII emission region. A discussion on the FeII templates can be found in Section 3.2.3. The FeII template used in the trials was that presented in Véron-Cetty et al. [2004].

The optimal method was selected based on a by eye inspection of the different fits. The

[1] https://lmfit.github.io/lmfit-py/

most important cause of misfitting is the proximity of the HeIIλ4686 and Hβ lines: the wings of the two lines overlap. Another complicating factor is the relatively high density of emission lines around Hβ, due to the presence of the other Balmer lines as well as of various Helium and Oxygen lines. This makes the fit of the optical FeII template particularly problematic. In order to keep the number of free parameters in the models to a minimum and get the best possible fix on the line centres and widths, the optimal fitting procedure was found to be to fit the HeII and Hβ lines separately. This approach cuts the overlap between the lines artificially, by confining the fitting regions. For HeII, the fitting region (in the QSO restframe) was selected to be 4400–4810Å, and for Hβ it was set to 4820–5050Å. Gaussian fits to the lines proved to be superior to Lorentzian profiles.

The final fitting model is deliberately minimal. All many-component models had a strong tendency towards overfitting: spurious components in the noise would be fit as real lines contributing to the flux, or part of the FeII emission would be fit as a very broad Gaussian. In all these cases the addition of components did not improve the quality of the fit, even if the χ^2 value was lower. The components included in the model for the HeII region are the continuum power law, and two Gaussians, for the broad and the narrow component of the line. The flux, width, and centre for the narrow lines are fixed: the values are set by the fitted narrow line value for the spectrum of MJD 53019, a high S/N Tillinghast spectrum. The narrow line flux from Mrk 110 is therefore assumed to be constant during the time spanned by the observations, which is approximately fifteen years. Fixing the HeII narrow line makes for a more reliable comparison with the changing flux and centre of the changing broad component of the line (see Section 4.4).

For the model of the region around Hβ I have included the power law and four Gaussian components. The Gaussian components are fit to broad and narrow Hβ and to the O[III]λ4959 and [OIII]λ5007 lines. The addition of the narrow [OIII] lines does not hamper the fit, as they are both strong and clearly defined. For Hβ the narrow line was allowed to vary, as the narrow component cannot be isolated quite as clearly from the broad component in the SDSS spectrum, as it can be in the case of HeII. The Oxygen lines are fit with single Gaussians, and the centre of the λ4959 line is fixed to have the same redshift as the λ5007 line. Examples of the fitting results for the two line windows are shown in Figure 3.1.

In the case of two spectra, taken on MJD 53021 and 53055, it was necessary for a spurious spectral feature to be masked out. An apparent emission line around 4920Å contaminated the region of the broad HeIIλ4686 line. This feature is almost certainly of instrumental origin, as the repeat appearance in two separate observations appears to rule out a cosmic ray. For the purpose of fitting the HeII line, the bins in the range $4905 < \lambda < 4930$ were masked out in these two spectra.

3.2. SDSS and New Observations: Pipeline

3.2.1 Pipeline Overview

For the MgII analysis, the spectra from the supervariable and the full population samples are fitted using a model similar to that used for the Mrk 110 spectra, using the `lmfit` package. The main difference with the fitting of the Mrk 110 spectra is that the fitting process is automated

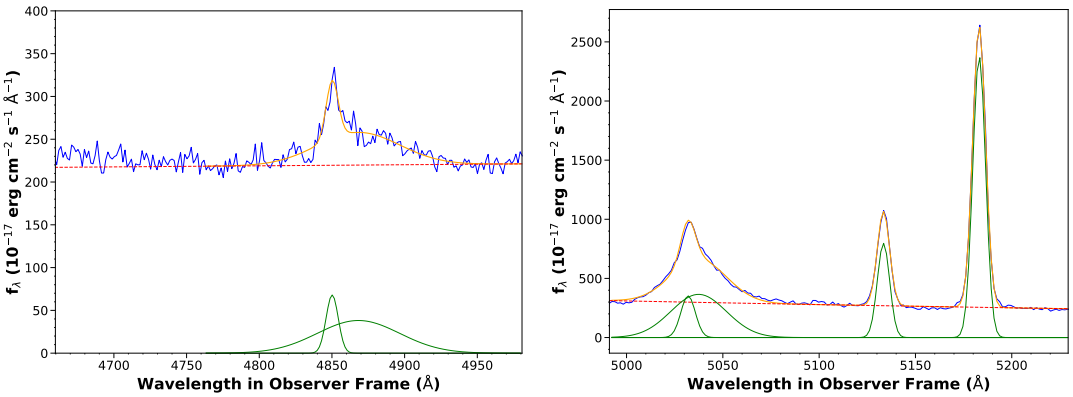

Figure 3.1: Example of the results of the `lmfit` method, using the final fitting method described in the text. Both fits are to Tillinghast spectra. *left*: The HeIIλ4686 line fit (orange) containing the power law continuum (dashed red) and two Gaussian components (green). The spectrum was taken on MJD 52997. *right*: The Hβ line fit, with power law continuum and Gaussian line fits to narrow Hβ, broad Hβ, and the two [OIII] lines. The spectrum was taken on MJD 53021.

in a pipeline. This pipeline uses an iterative process to improve the fit quality. Although the number of spectra for the supervariable sample is not too large for individual spectral fitting, these spectra are also fitted with the pipeline. The supervariable and full population samples are included in the same analysis (Chapter 5), therefore it is important that the spectra from the samples are fitted using the same method.

This section provides a description of the different steps making up the pipeline. In brief overview the stages of the pipeline are:

1. Load spectrum and create mask for low quality flux bins
2. Correct for Galactic dust extinction
3. Trim spectrum to fitting range
4. Fit the relevant spectral component
5. Use fitting results for the next iteration of fitting

The steps (3)-(4)-(5) can be repeated a number of times, for each spectral component, to improve the quality of the fit without manual tuning of the fitting parameters for each spectrum. The parameters that define this iterative process and the components that make up the model to be fit to the data are discussed in detail in Section 3.2.2.

Taking a closer look at the individual stages: (1) When the spectrum is loaded, the bins without an error associated with the flux measurement are masked out. This applies only to the SDSS spectra, as the new observations will have errors on all flux bins, either through the spectral reduction process, or as a post facto estimate (as described in Section 2.2.1). (2) The next step in the pipeline is to deredden the spectra, correcting for Galactic extinction. This extinction is due to dust in the Milky Way, along the line of sight to the target. The flux loss due to this interaction affects the blue side of the spectrum more than the red. As it is possible to make use of multiple empirical extinction curves to correct for this effect, it is worthwhile to briefly discuss the choice made for the pipeline. The dereddening curve applied to the spectra here is that described in Fitzpatrick [1999] (F99). The implementation of the F99 correction is

with a function from the python `extinction` package[2].

The choice of function is in accordance with the analysis of Schlafly & Finkbeiner [2011] (S&F), who compare the extinction models of F99 and Cardelli et al. [1989] (CCM), using SDSS stellar spectra. There are two parameters fixing the extinction function along a particular line of sight, often chosen to be A_V, which is defined as the total decrease in magnitude over the Johnson V bandpass, and E(B-V), the 'selective extinction' between the B and V filter bandpasses. In terms of the extinction functions, several of which are plotted in Figure 3.2, A_V represents the overall normalisation and E(B-V) is a measure of the gradient of the extinction curve between B and V. The two are related by:

$$R_V = \frac{A_V}{E(B-V)}, \tag{3.1}$$

where R_V has been empirically established, by e.g. F99 and S&F, to be a constant with a value of approximately 3.1. The difference between the various extinction functions is often characterised by E(λ-V)/E(B-V), the extinction as a function of wavelength relative to the extinction in the V band, and normalised to the selective extinction in the B band. Although not the simplest of definitions, this metric provides a good indicator of the overall behaviour of the modelled extinction curve. To find the extinction in a particular direction, we require A_V and E(B-V). S&F find that the curve provided by F99, with $R_V = 3.1$ is the best match to their data, and this function has therefore been adopted here as well. The reddening measure provided by S&F is the measure provided in the SDSS spectrum fits file (for the *ugriz* filters) in recent data releases.

The difference between the CCM and F99 corrections mainly manifests itself in the UV and the IR, whereas the differences in the spectral regions considered for the MgII samples and for Mrk 110 are relatively minor. This can be seen in Figure 3.2, in which various F99 curves are compared to those of CCM. The difference in the spectral correction with publications that use the CCM dereddening, should therefore be negligible in the case of optical spectra.

The values of A_V for the objects in the sample are downloaded from the NASA/IPAC IRSA website[3], which uses a map of galactic dust [Schlegel et al., 1998] to estimate the dust temperature and column density. The coordinates used for the objects are from DR7Q. The selected extinction measure is that based on the model of S&F, and the `extinction` function dereddens the spectrum according to the E(B-V) values set in F99. Following the extinction correction, (3) the spectrum is trimmed to the wavelength range for the initial fitting process. The different spectral components are fit in different wavelength windows. An overview of the relevant ranges is given in Table 3.2. The spectrum is not deredshifted yet. Rather, the spectral components are reshifted into the QSO restframe, so that z is also estimated in the fit. The application of the windows is followed by (4) calling the fitting algorithm. The algorithm consists of the methods provided by the `lmfit` package. The results of the fit are then (5) used in the next iteration of the fit, both in a sigma-clipping of the data and as initial estimates for the function parameters.

The power law continuum is the same as used for the Mrk 110 spectra: $A\nu^{-\alpha}$, where A is the amplitude and α the power law index. This is the first component to be fitted. The wavelength range is selected to contain as few contaminating features in the spectrum as

[2]https://extinction.readthedocs.io
[3]https://irsa.ipac.caltech.edu/applications/DUST/

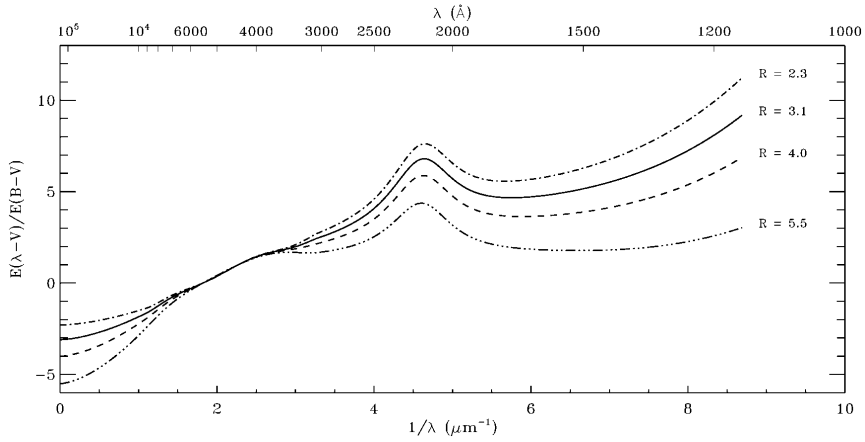

Figure 3.2: Extinction curves comparing the F99 and CCM extinction models, for different values of R_V. The horizontal axis is the inverse wavelength, and the vertical axis represents the normalised extinction. The solid lines are the curves for the F99 extinction, and the dashed and dash-dotted lines are those for the CCM extinction. In the optical and near-UV the curves are almost identical. Figure from F99.

possible, and to provide a good representation of the continuum in the near-UV. This step is only repeated once: after the initial fit has been completed, the pipeline calculates the standard deviation of the residuals, and then removes all data points that are further than 2 standard deviation away from this fit (sigma clipping). The fit is then repeated on the clipped data-set with the results of the previous fit as the initial estimate for the model parameters.

3.2.2 Spectral Components and Iterative Fitting

The components of the model used to fit the MgII line are the continuum power law, the FeII template, and one or two Gaussian profiles for the MgII line itself. Each component is fit iteratively, with the initial guesses for the model parameters, used as the starting point for the χ^2 minimisation algorithm, set to the same value for every spectrum. The number of iterations and the sigma-clipping limit are free parameters in the procedure, for every spectral component. The values of these parameters for the pipeline were optimised using the supervariable sample, checking the fits by eye as well as comparing the reduced χ^2 for different possible combinations. The definition of the reduced χ^2 is:

$$\chi^2_{red} = \frac{\chi^2}{N_{data} - N_{var}} = \frac{\sum_i^N \left(\frac{f_i - M_i}{\sigma_i}\right)^2}{N_{data} - N_{var}}. \tag{3.2}$$

Here N_{data} and N_{var} are the number of flux bins and the number of fitting parameters respectively, and f_i, M_i and σ_i are the flux, fit value and standard error on the flux for each bin. The pipeline was calibrated to the supervariable sample, which includes both SDSS and new spectra, before being applied to the much larger full population sample. An overview of the parameters used in the pipeline is displayed in Table 3.2. An example of a spectral fit, with all components identified, is shown in Figure 3.3.

Table 3.2: The components of the spectral fitting model for the MgII pipeline, and the parameters used for the fitting process. The columns, from left to right, are the name of the component, the wavelength window in which the component is fit, the number of iterations used in the pipeline in fitting the component, the number of standard deviations used as a measure to smooth the data after each iteration of the fit (σ-clipping), the parameters used to fit the model component, and finally the initial values for each parameter in `lmfit`, used in the first iteration of the fit. The redshift used in the parameter initialisation is that from DR14Q for the full population sample, and DR7Q for the supervariable sample.

Spectral Component	λ range (QSO restframe)	N_{iter}	σ_{clip}	Parameters	Initial value
Continuum	$2300 < \lambda < 2700$ $2900 < \lambda < 3088$	2	2	Amplitude Index	10^{-17} erg Å^{-1} s^{-1} cm^{-2} -1
FeII	$2300 < \lambda < 2700$ $2900 < \lambda < 3088$	4	2	Amplitude z Smoothing par.	10^{-15} erg s^{-1} cm^{-2} z from DR14Q 5 (min= 0)
MgII (Gaussian)	$2700 < \lambda < 2900$	3	3	Amplitude width centre	$5 \cdot 10^{-15}$ erg s^{-1} cm^{-2} 40 Å (max= 100Å) $2798 \cdot (1+z)$ Å
MgII (two Gaussians)	$2700 < \lambda < 2900$	3	3	1) Amplitude 1) width 1) centre 2) Amplitude 2) width 2) centre	$2 \cdot 10^{-15}$ erg s^{-1} cm^{-2} (min= 0) 10 Å (max= 25Å) $2798 \cdot (1+z)$ Å $7 \cdot 10^{-15}$ erg s^{-1} cm^{-2} (min= 0) 40 Å (min= 0, max= 65Å) $2798 \cdot (1+z)$ Å

One of the main benefits of the iterative fitting is that it circumvents a recurring issue with the `lmfit` algorithm, in which the algorithm cannot return errors on a fit with noisy data. By reducing the required exploration of the parameter space (using the new initial values) and reducing the noise in the data, it is possible to get a better estimate of the uncertainties involved in the fitting procedures. The errors returned in the basic `lmfit` functionality are the standard errors calculated from the covariance matrix. As discussed further in Section 5.2 these fitting errors are almost certainly an underestimate of the model uncertainties, and will be superseded by other estimates. However, for their use in the calculation of the reduced χ^2 and in the choice of the correct FeII template it is important to have these `lmfit` estimates available.

Following the power-law-only fit, the same spectral range is used to jointly fit the power law and the FeII template. The FeII template used in this step is that presented by Vestergaard & Wilkes [2001] (see the discussion in Section 3.2.3 for further details). The pipeline starts with the original data, but uses the results from the power-law fit as the initial parameter values for this component. This fit is made in as wide a spectral window as possible (see Table 3.2) The FeII component of the model has three parameters: the amplitude, representing the strength of Iron emission, the redshift, fixing the position of the lines, and a smoothing parameter. The smoothing parameter is defined as the width of the Gaussian kernel that is used in the smoothing process. The physical interpretation of this smoothing is kinematic broadening of the Iron lines: at least part of the FeII emission is expected to come from relatively deep in the potential well. The effect of this broadening on the template is to blend the many lines together, smoothing the overall profile. The fitting is repeated four times, with the same value for the sigma-clipping as for the power-law-only case. After the final iteration, the best-fit continuum+FeII model is subtracted from the full data-set.

The final component of the fit is the line itself, which is calculated in the window $2700 < \lambda < 2900$Å using the residuals derived in the previous step. The line is represented with one or two Gaussian profiles. Although most spectra are best approximated with a single Gaussian, there are examples (such as in Figure 3.3) where there is a clear second component, and two Gaussians are needed to best capture the line flux. Note that both components are 'broad' emission lines: the pipeline does not fit the narrow MgII component separately. The selection between the two models is left to the algorithm, and is based on the Akaike Information Criterion (AIC). The AIC is calculated in the fitting process, and is defined as:

$$\mathrm{AIC} = N\ln(\frac{\chi^2}{N}) + 2N_{var}. \tag{3.3}$$

The purpose of the AIC is to compare models with different numbers of parameters, penalising models with more parameters by taking both goodness of fit and the potential for overfitting into account. For the MgII line, both the single and double Gaussian model are fit to the data. The fitting procedure is the same for each: three iterations, with data being clipped when it is further than three σ away from the model. After this fitting, the AIC is calculated for both models and the model with the lowest AIC is selected.

Note that the second Gaussian, although narrower than the other component, does not constitute a 'narrow' line in the same sense as the HeII narrow line in the Mrk 110 fit. It is assumed that the true narrow component of MgII, in as far as it is present, is not resolved. In the case where two Gaussians are fit, their combined flux constitutes the broad MgII emission.

There is a large spread in the fitting methods applied to quasar spectra. Some of these

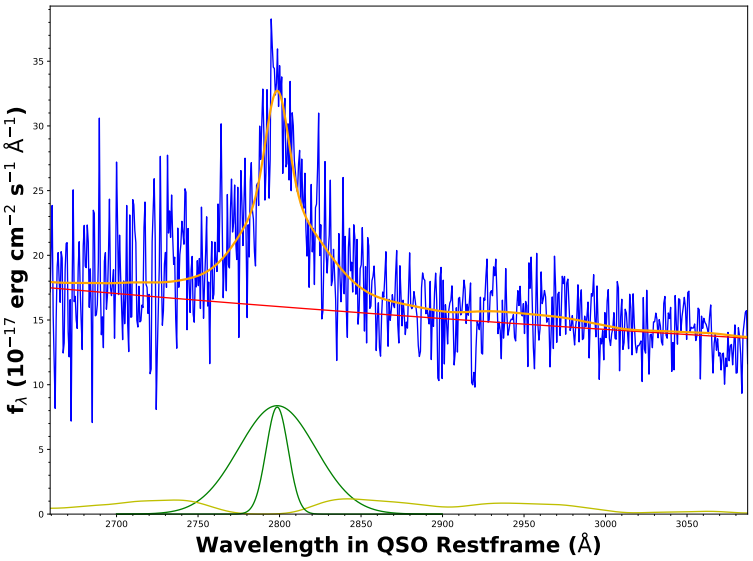

Figure 3.3: Example of the result of a fit by the pipeline, for the SDSS spectrum of J212436 taken on MJD 52200. The spectrum is shown in blue and the fit components are: *red*: power law continuum; *green*: Gaussian fit to MgII (this can be one or two Gaussians); *yellow*: FeII template by Vestergaard et al., smoothed with a Gaussian filter; *orange*: the combined fit to the spectrum. Note in particular the presence of FeII emission in both the red and the blue wing of the MgII line.

methods (e.g. Shen et al. [2011]; Zhu et al. [2017]) allow for a large number of components to the fit. In particular many Gaussian components are fit to capture the flux in a single broad line. I opted for a minimal approach. The reasoning is that for our purposes the many component approach brings with it a great risk of fitting non-physical spectral features, resulting in changes in the measured line flux. For example: both the red and the blue wings of the MgIIλ2798 line have a particular FeII contamination, as can be seen in Figure 3.3. Allowing for many Gaussian components at differing offsets from the system redshift makes it possible, if not likely, that this FeII emission is counted in the MgII flux. If the FeII flux changes independently of the MgII line, this can lead to artificial differences in the line flux between epochs. A minimalist method therefore allows for the most consistent measurement of the MgII flux when all components of the spectrum vary, which is what is required for a comparison across epochs.

3.2.3 Selecting the FeII Template

The presence of significant FeII emission in the wings of the MgIIλ2798 line means the choice of FeII template and the subsequent fitting are a source of possible uncertainty in the analysis. There are several FeII emission templates available and different templates cover different parts of the spectrum. To optimise the fitting process, it important to select the template that provides the most consistent measurement of the MgII flux. I have tested two UV FeII templates: the empirical template presented in Vestergaard & Wilkes [2001] (VW) and the template based on an FeII transition model presented in Bruhweiler & Verner [2008] (BV). The VW template is the template used in DR7Q for the MgII region.

The VW template is based on spectra from the narrow line Seyfert I galaxy I Zw 1, which

has unusually strong Iron emission lines. In applying this template to other AGN, the relative strength of the different emission lines found in I Zw 1 is therefore assumed to be universal, with only the overall amplitude varying in the fit. The BV template is based on a model of the FeII atom, covering 830 possible energy levels, and the associated transitions. This model was combined with the CLOUDY software [Ferland et al., 2013] to produce a synthetic FeII emission spectrum, which was also calibrated to I Zw 1. Although calibrated to the same object there are significant differences between the two templates, especially for the emission in the wings of MgII. Whereas the VW template has more or less symmetric bumps on either side, the BW template has significantly stronger emission on the blue side of the MgII line.

The comparison of the templates' applicability was made by fitting the models containing the two different templates to the same spectrum and comparing the errors. The other components of the model are the power law and only a single Gaussian. To account for a possible underestimation of the errors by `lmfit`, an error measure was calculated using a simple Monte Carlo simulation. For N=10^3 iterations Gaussian noise was added to the flux data, where the spread in the noise was chosen to be the measurement error on the flux. As described in Chapter 5, two main quantities under consideration for this study are the MgII line flux and the estimated continuum flux at 2798Å. For each of the 10^3 spectral fits these quantities are calculated. The spread in their distribution (the standard deviation σ_{MC}) is used as an error measure on the two model fits. The spectrum used for the fitting was the SDSS spectrum for J002714, an object in the supervariable sample. The model fitting followed the same procedure as outlined in Section 3.2.2.

The results of the comparison suggest a slight preference for the VW template. For VW $\sigma_{MC,line} = 3.19 \cdot 10^{-15}$ erg s^{-1} cm^{-2} and $\sigma_{MC,continuum} = 2.74 \cdot 10^{-17}$ Å^{-1} erg s^{-1} cm^{-2}. For the BV template the error measures are: $\sigma_{MC,line} = 3.19 \cdot 10^{-15}$ erg s^{-1} cm^{-2} and $\sigma_{MC,continuum} = 4.22 \cdot 10^{-17}$ Å^{-1} erg s^{-1} cm^{-2}. As an additional check, I compared the reduced χ^2 for the two fits. The ratio of $\chi^2_{red,VW}$ to $\chi^2_{red,BV}$ is approximately 0.92, again indicating a preference for the VW template. Inspection by eye did not suggest a strong favourite for either of the two templates. The VW template was selected for use in the pipeline, as this statistical comparison indicates it works better with the applied fitting procedure.

4. Markarian 110

In the study of the response of broad lines to changes in the ionising continuum Mrk 110 provides a unique opportunity for a detailed study. This nearby Seyfert 1 galaxy, at a redshift of 0.0355 [Ahn & et al., 2013], has been observed in various campaigns over decades, and often at a relatively high cadence of observations (see Section 2.1). The data-set allows us to track broad line variability in this AGN with great precision, and with the use of high S/N spectra. In contrast to the study of the MgIIλ2798 line among the broad population of quasars, this discussion on Mrk 110 is therefore a case study. Due to its low redshift, the optical spectra for Mrk 110 do not contain MgII in the wavelength range. However, the behaviour detected in this object can provide insight into the behaviour of the BLR in all quasars, complementary to the MgII population study. To understand how well we can extrapolate the results from this particular case to the general quasar population, I will first discuss what we know about Mrk 110 from the outset. Section 4.2 will cover the methods used in analysing the data from the fitted spectra and the fitting function used in establishing a new measure of broad line responsivity. The results for the flux responsivity will be presented in Section 4.3. The possible evolution of broad line profiles is covered in Section 4.4. This chapter will conclude with a discussion of the implications of the observed behaviour in Mrk 110 for quasar Broad Line Regions in general.

4.1. A Case Study of a Highly Variable AGN

Mrk 110 is a highly variable object: its bolometric luminosity is approximately 4×10^{44} erg s^{-1}, with continuum flux levels (at 5100 Å) varying up to factor $\sim$10 over the period of observation, see Figure 4.2 [Peterson et al., 1998; Bischoff & Kollatschny, 1999; Kollatschny et al., 2001]. The morphology of the object is somewhat peculiar [Hutchings & Craven, 1988; Bischoff & Kollatschny, 1999]. An image, based on imaging from SDSS-I, is shown in Figure 4.1. The first thing to note is the presence of a star in the foreground, which appears close to the nucleus, located to the north east. The second unusual aspect is the long tail extending WNW from the nucleus. The combination of a highly active nucleus and the extended shape make a tempting argument for recent merger activity, but no conclusive evidence has been presented to date (e.g. Hutchings & Craven [1988] confuse the foreground star with a second nucleus, to argue for a merger where the extended arm would be the result of an optical jet).

The proximity of the galaxy in combination with its strong variability have made Mrk 110 an object of continued study over a long period, including Reverberation Mapping campaigns. The studies providing data for this work are listed in Table 2.2, as are the new observations. In total they represent more than two decades worth of observations, at varying cadences over time. The light travel time lags (Kollatschny et al. [2001]: K01) used in this study are presented in Table 4.1; they are consistent with the model of a stratified BLR, with higher ionisation lines closer to the central engine. The BLR size scale is of the order of several dozen light days.

Using the 5100Å continuum flux, it is possible to construct a spectrophotometric lightcurve for Mrk 110. In Figure 4.2 this lightcurve is shown with the different origins of the data marked.

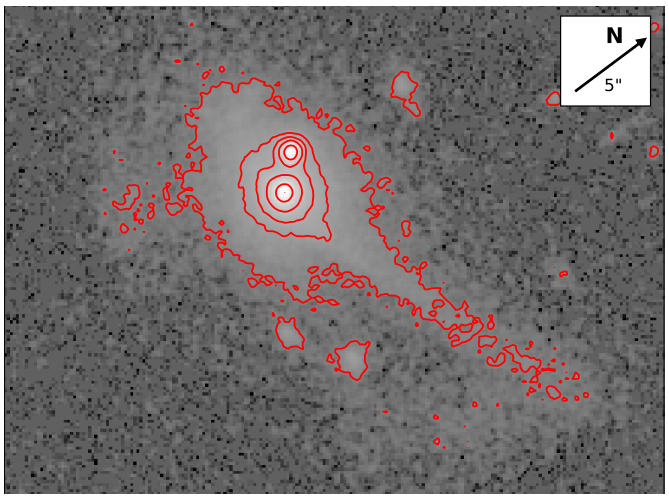

Figure 4.1: SDSS r-band image of Mrk 110. The scale of the image is indicated by the size of the arrow pointing North, which corresponds in length to a change in declination of 5 arcseconds. The contours represent levels of constant flux in SDSS units of nanomaggies. The contours are fixed at the levels 0.05, 0.2, 0.4, 1, 5, and 20 nanomaggies. Data from SDSS, the contours and orientation marker were added by me.

Table 4.1: Lags for the four broad emission lines of Mrk 110 used in this study, measured in the Reverberation Mapping study presented in K01. The errors are approximations of a 1-sigma error. This table is based on Table 6 in that paper.

Line	Lag (days)
HeIIλ4686	$3.9^{+2.8}_{-0.7}$
HeI λ5876	$10.7^{+7.0}_{-6.0}$
Hβ	$24.2^{+3.7}_{-3.3}$
Hα	$32.3^{+4.3}_{-4.9}$

The variability of the AGN is clearly visible in this lightcurve. Additional observations of the object have been made in X-rays and radio. The X-ray observations were made using XMM [Boller et al., 2007] and SWIFT/BAT [Winter et al., 2012], both with a clear detection of the nucleus. The radio observations were made with the VLA, as part of the NRAO VLA Sky Survey [Condon et al., 1998]. A radio flux of 10.1 mJy was registered at 1.4 GHz, making Mrk 110 a radio quiet AGN. The redshift is determined by the SDSS pipeline, which determines the target classification and redshift in the same process, through fitting a range of templates (at a range of redshifts) to the entire spectrum. This process provides an uncertainty in the redshift of approximately 1:10.000.

The various studies that have been conducted present a unified picture of a highly variable Seyfert 1. They are more difficult to unify when it comes to the SMBH mass. The virial mass derived from the RM studies in Bischoff & Kollatschny [1999] (B99) and K01 are $6 \pm 2.7 \times 10^7 M\odot$ and $1.8 \pm 0.4 \times 10^7 M_\odot$ respectively. The authors considered the latter estimate to be an improvement over the former, as it is based on higher cadence RM observations, allowing for better measurement of the line lags. Using the same data-set, Kollatschny & Bischoff [2002] and Kollatschny [2003a] also derive a mass $\sim 10^7 M_\odot$, by creating velocity resolved line profiles of several Balmer and Helium lines. However, a significantly different mass is derived in

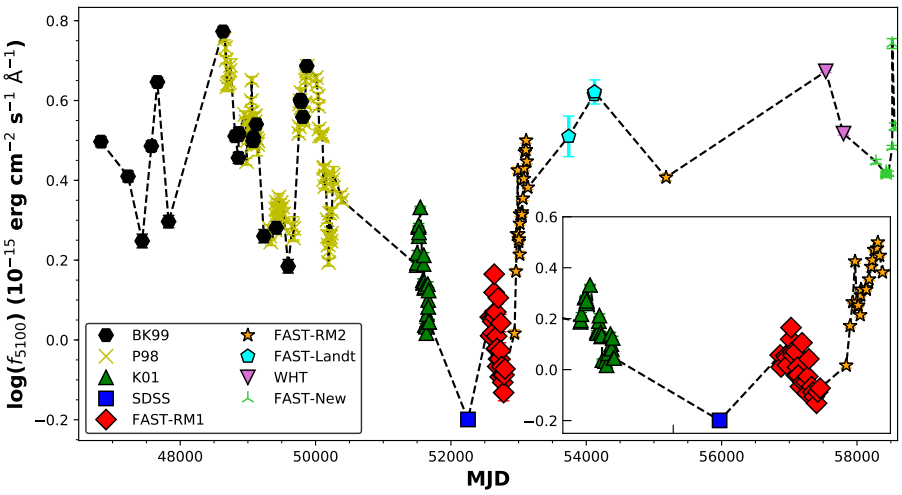

Figure 4.2: Continuum lightcurve for Mrk 110 based on the spectrophotometric fluxes at 5100Å (f_{5100}). The values for f_{5100} have been calculated following the method set out in Kollatschny et al. [2001]. The spectral epochs have been marked according to the origin of the data, with the abbreviations as introduced in the text. The archival FAST spectra have been divided into RM1 and RM2, as they were part of two separate (unpublished) Reverberation Mapping campaigns. The inset shows a closer view of the distribution of the observational epochs for the high cadence KO1, FAST-RM1 and FAST-RM2 data.

Kollatschny [2003b], based on a gravitational redshift argument. An offset between the narrow and broad component, which can be detected for several emission lines, is interpreted as the result of a difference in the gravitational redshifts to which the line components are subject. As the broad component is formed deeper in the potential, the redshift should be stronger for this component. By calculating the offset between the narrow and broad components in the rms spectrum, and combining this with the RM lags from K01, it is possible to calculate the black hole mass. The authors present a mass of $1.4 \pm 0.3 \times 10^8 M_\odot$, an order of magnitude larger than the earlier estimates.

The explanation for the difference in mass, as argued in Kollatschny [2003b], is the relatively low inclination at which we view the object, under the assumption the line widths are largely rotational. The estimates of the rotation speed are a lower limit, and the derivation of a black hole mass independent of the Keplerian velocities allows for the calculation of the inclination angle. The author derives $i = 21 \pm 5°$, close to face on. The gravitational redshift estimate is problematic for two reasons, however. The first is that there is a mass estimate independent of BLR kinematics: Ferrarese et al. [2001] estimate the virial mass of Mrk 110 using the velocities of circumnuclear stars, based on the M-σ_* relation (Ferrarese & Merritt [2000], see Section 1.3.2). Using widths of the CaII triplet ($\lambda\lambda$ 8498, 8542, and 8662Å) to derive the rotational speed of the stars, the authors find $M_{BH} \sim 7.7^{+3.8}_{-2.9} \times 10^6 M_\odot$, a factor of ∼20 below the gravitational redshift estimate.

The second reason to doubt the gravitational redshift interpretation is that the offset between broad and narrow components, for the HeIIλ4686 line, appears to have a more complicated behaviour. It is detected in other AGN as well [Barth et al., 2015]: Peterson et al. [2000] note a broad-narrow offset for HeII in NGC 4051, where the broad line is shifted to the blue with respect to the narrow line, as opposed to the shift to the red seen in Mrk 110. The relative

blueshift is wholly incompatible with the interpretation based on the relative positions in the gravitational potential of the line emitting regions. Although it is not certain that the blue and red offsets of the broad line are different representations of the same physical mechanism, I would argue that an explanation that incorporates both is preferred over separate explanations for the effects. For these reasons I reject the notion of the gravitational redshift as a cause for the line component offset, and deem the lower mass estimates to be more accurate. We will explore the issue of the offset further in Section 4.4, considering its evolution over time, and its evolution in comparison to other line parameters.

Returning now to the data available for the analysis, it is clear that the strong variability of the continuum (as indicated in Figure 4.2) is accompanied by large changes in the emission lines as well. Several examples of the spectra included in this study are shown in Figure 4.3. Among epochs the spectrum of Mrk 110 shows dramatic changes in line flux. Using the spectroscopic data from the newer observations and the older literature values, it is possible to investigate the correlation between the continuum and the lines, as well as the correlation among the lines themselves. In the discussion below I will focus on four lines in the spectrum for which it is possible to acquire reliable line flux measurements in most spectra: HeIIλ4686, Hβ, HeIλ5876, and Hα.

In the spectra in Figure 4.3, note in particular the HeIIλ4686 line: the difference between the lowest continuum flux spectrum, MJD 52252 from SDSS, and the highest state spectrum, MJD 57539 taken with the WHT, is quite remarkable. In the low state, the broad component of the flux seems to have disappeared almost entirely and only the narrow component is still present. The high state spectrum, on the contrary, shows a lot of energy being emitted in broad HeII. The other Helium and Balmer lines are also quite variable, but none so strongly as HeIIλ4686. It is this behaviour that was the initial motivation for the analysis presented in this chapter, and it will be the starting point for the next section.

4.2. Methods for the Analysis of Mrk 110 Data

4.2.1 Using HeII as a Proxy

The remarkable variability of HeIIλ4686 warrants a closer look, in particular its behaviour relative to the other broad emission lines. In the following analysis I define the manner in which I will use the HeII flux as a proxy for the ionising continuum. The analysis of line flux levels in Mrk 110 consists of several steps, which are detailed below.

Flux Correction of HeII

The pseudo-continuum method does not distinguish between the broad and narrow component of a line, but simply calculates all the emission above the continuum level in a given interval. As can be seen in Figure 4.3, however, the narrow component of the HeIIλ4686 line is approximately constant. To ensure only the changing part of the line is included in the analysis, a narrow line flux is subtracted from both the HeII flux. The narrow line flux used for this correction is calculated in the `lmfit` analysis of the SDSS spectrum. The value of the subtracted HeII flux is $3.81 \cdot 10^{-15}$ erg cm^{-2} s^{-1}.

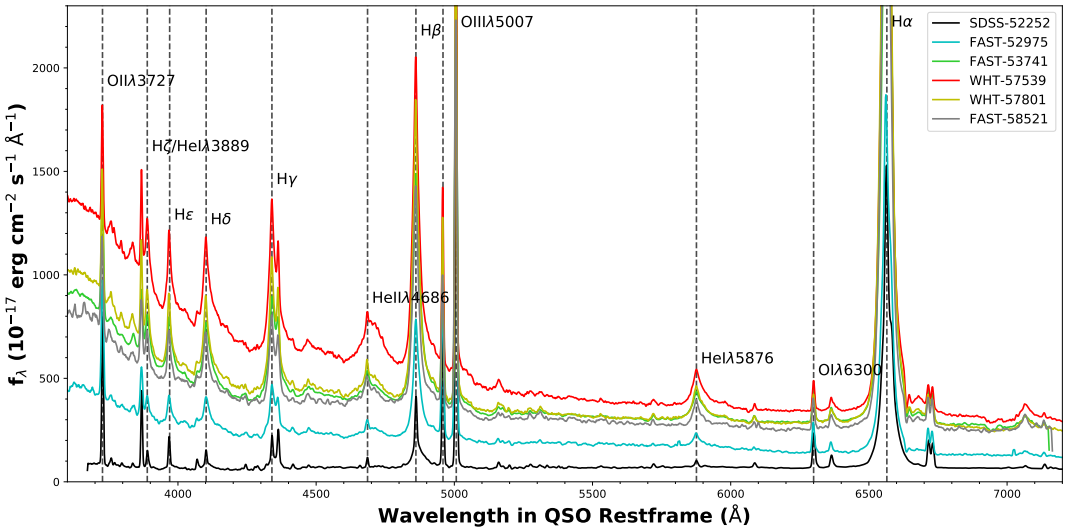

Figure 4.3: A selection of the spectroscopic data available for Mrk 110, with observational epochs spread out over almost two decades. Several of the most prominent emission lines have been identified. As indicated in the legend, the data is from SDSS, the Tillinghast telescope (FAST), and the WHT. Both the strong variability of the continuum and the change in the broad emission lines are clearly visible. Note in particular the change in the HeIIλ4686 line: in the SDSS spectrum (black) the broad component appears to have vanished, whereas in the WHT spectrum of MJD 57539 the broad component is present and strong.

Normalisation

In order to compare the data from the various observational epochs, I introduce a normalisation that will be used throughout this chapter. The normalisation is by date: the fluxes for one specific selected epoch are set to unity, and the other epochs are scaled to this observation. The selection of the date is arbitrary, only requiring an observational epoch with reliable measurements, excluding e.g. a very noisy FAST spectrum. The date used for normalisation is MJD 47574, an epoch from the BK99 data-set. All fluxes, both the literature values and those derived using the pseudo-continuum method (Section 3.1), are therefore divided by the flux values for MJD 47574.

Adjusting for the Lags

One further adjustment of the data is based on a consideration of the BLR's spatial stratification and the associated lags. The issue is the following: representing the line fluxes for the same epoch as synchronous measurements, implicitly assumes that the line forming regions are affected by the same ionising flux. It therefore ignores light travel times between the different regions of the BLR. RM results indicate that a change in FUV flux from the central engine will reach the different line forming regions at different times. For part of the data, namely those epochs belonging to the RM studies (KO1, FAST-RM1, and FAST-RM2), the cadence of observations was high enough to investigate the effects of a correction.

Using the lags from K01, as presented in 4.1, each of the line observations is shifted in date by subtracting the lag. The line flux is then matched to the line fluxes of the other line species, of the closest matching corrected epoch. In other words: the observational epoch of a given emission line is now matched up to the observational epochs of the other emission lines such that each of them is subject to the same FUV flux. As mentioned, only the RM data-sets have

a cadence high enough for the lag shifted epochs to be matched reasonably well to another observational epoch. The RM data-sets represent approximately 30% of the data, and the lag adjustment does not appear to have a discernible effect on the results. The matching of the line responses to the same FUV flux is a sensible correction, and will be applied in the data presented in this chapter. However the relative flux changes of the lines are, on these time-scales, quite small.

Quantifying the Changes in Flux

Following the narrow line correction for HeII, normalisation, and RM lag correction, the next step is to specify an efficient way to quantify the flux changes. It is possible to plot all line fluxes together, in order to compare their behaviour as the continuum changes. The resulting plot is shown in Figure 4.4, where the normalised line fluxes have been plotted against the normalised values of the continuum at 5100Å. The dashed red line indicates a 1:1 ratio of the line to the continuum flux. Most of the fluxes seem to follow a ratio quite close to that of the dashed line, but once again HeIIλ4686 clearly stands out. HeII increases much more rapidly than the continuum, and indeed than the other lines. As a final note on the normalisation: the fluxes on the axes are the ratios of the respective fluxes to fluxes in the spectrum of MJD 47574. They can be considered to represent a standardised flux measure.

The somewhat unique behaviour of HeIIλ4686 should be connected to the physical parameters that determine the emission line formation. The parameter that most clearly distinguishes HeII from Hα, Hβ, and HeIλ5876 is the ionisation energy. All four lines are recombination lines. The ionisation energies of neutral H and He are at 13.6 eV (912Å) and 24.6 (504Å) respectively. The ionisation energy of HeII is much larger, at 54.4 (228Å). This implies that the emission lines respond to different parts of the ionising continuum, with the HeIIλ4686 responding to changes much further into the UV than the other three. It can therefore be argued that the HeII flux, much more than the 5100Å continuum flux, is representative of the true ionising continuum. The ionising continuum cannot be observed directly and varies at a shorter timescale than the UV and optical parts of the continuum. In the analysis of this chapter I will therefore use the HeIIλ4686 flux as a proxy for the FUV ionising continuum.

Check for Reddening

Before continuing, it is important to consider whether the detected flux variations are indeed attributable to changes in the ionising flux, and subsequent reprocessing in the BLR, or whether they are due to obscuration from intervening dust. The obscuration is tested for by modelling the dust as a screen between BLR and observer. The dust incurs a wavelength-dependent attenuation of the light passing through it, that might mimic any changes in the flux ratio between different emission lines. The reddening is modelled with the F99 extinction curve (see Chapter 3). To check for reddening I compare the ratio Hα/Hβ as a function of the 5100Å continuum, for the Mrk 110 data with a theoretical value based on the extinction curve. The same is done for the HeIλ5876/Hα ratio, to cover the redder part of the spectrum.

The method of calculating the theoretical extinction values is the following. First, I select one epoch to use its continuum flux and ratio of line fluxes as reference points. The model works under the assumption that all changes in flux are due to dust extinction alone. For the value of f_{5100} in all other epochs I then calculate the change in extinction, ΔA_V, required to

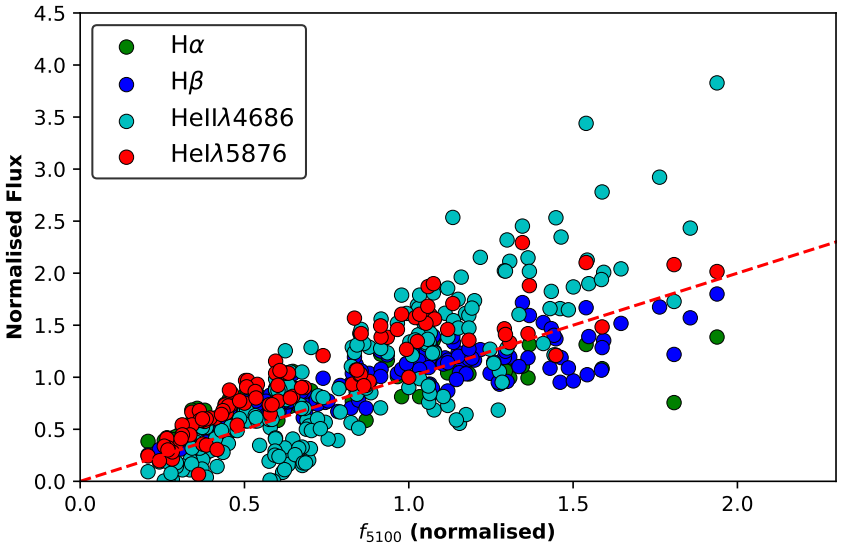

Figure 4.4: The broad line fluxes of four lines in the Mrk 110 optical spectra and literature data, plotted against the continuum flux at 5100Å. The lines shown are: Hα (green), Hβ (dark blue), HeIIλ4686 (cyan), and HeIλ5876 (red). All fluxes have been normalised by dividing by the flux values from the spectrum of MJD 47574. The red dashed line indicates a 1:1 ratio between the normalised line and continuum fluxes. The HeIIλ4686 flux clearly has a different responsiveness than the other lines.

produce the change in flux relative to the reference flux:

$$\mathrm{A}_V = -\frac{5}{2}\log_{10}\left(\frac{f_{new}}{f_{ref}}\right). \tag{4.1}$$

The change in the extinction level at 5100Å can be used to calculate the change in line ratio this would bring about. Note that due to the constraints of the available literature data, I use the fluxes at 5100Å, which is not the centre of the V band, where A_V is defined. This correction is therefore based on the assumption that the extinction does not change over that range of 400Å. Although the gradient in Figure 3.2 indicates that this is likely not fully accurate, the lack of available flux data at 5500Å means that this is the most accurate approximation I can make. For any particular wavelength, the change in extinction is based on the reddening curve, which sets the value of E(B−V), following from equation 3.1:

$$\Delta\mathrm{A}_\lambda = \frac{A_\lambda}{\mathrm{E(B-V)}} \cdot \frac{\Delta\mathrm{A}_V}{3.1}. \tag{4.2}$$

The difference in magnitude between the lines can then be calculated. For the example of Hα and Hβ:

$$\Delta(m_{H\alpha} - m_{H\beta}) = \Delta\mathrm{A}_{H\alpha} - \Delta\mathrm{A}_{H\beta} = \left[\frac{A_{H\alpha}}{\mathrm{E(B-V)}} - \frac{A_{H\beta}}{\mathrm{E(B-V)}}\right] \cdot \frac{\Delta\mathrm{A}_V}{3.1}. \tag{4.3}$$

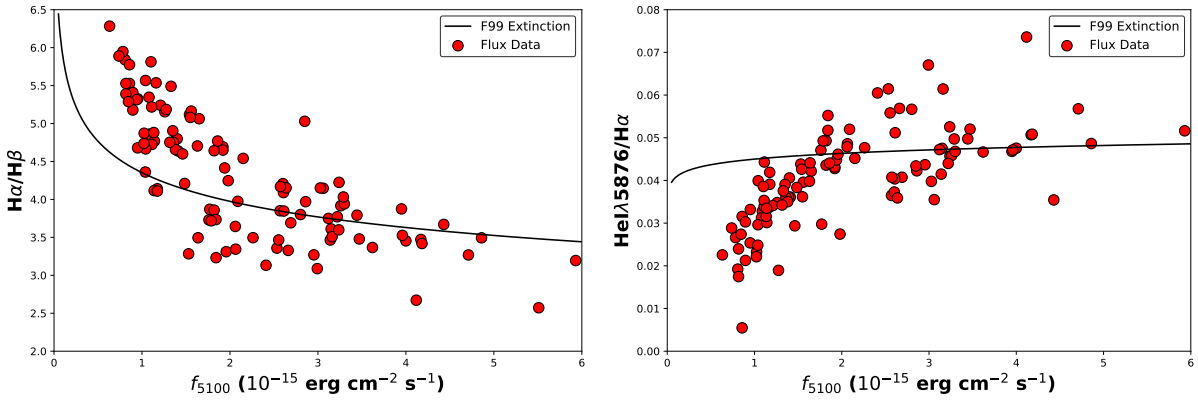

Figure 4.5: As a check on reddening as the cause of the spectral evolution in Mrk 110, the line flux ratios Hα/Hβ (*left*) and HeIλ5876/Hα (*right*) are plotted against the 5100Å continuum flux. The distribution of the flux data can then be compared to a theoretical reddening curve. The curve is calculated under the assumption that all changes in continuum flux are due to dust reddening, following the F99 extinction curve. The clear disparity between the distribution of the data and the curve indicates that the relative line flux changes, as seen in Figure 4.4, are likely not due to any attenuation caused by dust, but rather intrinsic to the AGN's central engine.

where $\Delta A_{H\alpha}$ and $\Delta A_{H\beta}$ are the changes in extinction at the centres of the two lines. The line ratio, altered by the new extinction value, is then given by:

$$\left(\frac{f_{H\alpha}}{f_{H\beta}}\right)_{new} = 10^{-0.4(m_{H\alpha}-m_{H\beta})_{new}} = 10^{-0.4((m_{H\alpha}-m_{H\beta})_{ref}+\Delta(m_{H\alpha}-m_{H\beta}))}. \quad (4.4)$$

Here $\Delta(m_{H\alpha} - m_{H\beta})_{ref}$ is simply the magnitude difference between the line fluxes for the reference epoch. The choice of reference epoch is arbitrary, as it only fixes the offset in line flux ratio. The relevant indicator for the test is the shape of the curve. If the effect is indeed caused by some form of dust reddening, the distribution of the Mrk 110 data points in the line flux ratio vs. continuum flux parameter space should show the same behaviour as the modelled curve.

The results of this comparison, for the two line ratios, are shown in Figure 4.5. The difference between the data and the curve is quite clear, especially for the HeIλ5876/Hα ratio. The latter two lines are close in wavelength and could therefore be expected to be extinguished at a similar level, however the ratio evolves strongly with f_{5100}, indicating another process than reddening is at work. It is therefore possible to safely rule out variable obscuration as the underlying cause for the line flux changes, implying that these changes are indeed intrinsic to the ionising continuum and the BLR.

Comparing the Line Fluxes

Having excluded variable extinction with reasonable confidence, the next step is to consider the behaviour of the individual lines (Hβ, HeIλ5876, and Hα) with respect to the HeIIλ4686 line. For this analysis I still make use of the normalised line fluxes. The results are shown in Figure 4.6, where the data for the individual lines has been split among the three panels. As was the case for HeIIλ4686, the calculation of the line fluxes with the pseudo-continuum method includes both the narrow and broad line component for these other three emission

lines. Assuming that only the broad component varies, the implication is that even if the broad flux were to disappear entirely, a flux would be detectable. In the presentation of the data in Figure 4.6 this manifests as a vertical offset of the normalised fluxes. At this point in the analysis the narrow line component of HeIIλ4686 has already been subtracted, the next step is to perform a similar correction for the other three lines.

To correct for the vertical offset I shift the flux data for each of the lines downward, such that a linear fit through the data (in the range where normalised HeII $\lesssim 1$) passes through the origin. The difference in approach with the narrow HeIIλ4686 correction is that the flux for the latter line can be easily found from the SDSS spectrum, whereas the narrow line component for the other lines is still mixed with the broad component, even in this very low state. The shifts of the normalised fluxes are 0.2, 0.35 and 0.45 for Hβ, HeIλ5876, and Hα respectively. Note that this does cause some of the very low flux values to end up just below the zero flux level. However, these slightly negative values fall well within the range of the scatter of the data, and can be interpreted as indicative of the uncertainties in the measurement. Note also that here is no formal error included with the data for this plot: this issue will addressed below, in the discussion on the fitting function for the data.

The main aspect to note in Figure 4.6 is that the line fluxes for Hβ, HeIλ5876, and Hα appear to have a diminishing response to HeIIλ4686, as it increases. For the highest HeII fluxes the response appears almost flat. This behaviour is particularly clear for HeIλ5876. There are also differences between the line species, especially in the maximum of the normalised flux and in the response to HeII at low fluxes. For the case of HeIλ5876, there is a relatively strong response to changes in HeII at low flux, and the maximum flux in considerably higher than for either Hα or Hβ. The goal of the analysis is to quantify this behaviour of the emission lines using a fitting function.

Fitting

As the physical mechanism underlying the behaviour of the lines is not clear, I will use an empirical function to fit the data. It is a simple two parameter function, consisting of two linear components. The first component is the initial slope, where the line species' flux tracks the HeII flux linearly as it increases. The second component is the plateau, capturing the lack of line response at high HeII fluxes. The slope is confined to pass through the origin, as the data were corrected using the vertical offset. The two parameters to be fit to the data are the gradient of the first component and the height of the second component. More complicated fitting functions, such as a broken power law, were also applied to the data, but failed to produce a stable fit. Together the two parameters capture the most interesting aspects of the behaviour, and allow to differentiate between line species by a different response to HeII at low fluxes, and different flux maxima. The combination of the slope and the plateau level also define the 'knee' of the function: the HeII flux at which the given line flux stops tracking the continuum. The result of the fitting can be seen in Figure 4.7.

The fitting process is a χ^2 minimisation, using the `leastsq` routines provided by `SciPy`. A difficulty is presented by the measurement errors on the data. As is clear from Figure 4.6 there is considerable scatter in this data-set. This scatter is a combined effect of the measurement errors and changes in the line response that are inherent to Mrk 110. This data-set is a combination of measurements taken over a long period, and the response to the HeII/FUV variability I try to extract from it will inevitably be an average effect. At each continuum flux

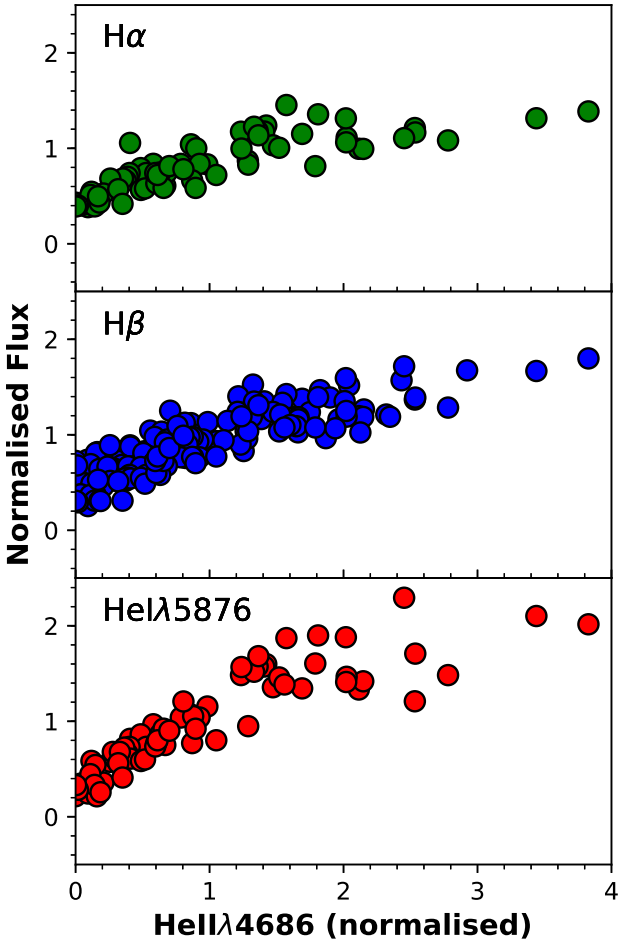

Figure 4.6: The normalised fluxes of Hα (*top*), Hβ (*centre*), and HeIλ5876 (*bottom*), plotted against the HeIIλ4686 flux. The HeII fluxes have been corrected by subtracting the narrow line emission (see text). Particularly noteworthy is that all three lines species appear to track the HeII up to a certain flux, after which the response to an increasing HeII levels off. Differences between the line species are evident in the line response at low flux, and the maximum flux each line is able to attain. It is these aspects of the lines' behaviour that will be represented with a function to be fitted to the data.

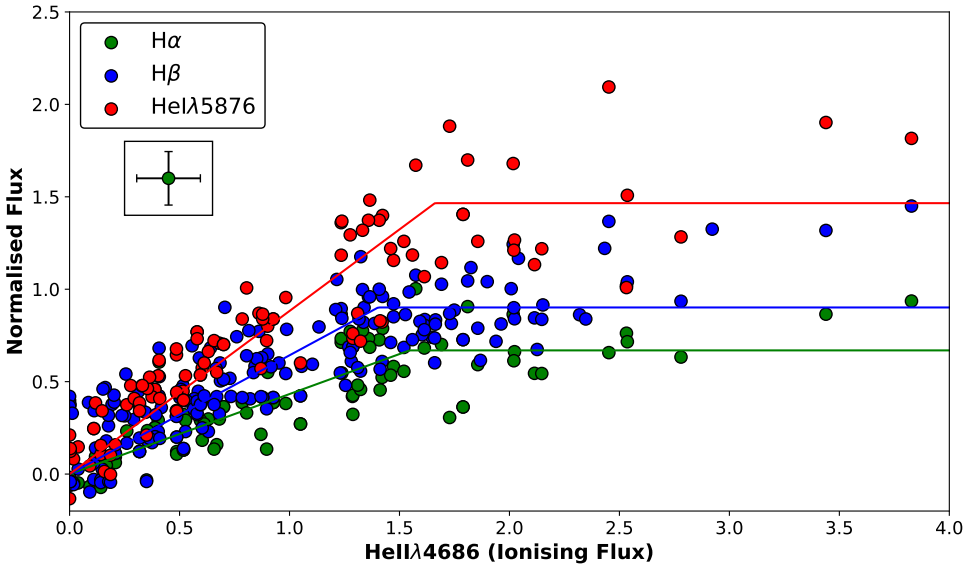

Figure 4.7: The combined data for Hα (*green*), Hβ (*blue*), and HeIλ5876 (*red*), plotted against HeIIλ4686. The response of the line fluxes has been approximated using a two-component fitting function. The stratification in the maxima of the three fitted functions and the difference in the initial slopes indicate that the slope and saturation level are efficient parameters for distinguishing the three lines species. The error bars indicated in the top left are calculated during the fitting process. The errors incorporate the intrinsic scatter apparent in the data (see text).

variation there will be myriad conditions that will contribute to a line's response. Changes in these conditions over time will cause a scatter of the line fluxes around the more general, average behaviour that is represented by the fitting function. When comparing the size of the measurement errors for each epoch with the scatter of the data, it is clear that the measurement errors are an underestimate of the uncertainty associated with the fit.

To account for this source-intrinsic scatter, I estimate the error on the fit incorporating the scatter. The fitting process is iterative: in the first iteration the data and the original measurement errors are used to calculate the χ^2 value and to optimise the fit. I then calculate a new error to the data, which is the standard deviation of the residuals with respect to this initial fit. This results in a uniform error for the data-set. In the second iteration the χ^2 minimisation is repeated using these new errors. For the measurement errors used in the first step the effect of the flux normalisation has been accounted for, using standard error propagation.

Following the corrections for contamination with narrow line fluxes, the exclusion of reddening as an underlying cause for the variability, and the definition of the fitting function, it is now possible to properly quantify the responsiveness of the broad emission lines in the Mrk 110 data-set. The results of this analysis will discussed in Section 4.3.

4.2.2 The HeIIλ4686 and Hβ Line Profiles

Considering the strong variability exhibited by Mrk 110, as visible in Figure 4.3, it is noticeable that the changes in the spectrum are not limited to the line and continuum fluxes: the line

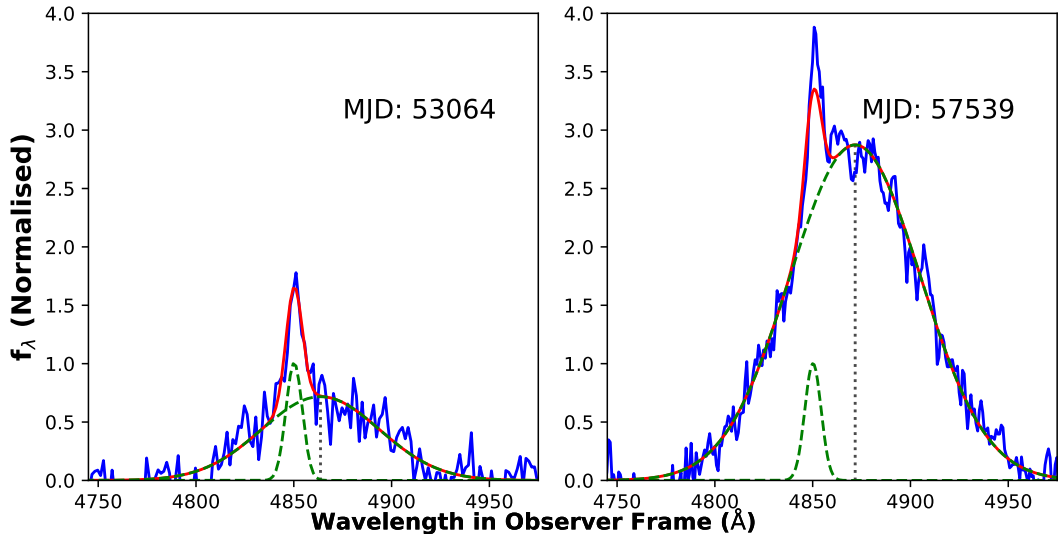

Figure 4.8: An example of the change in offset between the narrow and broad components of the HeIIλ4686 line. The left panel is the line from the spectrum of MJD 53064 and the right panel of MJD 57539. The fluxes have been normalised such that the maximum of the narrow line flux is equal to one. With the narrow line at a fixed wavelength (see Section 3.1 for details on the fitting method), the centre of the broad component shifts over time. The broad line centre is marked with a dotted grey line.

profiles for various emission lines can be observed to change as well. For the data-sets P98, BK99, and K01 only the published fluxes are available, however for the other data-sets there are spectra for all epochs. Using the large amount of information available in these spectra, it is possible to expand the investigation of Mrk 110 variability and to consider the underlying processes in greater detail. The focus of this section will be on HeIIλ4686 and Hβ.

There is an offset between the narrow and broad components of the HeIIλ4686 line, as discussed in Section 4.1. Because there are good reasons to reject the explanation in terms of a gravitational redshift presented in Kollatschny [2003b], a closer consideration of the component's offset should prove interesting. The large range of epochs for which there are spectra available makes it possible to track the line offset over the course of Mrk 110's central engine's dramatic changes. The main aspect of the changing profile revealed in this new data-set is that the offset between the components evolves with time. As the broad and narrow components are expected to be formed in physically distinct and spatially separated regions, the evolving relation between the components can potentially provide insight into the evolution of the BLR, as the narrow line forming region can be expected to remain unchanged.

An example of the behaviour of the HeIIλ4686 line is shown in Figure 4.8. The two panels show a close-up of the line in two different epochs: the relatively low state observed at MJD 53064 and the very high state from MJD 57539. In both epochs the centres of the two components are clearly offset from each other, with the broad component redward of the narrow component. Between the epochs this offset changed, with a stronger offset visible in the MJD 57539 observation. The analysis of this behaviour will therefore focus on this changing offset, as well as other, possibly related line parameters: line width and flux. The analysis can be extended to Hβ, which shows a similar offset between broad and narrow components.

The plots in Figure 4.8 illustrate the method used for the study of both the HeIIλ4686

and the Hβ line profiles: the fitting method set out in Section 3.1 captures the relevant aspects of the spectra. The centre of the narrow line has been fixed at 4686Å in Mrk 110's restframe, and the centre of the broad component is allowed to vary. Fixing the redshift of the narrow component makes for a reasonable assumption. An offset from the host redshift of the narrow lines would be due to a net flow of the emitting material in the NLR. A change in the flow speed as a result of changes in the central engine would take longer than the full time span of the data-set to come about, due to the required light travel time. The narrow line centre can therefore be expected to be constant and the change in offset can be associated with the result of changes in the BLR, rather than the NLR.

The Gaussian fit to the broad component will provide the necessary parameters for the analysis. The width of the line will simply be represented by σ and the flux by the Gaussian's amplitude. Note that this implies that the fluxes used in this part of the analysis differ from those used in the flux comparison. For the latter it was necessary to use the pseudo-continuum method in order to compare with literature values, for this part of the study a more detailed model fit can be used.

Finally, the results presented in Section 4.4 will also make use of the very low state FAST spectra, with relatively poor signal-to-noise. Using the stacking method set out in Section 2.2.2 it is possible to construct a normalised spectrum, which can be fit using the same method as the other spectra. Although it is unfortunately not possible to make proper fits to all the low flux spectra individually, this approach allows for the estimation of the relevant parameters and therefore the inclusion of the behaviour of HeIIλ4686 and Hβ in the lowest emission states in the analysis.

4.3. Flux Responsivity in the Broad Emission Lines

4.3.1 The Difference Among Line Species

By plotting the normalised fluxes for Hβ, HeIλ5876, and Hα against those of HeIIλ4686 (Figure 4.6) it is possible to see that the lines respond differently as the ionising flux changes. This difference can be seen even more clearly in Figure 4.7, where the data for the three lines have been combined in a single plot. The figure also shows the result of the two parameter fit to the data, as described in the previous section. The error estimates on the data follow from the iterative fitting method.

The initial slope of the flux responsivity and the levelling off at a maximum flux value clearly differentiate among the line species. The stratification of the maxima in response makes the three lines quite distinct. The position of the knee between the slope and the flat component is comparable for the three lines. However the difference in slopes, as exemplified by the sharp rise of HeIλ5876 compared to the other lines, is correctly represented by the fitting functions. The results indicate that the line response saturates for higher flux levels. Initially the different lines are able to track the FUV continuum as it increases: more of the ionising radiation is reprocessed in the line forming region, and the line emission rises. The ability to reprocess does not appear to be infinite, however, and as the HeIIλ4686 emission continues to rise the other lines, one after the other, fail to keep up.

In order to best capture the apparent saturation effect, other choices of fitting function were also considered. These functions included a double power law and a one-component linear fit.

In all cases a by eye comparison with the model displayed in Figure 4.7 indicated that the linear two-component model was superior. For the more complicated power-law models, it was possible to attain a 'better' fit in the sense of a lower χ^2. However, the large scatter in the data and the lack of a physical motivation for the greater complexity made these models less suitable to describe the data and resulted in less stable fits. Conversely, the one-component model failed to account for the clear turn-over in the responsivity, making a poor match to the data. In the end, the current choice of a simple and purely empirical fitting function proved superior.

The errors on the two fitted parameters, slope and saturation level, are illustrated in Figure 4.9. For a grid of parameter values the metric $\Delta\chi^2$ is calculated, which is defined as $\chi^2 - \chi^2_{min}$. Here χ^2_{min} is the lowest χ^2 value found in the parameter space, which corresponds to the best fit value. To find $\Delta\chi^2$, χ^2 is calculated at each point of the grid, using the errors as show in Figure 4.7. χ^2_{min} is subtracted from this value. At the point of the best fit values $\Delta\chi^2$ is therefore zero. This point is marked in Figure 4.9 by the intersection of the dotted lines.

The value $\Delta\chi^2$ is itself distributed according to a χ^2 distribution, in this case the distribution for two free parameters (χ^2_2). Levels of constant $\Delta\chi^2$ correspond to Gaussian spreads, in the case of χ^2_2, $\Delta\chi^2 = 2.30, 6.17, 11.8$ correspond to a 1,2, $3{-}\sigma$ Gaussian spread respectively. Notice that the shape of the $\Delta\chi^2$ surface (which is 2D in this case) is such that the gradient in the direction of one parameter is relevant for the estimate of the spread in the other parameter. For entirely uncorrelated parameters the $\Delta\chi^2$ surface would be paraboloid, and the contours of cuts made at $\Delta\chi^2 = c$ would form perfect circles. From Figure 4.9 it is clear that this is not the case for the parameters of the empirical fitting function.

To account for the correlation between the two parameters, the errors are therefore not estimated using the separate 1D $\Delta\chi^2$ distributions, but rather using the full 2D distribution. The difference between the two approaches can be best explained using the $\Delta\chi^2$ surface for Hβ. If one were to use the 1D approach, the 2-σ spread for the slope would be estimated as the range in between the two points where the dotted lines and the $\Delta\chi^2 = 6.17$ contour intersect. And similarly for the saturation level. This would ignore the fact that there is a part of parameter space where $\Delta\chi^2 < 6.17$, but that lies outside this range. The approach adopted here is therefore to associate the spread in the parameters with the bounding box that fully encapsulates the $\Delta\chi^2$ contour.

The fact the different line species appear to saturate in their response to the FUV at different levels is suggestive of a physical limitation in the line formation mechanism. Although Hα and Hβ are recombination lines responding to the same, E > 13.6 eV, ionising flux, the LOC interpretation of BLR emission implies that they are in fact formed in different regions. This notion is supported by RM results, which show a difference in lag time between the two lines. In fact, an interesting correlation can be revealed when combining the results from the line responsivity fit with the lags from the K01 RM study of Mrk 110 (as presented in Table 4.1). In Figure 4.10 I compare the line saturation level with the RM lag. The lag should correspond directly to the light travel time and therefore the distance between the central engine and the line forming region. The errors on the slope are those from Figure 4.9, and the errors on the lag are from KO1.

There is a clear inverse correlation between the saturation level and the RM lag: HeIλ5876, which is formed closer to the central engine, saturates at a higher level than the other two lines, and similarly Hβ saturates at a higher level than Hα. The ability of a line to track the

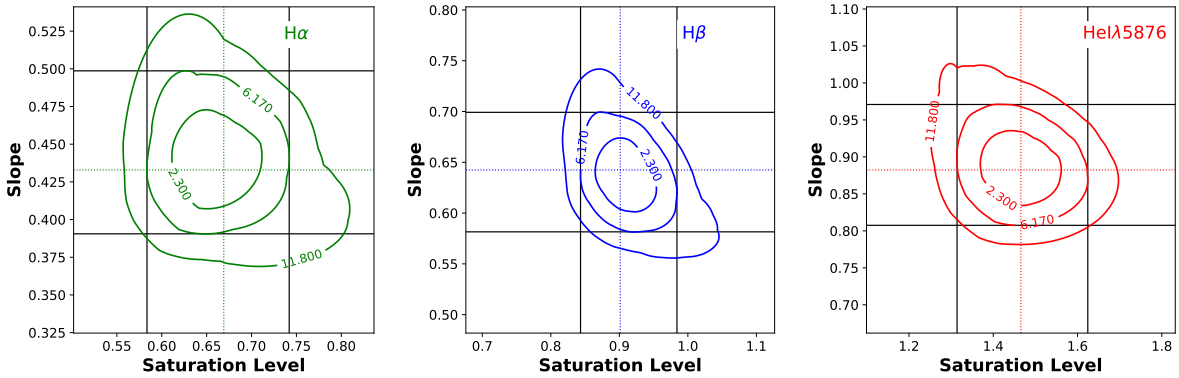

Figure 4.9: χ^2 contours in the two-dimensional parameter space, slope and saturation level, for the fit of the empirical responsivity function. The three panels are for Hα (*left*), Hβ (*centre*), and HeIλ5876 (*right*). The dotted lines represent the best-fit values, which are at the minima of the respective marginalised χ^2 distributions. The solid lines represent the errors used for the error estimates. The errors are taken from the rectangle that encloses the $\Delta\chi^2 < 2.30$ region of the $\Delta\chi^2$ surface, corresponding to a spread of 2σ, for Gaussian errors.

FUV continuum therefore appears closely related to the physical parameters that determine its position. This conclusion can be drawn without making any assumptions about what these physical parameters are, as the correlation is between two observable quantities. A similar correlation can be found when comparing the fitting function's initial slope parameter with the RM lag: a steeper slope corresponds to a line formed at a smaller radius inside the BLR.

4.3.2 Responsivity in Different Epochs

There is a clear pattern in Mrk 110's spectral changes and the manner in which broad emission lines respond to changes in the continuum. With the HeII-proxy method it is possible to establish a parameter for the limit to a line forming region's reprocessing capability, which correlates clearly with the RM lags, another observable value. Although this is a promising result, it is clear that the responsivity (Figure 4.7) shows considerable scatter, and it is worthwhile to consider this aspect of the data again. The question comes down to the origin of the scatter: is it entirely random, or is there an underlying pattern?

A first possible cause of the noisiness lies with the origin of the data. Differences in the data quality, differences in methods of reduction and calculation in the case of the literature values, and differences in the range of observational epochs could contribute to the scatter. It is worth to check the validity of the various steps taken to cast the data from various sources in the same format. To investigate the effect of a difference in the origin of the data, we can consider the Hβ data from Figure 4.7 split according to their origin. This is presented in Figure 4.11. Some of the observing campaigns coincide with a relatively low or high emission state of Mrk 110 (see Figure 4.2). However all of the data-sets show the same overall pattern (Figure 4.11). A direct connection between the range of data sources and the size of the scatter is therefore not likely. Instead the scatter appears intrinsic to the variability.

One particular effect that underlies the scatter in the data-set in its entirety is a difference in responsivity between epochs. Among the RM campaigns it is possible to discern two sets: the first consists of P98 and BK99 (yellow crosses and black hexagons) and the second of KO1,

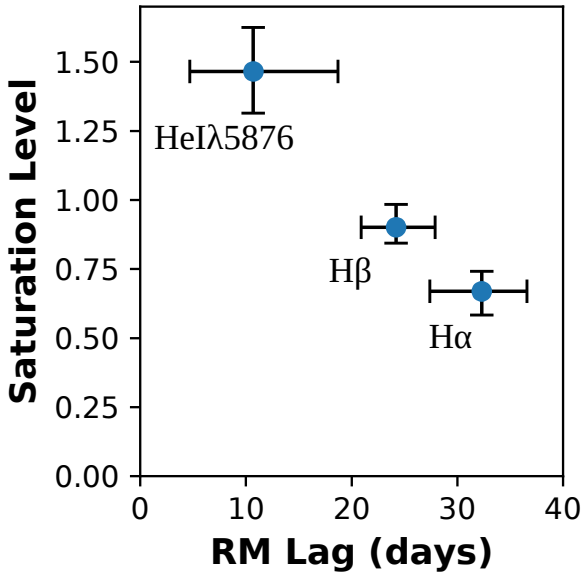

Figure 4.10: The saturation levels of the two-component responsivity functions for the three lines (Hα, Hβ, and HeIλ5876), plotted against the Reverberation Mapping lags presented in KO1. The results show a strong negative correlation between an emission line's ability to track the continuum and the distance of the line formation region from the Mrk 110's central engine.

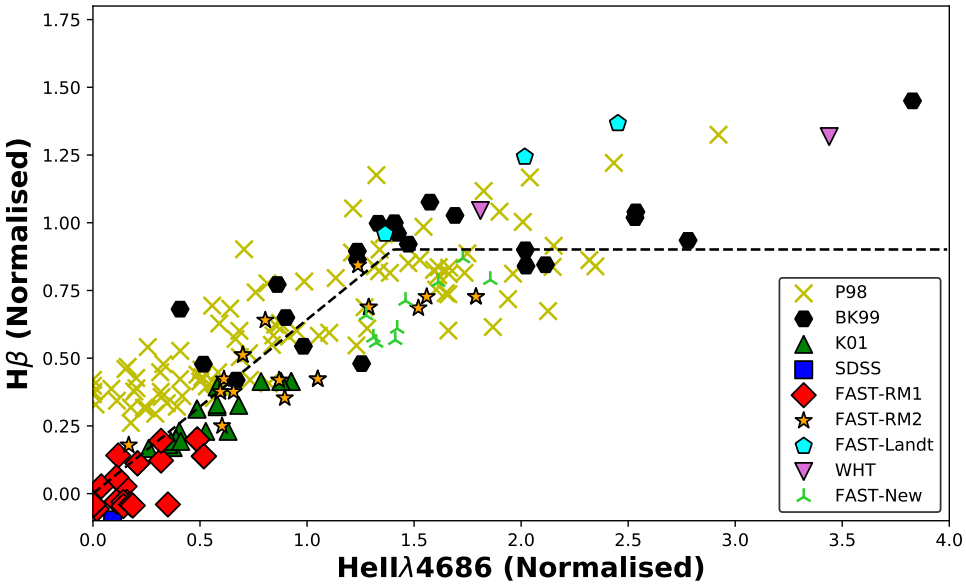

Figure 4.11: Overview of the origin of all the data used to calculate the responsivity fits. The data included in the plot are for Hβ only. Despite the various origins, the data points appear to show the same global behaviour. This indicates both the robustness of the conclusions presented here, as well as the reliability of the grey shift rescaling used in the reduction of the FAST spectra.

FAST-RM1, and FAST-RM2 (green triangles, red diamonds, and orange stars). The difference in gradients between the two sets is visible in Figure 4.11. For the same range in normalised HeII flux the line response differs significantly. This implies that as the FUV goes up and down, the line fluxes do not return to the same level. The two sets of RM campaigns represent two different observational epochs. The change in response between these epochs occurs on a timescale in the same order of magnitude as τ_{dyn} for the BLR (Table 1.4). It is therefore probable that the difference in response is the result of physical changes in the BLR, rather than of only the change in illumination by the central source. The latter effect is measured on the timescale of individual RM campaigns.

It is important, at this point, to consider the impact of the narrow line corrections. As discussed in Section 2.2.2, it is not likely that a partially resolved narrlow line component will cause problems with flux calibration, by being included in some observations, but not in others, depending on e.g. slit width and seeing. However, it is possible that any non-AGN narrow line component is not as constant over the period of observations as I assume the NLR emission is. The effect of this contamination would be similar to the potential issue of a partially resolved emission region. As I subtract a constant narrow line flux from the total flux for all line species, a changing narrow line flux would imply that this correction is too big or too small for at least some of the epochs.

If the correction is consistently too big or too small, this will result in an offset of the broad line fluxes. For the HeII correction this would imply an offset of all data points in Figure 4.7 in the horizontal direction. An error in the correction of any of the other lines would result in an offset in the vertical direction. In the case that the error on the flux correction differs from epoch to epoch, this would increase the overall scatter of the data-points. A non-constant narrow line flux component would therefore impact the reliability of both the correlation of the RM lags with the saturation level and the gradients of the line response (see the discussion concerning Figure 4.12). For the discussion of the Mrk 110 data the constancy of any non-AGN narrow line emission over the epochs of observations is therefore an important assumption.

Over time many physical aspects of the BLR could have changed. This implies that the combined data-set is formed of data representing different physical conditions in the line forming regions. To evaluate the effect of line responsivity evolving with time more closely, I consider data gathered in different short epochs and compare the responsivity for each subset. The RM-campaigns provide good data-sets to perform this comparison. The selected data are from P98 (restricted to MJD 49875–50192), K01, FAST-RM1, and FAST-RM2. The selection from the P98 data was made to ensure the subset only covers a short time-span, as well as one single dip in the light curve.

The goal of comparing the responsivity in these four subsets is to look for a possible correlation between Mrk 110's average initial state and the shape of the response function. As can be seen from Figure 4.2, the P98 dates correspond to Mrk 110 dimming from a bright state to a relatively low state, K01 corresponds to further dimming to the very low SDSS state, FAST-RM1 covers a range where the continuum again dips down to a very low state, and FAST-RM2 to a sharply rising continuum level, returning to a high emission state. The range of variability is not as large as for the full data set (as illustrated in Figure 4.11). The four subsets cover the initial slope ($f_{\mathrm{HeII}} \lesssim 1.5$). I have therefore limited the range in normalised HeIIλ4686 fluxes to [0, 1.25], so that the line responsivity is measured for a comparable change in ionising flux in all four subsets. The data are shown in Figure 4.12.

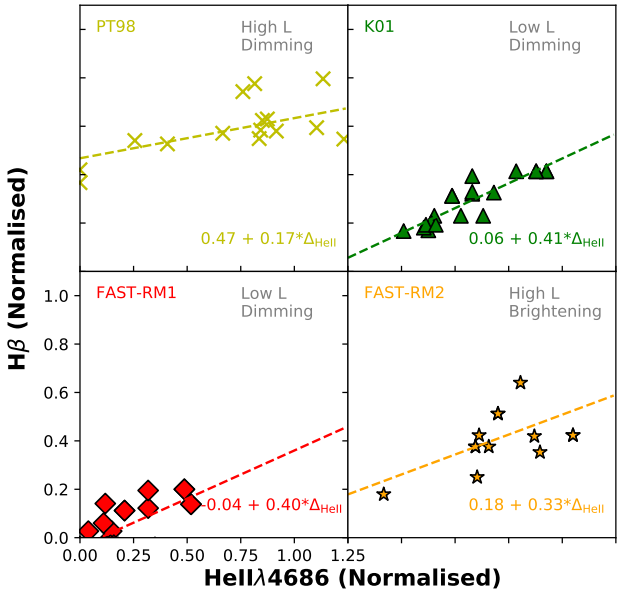

Figure 4.12: The Hβ data from four Reverberation Mapping campaigns P98 (*top left*), K01 (*top right*), FAST-RM1 (*bottom left*), and FAST-RM2 (*bottom right*). For the purpose of comparison the included data is limited to epochs with $f_{\rm HeII} < 1.25$. For each of the data subsets the result of a linear regression of the Hβ fluxes on the HeIIλ4686 fluxes is shown in the bottom right corner. In the top right of each plot the behaviour of the light curve (cf. Figure 4.2) in the period covered by the data is summarised in terms of the luminosity state and the direction of change in luminosity. There is a difference in the slopes among the different data-sets, contributing to the scatter visible in Figure 4.11.

A measure of the responsivity was constructed by linear regression of the line fluxes on the HeIIλ4686 fluxes. The limit on the HeII range deliberately excludes the saturated part of the responsivity function ($f_{\rm HeII} \gtrsim 1.25$), therefore a simple linear fit to the slope is the best approach. Note that the slopes in Figure 4.12 are not required to pass through the origin. The narrow line correction for all line species except HeII was made by eye, for the ensemble of data points. If the different subsets of the data have different slopes, forcing the line to go through the origin would suppress the difference in gradients. In other words: for these smaller subsets I relax the conditions on the fit, to allow for possible errors in the narrow line corrections, to focus on the difference in slopes.

The comparison is made using Hβ, as it is easily detectable in all spectra. The difference in the number of data points between the data-sets presented in Figure 4.12 and the lightcurve in Figure 4.2 is the result of the RM lag correction, described in Section 4.2. After correcting for the lags some of the epochs now have the same Hβ value. That is: the Hβ values have been mapped to the same HeII value and the included data point is the average of these Hβ values. This occurred when the best match in corrected epoch for these different data points was for the same date.

There is a difference in the offsets and gradients of the four lines, which will indeed contribute to the overall scatter when the data are combined. The results in Figure 4.12 show two important effects: the first is that the responsivity of the Hβ line changes with time. There is a

known anti-correlation over averages of the quasar population between L_{bol} and the amplitude of variability [MacLeod et al., 2016; Rumbaugh et al., 2018]. Here we possibly see the same effect occurring over Mrk 110's changing epochs. The second effect is that there is a dependence of the Hβ responsivity on both the initial luminosity and the direction in which the luminosity is changing. The gradient of the fit is shallower for both high luminosity subsets and the gradient is steeper when comparing the brightening and dimming data-sets with high initial luminosities.

4.4. An Offset Between the Broad and Narrow Components

To study Mrk 110's evolving line profiles I focus on two lines: HeIIλ4686 and Hβ. Each line is fit with two Gaussians. The relevant line characteristics are the offset between the narrow and the broad component, the width of the line (σ), and the line flux. The large amount of available spectra allow us to track the line evolution over time. The resulting correlations present a complex picture of Mrk 110's broad line variability. As was the case for the flux responsivity there is a lot of scatter in the data, however there are some clear correlations and noticeable differences between the behaviour of HeIIλ4686 and of Hβ.

The data-set used for this part of the study contains all FAST and WHT spectra. As explained in Section 4.2 the lowest state spectra are not included individually, but rather as an average by stacking the spectra to have enough S/N for a good fit. All spectra in FAST-RM1 as well as the very first spectrum of FAST-RM2 (MJD 52940) are stacked together. All other spectra are fit individually. The first correlation to be considered is that between the offset and the HeIIλ4686 flux. In similarity to the method set out for the flux responsivity, HeII can be considered to represent the high energy part of the ionising continuum. This comparison therefore concerns the offset in response to a changing FUV continuum.

The value of the offset, which is fitted in Å, is converted to km/s. The assumption for this conversion is that the difference in line centres is the result of a difference in velocity along the line of sight between the line forming regions. The conversion is made in the following way:

$$\Delta v = \frac{\lambda_{c,broad} - \lambda_{c,narrow}}{\lambda_{c,narrow}} \cdot \mathrm{c}. \tag{4.5}$$

Here $\lambda_{c,broad}$ and $\lambda_{c,narrow}$ are the broad and narrow line centre respectively, and c is the speed of light. As the redshift of the narrow line has been fixed in the fitting process, the offset is interpreted as a flow in the broad line region.

The offset between components plotted against the ionising flux is shown in Figure 4.13. The left panel shows the results for HeIIλ4686, and the right panel for Hβ. The data in the plots has been split between the FAST-RM2 data (*red*) and the newer FAST and WHT data (*blue*). The stacked low state spectra (*green*) are all from FAST-RM1. The epoch is indicated by the shading of the colours, going from light to dark for later epochs. In the Hβ plot, for example, one can trace the passage of time from the top left (light red) to the bottom right (dark blue). The associated increase in HeIIλ4686 flux is in accordance with the rise in the continuum lightcurve for this period (Figure 4.2).

The first aspect to note in Figure 4.13 is that the average offset for HeII is significantly larger than for Hβ. The second point is that both lines appear to have a negative correlation between HeII flux and offset. As the line flux increases, the offset becomes smaller. In other words: as

the ionising flux goes up, the relative redshift of the broad component becomes smaller. The correlation for Hβ remains contant over the different epochs, whereas the HeIIλ4686 offsets appear to evolve along two different branches, associated with the RM campaigns. This difference between epochs is consistent with the effect noted for the flux responsivity. The third point to note is that not just the average offset, but also the change in offset is larger for HeII. The somewhat aberrant high HeII flux point in the far right of both plots is associated with the WHT spectrum of MJD 57539, one of the highest S/N spectra in the sample.

The panels in Figure 4.13 also include two measures of the strength of the correlation between the plotted parameters: the Spearman ranked correlation coefficient (r_s) and a p-value based on Pearson's correlation coefficient (r) [Lawrence, 2019]. The Pearson correlation coefficient for data-sets A and B is defined as

$$r = \frac{cov(A,B)}{\sigma_A \sigma_B}, \tag{4.6}$$

where $cov(A,B)$ and σ_A are the covariance and standard deviation respectively. The Spearman coefficient is defined as the Pearson correlation of the rank values of two data-sets. It is more adept at quantifying the presence of a trend in the data than the Pearson coefficient. For the data discussed here the Spearman coefficient can be calculated as

$$r_s = 1 - \frac{6\sum_{i=1}^{N} d_i^2}{N(N^2-1)}. \tag{4.7}$$

In this expression N is the total number of included spectra and d_i is the difference between the rank of the line flux and the rank of the component offset. The sum runs over all epochs.

The p-values in Figure 4.13 are a measure of the strength of the Pearson correlation. The coefficient r can be converted to a variable that can be tested using Student's t-distribution. This variable is defined as

$$t_r = r\sqrt{\frac{N-2}{1-r^2}}. \tag{4.8}$$

If the parameters being tested are fully uncorrelated, t_r will be distributed according to a t-distribution with N-2 degrees of freedom. The stronger the correlation, the lower the probability that t_r is drawn from this t-distribution. The p-value therefore indicates the probability that the parameters are *not* correlated. The one-tailed p-value is calculated as $1 - CDF(t_r)$, where the $CDF(t_i)$ is the cumulative t-distribution function evaluated at t_i. As t_r can be both positive and negative, a two-tailed p-value is appropriate. The symmetry of the t-distribution means that this is simply twice the one-tailed value.

Interestingly, the correlation in offset and ionising flux is qualitatively consistent with the interpretation that the offset is caused by gravitational redshift [Kollatschny, 2003b]. This consistency requires that the increase in FUV flux, as indicated by HeII, will cause the line emitting regions to lie at larger radii in the BLR, which would be in accordance with results from RM studies detecting AGN breathing [De Rosa et al., 2015; Barth et al., 2015]. In this scenario a high FUV flux causes the broad lines to be formed in a shallower part of the potential well, decreasing the gravitational redshift of the broad component. As discussed in Section 4.1, there are good reasons to doubt this reading, however.

The offset can be considered the result of a flow in the emitting material and therefore

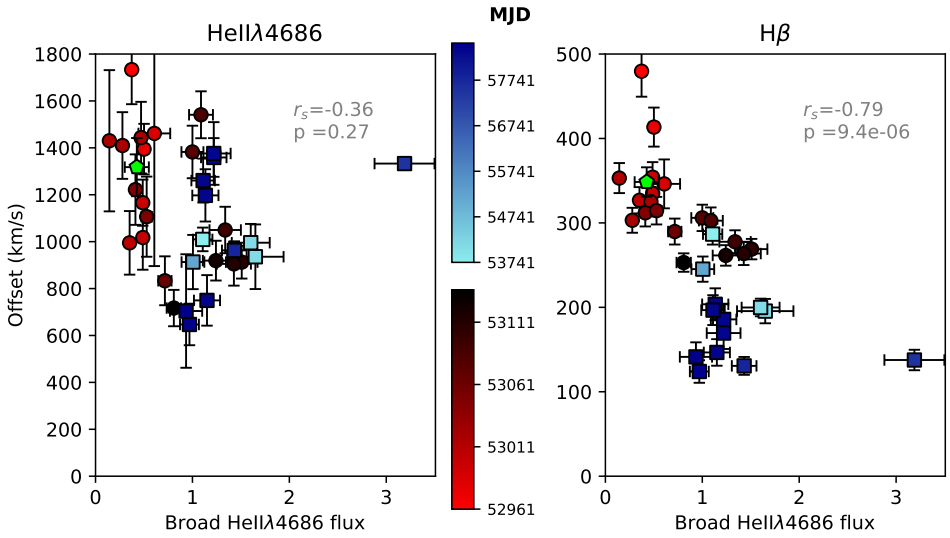

Figure 4.13: The offset between the line centres of the broad and narrow components of HeIIλ4686 (*left*) and Hβ (*right*), plotted against the normalised broad HeIIλ4686 flux. The shading of the colours indicates the time at which the spectrum for the data point was taken. The colour ranges represent the observational periods. Red covers the spectra of the FAST-RM2 campaign (over the date range MJD 52961–53137). Blue covers the newer FAST and WHT spectra (MJD 53741–58500). The green point represents the fits from the stacked 'low-state' FAST spectra (FAST-RM1: MJD 52252-52798). r_s is the Spearman ranked correlation coefficient. The p value is based on Pearson's correlation coefficient and indicates the probability that the parameters are not correlated.

as an indicator for kinematics in the BLR. In this interpretation the difference between the average offsets of HeII and Hβ implies that the region of the BLR where Hβ is formed flows at considerably lower velocities. The narrow components of the HeII and Hβ line are, in an average over all included spectra, at approximately systemic redshift. The average redshift of the narrow HeII component is at $z = 0.0352$ and that of the narrow Hβ component is at $z = 0.3503$. These differences correspond to a relative blueshift of approximately 2Å, which is small compared to that of the respective broad line components. The narrow line components can therefore be considered to belong to the same kinematic component.

To understand the scatter in the HeII data, and the weaker correlation it implies, we can consider explanations that are either extrinsic or intrinsic to Mrk 110. An extrinsic cause for the scatter lies with the relative quality of the fits. The HeII line is considerably weaker than Hβ in all spectra, making the fit more sensitive to noise and systematic offsets. This notion agrees with the fact that the scatter appears largest for the spectra at earlier epochs, when the emission was relatively low. If the scatter in the HeII data is intrinsic to the AGN, however, this implies that the flow speed is not only higher for gas closer to the central engine, but that the effect of a changing continuum is more erratic.

The next correlation to be considered is that between the offset and the line width. The line width can be used as an indicator for the kinematics of the line forming region, similar to its use in black hole mass estimation. Assuming Keplerian rotation around the black hole, the width is an indicator of the distance of the line forming region to the black hole. The results of this comparison are presented in Figure 4.14.

The average line width of HeII is clearly larger than that of Hβ, in agreement with RM

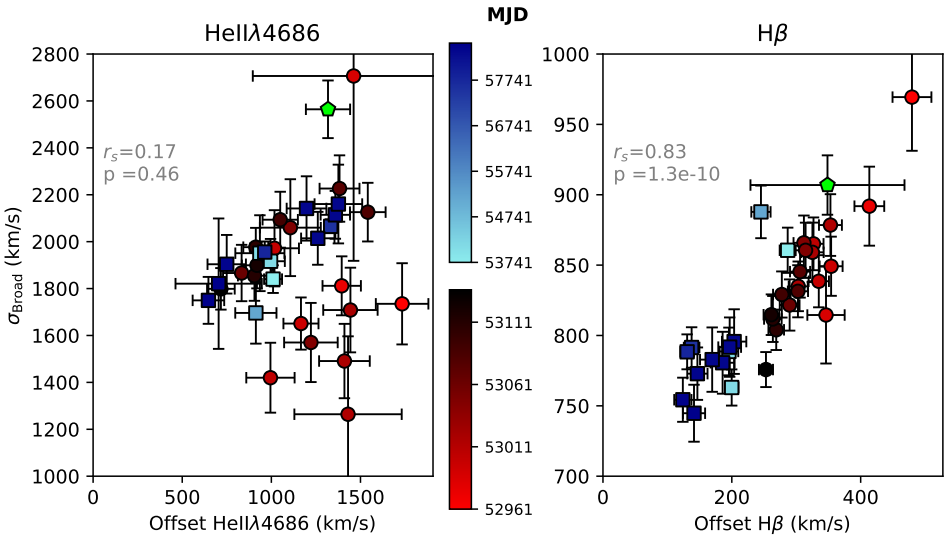

Figure 4.14: The line width of the broad component of HeIIλ4686 (*left*) and Hβ (*right*), plotted against the broad to narrow line offsets. The colours, shading, and correlation metrics are as described for Figure 4.13. The strong correlation seen for Hβ is consistent with the correlation between offset and flux evident in Figure 4.13.

results that high ionisation lines have larger widths. In the case of Hβ there is also a clear positive correlation between offset and line width. The HeII data do show more scatter, as well as a difference in correlation between epochs.

The positive correlation between offset and $\sigma_{\rm Broad}$ for Hβ can be interpreted in the same manner as the results in Figure 4.13: a larger offset occurs during a period of lower ionising flux, when the lines will be formed closer to the central engine, deeper in the potential well. In terms of the observables in Figure 4.14 larger widths indicate greater rotational speeds, which are associated with larger offsets.

The final correlation to consider is that between $\sigma_{\rm Broad}$ and the broad HeIIλ4686 flux. This comparison functions as a check on both the line fitting results and the basic assumptions made in the analysis presented so far. Any sign of a luminosity dependent line width, as would be the case for a breathing BLR should be evident when comparing these parameters. The results are shown in Figure 4.15.

The expected correlation is clearly visible in the results for Hβ. In agreement with the results shown in Figures 4.13 and 4.14 the distance of the Hβ emitting region (R_{BLR}(Hβ)) increases with luminosity. Remarkably, HeII shows the opposite trend. As was the case in the previous results the scatter in HeII data is considerably larger than for Hβ. However, the Spearman and Pearson correlation metrics indicate that the trend is significant.

The behaviour of the two line species presents an interesting discrepancy. A breathing effect for a HeII line has been detected for in NGC 5548 (De Rosa et al. [2015], HeIIλ1640 in this case) but is perhaps not universal. An alternative explanation is that the motion of the HeII emitting gas is not fully dominated by gravity, but also affected by radiation pressure. As discussed by Netzer & Marziani [2010] radiation pressure can affect the orbit of gas in the BLR. The radial dependence of the flux implies this effect would be stronger at small radii.

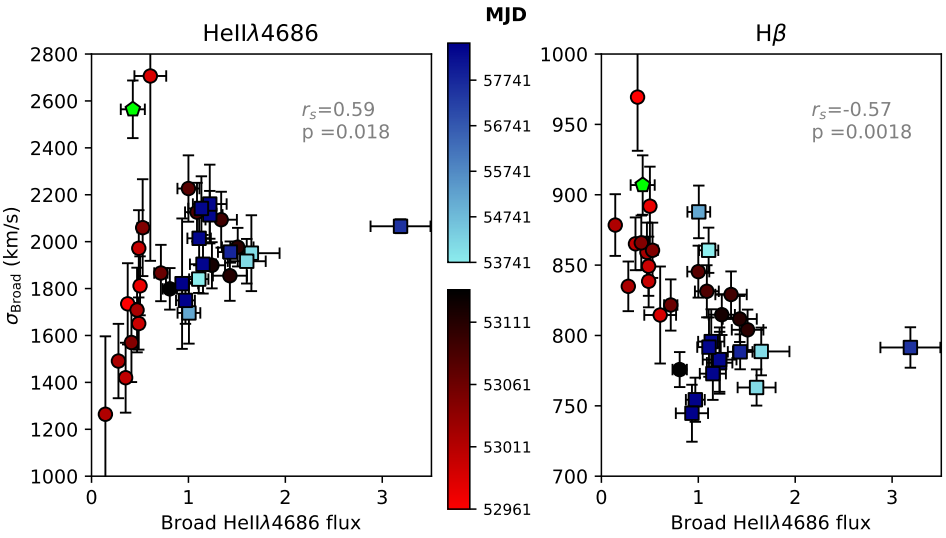

Figure 4.15: The line width of the broad components plotted against the broad HeIIλ4686 fluxes. The colours, shading, and correlation metrics are as described for Figure 4.13. The correlation for Hβ indicates that R$_{BLR}$(Hβ) increases with HeII, in agreement with previous results. HeII shows an opposite trend, which could indicate that the kinematics of the line forming region are not purely gravitational

.

4.5. The Spectral Variability of Mrk 110

4.5.1 Overview of Results

The results presented in this chapter describe the various ways in which the broad lines in Mrk 110's spectra changed over time. The discussion can be separated into two parts. The first is the response of the line fluxes, in particular when compared to the HeIIλ4686 flux. The line flux response can tell us something about the ability of the broad line gas to reprocess ionising radiation and can be compared to predictions of photoionisation models. The second part is the kinematics revealed by a closer inspection of the HeII and Hβ line profiles. The latter results can be compared with models of cloud formation and BLR dynamics. Below is a brief summary of the results.

Line Flux Response

i) Mrk 110 shows strong variability on all timescales, in both the continuum and the lines.

ii) Among the emission lines in the optical range the variability is most pronounced for the high ionisation line HeIIλ4686. This is in agreement with variability studies on a number of AGN, which show that the level of variability correlates with the ionisation level [Peterson, 2008; Bentz et al., 2010].

iii) The response of the Hα, Hβ, and HeIλ5876 emission lines to changes in the FUV flux (as indicated by the HeIIλ4686 flux) is dependent on the level of incident flux. Considering the full data-set, it is clear that for high levels of FUV flux an increase in flux is matched by a reduced rise in the emission lines. The effect can be approximated by a response function with a flat response once it reaches a saturation level, the maximum flux the

line can attain (Figure 4.7). It is important to note that the full data-set covers ∼30 years of observations. The responsivity discussed for this data-set is therefore different from the instantaneous responsivity used in photoionisation models (see Section 1.2.3, e.g. Figure 1.8).

iv) The level at which the response of the emission lines appears to saturate shows a strong negative correlation with the lags in line response found in RM measurements (Figure 4.10). This suggests that the saturation level for the lines is related to the physical location in the BLR. An alternative conclusion is that the ability of a line to track the ionising continuum increases with the ionisation energy required to power the line.

v) The response of the lines to changes in the FUV differs from epoch to epoch. Observational epochs that overlap in the range of FUV fluxes, but are separated by several years, show a different line response. This is most clearly evident in Figure 4.11. The time between different sets of observing campaigns (P98 & BK99 and K01, FAST-RM1 & FAST-RM2) is in the same order of magnitude as τ_{dyn} for the BLR.

vi) The direction of change in luminosity may impact the broad line response. The subsets included in Figure 4.12 do not show the saturation effect noted for the ensemble, possibly because the change in flux level is simply too small. However, the data do show a change in the linear response to flux changes. The response appears to depend on the history of the continuum up to the time of observation, with the direction of change in luminosity indicative of whether the continuum emission was previously in a high or a low state.

Kinematics

i) The line profiles of HeIIλ4686 and Hβ show a clear offset between the broad and narrow component. For both lines the broad component shows an offset to the red. The magnitude of the offset evolves over time.

ii) The offset shows a negative correlation with the broad HeII flux for both the HeII and Hβ line. The correlation is clearest for Hβ.

iii) The line width of the broad component shows a strong positive correlation with the offset for Hβ.

iv) The line width shows a negative correlation with the HeII flux for Hβ. This would be in agreement with an interpretation of a breathing BLR. HeII, however, shows a positive correlation. The difference between the behaviour of the lines indicates that the kinematics are perhaps influenced by different processes.

v) The HeII data consistently show weaker correlations than Hβ. This is at least partially the result of difficulties in the fitting process, but could also be indicative of a stronger intrinsic scatter in the HeII response to a varying continuum.

4.5.2 Interpretation

Flux Levels

The changing response of the broad line fluxes to the ionising continuum appears to be closely tied to the timescales over which the changes occur. The change in the gradient of the response function is evident when combining the data from the full three decades of observations. This effect was modelled as a complete saturation of the line response with the simple empirical model introduced in Section 4.2. For data collected over shorter timescales this saturation effect is not as clear.

A plausible reason for the simple linear response during the RM campaigns is that the change in the ionising continuum over the shorter periods is simply not large enough to make the saturation effect visible. As can be seen in Figure 4.2, the changes in flux during the RM campaigns do not cover the full range of luminosity changes observed in Mrk 110. This, however, does not explain the difference in responsivity between the two epochs of RM campaigns. There are therefore two processes at work: one is the approximately instantaneous responsivity seen in the RM campaigns, in which the conditions in the BLR dictate the response in line flux to changes in the FUV. This occurs on a timescale of days to weeks, relating to the light travel time (Table 1.4). The second process is a change of the physical conditions in the BLR, which alters the slope of the short term responsivity. The minimum timescale on which this process can take place is τ_{dyn}, which is $\sim$years.

Changes in the luminosity are a likely cause of structural changes in the BLR, for example by altering the replenishment of BLR material or by altering the radiation pressure on BLR clouds. A luminosity dependence of the responsivity profile has been a consistent result of photoionisation modelling [O'Brien et al., 1995; Korista & Goad, 2000, 2004]. For the four line species considered in this chapter Korista & Goad [2004] calculate that the responsivity at every radius is lower in a high luminosity state. In Mrk 110 the dependence on the initial luminosity can be seen in the difference in responsivities in Figure 4.12. The strongest linear response is found for the two RM campaigns that were conducted as the AGN was at a relatively low luminosity (and dimming). The negative correlation of responsivity with luminosity is in agreement with the results from photoionisation modelling [Korista & Goad, 2000].

Goad et al. [2019] reported large changes in the FUV continuum for NGC 5548 based on HeIIλ1640 and Hα fluxes. The two lines appeared to change by the same factor over the $\sim$40 day period during which the FUV collapsed. This strong linear response of the lower ionisation Balmer line to the FUV continuum matches the response seen in the initial slope in Figure 4.7, as well as the linear response seen in the RM subsets in Figure 4.12. Following the same reasoning as in the previous paragraphs, the analogy with the RM campaigns is apt: the responsivity of the lines was set by conditions at the start of the anomaly and did not have time to change over the course of the FUV dip. The responsivity seen in NGC 5548 is therefore reflective of the instantaneous responsivity measure derived in photoionisation models [Korista & Goad, 2004; Goad et al., 2012].

The flux response of the broad lines on the timescale of years to decades differs significantly from that on the short timescales used in RM studies. With regard to the notion of physical changes in the BLR, the full, long-term data-set can be viewed in two ways. The first view of

the data is as a collection of separate observational epochs. This interpretation is illustrated in Figure 4.11 and clearly indicates that the response of the BLR to the incident FUV flux changes over time. The line flux rises and falls in response to the continuum, but in different observational epochs the flux does not return to the same level. The observational epochs span multiple RM campaigns and are separated by several years.

The timescale on which the changes in the line responsivity occur are ∼years. This agrees with a dynamical timescale in the BLR. It is therefore likely that we are observing the effect of physical changes in the BLR. Whether the result of a different cloud configuration, of a different ionisation state in individual clouds, or possibly of a change in BLR outflow, the BLR in Mrk 110 has been continuously changing over the course of our decades of observation.

The second view of the full data-set is one of gradual evolution, where the differing response per epoch allows us to track changes in the BLR over time. The changing gradient in the responsivity with increasing HeII flux (Figure 4.6) is the result of combining the responses from various epochs. The curved responsivity profile seen for all three lines is the average of the linear responses over the different observational epochs.

Although it is unclear from the data whether the response at the highest FUV levels is indeed completely flat, the two-component fitting function does yield some tantalising results. The most interesting of these is the correlation between the saturation level and the RM lags. This anti-correlation suggests that the ability of a line to track the continuum corresponds to the location of the line forming region in the BLR.

In the basic LOC model the line forming region moves further outward as the ionising flux increases. The relative strength of the lines depends on the radial emissivity profile. The data for Mrk 110 indicate that we need to account for a structural response in the BLR and therefore a change in the emissivity profiles. A more precise test should therefore model the expected emissivity at each epoch. Unfortunately creation of these models is beyond the scope of the work presented here. An approximation of the effect can be made by considering the emissivity as a function of the ionisation parameter, U. The optimal line forming conditions depend on U: for too high a value line emission will be suppressed through overionisation of the BLR gas. O'Brien et al. [1995] calculated the emissivities as a function U for all the lines discussed here. The Hα emissivity shows an approximately log-linear dependence on U for $U < 0.1$, which flattens off for higher values. Hβ shows a very similar profile. The authors note that this flattening off is likely due to the clouds becoming optically thin at the Lyman limit (i.e. overionisation). This is in contrast to the HeIλ5876 profile, which shows a stronger dependence on U and, most importantly, an inversion of this dependence at a higher value (U∼1).

The above considerations could explain the stratification seen in the line response: under an increasing U, Hα and Hβ are not able to reprocess the ionising continuum to the same extent as HeI. These lines therefore saturate at a lower ionising flux. This is a simplified interpretation, however. The main simplification is the assumption that U only depends on the ionising flux. In reality it will also depend on n_e. Based on the simplified U consideration, the saturation levels of Hα and Hβ should be very similar, whereas they are quite distinct in Mrk 110. Differences in density in the line forming regions could explain this discrepancy. For changes on a dynamical timescale in the BLR it is quite likely that n_e in the line forming regions will also change. In the Radiation Pressure Confinement (RPC) model, the conditions inside the line forming clouds will adjust themselves such that $U \sim 0.1$ at the centre of the

cloud. In the RPC model changes in the luminosity can therefore alter U in the line forming region only temporarily. A new balance between gas and radiation pressure will establish itself at a different radius, shifting the line emitting region [Baskin et al., 2014a,b]. Significant changes to U would therefore be difficult to establish in this model.

In the interpretation discussed above, the connection between the saturation level and RM lag is the other side of the coin for the connection between the line species and sensitivity to U: line species that are predominantly formed at larger radii are less responsive to changes in U and therefore have a lower saturation level. An interesting alternative relies on the idea that the correlation of the saturation level with distance is based on the connection between the BLR and the dusty obscurer. In this interpretation the increasing luminosity causes the line to be formed at larger radii in the BLR until the dust sublimation radius is reached. At this point the obscuration of the dust mixing with the gas diminishes both the incident ionising flux and the emergent broad lines. This effect should occur first for the lines formed at the largest radii, affecting the other lines in reverse order of distance from the central engine.

An important condition for this 'dust wall' interpretation to be viable is that the dust sublimation radius does not move outward, or at least changes on a longer timescale than the radius of the BLR. Landt et al. [2014] find that the outer radius of the BLR has a similar radius as the hot silicate grain dust found in IR RM studies. Photoionisation modelling indicates that e.g. Hβ emissivity increases towards the outer edge of the BLR (see Figure 1.8). The proximity of the line emitting region to an obscuring medium implies that a relatively small change in the emission radius could lead to a noticeable extinction of the line by dust. This effect will occur as long as the inner radius of the dust changes less than the outer radius of the BLR.

In case the dust wall scenario is accurate, the observed line flux should decrease when the luminosity rises further, that is: the line flux has a negative responsivity. This effect would indicate that the optimal line forming region is 'disappearing' into the dusty obscurer. There is no evidence of this occurring in the Mrk 110 data, but it is possible this is because the change in ionising flux has not been sufficient to make the effect visible.

Kinematics

The line profiles show a number of interesting correlations. Understanding them, however, is complicated by two factors: the first is the difference in behaviour between HeII and Hβ, the second is the unknown orientation of the AGN. The strong orientation effects associated with a flattened BLR geometry [Gaskell, 2009; Grier et al., 2013; Pancoast et al., 2014] are of influence on the redshift along our line of sight. If we reject the gravitational redshift interpretation for the offset [Kollatschny, 2003b], there is little constraint on the possible orientation of MRK 110's nucleus, except the fact that Seyfert 1s are on average observed closer to face on. Depending on our line of sight through the BLR the Doppler shift of the broad emission line can therefore be associated with either an inflow or an outflow.

A likely effect to be associated with an outflow in the BLR is a radiation driven wind (e.g. Elvis [2000]; Elitzur & Ho [2009]; Richards et al. [2011]). In the case of Hβ, the correlations found for Mrk 110 can be described in the context of a BLR where the motion of the clouds combines a gravity dominated rotation and a radial outflow. The BLR breathing effect is

evident in the correlation between σ_{broad} and the HeII flux. This effect means that regions at a greater distance from the central engine are lit up as the luminosity increases. The negative correlation between offset and Hβ line flux can then be interpreted as a reduced outflow speed at larger radii. This would be in agreement with a decrease in the radiation pressure with increasing distance from the continuum source.

The behaviour displayed by the HeII profile suggests a more complex system, however. The most remarkable effect for HeII is the positive correlation between flux and line width, which is contrary to the expectation of BLR breathing. A possible explanation for this discrepancy is that the kinematics of the line are not fully determined by gravity. Netzer & Marziani [2010] argue that radiation pressure can significantly alter the orbits of BLR clouds, dependent on the cloud column density. In the case of HeII I suggest the following scenario: at first, part of the gravitational force on a BLR cloud is balanced by an outward pressure from the continuum, therefore the rotational speed of the cloud will be lower than in the purely gravitational case. Next, the pressure decreases and the cloud now moves at a sub-Keplerian speed without a balancing outward force. The cloud therefore migrates inward in the BLR, conserving its angular momentum, until the rotational speed is sufficient to balance gravity, thereby increasing the line width.

Following this scenario, the positive correlation seen in Figure 4.15 therefore requires an increase in HeII flux to lead to a decrease in radiation pressure. This is possible if the increase in FUV flux, as indicated by the HeII proxy, is such that the clouds in the HeII forming region become overionised. In overionised gas the ionisation parameter is so high that any line emission is suppressed by the strength of the incident flux. This would be in the same line of reasoning as the analysis of the CIVλ1549 blueshift presented in Richards et al. [2011]. The authors of this study argue that harder spectra overionise the gas, making the gas less susceptible to acceleration by line driving. Note that in the case of Mrk 110 this requires the ionising flux to be hard enough to impair the line driving of H through ionisation, but not so hard that the HeII emission itself is suppressed. As the radiation pressure drops in the line forming region, the BLR clouds will move at higher speeds as they are pulled deeper into the potential. The higher rotational speed of line emitting clouds will be the case even if the line forming region itself moves to a larger radius, in accordance with the LOC breathing mechanism. A mechanism where the radiation pressure depends on λ_{Edd} is discussed in Sun et al. [2018] to explain the anti-correlation of the CIVλ1549 linewidth and its systemic blueshift.

The combination of gravitational and radiation pressure effects is applicable to both an inflow and an outflow scenario, but there are subtle differences in the argument. The impact of radiation pressure does not apply to all clouds: the dependence of the pressure on N_H [Netzer & Marziani, 2010] implies that different clouds will be subject to different pressures, dependent on N_H. In the case of an outflow some of the clouds will be accelerated outwards, whereas others will be in gravitationally bound orbits. The resulting line profile will be a mix of these two cloud populations. For the clouds that form the outflow, the overionisation effect will reduce the flow speed, in accordance with observed anti-correlation in Figure 4.13. In the case of an inflow (see e.g. Gaskell [2009]) all clouds will be gravitationally bound and there is no separation into two cloud populations. The radiation pressure effect should therefore hold for all clouds.

The interpretation presented above does fit the behaviour of HeII, however it does not

explain the observed difference with Hβ. The behaviour of the latter line *does* seem to be dominated by gravity only. Both radiation pressure, which depends on the incident flux, and gravity, depend on the radius as r^{-2}. If the difference in behaviour between the two lines is caused by a stronger effect of radiation pressure on HeII, a correction mechanism is required to diminish the radiation pressure at the radii where Hβ is formed. A plausible process that could cause this is cloud self shielding, in which the inner BLR clouds obscure a fraction of the incident continuum from clouds at larger radii. Strong self shielding is a prominent feature of the BLR model proposed in Gaskell [2009].

A model that incorporates the effect of radiation pressure on BLR clouds is the 'quasar rain' model (Elvis [2017], Section 1.2.3). The motion of clouds in this model is along an elliptical orbit: clouds close to the central engine are ejected at high velocities, the clouds with $v < v_{esc}$ will lose their radial velocity due to interaction with the diffuse BLR medium, before falling back towards the disc. The results found for Mrk 110 broadly match this picture. The higher offset for HeII than for Hβ can be associated with a higher flow speed for the HeII emitting clouds. As Hβ is formed at larger radii, the line emitting clouds for this line species will have lost more of their initial radial momentum, resulting in a lower offset. In the quasar rain model the observed offset can be interpreted as either an outflow or an inflow, as both are expected to be present in the BLR. However, the fact that we only see one of the two requires a geometry that shields clouds in the other flow direction from our line of sight. This dependence on geometry is also relevant if the interpretation is expanded to include objects where the offset of the broad line is to the blue, rather than to the red (Barth et al. [2015]; see Section 4.1).

An alternative interpretation of the results is a BLR entirely in inflow [Gaskell, 2009]. Depending on orientation such an inflow could be associated with the redshift of the broad line components. The model presented in Gaskell [2009] assumes strong self shielding of the clouds, allowing the cloud motion to be fully gravitationally dominated down to small radii. This would agree with the self shielding needed to explain the discrepancy between HeII and Hβ.

The stronger offset for the HeII line could be the result of a higher inflow velocity, as the line is formed deeper in the gravitational potential. The arguments to interpret the correlations for Hβ based on BLR breathing, are also valid in this interpretation. As mentioned, the pressure-gravity balance argument to explain the behaviour of HeII would also hold in an inflow dominated scenario, without the need to separate between an outflowing and a rotating cloud population. There are therefore arguments in favour of an inflowing BLR scenario in Mrk 110. However, the unknown orientation and unknown details of the BLR geometry make distinguishing inflow and outflow scenarios impossible.

Future Work

An expansion of the investigation of Mrk 110 can be twofold. In the first place the research into this object would benefit from continued observation. The results in this chapter clearly illustrate the importance of high cadence spectroscopy, in particular for the ability to track changes in the BLR on multiple timescales. There is currently an observational programme underway with the FAST instrument at the Tillinghast telescope. The most recent observations from this programme have been included in the analysis presented here.

The second possible continuation of this study is the photionisation modelling of the flux response, in particular the dependence of the line emissivity on the luminosity state. Matching the observations to a photoionisation model which can include the observed luminosity changes in Mrk 110 would be an important test on the LOC interpretation. This comparison could confirm whether the observed stratification is indeed the result of photoionisation conditions, or whether an interpretation that relies more strongly on the BLR geometry, such as the 'dust wall' scenario, is required.

5. MgIIλ2798 Variability

The study of the broad MgIIλ2798 emission line presented here aims to be complementary to MacLeod et al. [2019] (MCL19). I will by look at a different part of the spectrum for the observed CLQ candidates than MCL19. This study will also expand on the insights gained from these highly variable objects by using a much larger QSO sample from SDSS. In contrast with the Mrk 110 study, which concerns multiple emission lines in a single object, this is a study of a single line observed in multiple objects. The objects under investigation are separated over the two samples introduced in Section 2.3: the **supervariable sample** and the **full population sample**. Combining new observations of CLQ candidates with the large archival data-set provided by SDSS DR14, it is possible to observe the behaviour of the MgIIλ2798 line across the QSO population.

The spectral fitting techniques set out in Chapter 3 will be applied to both samples. For many objects in the full population sample spectral fits including MgIIλ2798 are available in Shen et al. [2011] and Pâris et al. [2014] (DR12). At the outset of the study the aim was to use these two catalogues as the basis for the full population data-set. This option turned out not to be viable for two reasons. The first is the flux calibration issue discussed in Section 2.1.1, for which no correction had been made in DR12. The second issue with the data comparison lies with the FeII templates used in the fitting process. The two analyses use different templates, and as discussed in Section 3.2.3 the choice of FeII template can be of considerable influence on the derived MgII flux.

The difference between the measurements was already noted for DR9 [Pâris et al., 2012], where the authors compared their results with those of Shen et al. [2011]. Subsequent data releases used the same fitting methods as for DR9. The effect can be seen in Figure 5.1, comparing the equivalent widths found in DR7 and DR10 [Pâris et al., 2014] for the same objects. There is a clear offset in the distribution, with DR10 results tending to have a larger EW. This can be compared with Figure 30 in Pâris et al. [2012], where the comparison is made for CIVλ1549. For this line there is no clear effect visible, likely indicating the importance in the choice of FeII template for MgII. To ensure consistency in the fitted line and continuum parameters, the full sample was refitted using a single fitting method.

The purpose of this analysis is to refine our understanding of the BLR by testing ideas based on the Mrk 110 case on the MgII data-set. The key is to use spectral light curves, or pairs of spectra, that cover a period in the order of several years. The long temporal baseline allows us to track changes in the BLR that take longer to develop and would therefore remain undetected in shorter studies. Given the relative lack of response of MgIIλ2798 to changes in the continuum on the time scales of months in RM studies, as discussed in Chapter 1, this study on longer timescales can provide interesting insight into this apparent stability.

Starting with the supervariable sample, which exhibits the most extreme cases of both continuum and line fluctuations, I will first consider the possible types of MgII behaviour in Section 5.1. In Section 5.2 I will discuss the methods used in evaluating the results of fits to the spectra, the possible fit of a responsivity function, and the tests used to determine the

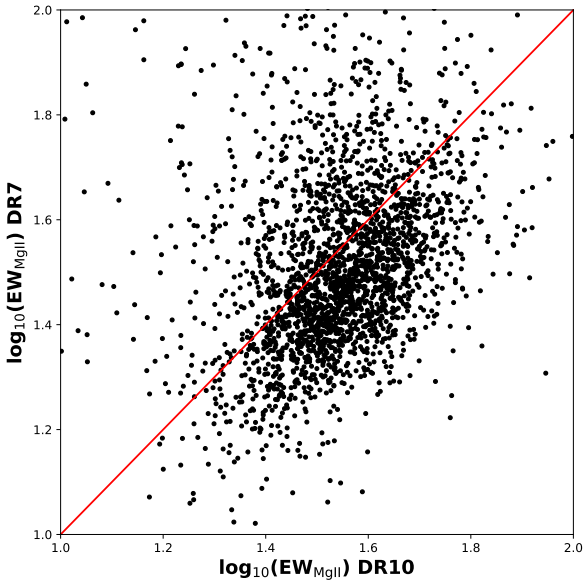

Figure 5.1: Equivalent widths calculated for MgIIλ2798 in Shen et al. [2011] (DR7) and Pâris et al. [2014] (DR10) show that the differences in fitting method between the two studies result in a systematic offset in the equivalent widths, and therefore other line parameters as well. This discrepancy was the motivation for fitting the entire full population sample with a single fitting method (see Chapter 3). The red line is included to indicate a 1:1 correspondence between the catalogues.

statistical significance of the results. This is followed in Section 5.3 with the discussion of the results for the supervariable sample, considering changes in the line flux, changes in the line profile, as well as the correlation with the results from MCL19.

The results for the full population sample are discussed in Section 5.4. This discussion covers the behaviour of the MgII line itself as well as a comparison of the responsivity results with the physical parameters derived in Shen et al. [2011]. These parameters include black hole mass and Eddington ratio. The location of objects with variable MgII in the parameter space spanned by these physical quantities can provide an interesting insight into the processes governing variability. The chapter will conclude with a comparison of the two samples in Section 5.5 and a discussion of possible interpretations in Section 5.6.

5.1. How Variable Can MgII Be?

The claims of limited variability of MgIIλ2798 on short timescales (e.g. Clavel et al. [1991]; Kokubo et al. [2014]; Cackett et al. [2015]), could be the result of an intrinsic limit of the response of the line. It could also imply that the line response materialises on longer timescales. In the latter case it is of particular relevance for experiments that rely on short timescale variations (e.g. Shen et al. [2016a] and Wang et al. [2019]) to understand whether there is a low frequency variability that forms the background to any observed rapid fluctuation. More specifically, it is of importance to understand what types of variability the MgII line exhibits on long timescales, as well as whether there is any correlation with other observable parameters. The supervariable sample provides the data-set to answer the first of these question, and we shall return to the

second question in Sections 5.4 and 5.5. Plots of all available spectra for the supervariable objects are included in Appendix A.

5.1.1 Flux Changes in the Supervariable Sample

The observed CLQ candidates of the supervariable sample were selected for optical variability. Following our understanding of AGN spectral changes (Section 1.3) this will almost certainly have been accompanied by even larger fluctuations at shorter wavelengths. It is therefore reasonable to assume that the supervariable objects will provide a good overview of the range of possible behaviours of the MgIIλ2798 emission line. Before considering this problem quantitatively in Section 5.2, an inspection by eye of the reduced and flux-corrected spectra already provides some interesting results.

The first observation is that there is a wide range of variability among the objects in the sample: in some cases the continuum changes and the line remains almost stable, as often occurs on short timescales, but in many spectra MgII traces or even outdoes the continuum in its variability. Examples of the behaviour are shown in Figure 5.2. There are five broad categories in which the objects in the sample fall: *i*) diminishing continuum, line flux is stable; *ii*) diminishing continuum, with the line tracing the continuum; *iii*) rising continuum, stable line; *iv*) rising continuum, rising line; *v*) little overall change. The latter category, which describes four targets, is likely the result of the new observation having been made once the AGN had returned to the state of the original observation. Although the continuum fluctuated strongly in between the spectral epochs, it is therefore difficult to know what the results of these changes on the spectrum were.

The spectra of the four objects included in Figure 5.2 cover the wavelength range from MgIIλ2798 to Hβ. All observations in the supervariable sample have Hβ in the wavelength range as this is largely a subsample from the MCL19 study, which focusses on this emission line. The four spectra were selected as examples of the four categories of MgII variability. The top two panels show objects with a dimming continuum, with the MgII line changing only in one of the two cases. The bottom two panels show the same difference, only for a rising continuum. Of particular interest is J002311 (panel *c*), for which the range of observations covers the object brightening and re-dimming. The response from MgII as the continuum rises (between MJD 51900 and 55480) is very limited, but once the continuum diminishes again (MJD 58037) the reaction is more pronounced. The responsivity of the line therefore not only differs from object to object, but also from epoch to epoch.

There are two conclusions that can be drawn with regard to the variability categories. The first is that the MgII line does indeed vary, and possibly with large amplitude, if one waits long enough (Δt is large), or if the continuum change is large enough (Δf_c is large). The distinction between Δt and Δf_c as the determining factor for changes in MgII line flux is difficult to make, however. The second conclusion is that there is another factor, likely to be a combination of many, that determines the responsivity of the MgII line emitting region. This hidden factor can simply be referred to as the 'initial state' of the BLR, the overall condition of the line forming region prior to the observed change in continuum flux. The initial state determines whether a seemingly similar change of the incident flux, such as in panels *a* and *b* of figure 5.2, results in a response from the line or not.

As the change of the MgII flux is only one part of the overall spectral variability, it is im-

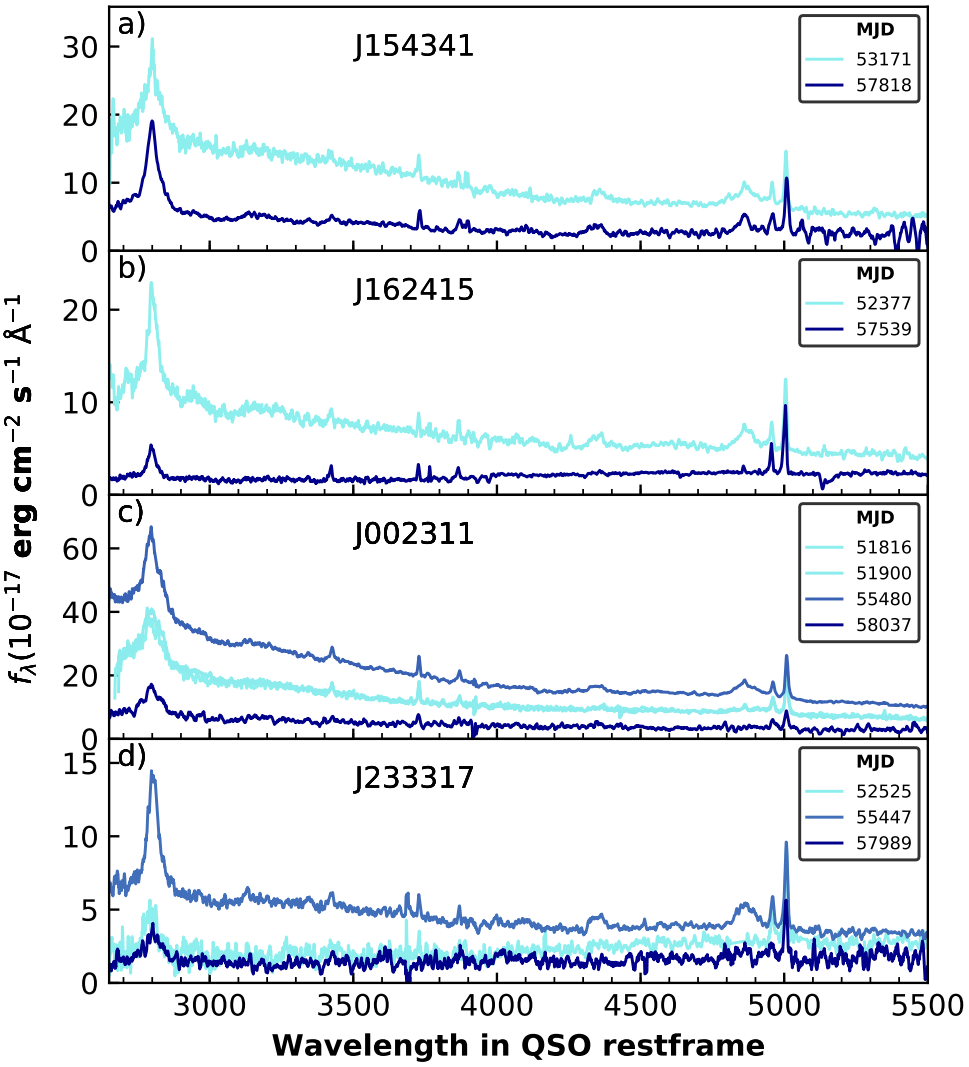

Figure 5.2: Examples of the wide range of behaviours detected for the MgIIλ2798 line in the supervariable sample. The colours are as in Figure 3.3. *a)*: J154341, which displays a diminishing continuum, whereas the MgII line flux remains stable. *b)*: J162415, where the MgII line flux tracks the lowering continuum quite closely. Note that this is also a clear CLQ. *c)*: J002311, where we see a rising continuum, without a strong response in the MgII flux. Interestingly we have enough spectra to see the spectrum both rise and fall: after the lack of response to a rising continuum, the MgII tracks the continuum more closely after it decreases. *d)*: J233317, which shows the MgII flux responding to a rising continuum, and returning to a lower state subsequently.

Table 5.1: Four categories of variability displayed in the supervariable sample, separating the objects based on Hβ and MgII line flux changes. The Hβ variability is based on a visual identification as a CLQ in MCL19 and the MgII is based on a visual inspection of this line. The second column lists the number of objects that fall in each category and the third column the average of the time spans between the spectral epochs for the included objects. The value in parentheses is the standard deviation of Δt in each category.

Type of Variability	N_{obj}	avg. Δt_{spec} in days
Hβ, MgII	11	3804 (205)
Hβ, no MgII	5	3300 (485)
no Hβ, MgII	7	3292 (759)
no Hβ, no MgII	20	3407 (738)

portant to consider the correlation with other spectral features, in particular with the change in Hβ.The bottom three objects in figure 5.2 can be classified as CLQs, as only the narrow line component of Hβ remains in the low state spectra. Although the relation between variability in MgII and in Hβ is not one-to-one, there does appear to be a connection. Out of the 43 objects in the sample, 16 show CLQ behaviour and of these 16, 11 objects are also variable in the MgII line. Conversely, there are 7 objects that have not been classified as a CLQ in MCL19, but that do show significant change in MgII. A full overview of the responsivity behaviour for the supervariable sample is given in Table 5.3. The relevant columns are labelled MgII Var and CLQ: the first indicates whether the line tracks the continuum when it changes (categories *i* and *iii* above) or remains stable (categories *ii* and *iv*) and the second column lists whether the object was identified as a CLQ in MCL19.

Combining the MgII and Hβ information, there is once more a range of behaviours across the sample. A possible cause is the difference in elapsed time between the first and the last available observation. This possibility can be considered using the information in Table 5.1, which shows the average elapsed time between spectral epochs for four categories of AGN behaviour, based on MgII and Hβ. The value in parentheses in the Δt_{spec} column is the standard deviation of the elapsed times, per category.

The categories in Table 5.1 are based on two classifications: variability in Hβ is based on whether the object was classified as a CLQ in MCL19 and the classification of MgII variability was made by eye, following the categories displayed in figure 5.2. The category 'no MgII' covers objects with a stable line flux while their continuum changes. For the supervariable sample there are 36 objects where the continuum level decreases, 4 where the continuum rises and 3 where it stays approximately constant. We therefore lack the statistics to split the responsivity categories up into brightening and dimming transitions. The discrepancy is likely due to a selection bias: objects that were in a high state during the SDSS epochs were more likely to be detected and included in DR7.

The categorisation in Table 5.1 indicates that there is no direct correlation between the elapsed time between spectral epochs and the type of variability detected. There is a large scatter in the range of Δt_{spec} (see also figure 5.6) and this scatter is present in all four categories. This is an indication that the change in ionising flux, rather than the elapsed time, with the associated possibility of large scale structural changes to the BLR, is the driving force behind the variability of MgII as well as of Hβ.

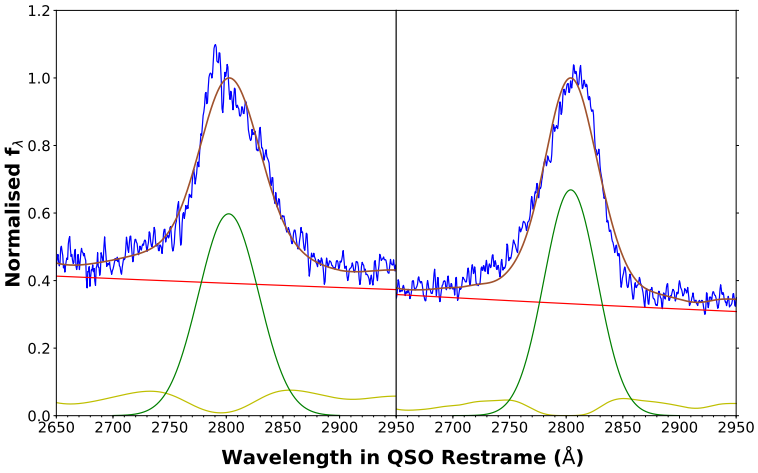

Figure 5.3: Examples of asymmetry in the MgII line: *left*: J225240 observed at 55500 (SDSS), *right*: J111348 observed at 57539 (WHT). The fluxes have been normalised to the maximum flux of the fitted functions. In both objects the line appears skewed with respect to the symmetric Gaussian. The skewness of the lines is to different sides: to the blue for J225240 and to the red for J111348. A possible explanation for this effect is an offset between different line components, similar to the situation for Mrk 110.

5.1.2 Line Profile Changes in the Supervariable Sample

In addition to changes in the line flux, which trace the radiation reprocessing capacity of the line forming regions I will consider the line profiles. These can provide information about the kinematics of the BLR. Most of the targets in the sample show a simple symmetric MgII profile. Some of the MgII lines appear skewed, however. Two examples of this behaviour are shown in figure 5.3. There are only five objects in the supervariable sample that clearly display this type of asymmetry in the profile: J022556, J034144, J111348, J225240, and J234623. Of these J034144 and J111348 show a skewness to the red, the others to the blue. There are more spectra that can tentatively be identified as asymmetric, but the data quality does not allow for a definitive identification.

A possible explanation for the profile asymmetry is an offset among line components. As mentioned in Chapter 3 the MgII line is fit with one or two Gaussians, with the selection dependent on a goodness of fit statistic. A two Gaussian fit would allow for some asymmetry in the line to be captured in the fit, as the line centres are not required to be at the same wavelength. However, the AIC selection process indicates the skewed lines are still best fit with a single Gaussian. The results of the fitting procedure (which will be discussed further in Section 5.3) show that for line profiles that require two components, the second component is most often a wide, low-peaked Gaussian, extending into the wings of the line. The type of asymmetry seen here is therefore unlikely to be fully captured by the fitting procedure, as can be seen in figure 5.3.

In the scenario where the relative redshift of line components is the cause of the skewness, a small offset between a broad and an unresolved narrow component appears more likely. This would be akin to the offsets visible for Mrk 110 in HeIIλ4686 and Hβ. As discussed in Section 4.1 the HeIIλ4686 offset has been observed in other objects both to the red and to the

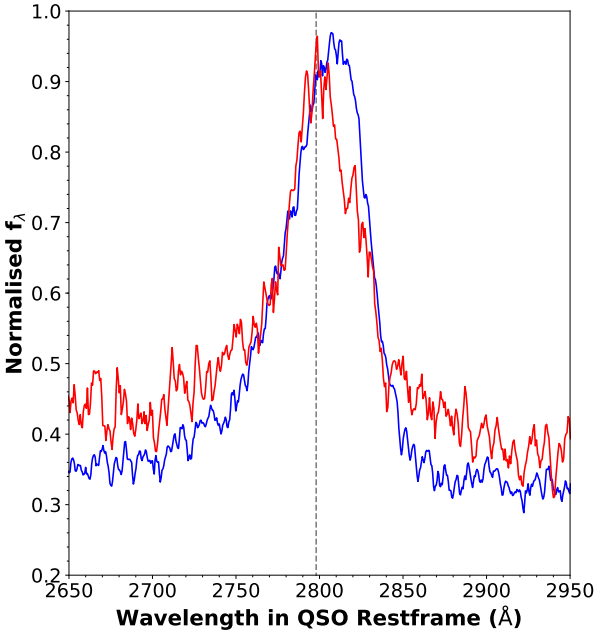

Figure 5.4: The profile of the MgIIλ2798 line in J111348 as observed on MJD 52438 (*red*) and 57539 (*blue*). The fluxes have been normalised to the maximum of the MgII line flux, for an easier comparison of the line profile. Over the period between the two epochs the line flux dropped by a factor ∼4. In the more recent spectrum, associated with the lower emission state, the line has acquired a skewness to the red. The vertical line marks 2798Å in the QSO restframe.

blue. Although the identification of the MgII narrow line is more tentative than in the case of the Mrk 110 spectra, the association with a possible outflow could prove a useful measure of BLR kinematics.

An interesting question is whether the skewness of the profiles is subject to change. The number of skewed profiles in the sample is insufficient to make any statistical assessment of the incidence of these changes, however it is possible to consider the five cases at hand as examples. Only one of the five objects, J111348, shows an indication of a variable line profile over time. Between the two available spectral epochs for J111348, the maximum of the line, possibly associated with the narrow component, appears to shift from the centre to the red. The two epochs are shown in figure 5.4.

The change to a more asymmetric profile in J111348 was associated with a large drop in flux, where the 2798Å continuum dropped by a factor of approximately 4. In terms of the narrow-broad explanation considered above, this could mean that in the high state profile (*red*) the offset narrow line is simply lost in the broad flux. The narrow component could possibly be identified as the secondary peak in the red wing of the high state line profile. The grey vertical line in figure 5.4 represent 2798Å in the QSO restframe. The conversion to restframe wavelengths was made using the SDSS redshift estimate. The SDSS z estimate is based on a fit to the (broad) MgII line: the location of the broad line centre at this wavelength is therefore not coincidental. It is the relative offset between the two epochs that provides the most interesting information, not the absolute redshift.

Given the small number of objects with clearly identifiable asymmetry in their profiles, a simpler metric of the line profile, the line width σ, can be used to apply to the full sample. The

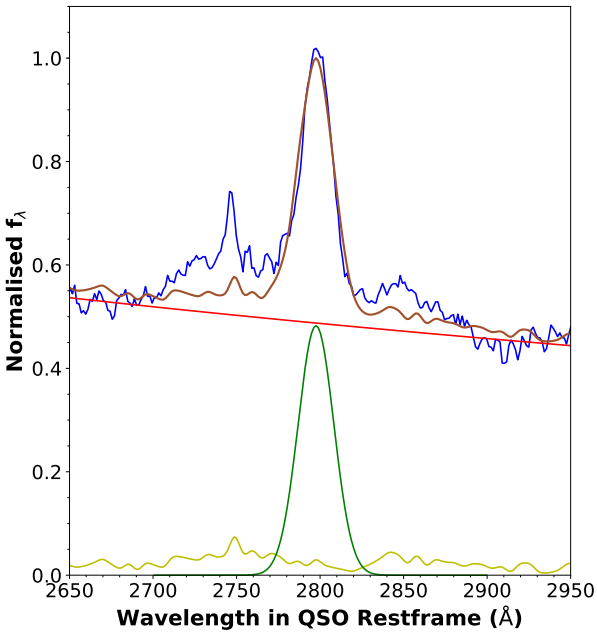

Figure 5.5: The MgII line for J002714 observed at MJD 57726 with the MMT. The spectrum is remarkable due to the prominent emission feature around 2740Å. The fitted function includes the Bruhweiler-Verner FeII template, rather than the Vestergaard-Wilkes template used throughout the rest of this chapter. Although there is an emission feature in the template that approximately matches the apparent line, it is not nearly strong enough to account for the observed flux.

line width can be used to track basic information about BLR kinematics when one assumes Keplerian rotation of the line emitting gas. Clouds closer to the central mass of the AGN should rotate more rapidly, so that based on the LOC model one would expect a negative correlation between $f_{\rm continuum}$ and σ (see also the discussion in Section 4.4). The evolution of σ as the continuum fluctuates in the supervariable sample will be presented in Section 5.3.

The final spectral feature to stand out in an inspection by eye of the supervariable sample is most evident in the MMT spectrum of J002714. As can be seen in figure 5.5 there is a prominent narrow line emission feature in the blue wing of MgII, at approximately 2740Å in the QSO restframe. The most likely identification is an FeII emission line, as the observed wavelength (∼4233Å) does not appear to match any prominent atmospheric line. The FeII feature is prominent in the Bruhweiler-Verner template, but weaker in the Vestergaard-Wilkes template (see the discussion in Chapter 3). Re-fitting the spectrum for J002714 with the BV template results in a marginally better fit, but the template cannot account for the strength of the feature. There are also no signs or particularly strong FeII emission in other parts of the spectrum.

A cosmic ray or other contamination of the spectrum appears unlikely, as the 2740Å feature appears in the SDSS spectrum of J002714 as well, although significantly weaker. And indeed a feature around 2740Å can be detected in several objects. Whether to identify this emission with the FeII feature remains unclear, however.

5.2. Methods for Quantifying the MgII Variability

Following the initial classification of the possible types of MgII variability, it is necessary to quantify the spectral changes over time with more precision. This is also required for the full population sample, for which inspection of each spectrum is no longer possible. The spectra of both samples are fit using the pipeline described in Section 3.2. For each epoch the spectral fitting provides: a power law describing the continuum, a MgII line flux, a MgII line width, and the central wavelength of the MgII line. The MgII line centre provides the QSO redshift, which will be used in all subsequent calculations, rather than the SDSS value. In the case of a two Gaussian fit the line centre of the narrower component is used. Note that both that both Gaussian components correspond to 'broad' emission lines (i.e. in the order of tens of Å).

The parameters used in the analysis in this chapter are the continuum flux, the line flux, and the line width. The continuum flux is defined as the value of the power law at the line centre, using the same definition for the line centre as for calculating z. The continuum flux is therefore taken to be the value of the power law under the line, and can be seen as representative of the continuum level in the UV. The continuum power law is fitted to the region around MgII, and the amplitude and index are used to calculate the value at the line centre. The flux is given in units of erg cm^{-2} s^{-1} Å^{-1}. The line flux is simply the area under the Gaussian, or the sum of the areas of the two Gaussians, and has units erg cm^{-2} s^{-1}. The line width is given in Å and in the case of two components is calculated as the width of the wider of the two Gaussians. This choice is motivated by the fitting constraint, based on performance of the algorithm, on the broader component: it can be no wider than 1.5 times the width of the narrower Gaussian. The width of the broad component is therefore still an appropriate measurement of the line width. The parameters will be referred to as f_{2798}, the continuum flux under the line, f_{MgII}, the line flux, and σ_{MgII}, the line width.

The errors on the fitted parameters are provided by the `lmfit` routines in the pipeline. The errors on the line flux and line width are provided directly. The error on the continuum flux is found through propagation of the errors on the power law amplitude and index (A and σ_A, and α and σ_α respectively), where λ_c is the wavelength of the line centre:

$$\sigma_{F_c} = \lambda_c^{\alpha}\sqrt{\sigma_A^2 + (A \cdot \ln(\lambda_c \sigma_\alpha))^2}. \tag{5.1}$$

The measure of emission strength for the main results is a flux rather than an equivalent width (EW). This is similar to the method used in e.g. Zhu et al. [2017] and Yang et al. [2019]. Although a study of the EW can provide a lot of information about the behaviour of broad emission lines [Shen et al., 2011; Dong et al., 2009; Korista & Goad, 2004], I believe considering the line and continuum flux as separate parameters will allow for more insight into the behaviour of each component. The EW combines the continuum and line flux in a single measure, making it difficult to separate their evolutions. Like the deliberately minimalist approach to the fitting function, the choice of line flux aims for a simpler interpretation.

For the purpose of comparison, the EW is used in one part of the analysis, however. The EW is calculated to find the intrinsic Baldwin Effect. Calculation of the slope $\mathrm{dlog}_{10}(\mathrm{EW})/\mathrm{dlog}_{10}(L_c)$ allows for a comparison with literature values (Shen et al. [2011]; Osmer & Shields [1999]; see also Section 1.2.2), giving extra context to the level of fluctuations seen in the supervariable sample. The equivalent width is calculated from the fitting results,

using the power law to represent the continuum and the Gaussian(s) to represent the line:

$$\mathrm{EW} = \int_{\lambda_{min}}^{\lambda_{max}} \frac{F_{line}}{F_{continuum}}\,\mathrm{d}\lambda, \qquad \sigma_{EW}^2 = \left(\frac{\sigma_{F_l}}{F_c}\right)^2 + \left(\frac{F_l \cdot \sigma_{F_c}}{F_c^2}\right)^2. \tag{5.2}$$

Here λ_{min} and λ_{max} are the limits of the wavelength range, chosen to be $\pm 8\sigma_{\mathrm{MgII}}$ around the centre of the narrowest Gaussian component. σ_{EW} is the standard error on the EW, propagated from the errors on the line and continuum flux, which were themselves found by propagating the χ^2 errors calculated by the `lmfit` routines in the pipeline. Note that the term F_{line} does not include the continuum flux, because the flux is defined as the fitted Gaussians. The calculation is performed using a numerical integration method provided in the `scipy` package.

Not all spectra can be fit successfully by the pipeline, due to data quality. This issue only applies to the full population sample: the pipeline was calibrated using the supervariable sample, therefore all spectra for this sample are fit correctly. For the full population sample, objects with one or both spectra for which no correct fit could be found are excluded. This affects only a relatively small fraction of the sample: 1446 spectra (∼5%). In the results presented below, the number of objects in the full population sample is 15,101.

5.2.1 Comparing Epochs

In this section I will introduce several measures to quantify MgII variability. These measures will be used in the rest of this chapter. The data consist of spectra from multiple epochs and many objects. For that reason it is necessary to define a method enabling a comparison on equal footing of all spectral fit results. This method will be applied to both the full population and the highly variable samples. The two samples will be analysed in the same manner, with the aim of comparing the results for the two data-sets and investigating the relation of the highly variable objects to the general QSO population.

The first method of comparison is based on a normalisation of the data to a specific epoch, similar to that introduced for the data from Mrk 110 (Section 4.2). The difference with the Mrk 110 data-set is that for most objects there are only two epochs available, making the choice of epoch more important. Two different epoch-based normalisations are considered: normalisation to the state of the highest continuum level, and normalisation to the state of the lowest continuum level. The aim for the two normalisations is to allow for two different views of the data, visualising a different category of variability.

For normalisation to the high state, the spectral epoch with the highest *continuum* flux is identified for each object. The values f_{MgII} and f_{2798} of the same epoch in all other epochs are then divided by f_{MgII} and f_{2798} of the reference spectrum. This implies that the normalised flux values are defined as fractions of the flux levels in the state of highest continuum. The normalised continuum flux is therefore in the range [0,1], whereas the normalised line flux can exceed unity, depending on how the line varies with respect to the continuum. The emphasis in this normalisation is on small flux changes (see figure 5.8), and the associated changes in line flux.

The case of normalisation to the low state is more akin to the normalisation used in the discussion of Mrk 110. The question that can be best addressed in this case is whether the line flux can track the continuum as it rises. Due to the smaller number of observations per

object it is impossible to know whether the line response for any object changes over time. However, the range in variability seen in the sample implies that considering the response of the ensemble should yield an average of the possible behaviours.

It is interesting to investigate whether a levelling off, or saturation, of the responsivity can be detected for MgII, as it was for other emission lines in Mrk 110. As f_{2798} is representative of the continuum in the UV, its connection to the ionising continuum in the EUV needs to be considered. The fit to the continuum is based on the spectral region around MgII. It is not possible to reliably extrapolate this to an EUV flux density, as it is uncertain whether the UV-optical power law will be valid for shorter wavelengths. This is therefore a different comparison than the one presented for Mrk 110, where a measure of the true ionising continuum was constructed.

Looking ahead at the results of the normalisation to the low state for the supervariable sample (the top panel of figure 5.9), the data do not indicate a preferred fitting function. The question is therefore what kind of responsivity curve best matches the data. This question can be approached by fitting two functions to the data: one a simple line through the origin, the other the two component function defined in Section 4.2. A comparison of these two fits will reveal any possible similarities between MgII and other broad lines. It can also provide a more precise definition of the responsivity: from the discussion in Section 5.1 it is clear that the MgII line can indeed vary strongly, and the slope of a response curve will quantify this. The fitting method used is similar to the method introduced for the fitting of the responsivity function to the Mrk 110 data. The errors on the fluxes (propagated as in equation 5.1) seem to underestimate the uncertainties in the data, as indicated by the scatter. The uncertainties are therefore estimated using an initial fit to the data, after which the standard deviation of the residuals is set to be the uniform error. The next iteration of the fit provides the final result.

In addition to the epoch-based normalisations, which qualify the overall level of variability, a slightly different measure of normalised flux is introduced to consider the change in flux between spectra. The quantities Δf_{2798} and Δf_{MgII} are defined as the change in flux, from epoch to epoch, divided by the flux of the first epoch. These are therefore measures of the fractional change in flux, positive or negative, when the objects were re-observed. Δf_{2798} and Δf_{MgII} are good metrics to characterise the distribution of the flux changes, investigating whether there are correlations between the direction and the size of the change, or between the elapsed time between epochs and the magnitude of the change. These correlations will be explored in Sections 5.4 and 5.5.

5.2.2 Statistical Tests for Comparing the Results

This section will provide an overview of the various statistical tests used in the rest of this chapter. Some of these tests are devised to make an informed choice between different functions to fit to the data, others to help characterise a given distribution. This section will therefore serve as a reference for the methodology applied in Sections 5.3 and 5.4. In addition to the methods listed below, the analysis in this chapter will make use of the Pearson and Spearman correlation coefficients introduced in Section 4.4.

χ^2 Tests

When comparing the different responsivity functions to the data, χ^2 is one useful goodness of fit metric, based on the variance weighted residuals of the fit. As the responsivity functions under consideration have a different number of parameters, the reduced χ^2 (equation 3.2) is the proper value to use in the comparison.

The 'saturation' responsivity function (Section 4.2) can be constructed from a simple linear function by the addition of one parameter. The two functions can therefore said to be nested. In the case of nested functions, the difference between the two χ^2 (note: not χ^2_{red}) of the fits is itself a value distributed according to a χ^2 distribution, where the degrees of freedom (d.o.f.) of the distribution are equal to the difference in number of parameters between the functions [Lawrence, 2019]. The difference in χ^2 will be referred to as $\Delta\chi^2_f$, not to be confused with the $\Delta\chi^2$ introduced in Section 4.3, which is defined as $\chi^2 - \chi^2_{min}$ for a single model.

The difference in the number of parameters between the responsivity functions is 1. Therefore $\Delta\chi^2_f$ should follow a χ^2 distribution with 1 d.o.f. $\Delta\chi^2_f$ is associated with a probability: $P(\chi^2_1 > \Delta\chi^2_f) = 1 - \mathrm{CDF}(\Delta\chi^2_f)$, where χ^2_1 is a variable distributed according to the one d.o.f. χ^2 distribution and CDF is the associated cumulative distribution function. If the p-value is smaller than a given significance threshold, this indicates that the two-component fit is the preferred model.

Sequence Test

The 'sequence test' is intended to check the distribution of the data points around the fitted responsivity functions. If the function truly represents the behaviour of the fluxes, the scatter of the data points should be random, as it would result only from the uncertainties in the measurements. This can be pictured by considering the residuals (see figure 5.8). Any data point is just as likely to be above the line of the function as it is to be below it. A long series of data points on the same side of the line could therefore be indicative of the function over- or underestimating the responsivity in that particular range.

The sequence test is performed on the residuals of the fit, and simply counts the number of data points that have the same sign ($\pm$) as the preceding data point. The test statistic is labelled S, and represents the number of data points that have the same sign as the preceding point. The sampling distribution for this statistic is the binomial distribution for N-1 trials, where N is the sample size. For a perfect fit each data point (after the first one) has a $\frac{1}{2}$ probability of lying on the same side of the response function. S is normalised by dividing by N-1. The expectation value for S is therefore $\frac{1}{2}$ and the variance $\frac{1}{4}$. A significant deviation from the expectation value indicates that the function in question is not an optimal fit. Using the sample distribution, a p-value can be calculated for a given S statistic (p_s). This value represents the probability that the S statistic is not drawn from the binomial distribution. A relatively low value of p_s suggests a good fit.

When analysing the fitting results, the robustness of both the sequence test and the χ^2 tests are checked using a bootstrap Monte Carlo simulation. For a total N=10^4 iterations the normalised line flux and normalised continuum flux are resampled, by randomly deleting one epoch each iteration. The data are then fit again with the two functions, and the two test statistics, p_s and $\Delta\chi^2_f$, are calculated. The assessment of the robustness is based on the distributions of

the parameters. A narrow distribution of the test statistics, measured over N iterations, will support the reliability of any conclusion based on the tests.

Responsivity Measure: α_{rm}

Once a responsivity function has been established for the sample as a whole, the next step is to define a measure for the individual responsivity of the objects in the sample. The responsivity measure is constructed using the normalisation to the minimum continuum state, as this normalisation emphasizes large flux changes. This metric is based on a simple criterion: the perpendicular distance in the normalised flux plane from the line that would indicate a 1:1 correspondence between line and continuum flux. The responsivity measure will referred to as α_{rm}.

The various types of behaviour identified in Section 5.1 can then be associated with different values of α_{rm}. The tracking of the line by the continuum (included in categories *ii* and *iv*) will result in $\alpha_{rm} \sim 0$, as will a stable line and continuum (*v*). A positive responsivity measure is associated with a larger line flux change than continuum flux change. This class comprises the more extreme cases of categories *ii* and *iv*. A negative measure corresponds to objects with a continuum flux change that outdoes the line flux change, corresponding to categories *i* and *iii*.

In this manner the responsivity measure can assist in quantifying the variability behaviour. The difference in MgII variability should be visible in the distribution of α_{rm} across the samples. The parametrisation can also assist in defining specific variability subsamples, for which one can compare physical parameters such as the Eddington ratio and M_{BH} (Section 5.5).

Test for Normal Distribution

Considering Δf_{2798} and $\Delta f_{\rm MgII}$, an interesting question regards the nature of their distribution and in particular whether this distribution evolves with time. A correlation between time-scale and the changes in emission state would be a helpful indicator in understanding the physics underlying the transition. To test this possibility I will divide the sample in bins of different elapsed time (Δt). For each Δt bin the Δf_{2798} and $\Delta f_{\rm MgII}$ distribution can be tested. In the absence of a correlation, the flux changes can be expected to follow a normal distribution. The test to be conducted is therefore whether a given sample distribution follows the normal distribution.

There are several statistical tests available to address this problem. Prominent examples are the Kolmogorov-Smirnov (KS) test, and the closely associated Lilliefors test, and the Shapiro-Wilk (SW) test. For the purposes of this analysis I have applied the Lilliefors and SW tests to a sample data-set of $\Delta f_{\rm MgII}$. The KS test was not directly applicable, as it requires the normalisation of the data, which requires the sample average and sample variance. The Lilliefors test is an adaptation of the KS test, designed to account for the fact that the normalisation uses properties derived from the sample distribution.

Using a bootstrap Monte Carlo simulation (N= 10^4) to test the consistency of the test statistics, I determined that the Lilliefors distribution provided the most reliable test for normalcy on the MgII data-set. The algorithm for the SW test is included in the `scipy` package, and the Lilliefors by the `statsmodels` package[1]. The resampling of the data-set did not greatly alter the outcomes of the two tests, but the distribution of the p-values had a slightly larger spread for the SW test.

[1] https://www.statsmodels.org/dev/generated/statsmodels.stats.diagnostic.lilliefors.html

To verify the bootstrap MC comparison, I also performed a MC simulation on a test data-set drawn from the normal distribution. Using the same resampling method, the Lilliefors again proved the most consistent. This could indicate that the larger spread in p-values of the SW test was an artefact resulting from the bootstrap MC method. However, given the strength and reliability of both tests, the choice of test should not significantly alter the outcome or reliability of its conclusion. The Lilliefors test is used as the test for normalcy in this chapter.

5.3. MgII Variability in the Supervariable Sample

This section covers the results of the fitting pipeline for the spectra of the supervariable sample. The discussion of the results is split between an overview of the changes in the line and continuum flux levels and an overview of the changing MgII line profile. The analysis presented here will draw from the techniques described in Section 5.2.

The results of the spectral fitting of of the supervariable sample are summarised in Table 5.3. In the following I will provide a brief description of the manner in which the data in the table is organised. The first column lists the SDSS name, matching Table 2.6. The second and third column identify the type of variability behaviour exhibited by the object, as classified in Section 5.1, and the fourth column lists the time range over which the spectral observations were conducted. Columns 5–8 list the change in line and continuum luminosity and their associated errors. All values included in columns 5–12 are for the epoch showing the largest continuum change. The continuum luminosity is calculated as follows:

$$\mathrm{L}_\lambda = 4\pi D_L^2 \left(\frac{\lambda_{obs}}{1+z}\right) f_{\lambda_{obs}} \tag{5.3}$$

Here D_L is the luminosity distance from the QSO to the Milky Way, which is $(1+z)\cdot \mathrm{D}_M$, where D_M is the comoving distance. D_M is calculated using the `astropy` cosmology package[2], with the cosmological parameters as defined by the 2015 Planck results [Planck Collaboration et al., 2016]. The line luminosity, $\mathrm{L}_{\mathrm{MgII}}$, is calculated in a similar manner, by multiplying the fitted line flux with $4\pi D_L^2$.

The columns 9–10 of Table 5.3 provide the fractional changes in the line fluxes, Δf_{2798} and Δf_{MgII}. These values are normalised epoch to epoch, as defined in Section 5.2. The final two columns list the change in line width, and its associated error. As was noted in Chapter 4, the errors produced by the fitting pipeline appear to underestimate the uncertainties. For that reason the errors in this table, as well as in figure 5.7, were estimated using the same MC method (N= 10^2) as described in Section 3.2.3.

The parameters calculated for the supervariable sample represent the behaviour of the MgII line in a sample with a large range in time-spans between observations. The distribution of the rest frame time-spans between epochs (summarised in column 4 in Table 5.3) are displayed in figure 5.6. The figure shows an overview of Δt for all sequential spectral pairs. For QSOs with more than two spectra available, the sequential pairs are spectra 1–2, 2–3, up to (N-1)–N, in chronological order. Because the objects in the sample were selected based on optical variability, the responsivity behaviour characterised in this section can be related to both large changes in time and large changes in continuum flux. These two parameters can be connected to different mechanisms controlling the responsivity. A Δt in the order of years matches the dynamical

[2] http://docs.astropy.org/en/stable/cosmology/

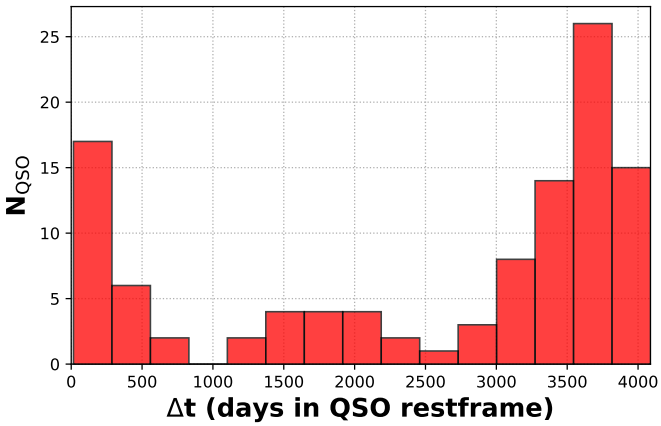

Figure 5.6: Histogram of the elapsed time between spectral epochs for the supervariable sample: the sample covers a large range in Δt. The sample could therefore contain changes as a result of two different underlying effects: structural changes in the BLR, possible only for $\Delta t \sim$years, and large fluctuations of the continuum. Δt is defined as the time between two sequential spectra, from which the values of Δf_{2798} and $\Delta f_{\rm MgII}$ are calculated.

timescale of the BLR (see Table 1.4 and the discussion in Section 1.4). The connection between responsivity and timescale will be discussed further in Section 5.5.

5.3.1 Following the Flux Changes

Luminosities

An overview of the change in line and continuum luminosities, using the absolute values of the changes, is shown in figure 5.7. The data in this figure concern the change from epoch to epoch in total energy emitted per second. It is clear that there is a positive correlation between the line and luminosity changes. Even for the most variable objects the absolute change in the MgII line is smaller than the change in the continuum. The plot also illustrates the large range in luminosities covered by the supervariable sample.

Flux Normalisations

Interpreting the responsivity behaviour from figure 5.7 is complicated: a large change in absolute flux does not necessarily imply a large fractional change. An intrinsically bright object can show large absolute changes in output, without a significant fractional change. In addition, the difference in initial flux and continuum level is not taken into account. In order to compare like with like, from object to object, the spectra are normalised as set out in Section 5.2. In the following I will present the results of the fitting process using two normalisations: first the normalisation to the state of maximum continuum and second the normalisation to the epoch of minimum continuum.

The results of the normalisation to the epoch of the highest continuum are presented in the upper panel of figure 5.8. All fluxes in this figure are fractional changes in flux: the further away from unity the normalised value is, the greater the relative change. The data show a strong scatter but there is a pattern to the relation between line and continuum fluxes. Large

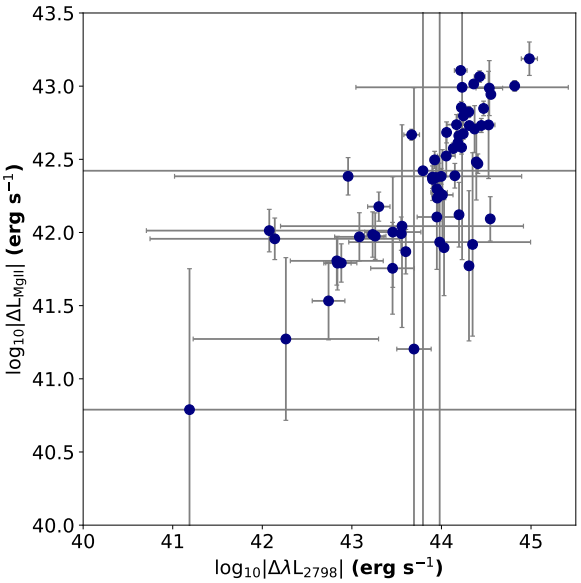

Figure 5.7: There is a clear positive correlation between the changes in line (L_{MgII}) and continuum (L_{2798}) luminosity for the supervariable sample. The plot displays the changes in luminosity from epoch to epoch, including the information from all spectra available for every objects. The horizontal axis represents the absolute value of the change in continuum luminosity (equation 5.3) at 2798Å and the vertical axis absolute value of the change in the MgII line luminosity.

relative changes in continuum are matched by large relative changes in line emission. For smaller changes in continuum flux, moving to the right in the plot, the scatter in line fluxes becomes greater. The Spearman coefficient r_s is 0.78, and the Pearson coefficient yields a probability of $1.6 \cdot 10^{-13}$ that the data are not correlated. A summary of results of the relevant statistical tests is given in Table 5.2.

The normalised fluxes in figure 5.9 are fit with a linear response function, which is included in red in the plot. The bottom panel shows the associated residuals, as well as the χ^2_{red}. The sequence test statistic, S, for this fit is 31 corresponding to a p-value (p_s) of 0.1. Given the small sample size (N=64) this is a highly significant value. A two component fit to this data-set yielded a $\chi^2_{red} = 0.95$, and a $p_s = 0.47$. The χ^2_{red} value indicates that this function slightly overfits the data, and p_s also signals that the linear fit is preferred. These test results are all robust, when checked with the bootstrap MC simulation.

The next approach is normalisation to the minimum continuum state (figure 5.9). In this normalisation the scatter in the data is also prominently visible. The distribution of the data shows a pattern different from simple linear correspondence. There is a sharp initial rise, followed by a possible flattening of the responsivity. Note, however, that the scatter for $f_c \gtrsim 6$ is particularly large. This is reflected in a lower Spearman correlation coefficient, 0.67. The p-value for the Pearson r, $\sim 10^{-5}$, does indicate that the data are very likely correlated.

This tentative pattern in the data can be tested using the two responsivity functions. The results of both fits are included in figure 5.9. The residuals are shown in the bottom two panels. The reduced χ^2 value is lower for the two component fit, however the fact that the value is below one indicates this function is likely overfitting the data. The results of the sequence

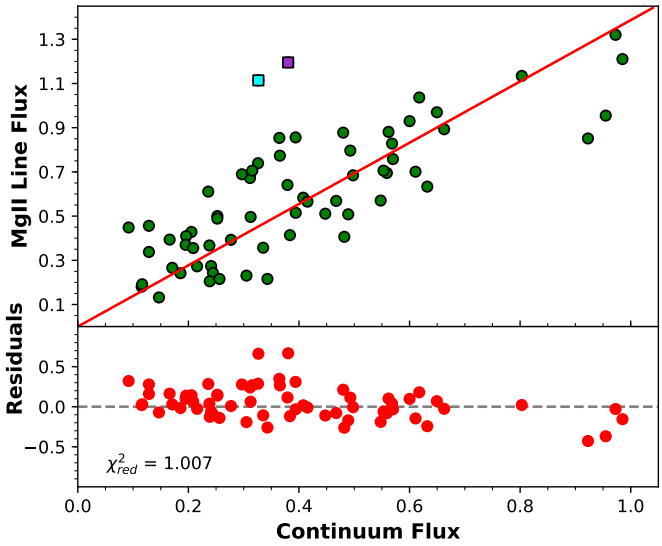

Figure 5.8: *top*: Fluxes in the supervariable sample, normalised to the epoch of *maximum* continuum. There is a correlation between large continuum changes and large line flux changes. The plot shows the line flux plotted against the continuum as well as the fitted linear responsivity function. Two outlying data points have been marked with squares: J154341 on MJD 57818 (cyan) and J123228 on MJD 57845 (purple). These spectra will be discussed at the end of Section 5.3.1. *bottom*: The residuals and χ^2_{red} for the response function.

test (listed in Table 5.2) indicate that neither fit describes the data well. $\Delta\chi^2_f = 38.9$, which indicates a very strong preference for the two component function. As indicated by χ^2_{red} this is likely the result of overfitting, however.

For normalisation to the low continuum state it is difficult to make a strong conclusion about the shape of the responsivity function. It is quite certain the data are correlated, and line fluxes can make significant changes if the continuum changes also, however the scatter in the data make the shape of the relation less clear. At large relative changes in continuum flux, the line flux can show a strong response, but it does not do so in all cases. For smaller fractional changes, of factors 1–4, the correlation is more clear.

Table 5.2: Correlation coefficients and the fitting statistics for the two normalisations used for the supervariable sample. The top row lists the Spearman (r_s) and Pearson (r) correlation coefficients. The bottom rows list the χ^2_{red} and the p-value associated with the sequence test statistic S, for the one and two component linear fits.

		Norm: max	Norm: min
r_s		0.78	0.67
r		0.76	0.46
1C:	χ^2_{red}	1.01	1.39
	p_s	0.10	0.94
2C:	χ^2_{red}	0.92	0.77
	p_s	0.47	0.97

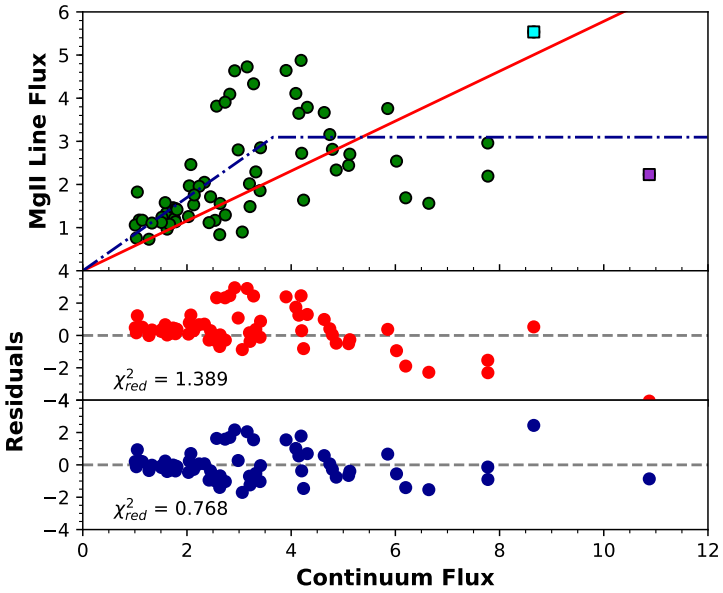

Figure 5.9: *top*: Normalised to the epoch of *minimum* continuum level, the data for the supervariable AGN sample show a significant scatter. This is particularly clear for the largest fractional flux changes. The panel also shows the two fitted responsivity functions. Two outliers are marked with squares: J022556 on MJD (cyan) and J002311 on MJD 55480 (purple). These objects are discussed in more detail at the end of Section 5.3.1. *bottom* The residuals from the two fitted functions as well as the χ^2_{red} for the fits. The two component fit (lower) results in a smaller reduced χ^2 value. As $\chi^2_{red} < 1$, this could be a result over overfitting.

The Responsivity Measure

A different method to investigate the variability in the sample is the responsivity measure α_{rm}. α_{rm} indicates the difference to a 1:1 response in terms of the normalised fluxes in figure 5.9. The distribution of α_{rm} is shown in figure 5.10. The centre of the histogram is slightly to the negative of $\alpha_{rm} = 0$. This corresponds to objects for which the fractional line flux change is slightly below the fractional change of the continuum.

The distribution of α_{rm} is evidently asymmetric. The tail toward negative values, which correspond to low line responsivities, is decidedly longer than towards positive α_{rm}. This means that large continuum changes accompanied by relatively small changes in the line flux are more common than large changes in line flux while the continuum moves less. There are a number of spectra on the positive side of the distribution, representing strong responses in the MgII line. For these objects that show a greater than 1:1 response, the extremes in α_{rm} are not as great as for the low-responsivity cases. This implies that the difference between fractional flux changes in continuum and line flux for objects with $\alpha_{rm} > 0$ is overall smaller than for the less responsive objects. It should be noted, however, that if the average response function is shallower than a 1:1 response (as is indicated by the slope of the fits in figure 5.10), the objects with $\alpha_{rm} > 0$ are truly exceptionally responsive.

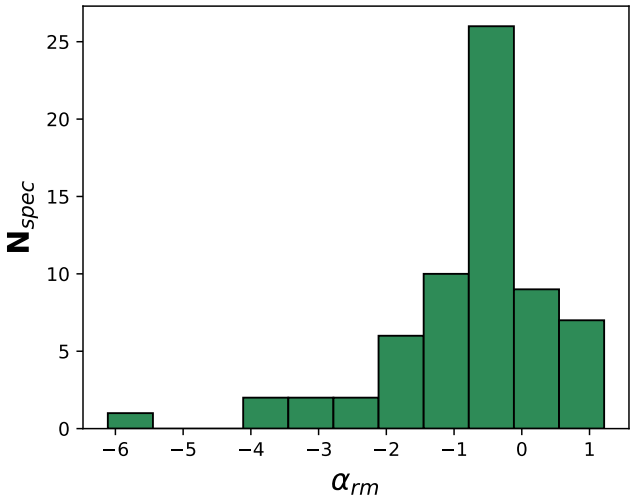

Figure 5.10: The distribution of the responsivity measure α_{rm} in the supervariable sample. The distribution is concentrated slightly below $\alpha_{rm} = 0$. The zero point of α_{rm} indicates a 1:1 response between line and continuum flux. The peak in the distribution consists of spectra that exhibit a line change slightly smaller than the continuum. The distribution is also clearly asymmetric with a longer tail extending into the negative values. This tail corresponds to objects showing a relatively small response in the MgII line.

Interesting Outliers

The responsivity functions and α_{rm} were used to define the response of the supervariable sample as a whole. Compared to these measures there are some individual spectra that stand out. The first of these are identified in figure 5.8, using the normalisation to the epoch of maximum continuum. The two remarkable data points are found at the top left of the plot. They represent a large decrease of the continuum associated with an increase in the line flux. For these two spectra, associated with J123228 and J154341, the line flux rose as the continuum dropped. Visual inspection of the spectra (see Appendix A) shows that neither of the objects lose their broad Hβ flux. This could indicate that the response of the BLR to the drop in continuum has not occurred yet. The elapsed rest frame time in both cases is close to two decades, however. An alternative hypothesis is that the observed line fluxes are in response to a flare in the continuum that occurred in the intervening years. Interestingly, the increasing line flux in J154341 seems coupled to a narrowing of the line, indicating a change in the physical conditions in the line forming region.

The clearest outlier with respect to the other normalisation (figure 5.9; marked in purple), shows a continuum change of a factor ∼10 coupled to a line flux change of a factor ∼2. The object associated with this spectrum is J002311. The spectra for this object are shown in panel *c* of figure 5.2. The spectrum marked in figure 5.9 was taken on MJD 55480. The high state continuum was associated with a strong broad Hβ line, which disappears in the lower state spectra. The cadence of observations for J002311 allows for a more detailed view of the evolution. The object is varying rapidly: it doubles its continuum flux on a restframe timescale of 14 years, and drops it by a factor 10 in the following decade. It is plausible the observation was made before the line had had enough time to respond in full to the continuum changes.

Another remarkable spectrum is marked in cyan in figure 5.9. This epoch shows a line flux

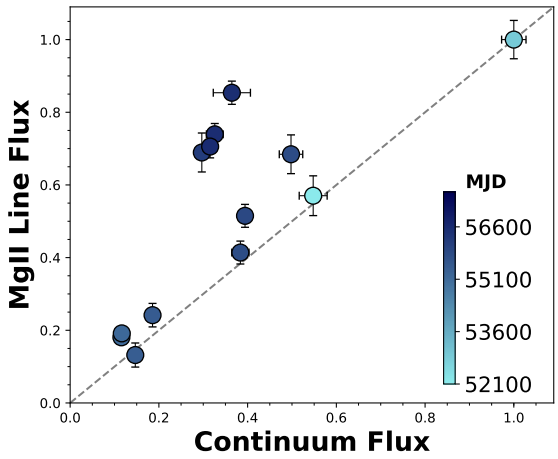

Figure 5.11: The changing responsivity in the MgII line flux in J022556. The high cadence of observations for this object allows us to track the line flux as the continuum falls and rises over the course of ∼8 years in the QSO restframe (see figure 1.15). The epochs of the spectra are indicated with the colour, increasing chronologically from light to dark. This plot is based on the normalisation of the fluxes to the epoch of maximum continuum. A 1:1 response is indicated with the dashed grey line. The initial increase in line flux is matched approximately 1:1 by the MgII line. Following a collapse in line and continuum, however, the gradient of the line responsivity is considerably steeper as the continuum recovers.

change greater than a factor 5. The spectrum belongs to J022556, for which we have a high number of spectra available because the object was part of extra deep BOSS plates[3]. This QSO is highly variable in MgII, as can be seen in figure 1.15. The higher cadence of observations allows us to see there is evidence of varying responsivity for this object.

Figure 5.11 shows the line and continuum fluxes for J022556 using the normalisation to the maximum continuum. The spectra cover ∼8 years in the QSO restframe. The shading of the markers indicates the progression of time. The first epoch available (SDSS, MJD 52200) is represented by the light blue marker in the centre of the plot. The first rise in the continuum is to the epoch of maximum continuum in the top right of the plot. The gradient of this response is approximately 1:1 to the marker in the top right. In the next available spectrum the continuum has collapsed, and the line has almost disappeared as well (bottom left corner). When the continuum rises again, the gradient is considerably steeper.

The change in responsivity between periods is also observed in Mrk 110 (Section 4.3). As these changes occur on a timescale similar to τ_{dyn} (see Table 1.4) it is possible that they reflect a physical change in the BLR. The epoch-dependent responsivity visible in both J002311 and J022556 indicates that the scatter around the responsivity functions could be the result of sampling the varying objects at different stages during the BLR response to the continuum.

5.3.2 Changes in the Line Profile

The measure used to quantify the MgII profile is the width (σ) of the broadest Gaussian fit to the line. The widths are defined in the QSO rest frame. Table 5.3 lists the change in line width for the spectral pair with the largest change in continuum ($\Delta\sigma_{\rm MgII}$) for all targets in the supervariable sample. The distribution of the absolute value of $\Delta\sigma_{\rm MgII}$ is shown in the left

[3]http://www.sdss.org/dr12/spectro/special_plates/

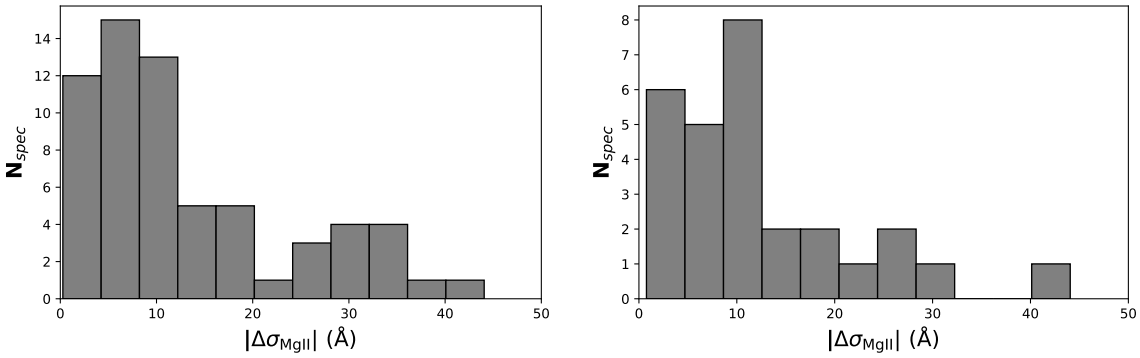

Figure 5.12: *left* The distribution of $|\Delta\sigma_{\rm MgII}|$ in the supervariable sample shows there is a broad range of line width changes in the sample. The long tail towards larger $\Delta\sigma$ is possibly a result of the fitting procedure, as spectra for the same object can be fit with one or two broad components. *right* The distribution of $\Delta\sigma_{\rm MgII}$ for sequential pairs of spectra where each of the spectra was fit with a single Gaussian. This distribution shows a similar spread as seen in the left panel.

panel of figure 5.12. The distribution shows that most objects have relatively small changes in line width (< 10Å). However, there is also an extended tail towards larger changes. The large spread in the sample is another indication of the broad range of MgII variability among extremely variable quasars.

The fitting method could have been of influence on the distribution of $\Delta\sigma_{\rm MgII}$, as the pipeline uses either one or two Gaussians, based on a goodness-of-fit parameter (see Chapter 3). To test the influence of the fitting procedure, the right plot in figure 5.12 shows the histogram of $|\Delta\sigma_{\rm MgII}|$ for all pairs of spectra where both spectra have been fitted with a single Gaussian. The distribution of this subset shows the same range and overall shape as the distribution in the left panel. It therefore appears that the impact of the fitting procedure is small enough to include all fitted spectra in the following analysis.

The largest values of $|\Delta\sigma_{\rm MgII}|$ shown in figure 5.12 are $\sim$40Å. A change of this magnitude could correspond to a significant change in the physical conditions in the line forming region. Under the assumption of Keplerian rotation of the BLR gas, a change of 40Å corresponds to a change in rotational speed (along our line of sight) of approximately 4,200 km/s. For MgII the Keplerian speeds deduced from the FWHM are in the order $10^{3.6}$ km/s [Shen et al., 2011]. The extremes in the observed changes in line width could therefore signal large transitions.

An interesting question is whether there is a correlation between $\sigma_{\rm MgII}$ and other parameters, such as line or continuum flux. Comparing $|\Delta\sigma_{\rm MgII}|$ with the line and continuum flux did not yield any indication of a correlation, as the data are dominated by scatter. When considering the fractional changes in the line width from epoch to epoch, however, a tentative correlation is visible. Figure 5.13 shows the change in line width plotted against the change in line flux, where both values have been normalised to the previous epoch. The plot also includes the results of a linear regression of $\Delta\sigma_{\rm MgII}$ on $\Delta f_{\rm MgII}$. The slope of the line is 0.07. Although the scatter in the data is strong, it is possible that there is a positive correlation between the magnitude *and* direction of $\Delta\sigma_{\rm MgII}$ on $\Delta f_{\rm MgII}$. Comparing $\Delta\sigma_{\rm MgII}$ with the change in continuum flux show a similar scatter and a weaker correlation between the parameters.

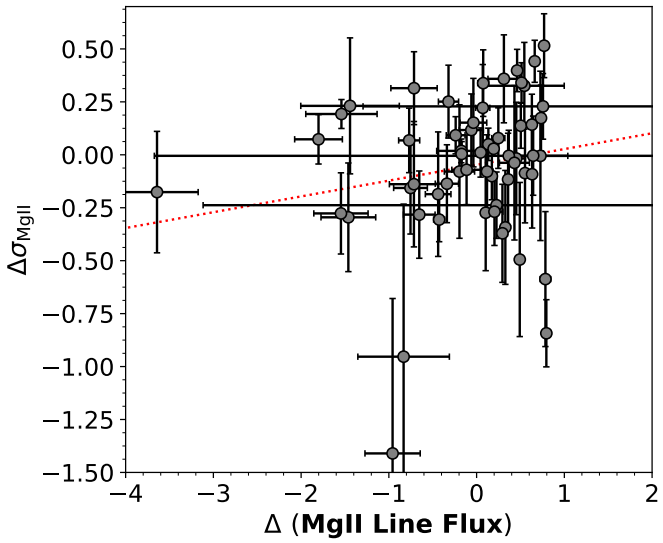

Figure 5.13: The change in line width ($\Delta\sigma_{\mathrm{MgII}}$) plotted against the change in line flux. Both parameters have been normalised to the preceding epoch and therefore represent a fractional change with respect to the older spectrum. There is significant scatter in the data-set. The result of a linear regression of $\Delta\sigma_{\mathrm{MgII}}$ on Δf_{MgII} is plotted in red.

Table 5.3: (Next Page) Overview of the results of the spectral fitting for the supervariable sample, listed by SDSS name in column 1. Column 2 indicates whether MgII traces the continuum (✓), stays stable (✗), or the continuum is stable (-). Column 3 lists whether the object was identified as a CLQ in MCL19. Column 4 is the time span between the spectral epochs, in the AGN restframe. Columns 5–8 list the changes in line and continuum luminosity, columns 9–10 are the fractional changes in line flux, and columns 11–12 the change in line width. For objects with more than two spectra available the values in columns 5–12 are between the two spectra with the largest $\Delta\mathrm{L}_{2798}$.

	SDSS name	MgII Var	CLQ	max $\Delta t_{\rm spec}$ (RF days)	ΔL_{2798} (10^{42} erg s^{-1})	Error on ΔL_{2798} (10^{42} erg s^{-1})	$\Delta L_{\rm MgII}$ (10^{42} erg s^{-1})	Error on $\Delta L_{\rm MgII}$ (10^{42} erg s^{-1})	Δf_{2798}	$\Delta f_{\rm MgII}$	$\Delta\sigma$ (Å)	Error on $\Delta\sigma$ (Å)
1	001113.46−110023.5	✗	✓	3906	39.5	3.7	0.9	0.2	0.69	0.5	4.2	3.6
2	001206.25−094536.3	✗	✓	3484	135.6	21.9	2.2	1.8	0.87	0.54	17.1	11.1
3	002311.06+003517.5	✓	✓	4378	319.9	10.8	4.9	0.4	0.91	0.55	−4.9	13.2
4	002450.50+003447.7	✗	✗	3795	110.4	9.2	1.3	0.2	0.69	0.33	−10.7	6.7
5	002714.21+001203.7	-	✗	4086	−17.2	53.6	−0.5	0.8	−0.08	−0.17	0.5	1.4
6	010529.61−001104.0	✓	✗	3353	29.4	15.0	0.4	0.4	0.52	0.12	−3.6	6.8
7	013458.36−091435.4	✗	✓	4041	168.0	7.6	0.6	0.2	0.59	0.1	−8.4	7.1
8	022556.07+003026.7	✓	✓	2920	68.9	2.3	2.0	0.1	0.88	0.82	−9.9	11.3
9	022652.24−003916.5	✓	✓	2206	30.0	2.5	0.9	0.3	0.75	0.5	3.0	16.6
10	034144.72−002854.3	✓	✗	3419	−100.8	13.9	−4.4	0.4	−1.98	−1.8	5.8	11.5
11	034330.48−073703.1	✗	✗	2404	97.0	10.7	2.3	0.3	0.71	0.46	20.1	5.6
12	074502.90+374947.0	✗	✗	3895	66.2	3.5	1.5	0.2	0.69	0.77	21.3	8.2
13	074719.65+215245.9	✗	✗	3674	39.7	4.2	1.5	0.2	0.62	0.36	−4.9	8.5
14	075228.65+405931.7	✗	✗	4349	48.9	4.9	1.2	0.1	0.34	0.19	1.1	1.2
15	081916.15+345050.3	✗	✗	767	19.7	2.1	0.4	0.1	0.43	0.17	7.0	5.4
16	090104.75+345524.2	✓	✓	2855	140.4	48.0	4.0	1.7	0.78	0.73	−0.3	21.2
17	092223.17+444629.0	✓	✗	3322	74.5	419.0	4.3	24.0	0.76	0.76	11.5	8.6
18	094132.89+000731.1	✗	✗	3911	28.2	325.2	1.2	13.2	0.37	0.37	−0.2	4.8
19	102016.04+014231.7	✗	✗	3746	−54.2	10.9	−1.6	0.4	−0.79	−0.44	−5.6	8.0
20	111348.64+494522.4	✗	✗	3071	88.3	10.0	1.1	0.7	0.44	0.12	−2.8	5.6
21	123228.08+141558.7	✗	✗	3084	53.1	5.2	−0.4	0.3	0.62	−0.2	−2.5	9.0
22	132815.50+223823.8	✓	✗	2149	78.6	5.8	2.1	0.2	0.76	0.63	−2.8	7.7
23	145519.88+364800.4	-	✗	3043	3.9	19.2	−1.0	0.4	0.03	−0.32	9.8	7.8
24	152044.63+394930.3	-	✗	3581	23.9	10.4	−0.1	0.3	0.38	−0.04	4.7	7.0
25	153734.06+461358.9	✓	✓	3704	92.2	17.6	3.3	0.6	0.76	0.79	−24.2	3.2
26	153912.76+524540.2	✓	✓	3896	43.1	8.9	1.2	0.3	0.66	0.78	−10.7	4.8
27	154341.64+385319.3	✗	✗	3241	109.3	14.6	−0.4	1.1	0.67	−0.11	−3.4	7.4
28	160226.01+323019.1	✗	✗	3350	83.6	8.8	0.2	0.3	0.4	0.07	7.0	6.9
29	162415.02+455130.0	✓	✓	3479	93.9	5.7	2.5	0.1	0.83	0.73	6.4	5.9
30	163031.47+410145.8	✓	✗	3603	88.2	5.9	2.9	0.3	0.51	0.49	−17.5	10.5
31	164053.05+451033.7	✗	✗	3766	47.7	197.6	0.4	11.3	0.63	0.23	−7.2	4.3
32	212436.64−065722.1	✗	✗	3734	76.7	6.5	0.6	0.3	0.51	0.2	−8.1	4.2
33	214613.31+000930.8	✓	✓	1547	−43.5	4.2	−1.8	0.3	−4.1	−1.44	13.5	24.2
34	223133.89+003312.7	✗	✓	3917	41.4	4.3	0.8	0.2	0.45	0.29	−12.3	6.1
35	223500.50−004940.7	✗	✗	3559	−86.4	36.7	−1.9	1.3	−1.45	−0.71	−4.5	9.0
36	224017.28−011442.8	✗	✗	3396	−62.2	6.1	−1.1	0.2	−1.23	−0.96	−20.1	4.9
37	224829.47+144418.0	✓	✓	3634	173.2	4.4	4.3	0.3	0.87	0.66	25.6	7.7
38	225240.37+010958.7	✓	✓	3529	98.7	5.5	4.5	0.3	0.8	0.63	5.7	7.5
39	230427.86−000803.2	✓	✗	3632	−63.3	16.1	−2.3	0.4	−1.07	−1.46	−8.0	6.4
40	231552.95+011406.1	✗	✗	3643	−17.9	14.0	−0.1	0.3	−0.51	−0.12	−5.3	9.1
41	231742.68+011425.2	✗	✓	3654	40.6	11.9	0.8	0.5	0.53	0.43	−1.9	17.7
42	233317.38−002303.4	✓	✓	3821	66.8	2.1	1.8	0.1	0.79	0.64	−0.2	7.9
43	234623.42+010918.1	✓	✗	3635	−71.5	11.7	−5.6	0.2	−2.9	−3.64	−7.0	9.7

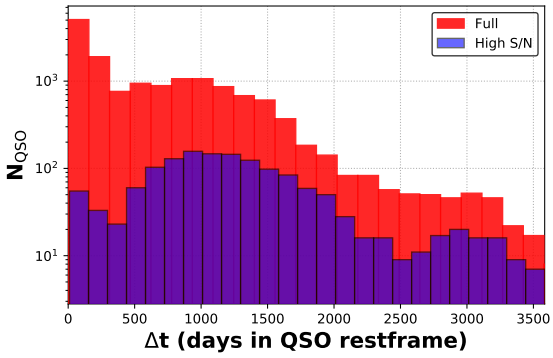

Figure 5.14: Histogram of the elapsed times in the QSO rest-frame for the full population sample (red). The elapsed times are defined between the two spectral epochs used for each object. The Δt distribution for the high S/N subsample ($blue$) is very similar to its parent sample.

5.4. Results for the Full Population Sample

The results for the full population sample are analysed with the same methods as the super-variable sample. As can be seen in figure 5.14 the full population sample covers a broad range in elapsed times between spectral epochs in the QSO restframe. The figure includes the Δt distributions for both the full sample and the high Signal to Noise subsample. The latter contains the objects that have a pair of spectra with S/N>20 (Section 2.3). The distribution in Δt for the subsample is very similar to that of the full sample. This makes the high S/N data-set useful as a check on any results for the full population: a pattern in the full data-set is more likely to be spurious if it cannot also be detected in the high S/N sample.

5.4.1 Flux Normalisations

Figure 5.15 shows the normalisation of the fit results to the epoch of maximum continuum. The sample is plotted as a 2D histogram where the colour indicates the number of counts in each bin. To emphasise the shape of the distribution, contours have been included in the plot, at count levels of 0, 25, 50, 75, 90, and 95% of the maximum number of counts per bin in the sample. There are two important things to note about the distribution of the data. The first is that is is quite strongly concentrated in the region where normalised line and continuum fluxes are ∼1. These are spectral pairs where the overall flux change has been small, likely relating to quasars that were not varying much over the period of observation. Clear outliers in the plot (those in the top left, bottom left, and bottom right corners) were checked by eye to ensure that they represent physical changes in the spectra. Although a small fraction of the spectral pairs showed poor fits as a results of data quality, the large majority did indeed show a clear change in the continuum and/or MgII line.

The second point to note in Figure 5.15 is the evident slope in the data. There is a linear correspondence between the continuum and line fluxes, across the full range of the continuum. This assessment by eye can again be checked using the statistical tests outlined in Section 5.2.2. In order for the tests to be applied successfully, the normalised results are filtered for any erroneous values, removing objects were the normalised $f_{\rm MgII} > 2$ or $f_{2798} < 0.01$ ($\sim 2.7\%$ of the sample). This limit on $f_{\rm MgII}$ is chosen based on the extreme variability seen in the

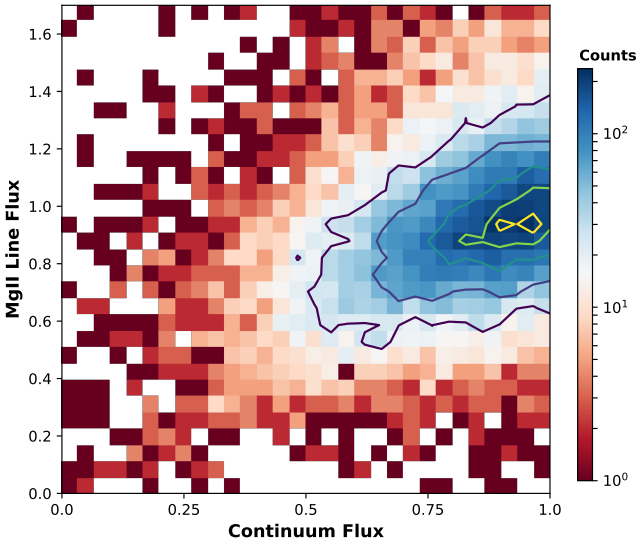

Figure 5.15: The MgII line and 2800Å continuum fluxes for the full population sample, normalised to the epoch of *highest continuum*. The data show a clear correlation. Most objects in the sample are concentrated on the right side of the plot, exhibiting only small changes in both line and continuum. The colours in this 2D histogram correspond to the number of objects in the respective histogram bin. The contours are placed at 10, 25, 50, 75, and 90% of the maximum count number for the sample.

supervariable sample, indicating a reasonable maximum for the MgII responsivity (compare Figure 5.8). The lower limit on f_{2798} excludes a number of very low flux objects for which the line flux showed an unusually large scatter. Following this correction, the Spearman ranked correlation coefficient for the data is 0.32, and Pearson's coefficient 0.30. The p-value associated with the latter is ∼0. Both values indicate a significant positive correlation. The results of the statistical tests are listed in Table 5.4.

The next step is to quantify the responsivity using the two fitting functions. The reduced χ^2 for the two fits indicate a preference for the two component function and $\Delta\chi^2$ gives a p-value of approximately zero, thereby rejecting the one-fit function. The sequence test rejects both fits. The results for the full population sample can be checked with the high S/N subset. The higher quality of these spectra reduces the noise introduced by fitting errors. The data for the high S/N sample are shown in the left plot in Figure 5.17. The high quality spectra show the same behaviour as the full population. As can be seen from the test results listed in Table 5.4, the correlation between line and continuum flux is stronger for this subsample. The preference for the two-component fit is not as clear for this sample, however. The χ^2_{red} shows slight overfitting, and the results of the sequence test indicate a preference for the one-component fit.

The normalisation to the minimum continuum state is shown in Figure 5.16. A close-up of the region of highest density for this distribution is shown in the left panel of the figure. For this subset the correlation between the 2800Å continuum and $f_{\rm MgII}$ is clearly visible, as it was for the other normalisation. The centre of the distribution appears to show a response of the line to the continuum, even at small changes, however the gradient of the responsivity is quite

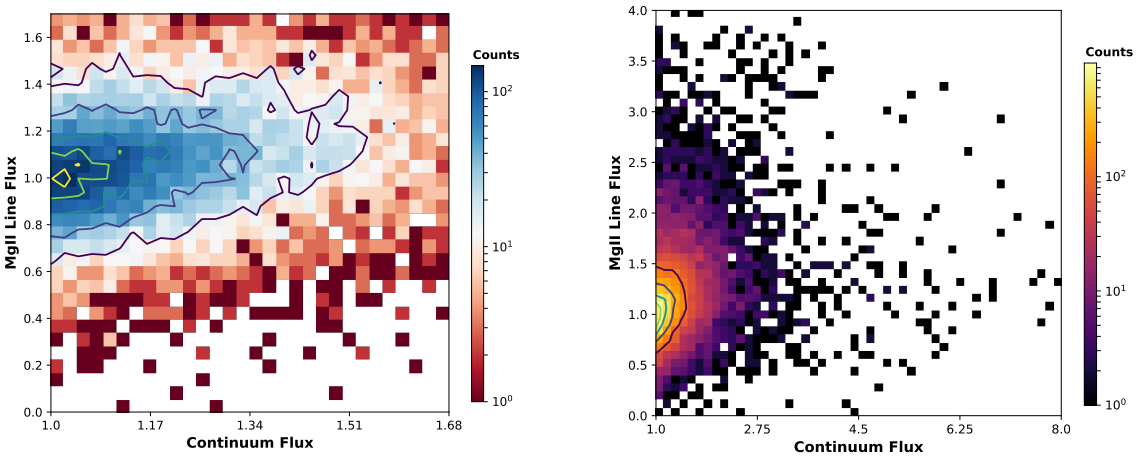

Figure 5.16: *left*: The high density centre of the distribution in the $f_{2800}/f_{\mathrm{MgII}}$ parameter space of the full population sample, when normalised to the epoch of *lowest continuum*. This again shows a linear correlation. The layout of this figure is the same as that of Figure 5.16. *right*: A wider view of the same data used for the left plot shows that there is considerable scatter when it comes to large flux changes. The colour representation of the counts used a logarithmically normalised scale, to show the distribution of the outliers.

shallow. For this normalisation $r_s = 0.30$ and $r = 0.32$. Both coefficients indicate a positive correlation. As for the previous normalisation, the data were filtered with conservative limits on the results, requiring: $0 < f_{\mathrm{MgII}} < 15$ and $1 < f_{2800} < 20$. Evidence of levelling off as was present in the supervariable sample (compare Figure 5.9), is not clear however. This is possibly due to the strong concentration of the distribution around objects with relatively small flux and continuum changes.

The possibility of a saturation effect can be better explored if we zoom out from the centre of the distribution, as seen in the left panel of Figure 5.16, and consider the full view in the plot in the right panel. In this plot there is considerable scatter in the data at larger flux changes, as was the case for the supervariable sample. A comparison of the two fitting functions can help discern changes in responsivity with flux level. The results of the fitting are $\chi^2_{red} = 1.28$ for the one component fit, and $\chi^2_{red} = 0.93$. The overfitting of the two parameter function results in an unreliable $\Delta\chi^2$ measure. The sequence test shows a stronger result for the two component fit, although the p_s for the line (0.98) suggests this is a poor fit as well.

The evidence for any saturation effect in the line responsivity is tentative: the strong scatter in the data makes the fitting process of a simple empirical function susceptible to the influence of outliers. A firm conclusion is that the MgII line and UV continuum flux are clearly correlated, and appear to scale linearly. This is an ensemble effect: the large scatter suggests that the individual objects can show a different correspondence between line and continuum. The difference from object to object will be a combination of intrinsic differences between the objects, and an artefact of the cadence of observations. The latter effect is caused by the fact that we only have two snapshots of the full line response, which means we will observe the line in different stages of its response for every target.

The conclusions for the full population sample hold for the high S/N subsample. The plots for the high S/N sample are included in Figure 5.17 and test statistics are included in Table 5.4

Table 5.4: The test results for the full population sample and for the subset of high quality spectral pairs with Signal-to-Noise>20. The included metrics (Section 5.2.2) are Spearman's coefficient (r_S) and Pearson's coefficient (r). For the one and two component fits, '1C' and '2C' respectively, the table includes χ^2_{red} and the p-value from the sequence test (p_s). The sequence test results are calculated using a bootstrap MC simulation (N=10^3).

		Norm: max		Norm: min	
		Full Sample	High S/N	Full Sample	High S/N
r_s		0.32	0.38	0.30	0.38
r		0.30	0.39	0.32	0.19
1C:	χ^2_{red}	1.15	1.17	1.28	1.04
	p_s	∼1	0.63	∼1	∼1
2C:	χ^2_{red}	1.02	0.98	0.93	0.75
	p_s	∼1	0.37	0.98	0.59

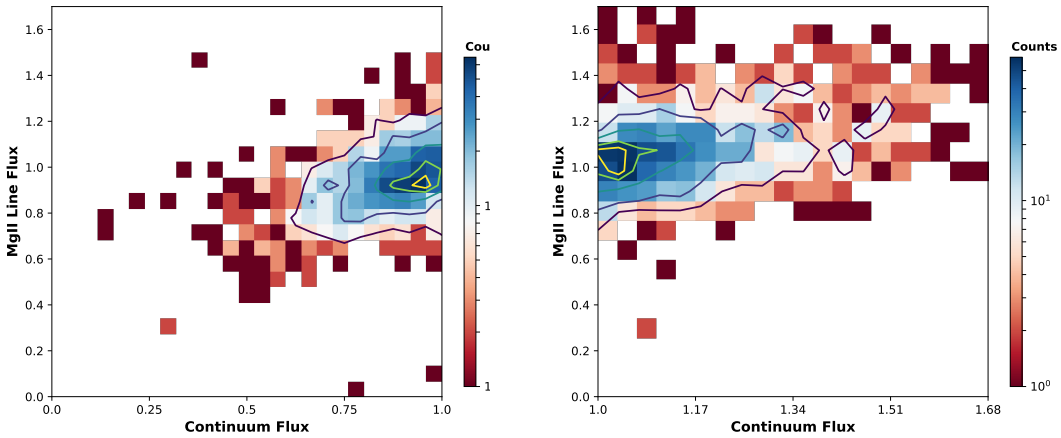

Figure 5.17: The high S/N subsample shows the same distribution as the full population sample for the two normalisations. *left*: The high S/N sample normalised to the epoch of maximum continuum flux. *right*: The same sample normalised to the epoch of minimum continuum flux. These plots can be compared with Figure 5.15 and Figure 5.16 respectively.

for comparison. For both the high and low state normalisations the results are consistent between the full sample and the high quality subset. This indicates that the behaviour seen in the SDSS data is not an artefact of fitting many lower quality spectra.

Beyond the responsivity visible in the normalised flux plots, the response of the line can be quantified using the responsivity measure. The distribution of α_{rm} among the full quasar population is shown in Figure 5.18. The distribution is centred around $\alpha_{rm} = 0$. This value is associated with a 1:1 relation between line and continuum. The large wings are not fully symmetric. There are more objects in the bins associated with negative responsivity measures. In other words: there are more objects where the relative line flux change is smaller than the change in the 2800Å continuum.

The α_{rm} distribution shows the same pattern observed in the normalisation plots. Most objects show only limited variability, resulting in a responsivity measure close to zero. There are strongly variable objects in the full population sample, whose line and continuum changes

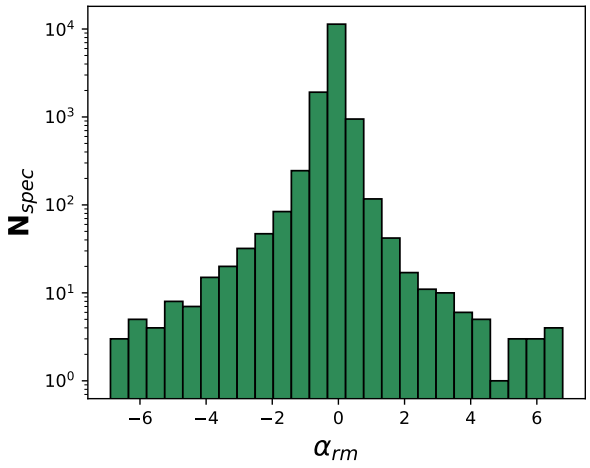

Figure 5.18: The distribution of the responsivity measure among the full quasar population is skewed to the negative values of α_{rm}. This corresponds to a dominance of objects with limited MgII responsivity in the sample. The strong concentration around $\alpha_{rm} = 0$ is due to a large number of objects with very small variations in both line and continuum, resulting in an approximately 1:1 correspondence in normalised fluxes.

appear to differ strongly. These strong changes could be due to several contributing factors. The first is the cadence of observations,as we could catch the movement of one component, while the other has not had time to respond. The second factor is uncertainties in both the observations and the fitting. These would produce spurious results. However, the high S/N sample does show a similar α_{rm} distribution. Finally, we could observe actual changes in the BLR: if enough time elapses we are observing emission from a BLR with new physical parameters. This is the effect this study is trying find.

5.4.2 Line Responsivity over Time

If the line responsivity changes over time, this should manifest itself as a dependency on Δt, the elapsed time between the spectral measurements for each pair. In contrast to the supervariable sample the full population sample is large enough to investigate the effect of Δt in more detail. The first test of the possible dependency is to divide the data-set into Δt bins and to calculate the normalised fluxes in the subsets as in the previous section. The results are shown in Figure 5.19. To emphasise the visualisation of the outliers, the normalisation to the epoch of minimum continuum is used. In Figure 5.19 the elapsed time and number of included spectral pairs for each subplot is shown in the bottom left corner; the time is in units of days and is defined in the QSO restframe.

To ensure a good sample size in each Δt bin, the bin size increases for longer elapsed times. The time bins represent re-observations of the object within one year, between one and two years, between two and three-and-a-half years, and three-and-a-half up to 10 years respectively. The contours in Figure 5.19 are placed at 10, 25, 50, 75, and 90% of the maximum counts in a single bin. To compare the four plots, all count numbers have been normalised by dividing by the maximum per plot.

Two changes take place in the Δt bins in Figure 5.19: the shape of the contours changes and the gradients of the line responsivity appears to decrease. The first effect is visible as an

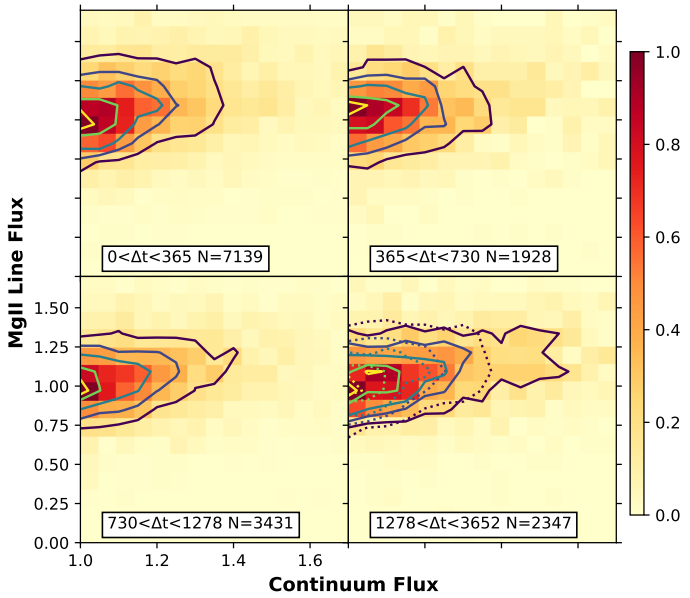

Figure 5.19: The full population sample, binned by Δt between observations, in days in the QSO restframe). The contours are set to 10, 25, 50, 75, and 90% of the maximum value. To observe any difference in response over time the contours from the shortest elapsed time bin (*top left*) are included in the panel for the longest elapsed time (*bottom right*). The maximum number of counts per bin in each panel has been normalised to one, to allow for comparison between the four subsets.

elongation of the contours as Δt increases. This implies that large changes in the continuum are more common for large Δt. Changes in flux that are very unlikely to occur within the first year become more likely as Δt increases. A longer waiting time means a greater chance of observing large change in UV continuum. This agrees with established results on quasar continuum variability (MacLeod et al. [2010]; Welsh et al. [2011]; see Section 1.3). The change in shape also implies that for greater Δt the distribution has a larger spread.

The second change visible in Figure 5.19 is in the slope of the linear correlation and can be seen in the plots as a gradual tilting of the contours. The contrast is most pronounced between the shortest and longest time differences: as a visual aid the contours from the top left plot have been included as dotted lines in the bottom right plot. Although the effect is subtle, the slope decreases over time. This effect can be quantified by a linear fit to the data. This is the same one-component fitting function used in the previous section. The fitted slopes and the errors are listed in Table 5.5. The results show a steady decline with Δt in the slope of the responsivity. For a larger elapsed time between observations the response of the line to continuum changes therefore appears to be smaller.

A different approach to investigating the effect of elapsed time on the line responsivity is illustrated in Figure 5.20. The method compares the distribution of the normalised change in line flux (Δf_{MgII}) for several Δt subsets. The top panel of Figure 5.20 shows the distribution of Δf_{MgII} against Δt. The first thing to note is that the full population sample is skewed toward objects with a relatively small Δt, as is also evident in Figure 5.14. The sections in Δt

Table 5.5: Slopes of the linear correlation between normalised $f_{\rm MgII}$ and f_{2800} for the Δt subsets shown in Figure 5.19. The slope shows a slight but steady evolution with Δt: the line responsivity decreases for longer time intervals between measurements. The error on the slopes is calculated from the covariance matrix produced by the `scipy` fitting routine. The error on the measurements was estimated based on the scatter, as described in Section 5.2.2. Δt is given in the QSO restframe.

RF Δt (days)	Slope	Uncertainty
$0 < \Delta t < 365$	0.746	0.006
$365 < \Delta t < 730$	0.745	0.011
$730 < \Delta t < 1278$	0.738	0.007
$1278 < \Delta t < 3652$	0.724	0.007

have been chosen to cover the full range of elapsed times and to include enough objects in each subsample to allow for meaningful statistical analysis. The Δt bins are listed in the bottom three panels and the associated sample sizes are included in Table 5.6.

If there is no pattern to the flux changes, we expect the data in each bin to follow a normal distribution. For each of the three subsets the distribution of $\Delta f_{\rm MgII}$ is therefore compared with a normal distribution using the Lilliefors test (Section 5.2.2). The bottom three panels of Figure 5.20 show the cumulative distributions of the three subsets, as well as the CDF of the normal distribution, for a visual comparison. The results of the test are quite clear, rejecting the hypothesis the data are drawn from the normal distribution. The Lilliefors test provides a p-value$< 10^{-10}$ for each Δt subset. Figure 5.21 shows the same comparison, made for the change in continuum flux, Δf_{2798}. The test results are the same for this data-set.

The distributions of $\Delta f_{\rm MgII}$ and Δf_{2800} in the Δt bins indicated in Figures 5.20 and 5.21 and their deviation from a normal distribution can also be quantified by calculating the sample moments. These are presented in Table 5.6. The moments of the distribution do change with time. The mean shifts to negative values as Δt increases. This is likely the result of a selection bias: the spectral pairs in the lowest Δt bin are more likely to have both observations made during the BOSS survey. For sources in the higher Δt bins the probability is higher that the first of the spectra is from SDSS I/II. Sources that were in a relatively bright state during SDSS I/II were more likely to be included in DR7Q and therefore included in the full population sample. This makes it more likely to see transitions to dimmer states.

The more interesting effects occur in the third and fourth moments of the distribution. The skewness indicates the distributions are skewed towards more positive values. This effect seems to decrease with Δt, however, particularly in the case of $\Delta f_{\rm MgII}$. A similar trend with Δt can be seen in the kurtosis, which can be considered to indicate the weight of the tails of a distribution. The two lower Δt bins have quite prominent tails. This is also evident from the scatter in the top panel of Figures 5.20 and 5.21. The moment is significantly smaller for the higher bins, and more so for the line flux than for the continuum flux. The reduced number of strong outliers could indicate a reduced responsivity for objects in this bin.

The derived moments for Δf_{2800} imply that the magnitude of changes in continuum flux increases with Δt. $|\Delta f_{2800}|$ and Δt are therefore correlated parameters, making it difficult to see which of the two parameters most strongly affects the observed changes in the MgII line

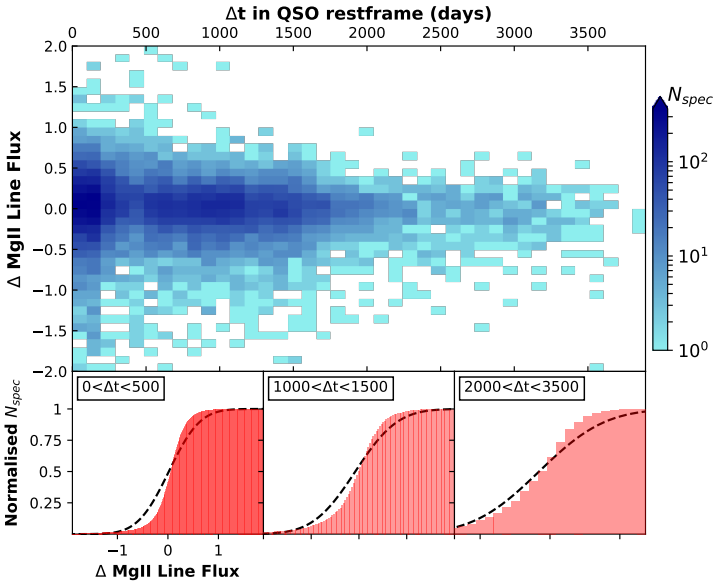

Figure 5.20: *top*: The normalised change in line fluxes (Δf_{MgII}) plotted against the elapsed time between observations, in days in the QSO rest frame. *bottom*: Testing for normalcy on three different Δt cuts in the data a significant deviation from a normal distribution. The three cumulative histograms represent the subsamples, marginalised over Δt. The normal CDF, calculated with the sample average and sample standard deviation, is plotted as the black dashed line, as a visual aid for the comparison.

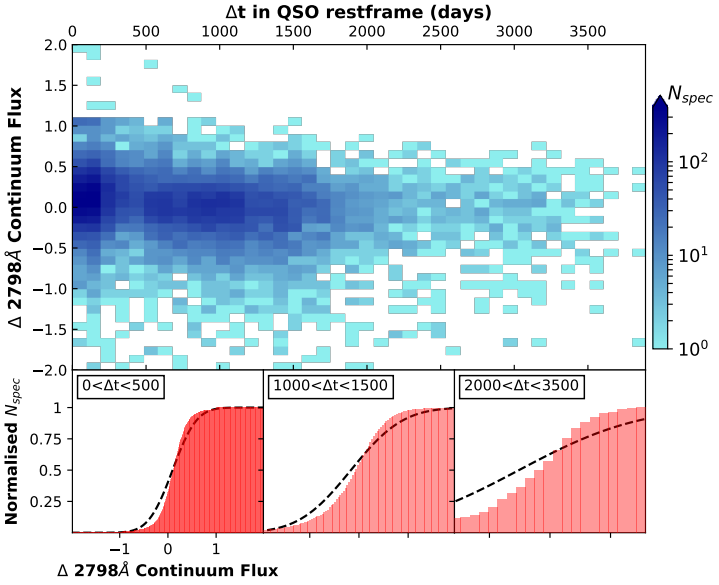

Figure 5.21: The normalised change in continuum fluxes (Δf_{2798}). The layout is the same as Figure 5.20. As was the case for Δf_{MgII} there is evidence of a significant deviation from a normal distribution for each of the Δt subsets.

flux. The changes in the shape of the distributions of $\Delta f_{\rm MgII}$ and Δf_{2800} can provide insight into the driving effect behind the line responsivity.

Table 5.6: The sample moments of the $\Delta f_{\rm MgII}$ and Δf_{2800} distributions for the Δt subsamples shown in Figures 5.20 and 5.21. Δt is in days in the rest frame. There is indication of a change in the sample distributions over time. For the calculation of the moments the distributions have been filtered requiring $|\Delta f| < 7$ (i.e. no flux changes greater than a factor 7 between epochs).

	$\Delta f_{\rm MgII}$		
	$0 < \Delta t < 500$	$1000 < \Delta t < 1500$	$2000 < \Delta t < 3500$
N	6282	2472	502
μ	0.02	−0.04	−0.08
σ	0.48	0.35	0.37
skewness	−2.71	−3.16	0.04
kurtosis	41.9	23.9	12.7
	Δf_{2800}		
	$0 < \Delta t < 500$	$1000 < \Delta t < 1500$	$2000 < \Delta t < 3500$
N	6273	2475	499
μ	0.10	−0.08	−0.26
σ	0.39	0.42	0.78
skewness	−4.13	−3.54	−3.35
kurtosis	60.4	32.0	17.2

5.4.3 The MgII Line Profile

As for the supervariable sample we can consider changes to the MgII line profile, characterised by the line width. A comparison of $\sigma_{\rm MgII}$ with the fitted line and continuum luminosities is shown in Figure 5.22. For the bulk of the spectra the line width appears unrelated to either the line or the continuum luminosity. This would be in agreement with results from Shen et al. [2011], who find no correlation between the FWHM of MgII and the 3000Å luminosity.

At continuum luminosities $\lambda L_{2800} < 10^{45}$ there does appear to be a correlation between the parameters. Interestingly this correlation of the line width with both the continuum and the line luminosity is positive. This is in contradiction with the expectation based on BLR breathing. For lower line luminosities the measurement of the width becomes more uncertain, therefore this correlation is tentative. However, it could be an indication that the MgII line width is not purely set by the gravitational potential. Other effects such as turbulence could be of significance as well.

For each object we can define the change in linewidth ($\Delta\sigma_{\rm MgII}$) between spectra. An overview of this parameter in the full population sample is shown in Figure 5.23. The distribution is strongly peaked around $\Delta\sigma_{\rm MgII} = 0$, with a slight asymmetry towards decreasing line widths. Large changes in σ are possible, but most objects exhibit only limited variability. This is likely the same effect as the observed concentration of flux changes around small values: most quasars in the sample have changed only slightly between epochs.

An interesting question is whether the change in line width is correlated with a change in line or continuum flux. This possibility is explored in Figure 5.24. The plot shows the change in line width plotted against the change in MgII flux, where both quantities have been normalised by dividing by the value from the first epoch of the pair. The two parameters therefore

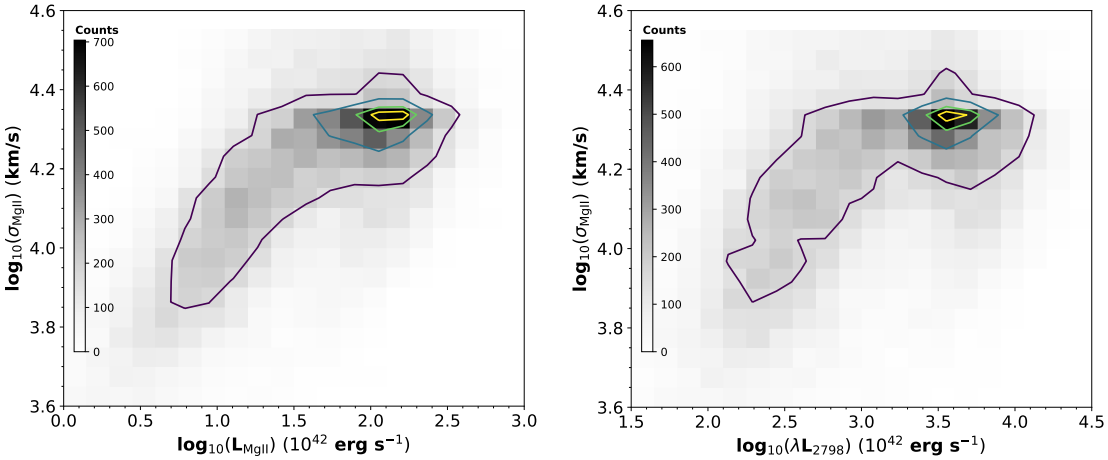

Figure 5.22: *left*: The line width (σ_{MgII}) plotted against the line luminosity. *right*: σ_{MgII} compared to the continuum luminosity. Contours in the two plots mark 25, 50, 75, and 90% of the maximum number of counts. For both parameters a correlation is possibly present for lower luminosities, however most objects do not show such a correlation. A lack of correlation between line width and continuum luminosity would be in agreement with the findings in Shen et al. [2011].

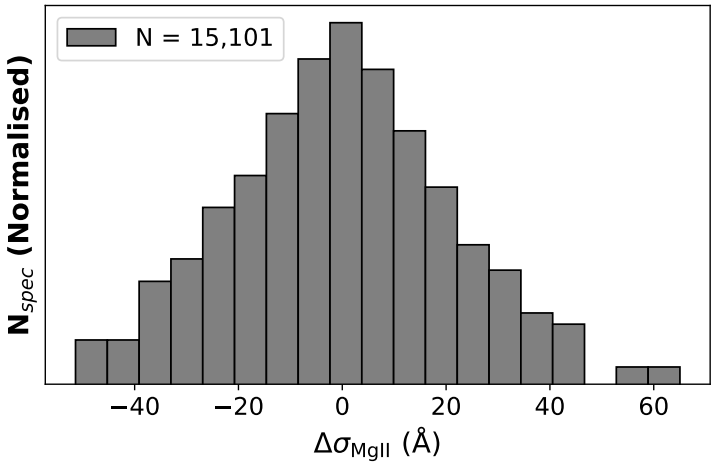

Figure 5.23: The distribution of $\Delta\sigma_{\mathrm{MgII}}$ for the full population sample (compare with the supervariable sample Figure 5.12, *right*). The distribution is strongly centered around objects with no observable change in line width. Note that the y-axis is logarithmic.

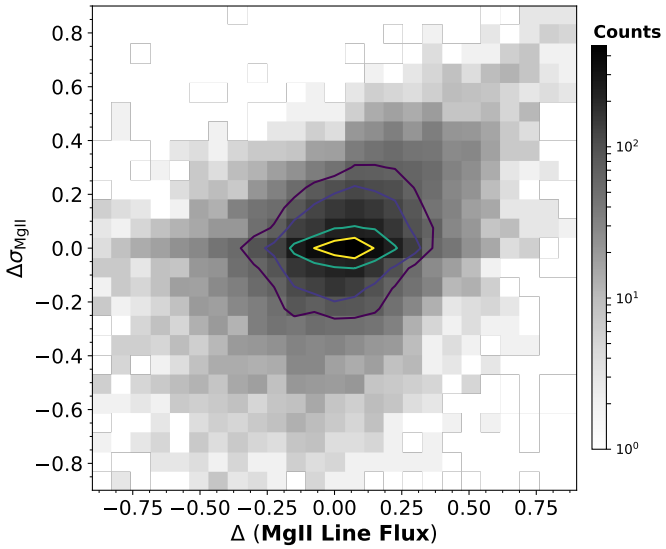

Figure 5.24: The normalised change in line width plotted against the normalised change in line flux. The normalisation is to the oldest epoch of the pair of spectra. The data lack a clear correlation: for most objects the two parameters do not seem to correspond at all. For large changes in line flux, associated with more extreme variability, a connection is possibly present. The data presented here do not allow for a clear conclusion on that, however.

both represent a fractional change over time. The core of the distribution shows no sign of a correlation. It is possible that the connection exists for larger fractional changes of the two parameters. This connection is hinted at by the data in Figure 5.22 and would be in agreement with the results for the supervariable sample. However, a linear regression of $\Delta\sigma_{\mathrm{MgII}}$ on the change in line flux shows a slope of ∼0. It is possible the number of objects in this sample with strong variability is too small to make the correlation significant.

5.5. Comparison of the Supervariable and Full Population Samples

The analyses of the two samples presented in Sections 5.3 and 5.4 allow for some preliminary conclusions about MgII responsivity. The first is that there can be a strong correspondence between line and continuum flux levels, with the possibility of very large changes (up to a factor ∼5) in MgII line flux. It is clear from both samples that this is not the case for every object. Even in extremely variable objects MgII does not always show strong fluctuations. The responsivity is evidently more complex. There is, however, a detectable linear trend, which indicates that the MgII line tracks the continuum. The slope of this responsivity appears to differ between the two samples (compare e.g. Figures 5.9 and 5.16). The first part of this section will quantify this difference in behaviour between the samples.

A second conclusion is that there is significant scatter in the data, in both samples. This scatter is partially due to uncertainties in the measurements, but it can also be attributed to a large spread in the underlying distribution of quasar spectral properties. To investigate whether the differences in spectral variability are connected to physical parameters, I will compare subsets of the samples based on sections in the parameter space of the normalised fluxes. The most important physical parameters to consider are the bolometric luminosity (L_{bol}), the black

hole mass (M_{BH}), and the combination of these two values in the Eddington ratio (λ_{Edd}).

The focus on the Eddington ratio follows from the discussion in Section 1.4. The Eddington ratio can be used as a measure of the accretion rate. EVQs appear to have relatively low Eddington rates on average (Rumbaugh et al. [2018], MCL19). The influence of this parameter on the variability of MgII is therefore worth investigating. For the values of L_{bol}, M_{BH}, and λ_{Edd} I will rely on Shen et al. [2011]. This means the quasars included in this part of the analysis (presented in Section 5.5.2) are objects that were included in DR7Q. The black hole masses are the fiducial estimates, based on the single epoch virial method [Shen et al., 2011].

The final, tentative, conclusion is that the line responsivity changes with Δt, the rest frame time difference between successive observations. This change is suggested by the change in slope of the linear response in the normalised data (Figure 5.19) and in the flux changes from epoch to epoch (Table 5.6). Understanding this dependency is hampered by the correlation between Δt and $|\Delta f_{2800}|$. It is interesting, however, that very large line flux changes are observed on all time scales (Figure 5.20). This is at least an indication that large continuum changes are an important driving force.

5.5.1 The Two Samples

The distributions of L_{bol}, M_{BH}, λ_{Edd}, and the redshift for the two samples are shown Figure 5.25. The supervariable sample stands out from the general quasar population for each of the four parameters. Most remarkably the median Eddington ratio is approximately five times lower for the strongly variable objects. This is in agreement with the results presented in Figure 6 of MCL19 and the EVQ sample discussed by Rumbaugh et al. [2018]. There is also a clear selection bias, however, evidenced by the z distribution in the bottom right panel of Figure 5.25. The selection criteria for the supervariable sample require $z<0.8$. The redshift limit makes the sample biased towards lower luminosity objects. This effect is due to both the flux limits in the SDSS sample and to AGN downsizing. Although the selection bias is towards lower luminosities, it is not necessarily towards lower λ_{Edd}.

The metrics of correlation and responsivity for the two samples derived in Sections 5.3 and 5.4 are summarised in Table 5.7. The table includes the results for both normalisations, to the epochs of maximum and minimum state respectively. In all cases the Pearson and Spearman coefficients show a strong correlation between the line and the continuum flux. The columns labelled 'slope' list the gradient of the one component linear fit to the data. The slopes for the two data-sets differ significantly. The fitting results are not consistent between the normalisations, as the supervariable sample appears to have a stronger gradient than the full population sample in the maximum normalisation, but weaker in the minimum normalisation. However, the data-sets are clearly distincs in each case. This means that for a sample dominated by large flux changes the line responsivity differs from a sample dominated by quasars with a more tranquil continuum.

5.5.2 Data Subsets Based on Normalised Flux

Following the comparison of the samples in their entirety, we can consider interesting subsets of the data. As was noted for both the supervariable and full population samples, the data cover a wide range of the normalised flux. By making selections in this parameter space, it is possible to create subsets of the samples based on spectral variability. This allows for a comparison

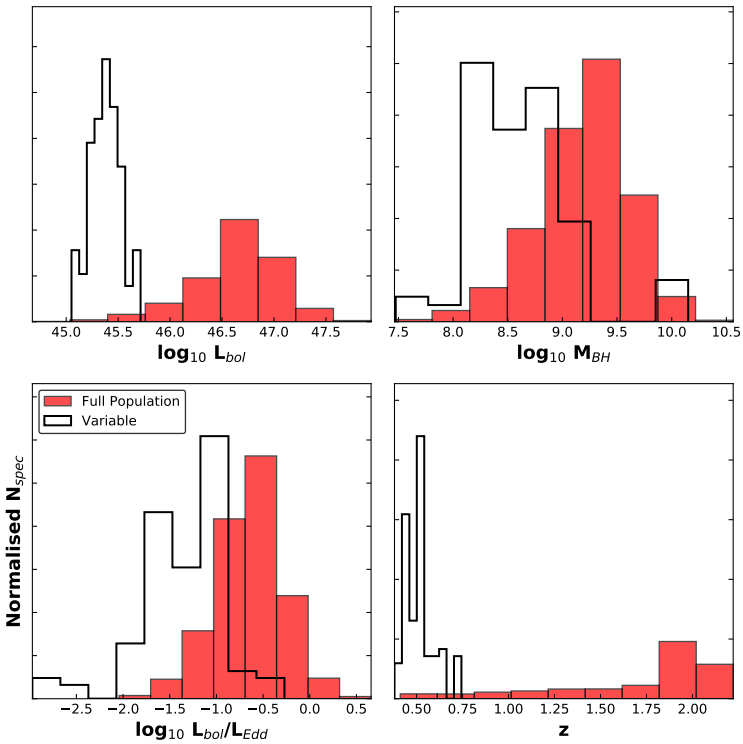

Figure 5.25: The distributions of the bolometric luminosity (*top left*), black hole mass (*top right*), Eddington ratio (*bottom left*), and redshift (*bottom right*) for the two QSO samples. The two data-sets are clearly distinct in each case, with the supervariable sample both intrinsically dimmer and with a significantly lower Eddington ratio. The clear offset in the z distribution for the supervariable sample, a result of the sample's selection criteria, indicates that the observed trends are at least partly the result of a selection bias in the data.

Table 5.7: A comparison of various metrics of responsivity between the supervariable and the full population sample for both normalisations used in Sections 5.3 and 5.4. The included values are the slope of a linear fit to the data, the Pearson coefficient (r) and the Spearman coefficient (r_S). The metrics are defined in Section 5.2.

	Maximum			Minimum		
	Slope	r	r_S	Slope	r	r_S
Supervariable	1.39	0.76	0.78	0.58	0.46	0.67
Full Population	1.13	0.30	0.32	0.74	0.32	0.30

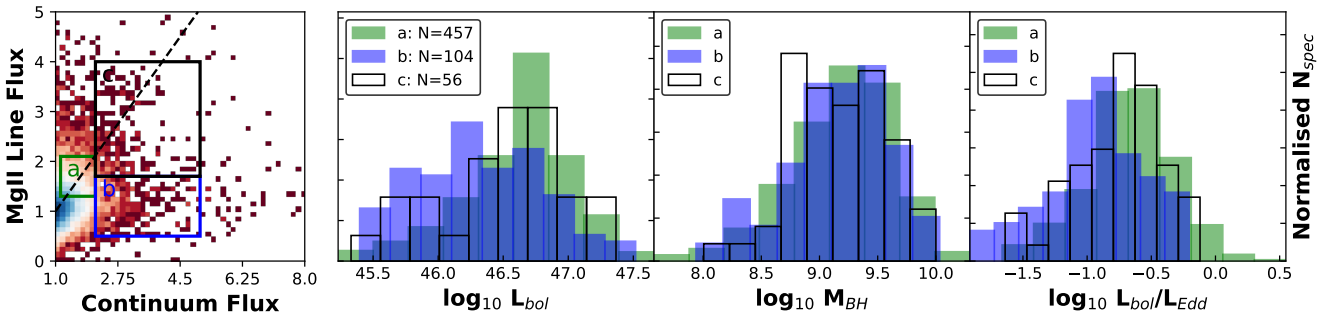

Figure 5.26: Quasar properties for the subsets of the full population sample, normalised to the epoch of lowest continuum emission. *left*: The selection in the normalised flux space. A 1:1 ration of line and continuum flux is indicated by the dashed line. *right*: Three histograms displaying (from left to right) the normalised distribution of the bolometric luminosity, the fiducial black hole mass, and the Eddington ratio. The values for the distributions are from Shen et al. [2011].

of spectral variability with physical AGN parameters. Figures 5.26 and 5.27 illustrate this comparison. In the figures the sections of parameter space outlined in the left panel define the data subsets for which the distributions are shown in the three panels on the right. Summary statistics of the distribution of the λ_{Edd} of all subsamples are listed in Table 5.8.

Figure 5.26 is based on the normalisation to the minimum continuum epoch. The three sections have been selected to represent different types of responsivity. All cuts in the data avoid the highest density region with objects showing very small changes in both continuum and line. Section *a* represents an approximately 1:1 relation between line and continuum. Section *b* is distinguished from *a* by having significantly larger continuum changes, but these changes are not matched by a change in line flux. The objects in section *b* can therefore be considered under-responsive. Section *c* is defined as a control group for section *b*: it has the same range in continuum flux, but contains objects with larger MgII fluctuations.

Comparing the parameters for these subsections *a* and *b*, we can note that the black hole masses are similar, but that the luminosities are on average lower for subsample *b*. This implies that these objects are on average accreting at lower efficiencies, as indicated by the lower Eddington ratio for the objects in *b*. The large continuum flares therefore appear associated with objects with a lower accretion rate [in agreement with Rumbaugh et al., 2018; Graham et al., 2019]. To investigate whether the lack of line response is related to this accretion parameter as well, we can compare the sections *b* and *c*. As noted *b* and *c* cover the same range in continuum variability but *c* is more variable in MgII. In the distributions of λ_{Edd} it is clear that the AGN in section *c* more closely resemble those is section *a*, than those in *b*. In other words: AGN with low line responsivity on average show a lower accretion rate than more responsive AGN. The offset in the centres of the λ_{Edd} distributions is also evident in the average and median listed in Table 5.8.

We can extend the comparison to the supervariable sample, making the exact same selections in the flux-flux parameter space. Although the number of data points is too low for display in a histogram, it is possible to characterise the distributions, calculating the median, sample average, and standard deviation of the data subsets (Table 5.8). The Eddington ratio for the supervariable subsamples are overall lower, in accordance with the overall difference

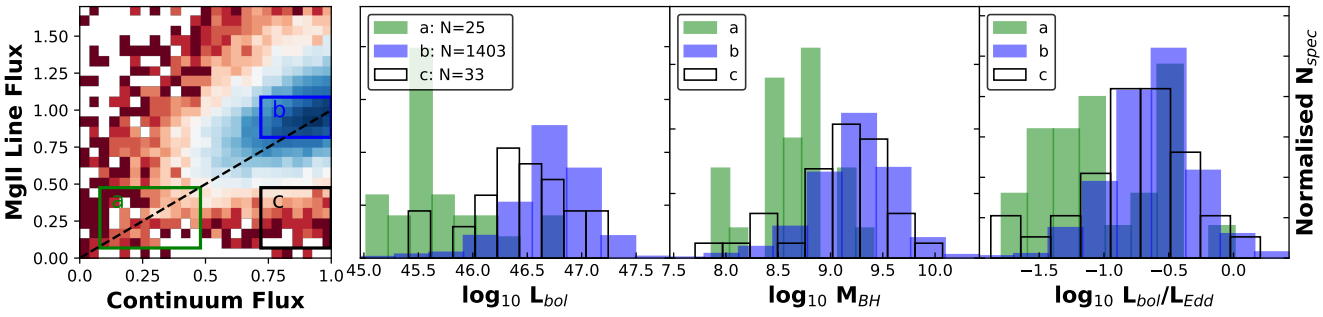

Figure 5.27: Quasar properties for subsets of the full population sample, normalised to the epoch of highest continuum emission. The description of the information in the panels is as for Figure 5.26.

in distributions illustrated in Figure 5.25. The effects seen for the full population are largely mirrored by the EVQs: the larger continuum variations are associated with a lower λ_{Edd} and a weaker line responsivity is associated with a lower Eddington rate as well. The latter association is not as strong in the supervariable sample, however: although the medians for b and c are quite distinct, the averages are quite similar.

A similar analysis of subsets is applied to the data normalised to the epoch of maximum continuum, as displayed in Figure 5.27. For this normalisation the sections have been made as follows: section a targets highly variable and highly responsive objects, section b selects a general quiescent sample, and section c targets objects where the line is relatively more variable than the continuum. Section c again overlaps with b in the range of continuum fluxes, and with a in the range of line fluxes. This will allow a comparison of objects with similar continuum changes, but differing changes in line flux and vice versa.

The distributions in Figure 5.27 show that the subset a is a clearly distinct selection of the quasar population from b and c. The most variable objects (a) are characterised by lower luminosities, lower masses, and lower Eddington ratios. The correlation between continuum variability and Eddington ratio is therefore clear, however a comparison of the distributions for b and c indicates that the correlation with MgII line variability is not as strong. A visual inspection of the λ_{Edd} distributions of the objects in b and c indicates that these populations are quite similar. The averages and means for the two distributions (Table 5.8) do show an offset: the objects with greater line variability have on average somewhat smaller Eddington ratios. This could be expected based on the results in Figure 5.26. However, the connection of MgII flux variability with the Eddington ratio is noticeably weaker than the connection between λ_{Edd} and the continuum flux.

For the supervariable sample the comparison of the same regions in flux-flux space shows that the dependence of the magnitude of relative continuum changes on the Eddington ratio holds. The average value of $\log_{10}(\lambda_{Edd})$ for the highest continuum variability subset a is -1.48 and for b $\log_{10}(\lambda_{Edd})$=-0.90. The number of objects in the subsets of the supervariable sample is quite low however, making a reliable comparison more difficult. No objects matched the requirements for subset c.

Table 5.8: Summary statistics of the distributions of $\log_{10}\lambda_{\rm Edd}$ distributions for the data subsets defined in Figures 5.26 and 5.27. The results for the full population and supervariable sample are included. The sections in the normalised flux space that define the subset were the same for each sample. The columns represent, from left to right, the sample size, median, sample average, and standard deviation.

		Full Population				Supervariable			
Normalisation	subset	N	Median	$\bar{\rm X}$	σ	N	Median	$\bar{\rm X}$	σ
Minimum	a	457	-0.67	-0.67	0.34	5	-1.10	-1.07	0.26
	b	104	-0.92	-0.93	0.40	9	-1.41	-1.41	0.26
	c	56	-0.68	-0.76	0.35	18	-1.15	-1.39	0.59
Maximum	a	25	-1.14	-1.02	0.45	24	-1.23	-1.48	0.62
	b	1403	-0.61	-0.62	0.33	2	–	-0.90	0.13
	c	33	-0.73	-0.75	0.44	0	–	–	–

5.5.3 Considering α_{rm}

The distribution of the responsivity measure, α_{rm}, in each of the two samples is compared in Figure 5.28. As was noted in Section 5.3, the distribution of the supervariable sample is clearly skewed to the negative values. The same skewness can be seen in the distribution of α_{rm} for the full population sample, although in this case the distribution is strongly dominated by objects with $\alpha_{rm}\sim 0$.

The responsivity measure was chosen to easily identify over- and under-responsive objects in the data-set. Objects with $\alpha_{rm} > 0$ have a larger relative change in line flux than in the continuum and can be considered over-responsive. Conversely, $\alpha_{rm} < 0$ indicates an under-responsive object. The selections made for the α_{rm} subsamples are based on their distribution around $\alpha_{rm} = 0$. The first selection simply splits the samples between positive and negative α_{rm}, i.e. the over- and under-responsive subsets respectively. A second selection will look at the more extreme cases, requiring $|\alpha_{rm}| > 0.75$. This selection will function as a check on the first results: if there is a distinction in physical parameters based on α_{rm}, the separation should be more prominent among the outliers.

The selection based on α_{rm} does not appear to result in a clear distinction based on observed parameters. The results for the selection $|\alpha_{rm}| > 0.75$ are shown in Figure 5.25. For none of the four parameters considered (L_{bol}, M_{BH}, λ_{Edd}, and z) do the populations differ visibly. For the distributions of λ_{Edd} summary statistics are listed in Table 5.9, for both selections in α_{rm}, as well as the samples in their entirety. Based on the these values it is possible to make a distinction between the two $|\alpha_{rm}| > 0.75$ samples: the over-responsive objects have a slightly higher λ_{Edd}.

A lower value of the Eddington ratio for objects with a negative responsivity measure would be in agreement with the results based on the subsets in flux. The correlation between continuum and λ_{Edd} is stronger than that for the line flux, therefore objects in which the continuum has changed more ($\alpha_{rm} < 0$) can be expected to have lower Eddington ratios. It should be noted that the difference between the two distributions is slight, making a firmer conclusion impossible. For the supervariable sample a similarly small distinction based on α_{rm} can be detected (Table 5.9).

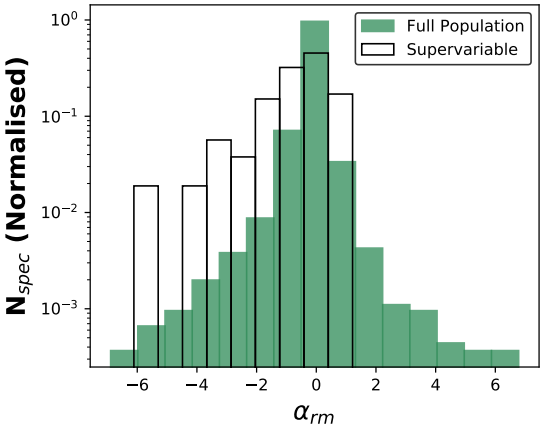

Figure 5.28: A comparison of the distribution of α_{rm} in the two MgII samples. Both the supervariable and the full population sample appear skewed to negative values of α_{rm}, although this trend is more prominent for the supervariable sample. Negative values are associated with an under-responsive MgII line flux and positive values with over-responsivity.

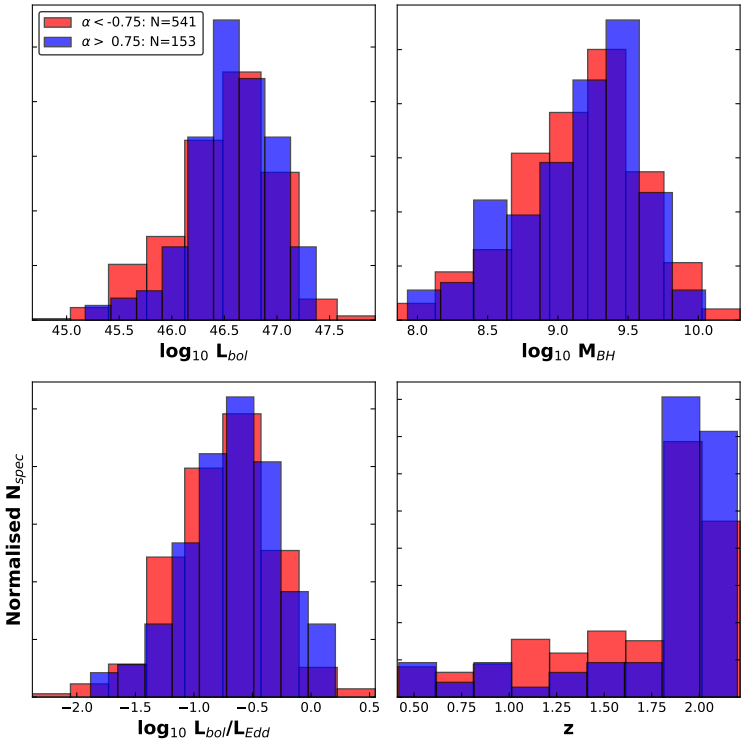

Figure 5.29: A comparison of the distribution of AGN properties among subsections of the full population sample based on the responsivity measure. The properties are: bolometric luminosity (*top left*), black hole mass (*top right*), Eddington ratio (*bottom left*), and redshift (*bottom right*). No clear distinction is visible between the subsets, despite a cut based on a relatively large value of $|\alpha_{rm}|$.

Table 5.9: Summary for the distributions of the Eddington ratio in subsets of the full population and supervariable samples, based on α_{rm}. The listed statistics are, from left to right, the sample size, median, sample average, and standard deviation. The same statistics for the entire samples are listed in the bottom row. J081916 was not part of DR7, reducing the total size of the supervariable sample from 43 to 42.

	Full Population				Supervariable			
Sample	N	Median	$\bar{X}$	σ	N	Median	$\bar{X}$	σ
$\alpha_{rm} < 0$	5374	-0.64	-0.65	0.37	35	-1.38	-1.40	0.48
$\alpha_{rm} > 0$	1979	-0.63	-0.65	0.36	7	-1.29	-1.33	0.31
$\alpha_{rm} < 0.75$	541	-0.72	-0.76	0.42	18	-1.34	-1.38	0.28
$\alpha_{rm} > 0.75$	153	-0.65	-0.67	0.41	2	–	-1.16	0.00
Full Sample	7407	-0.63	-0.65	0.36	42	-1.28	-1.36	0.47

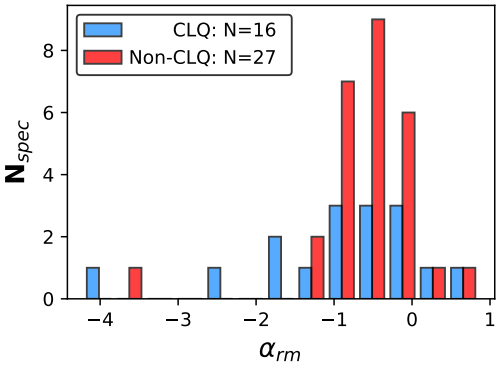

Figure 5.30: The distribution of the responsivity measure among the CLQs and non-CLQs in the supervariable sample. The average value of α_{rm} is used for objects with more than two spectra available.

The responsivity parameter can also be used to quantify the link between MgII and Hβ variability. As can be seen in the data in Table 5.1, the correspondence between CLQ behaviour and MgII variability varies from object to object. Figure 5.30 show the distribution of α_{rm} for CLQ and non-CLQ objects in the supervariable sample. For objects with more than one spectrum the average of the responsivity measures is used. The distribution for the CLQs is clearly broader than for the non-CLQ objects and stretches to more negative values. For both distributions the centre lies slightly below 0, corresponding to objects where MgII only slightly tracks the continuum. We therefore again see a range of behaviours: some CLQs show an almost equal variability in MgII and continuum, whereas for other CLQs MgII barely responds at all, as the continuum varies.

5.5.4 The Intrinsic Baldwin Effect

A final measure for the responsivity is the intrinsic Baldwin Effect (iBE; Section 1.3), which measures the change in EW compared to the change in continuum luminosity for individual objects. For the full population sample the iBE is calculated as $\Delta EW/\Delta L_{2800}$ for each spectral pair. For the supervariable sample the same is done for each chronologically sequential pair.

The distribution is largely symmetric and centered around a slope of -0.5. For the supervariable sample the average slope is -0.54. Unfortunately there are no literature values of the

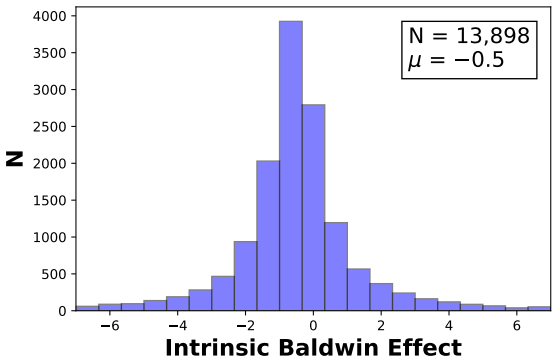

Figure 5.31: A histogram of the intrinsic Baldwin Effect for the full population sample. The number of spectral pairs, N, and the sample average, μ, are listed in the top right corner. The iBE is calculated as $\Delta EW/\Delta L_{2800}$ for each pair. Although there are some strong outliers, the distribution is clearly centered around -0.5. This is significantly lower than the slope of the ensemble BE of -0.16 calculated for the data from Shen et al. [2011] (Figure 1.6).

MgII iBE to compare these results to. For other UV lines such as CIVλ1549 and for the Balmer lines the slope of the intrinsic BE is significantly steeper than for the ensemble BE [Osmer & Shields, 1999; Rakić et al., 2017]. I find that the same holds for MgII: the eBE of the DR7 sample (Figure 1.6) has a slope of -0.16.

5.6. The Variability of the MgIIλ2798 Line

5.6.1 Overview of Results

The spectra of the supervariable and full population samples have provided a great deal of information about the variability of the MgII line. Some of the correlations paint a clear picture of MgII responsivity, whereas other trends are more difficult to interpret. It is evident the MgII line exhibits a complex behaviour. The analysis of the data presented in this chapter falls into two broad categories, each of which combines results from both MgII samples. The first category is the MgII flux responsivity: the changing levels of the line flux under a varying continuum provide information about the incident ionising flux and the physical conditions in the line forming region. The second category is the MgII line profile: changes observed for individual sources can provide information about the kinematics of the gas that creates the MgII emission. The same is true for the population statistics provided by the measurement of $\sigma_{\rm MgII}$. In this section I will discuss the findings of this chapter in the context of previous studies on MgII variability. Below is a brief summary of the results.

Flux Responsivity

i) There is a broad range of behaviour in MgII variability. In some objects the line changes more than the continuum, whereas in others the line shows barely any response at all. Based on the responsivity measure, it is clear that the objects where the line varies less than the continuum form the largest part of the quasar population.

ii) $|\Delta L_{\rm MgII}|$ and $|\Delta\lambda L_{2800}|$ show a linear correlation, visible for the supervariable sample (Figure 5.7). The relation holds over five orders of magnitude.

iii) The connection between MgII variability and CLQ behaviour is not one-to-one. Considering Hβ and MgII in the same object, the supervariable sample contains objects where either, both, and neither of the lines vary. The statistics indicate joint and separate variability occur in approximately equal measure.

iv) When normalised, the fluxes show a linear correlation between MgII line and the 2800Å continuum. This holds for both normalisations, to the minimum and the maximum state (Figures 5.15 and 5.16; Table 5.7). The scatter in the full population as well as in the supervariable sample is considerable, for both normalisations. Although the scatter is partially the result of measurement and fitting uncertainties, it is also indicative of the range in MgII variability.

v) A saturation effect is possibly present in the data when normalised to the minimum continuum state. This would be similar to the effect observed in Mrk 110. Due the large scatter, the preference of the two-component 'saturated' fit over the simple linear response is uncertain, however.

vi) There is clear evidence of a changing responsivity over time in the spectra of J022556 (Figure 5.11), for which relatively high cadence observations are available. The response of MgII not only changes from object to object, but also from epoch to epoch. This agrees with conclusions drawn about other line species in Mrk 110.

vii) A change in the linear responsivity of MgII with time can be observed in the full population sample. The responsivity appears to decrease for longer elapsed time between spectral epochs (Figure 5.19). When modelled as a simple linear response, the change in gradient is modest, but steady over the Δt bins (Table 5.5).

viii) The distributions of Δf_{MgII} and Δf_{2800} change with Δt. The averages of the distributions become more negative over time and the skewness increases. The change in the average is likely the result of a selection bias (see the discussion in Section 5.4.2).

ix) The Eddington ratio is connected to the magnitude of changes in the continuum. Objects with larger continuum changes on average have a lower λ_{Edd}. The difference is visible in the offset between the λ_{Edd} distributions of the super variable sample and the full population sample (5.8). This is in agreement with previous results [Rumbaugh et al., 2018; Graham et al., 2019]. For changes in the line flux this connection possibly also exists, but is not as strong as for the continuum.

Kinematics

i) Some of the objects in the supervariable sample show a clear asymmetry in the MgII profile. This asymmetry manifests itself as a skewness of the lines. The skewness can be both to the blue and the red of the line centre (Figure 5.3).

ii) Asymmetry of the MgII line can evolve over time, as observed for J111348 (Figure 5.4). The evolution of the line profile could be due to a change in the relative strength of different line components. These could be the broad and narrow components, but it is also possible they represent a more dynamic structure.

iii) The MgII line width lacks a correlation with either the 2800Å continuum or the line flux (Figure 5.22). There is some tentative evidence of a correspondence for the lowest luminosities, however the bulk of the distribution shows a flat response. This is in agreement with previous results (e.g. Shen et al. [2011]).

iv) The change in line width tentatively show a positive correlation with the change in line flux (Figure 5.24). This effect can be seen in both the supervariable sample and the full population sample. If the correlation exists, it is more prominent for objects that exhibit large changes in line flux. This effect would be contrary to expectations for AGN breathing. The bulk of the distribution does not show this correlation.

5.6.2 Interpretation

Flux Variability

The broad range in MgII variability noted in both the samples discussed in this chapter agrees with previous studies. The difference from object to object can be seen among RM studies (e.g. Clavel et al. [1991]; Hryniewicz et al. [2014]; Trevese et al. [2007]; Cackett et al. [2015]) and is a likely contribution to the strong scatter found in MgII variability in larger samples of quasars [Kokubo et al., 2014; Sun et al., 2015; Zhu et al., 2017], as well as in the EVQ sample presented by Yang et al. [2019]. Even for very large variations, the response can differ considerably. As was evident from the example of J022556, the behaviour does not only differ among objects, but evolves for individual quasars over time.

The range in behaviours illustrated in Figure 5.2 appears representative of the EVQ population, when compared to other objects in the literature. The object presented in Ross et al. [2018] shows significant dimming and re-brightening of the UV continuum, accompanied by a sharp drop and recovery of the MgII flux. Similarly Yang et al. [2018] find an object in their EVQ sample where the MgII and continuum both decrease strongly. The changes in these two objects occur on the timescale of years in the rest frame. The tracking of the continuum is in sharp contrast with the behaviour of the object described by Kynoch et al. [2019], in which the continuum flux drops by a factor $\sim$2 over a period of 4 years before recovering, without any noticeable change in MgII. A combination of available optical and IR data for this object indicate that the drop in the continuum is definitely intrinsic to the source, as the emission from the dusty region echoes the dimming of the optical continuum. Despite a dramatic decrease in the irradiation of the BLR, the MgII line flux is stable. The marked difference in possible responses among the AGN population indicates that the response is not determined by changes in the luminosity alone. Rather, a range of conditions in the BLR likely conspire to create a specific responsivity, in similarity to the evolving broad line behaviour seen in Mrk 110.

The primary behaviour observed in the MgII response is that the line tracks the continuum. This is true for both the supervariable and the full population sample. The correlation between line and continuum has been found in other recent studies as well [Sun et al., 2015; Zhu et al., 2017; Yang et al., 2019], although not all authors agree on the strength of the response [Kokubo et al., 2014]. Although a more complex flux response (e.g. a saturation effect, Figure 5.9) is certainly possible, the approximation to first order is the clearest effect in the data.

To quantify the linear response I have made use of the one-component and two-component

fitting functions. A different metric is calculated in Yang et al. [2019], where the slope of the change in line luminosity versus the change in continuum luminosity ($\Delta\log_{10}L_{MgII}/\Delta\log_{10}L_{3000}$) is used. As a check I compare these values with $\Delta\log_{10}L_{MgII}/\Delta\log_{10}L_{2800}$ calculated for the two samples discussed in this chapter. Yang et al. [2019] find a slope of 0.39 ± 0.07 for their EVQ sample and 0.47 ± 0.05 for a larger sample expanded by including EVQ objects from SDSS DR14. Using a linear regression, I find $\Delta\log_{10}L_{MgII} = (0.58 \pm 0.05)\Delta\log_{10}L_{2800}$ for the supervariable sample, and 0.35 ± 0.01 for the full population sample. The results are consistent and, furthermore, emphasise the stronger overall response observed in the supervariable sample.

The timescales for the MgII variability discussed in the literature are ∼years. For the objects in the supervariable sample as well as a large fraction of the objects in the full population sample (see Figure 5.6) the timescales are of the same order of magnitude. On shorter timescales the linear correlation between line and continuum is not as clear, although it can be detected for a fraction of the population [Shen et al., 2016a]. Interestingly, a timescale of years corresponds with a dynamical timescale (τ_{dyn}) in the BLR (Table 1.4). The fact that a consistent positive correlation, although with a large scatter in the amplitude of response, is clearer on longer timescales, could indicate that the changing ability of the MgII line to respond the ionising flux represents a physical change in the BLR.

A difficulty in linking the evolution over time to τ_{dyn} is that a large Δt is on average related to a larger change in continuum. The entanglement of $\Delta f_{\rm MgII}$ and Δf_{2800} makes a firm conclusion about the effect problematic. The moments of the distributions of $\Delta f_{\rm MgII}$ and Δf_{2800} in different Δt bins, listed in Table 5.6, show that the distributions evolve in a similar way. Disentangling the two parameters in this manner therefore does not appear possible. An indicator that Δt is of importance is that the gradient of the responsivity is larger in the full population sample than in the supervariable sample (Table 5.7). It should be stressed that this response is to *fractional changes*: the full population sample is dominated by objects with only small changes in both continuum and MgII. For the most dramatic changes in MgII flux a large continuum flare or drop might still be required.

The physical origin of the spectral variability can be investigated through the correlations with quasar parameters such as the black hole mass and the bolometric luminosity. The clearest example of this is the amplitude of the continuum variability, which appears to be anti-correlated with the Eddington ratio [MacLeod et al., 2012; Rumbaugh et al., 2018; Graham et al., 2019]. Objects with larger Eddington ratios, linked to higher accretion rates, on average show a smaller amplitude in variability. This effect is evident in both samples, as can be seen in Figures 5.26 and 5.27, as well as Table 5.8. The data also show a tentative correlation with the change in MgII line flux and λ_{Edd}. As the line flux tracks the continuum, a correspondence between the line flux and λ_{Edd} can be expected, based on the correlation between the continuum variability and this parameter. A similar relation is reported by Dong et al. [2009], who find that the EW of MgII has an inverse correlation with λ_{Edd}.

Both Sun et al. [2015] and Zhu et al. [2017] find that the response of the MgII line depends on L_{bol}. Sun et al. [2015] report a decrease in the line variability with increasing L_{bol}. Zhu et al. [2017] find that more luminous objects have a shallower slope in the linear response. The connection between L_{bol} and the MgII line change is not clear in the data for the supervariable sample, although the effect *is* visible for the continuum variability (Figure 5.27). The decrease

of the continuum variability with bolometric luminosity is also found in DRW studies [MacLeod et al., 2010].

The connection between Hβ and MgII variability can also provide information about the BLR processes that govern the emission. The line forming regions for these two species are thought to be in close proximity. This is argued for by Woo [2008] on the basis of RM results and by Shen & Liu [2012] based on the similarity in line widths for MgII, Hα, and Hβ. A theoretical argument is found in the photoionisation modelling presented in Korista & Goad [2004], who find that Hβ and MgII are formed in similar regions inside the broad line clouds.

The variability of the two lines in relation to each other can show a wide range, as is clear from the lack of correlation between MgII variability and CLQ behaviour for a subset of the supervariable sample (Table 5.1). A class of objects in which MgII and Hβ vary independently would agree with the BOSS objects presented in Roig et al. [2014]. The authors reveal the presence of a class of objects in the BOSS sample for which MgII is significantly stronger than the Balmer emission lines, but which lack signs of reddening. Kokubo et al. [2014] argue that MgII is intrinsically less variable than Hβ in the entire quasar population. Although this is in agreement with RM studies, the research presented here indicates that the MgII behaviour is more complex than only a suppressed response compared to the Balmer lines.

Several causes for the difference between Hβ and MgII are discussed in the literature. The first possibility is that the material emitting Hβ has a different geometric distribution than the MgII emitting material [Sun et al., 2015]. The 'BLR' that forms Hβ would then be physically distinct from the one that forms MgII. For a more extended MgII region, any change in incident flux would be geometrically diluted, illuminating different radii at different times. This could explain the lack of effect in some of the RM studies, although it is more difficult to explain the strong instantaneous response measured by e.g. Hryniewicz et al. [2014] in this scenario.

Another issue with an interpretation based on differing BLR geometries is the physical conditions in which the two lines are formed (see also Section 1.2.3). For collisional excitation of the atom, a population of MgII needs to be present. As can be seen in the modelled ionisation structure of an RPC cloud (Figure 1.9; Baskin et al. [2014a]), the MgII population is likely present in the higher density 'back' of the cloud. This region largely overlaps with the parts of the cloud where H is neutral, such that the E>13.6 eV flux, which ionises MgII to form MgIII, is strongly attenuated. In the front of the cloud, where all H is ionised, the MgII population is likely too small to contribute to the MgII flux [Guo et al., 2019]. Conversely, the temperature of the gas in the back of the cloud can become too low for the collisional excitation of MgII. For these reasons MgIIλ2798 is likely associated with the transition region between the HII and HI regions of BLR clouds [MacAlpine, 1972; Netzer, 1980; Collin-Souffrin et al., 1986; Krolik, 1999; Guo et al., 2019]. This is also the region where most of the Balmer emission is formed [Krolik, 1999; Guo et al., 2019]. If the line forming regions of Hβ and MgII are so intimately linked, a very different geometry for the two appears less probable.

A second possible explanation is based on the difference in optical depths between the two lines [Korista & Goad, 2004; Sun et al., 2015; Yang et al., 2019]. MgII is a resonance line, whereas Hβ is not. MgII can therefore be expected to have a greater optical depth, increasing the number of absorptions and reemissions of any line photon before it escapes the cloud. This could also dilute the response to a change in incident flux, spreading it out over time. A possible problem with this interpretation is that although MgII is a resonance line, the population of

ground state atoms is itself subject to photoionisation which could suppress the number of absorbing atoms. Photoionisation modelling does indicate the optical depth effect could be significant [Korista & Goad, 2004; Baskin et al., 2014a]. If optical depth for the lines is a critical factor, the observed evolution with λ_{Edd} could be the result of a changing ionisation structure in the cloud, as a result of a changing shape of the SED. A difference in temperature or n_e could affect the MgII population in BLR clouds.

As the MgII line is not based on photoionisation, but rather collisional excitation, the effect of changes in the incoming flux on the total line flux is reduced [Yang et al., 2019]. This effect can certainly explain the relatively low responsivity of MgII in RM studies [Guo et al., 2019]. It could also provide an explanation of the evolution of the responsivity on longer timescales (τ_{dyn}), in terms of a changing density of the clouds. The RPC model provides a natural reason for gas pressure to evolve with luminosity and the accretion rate [Baskin et al., 2014a,b] and the gas pressure and temperature are determining factors in setting the collisional excitation rate. Without detailed photoionisation modelling it is difficult to judge the precise trajectory of this effect.

Line Profile

The MgII line profile can differ from object to object and over time. In the supervariable sample this is evidenced by two objects that have asymmetric MgII profiles. Because it is not possible to resolve the different line components, it is unclear what the origin of the asymmetry is. If the skewness results from an offset between broad and narrow components, a radial outflow or inflow would be a plausible explanation. Another option is to associate the different line components with a blueshifted and a redshifted broad component. These components could be the result of rotation of the BLR or possibly even the outer regions of the disc, where the line could be formed. Such a scenario would be akin to the interpretation for quasars with double peaked emission lines (e.g. Eracleous et al. [2009]). It is impossible to discern the different dynamic components in either of the two samples, however.

To quantify the behaviour of the line profile, I have made use of the line width (σ) of the broadest Gaussian fit to the line. For both the supervariable and the full population sample σ lacks a correlation with the luminosity. This is in agreement with other results [Woo, 2008; Shen et al., 2011; Yang et al., 2019] and indicates that the MgII line does not 'breathe'. Again, this presents a marked difference with the behaviour of Hβ [Bentz et al., 2013]. A possible explanation is that the MgII emission region is confined to a smaller set of radii [Yang et al., 2019], perhaps as the result of the small geometrical depth of the MgII line emitting region in each cloud. The lack of correlation between luminosity and σ at low values of L_{2800} is an indication that the line width is not fully set by the gravitational potential. This could be in agreement with the interpretation that the line flux is the result of collisional ionisation, as the line responds to changes in the temperature, not the ionising flux. However, a contribution by turbulence to the line width is likely also present.

Considering the fractional change in line width compared to the fractional change in line luminosity the bulk of the distribution lacks a correlation. Yang et al. [2019] calculate the value $\Delta\log_{10}\mathrm{FWHM_{MgII}}/\Delta\log_{10}\mathrm{L_{3000}}$, and find slopes of -0.014 ± 0.030 and 0.012 ± 0.012 for their new EVQ and extended sample respectively. In comparison, I find a slope for $\Delta\log_{10}\mathrm{FWHM_{MgII}}/\Delta\log_{10}\mathrm{L_{2800}}$ of 0.013 ± 0.035 for the supervariable sample and 0.008 ± 0.066 for the full population sample. Both correlations are consistent with 0. Although there is some

tentative evidence for a positive response among the outliers in continuum luminosity change, the number of objects is too low to confirm its existence.

Future Work

An extension of the research into the variability of MgII could investigate the correlation between the spectral changes and the evolution of the light curve. An interesting question is whether the direction of change in the optical or UV spectrum has an impact on the change in the MgII line. Such an effect is tentatively present in the data for Mrk 110 (Figure 4.12) and could indicate the importance of an AGN's history of luminosity changes on the current state of the BLR.

A second line of investigation would be the continued observation of the EVQ sample. Further tracking of the MgII line could clarify the importance of timescale in the line's evolution. The high cadence spectra of J022556 indicate the usefulness of repeat observations. Continued monitoring could be of particular importance in discerning the variability of MgII and Hβ: is the observed difference between the lines in the supervariable sample only the result of measurements at different points in the spectral evolution? In other words: will one of the lines 'catch up' with the evolution of the other, or do the different states of the two lines persist over time, indicating that the associated AGN are fundamentally different?

6. Conclusion

The analysis of the samples presented in this thesis has yielded several interesting conclusions, as discussed in sections 4.5 and 5.6. Some of these conclusions are particular to one of the two studies. Others are common to both, providing new information on the general behaviour of AGN broad emission lines on long timescales. This section provides an overview of these conclusions. I will discuss the ways in which we can combine results from the Mrk 110 and MgII studies to better our understanding of the BLR.

Previously established results about AGN behaviour were also confirmed. The first is the response of broad emission lines to changes in the ionising flux, which has been observed for all emission lines studies here, including MgII. The second result is the correlation between the degree of line variability and the ionisation potential of the line emitting atom, as observed in the strong variability of HeIIλ4686. Third, although less responsive than other lines, the linear response of the MgII line has also been observed in other samples. Finally, the correlation of line width and ionising flux for Hβ in the Mrk 110 data is in good agreement with other observations of BLR breathing. Observations and conclusions that do not have such well established interpretations, or are entirely new, are discussed below.

6.1. Broad Line Variability on Long Timescales

i) The response of broad line flux to variations in the continuum changes with time

The clearest evidence of an evolution in the broad line response is provided by Mrk 110. RM campaigns conducted in different epochs, separated by several years, show a significant difference in the linear response of the line fluxes to the FUV continuum, using HeIIλ4686 as a proxy. When combined into a single response curve, the data also show a levelling off of the line response towards higher FUV fluxes. The reprocessing capability of the three lines considered for Mrk 110 (Hα, Hβ, and HeIλ5876) appears to saturate at higher levels of the incident flux. Furthermore, the level of flux at which the lines saturate appears correlated with either the radial distance of the line forming region in the BLR or the photoionisation parameters that determine the line formation. Overall, then, the Mrk 110 data show a clear dependence of the responsivity on the time of observation and a strong indication that the line responsivity on short timescales (such as in RM studies) is subject to a change occurring on a timescale of years.

The data from the MgII samples yield the same conclusion. The example of J022556 indicates that there is some form of hysteresis in the response: the evolution of the BLR up to the current state 'sets the stage' for the shorter term responsivity. In the samples the effect is evident in the broad scatter of the MgII response. As the number of observations per object is restricted, we detect changes in the MgII and continuum fluxes at random points along an average MgII responsivity curve, determined by the elapsed time between observations. The difference between the impact of evolution over time and the impact of large instantaneous flux changes is difficult to establish in these two samples. However, the large range in variability

behaviour exhibited by MgII indicates the presence of some form of evolution. The changing linear response over time indicates the same.

The evolution of the line responses occurs on the timescales of years, which is the same order of magnitude as τ_{dyn} for the BLR. It is therefore likely that in studies covering these timescales we are seeing two different effects in the variability occur simultaneously: a short term responsivity, where the central engine lights up different parts of a pre-existing structure, in agreement with BLR breathing, and a long term response in which the BLR structure changes. The nature of the longer, structural changes in not clear. They could entail a different cloud distribution, a different ionisation structure in individual clouds, or a change in the BLR size relative to the dusty obscurer.

ii) The BLR likely contains a component in radial flow

The offset between the broad and narrow component is clearly observed in both HeIIλ4686 and Hβ for Mrk 110. For both lines the broad component is redshifted with respect to the narrow component. The magnitude of the offset varies with the FUV flux. This evolution is consistent with both an inflow and a radiatively driven outflow scenario. In the inflow scenario the higher continuum luminosity lights up clouds at greater radii, for which the inward acceleration due to gravity is smaller. In the outflow scenario the same luminosity effect occurs, now lighting up clouds for which the radiative pressure is smaller due to the larger radii and the radial outflow is slower. For HeII a form of hysteresis is visible in the change with flux: the change in offset with changing flux differs from epoch to epoch. This is in agreement with the hysteresis effect noted for the flux responsivity.

The MgII line profiles lack the clear kinematic signature seen in Mrk 110, however the fact that the asymmetry of the line profile can evolve over time suggests that we can observe a structural evolution occur in the MgII line forming region. In both the MgII and Mrk 110 data-sets it is therefore possible to observe an evolution of the BLR structure over the course of approximately τ_{dyn}. The fact that for HeII a difference between epochs is noted for both the flux response and the kinematic offset parameter strengthens the conclusion that the different flux responsivities are indeed the result of a physical evolution in the BLR.

iii) The broad lines species are subject to different kinematic effects

The difference in the behaviour of Hβ and HeIIλ4686 in Mrk 110 is remarkable. The dependence in the HeII correlations on the epoch of observation has been noted above. However, the most prominent difference is in the correlation between FUV flux and line width: $\sigma_{\mathrm{H}\beta}$ shows the expected BLR breathing effect, but σ_{HeII} does not. As discussed in section 4.5, this implies that the HeII line width is not purely set by a Keplerian orbit. Radiative pressure, in combination with the required self-shielding and changing continuum SED, is a likely candidate to create this difference between the line species.

The MgII line lacks any sign of breathing as well, tentatively even showing a positive correlation between the line width and luminosity, akin to the correlation observed for HeII. Given the large difference with HeII in ionisation potential and line forming radius, it is unlikely that radiative pressure is of importance for the MgII line. This makes its difference with Hβ, which is formed at similar radii, the more remarkable. It is possible that the MgII line width is fully gravitational, but that the breathing effect is reduced by the narrow geometrical emission region. However, a turbulent contribution to the line width can certainly not be

excluded. At different radii in the BLR, in fact: at the inner and outer edges, the kinematics of the line forming regions can therefore deviate from purely gravitationally dominated rotation.

6.2. Future Work

An interesting line of investigation for both Mrk 110 and the MgII samples is the connection between the direction of change in the luminosity and the response of the broad lines. This connection is possibly present in the Mrk 110 data and could be studied for the MgII samples as well. A comparison of the spectral variability with the evolution of the light-curves for the supervariable sample would be a good starting point to examine this possibility more closely.

The most important requirement for future research is continued observation of highly variable objects. Repeat spectroscopy is necessary to develop our understanding of the changes in these AGN. The Mrk 110 data-set, and even the set of spectra for J022556, indicate the importance of high cadence spectroscopic observations. The level of detail in which we are able to analyse these objects provides significantly deeper insight into the behaviour of the BLR. Without the spectra in the intervening years, it would have been impossible to detect the changing responsivity of J022556. And the evolution of the offset in the line profile and of the line width in Mrk 110 required a large number of spectra to track effectively. Continued spectroscopic observations of EVQs, and known CLQs in particular, will yield important new information on the evolution of the broad emission lines, both with respect to the continuum and relative to one another.

Spectra of the Supervariable Sample

This appendix contains an overview of the spectra of the 43 objects that form the supervariable sample, as used in the analysis in chapter 5. 40 of the objects belong to the sample presented in MCL19, the additional objects are presented in MacLeod et al. [2016] and Lawrence et al. [2016] (see section 2.3). The inclusion of the spectra in this appendix is with the aim of providing the interested reader with a helpful visual comparison to the various abstract metrics of variability used in the discussion.

The focus of the discussion of the supervariable sample has been on the relation between the MgIIλ2798 line and the UV continuum. In the figures below and on the following pages one can clearly see the range of variability exhibited by the objects in the sample. The spectra in the figures are labelled with colour according to their date of observation. A darker shade of blue corresponds to a more recent observation, as can be seen from the dates (MJD) listed on the right hand side of each plot. Several of the most prominent broad and narrow lines in the AGN spectra have been labelled. The spectra have been smoothed with a running median to make them more suitable for visual inspection.

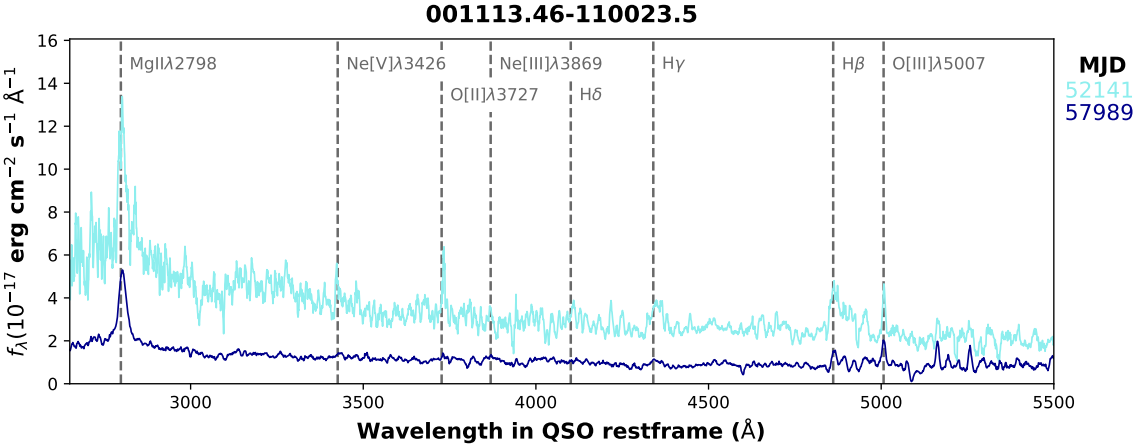

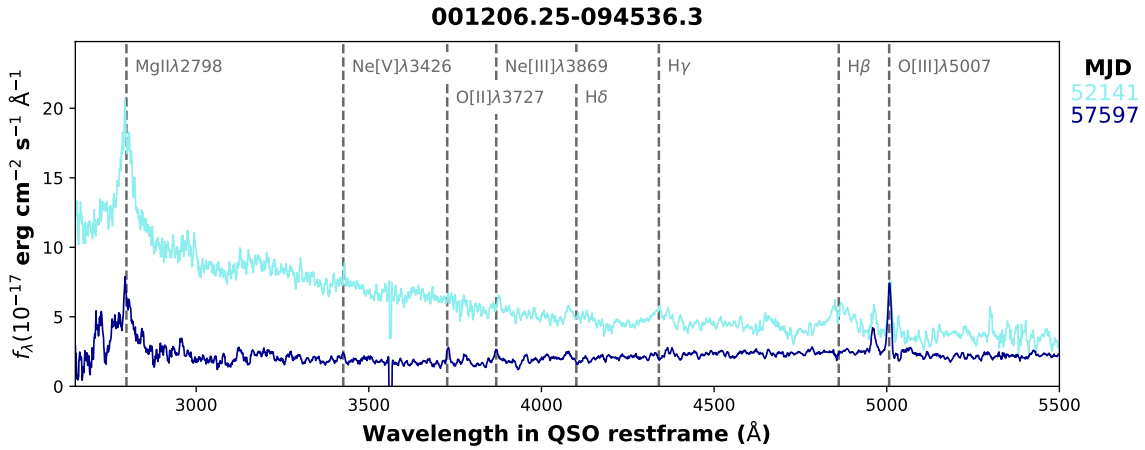
001206.25-094536.3
MgIIλ2798
Ne[V]λ3426
Ne[III]λ3869
Hγ
Hβ
O[III]λ5007
O[II]λ3727
Hδ
MJD
52141
57597
$f_\lambda(10^{-17}$ erg cm^{-2} s^{-1} Å^{-1}
Wavelength in QSO restframe (Å)

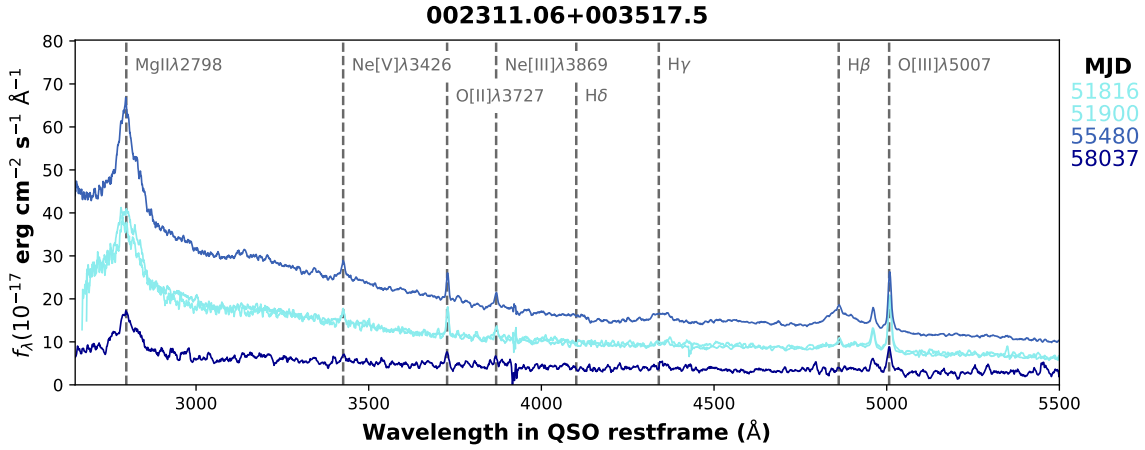
002311.06+003517.5
MgIIλ2798
Ne[V]λ3426
Ne[III]λ3869
Hγ
Hβ
O[III]λ5007
O[II]λ3727
Hδ
MJD
51816
51900
55480
58037
$f_\lambda(10^{-17}$ erg cm^{-2} s^{-1} Å^{-1}
Wavelength in QSO restframe (Å)

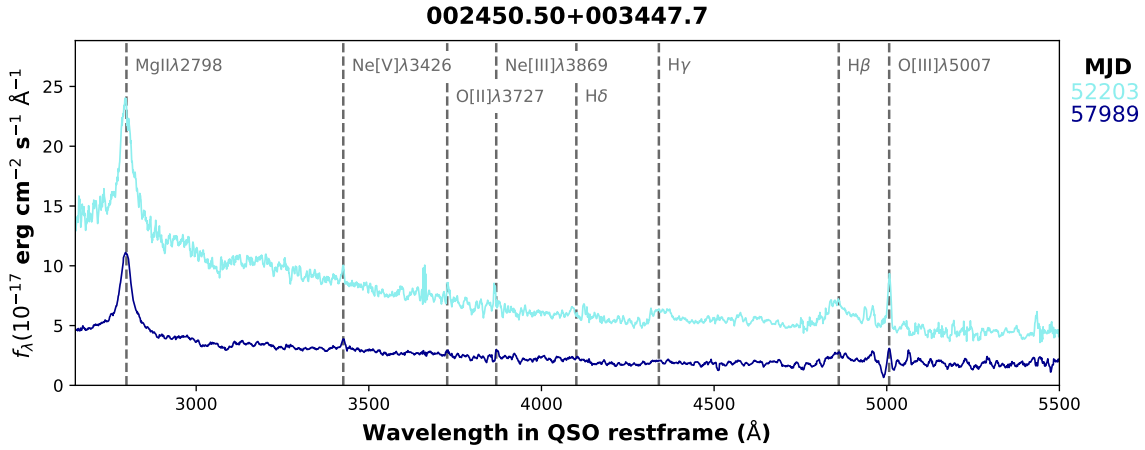
002450.50+003447.7
MgIIλ2798
Ne[V]λ3426
Ne[III]λ3869
Hγ
Hβ
O[III]λ5007
O[II]λ3727
Hδ
MJD
52203
57989
$f_\lambda(10^{-17}$ erg cm^{-2} s^{-1} Å^{-1}
Wavelength in QSO restframe (Å)

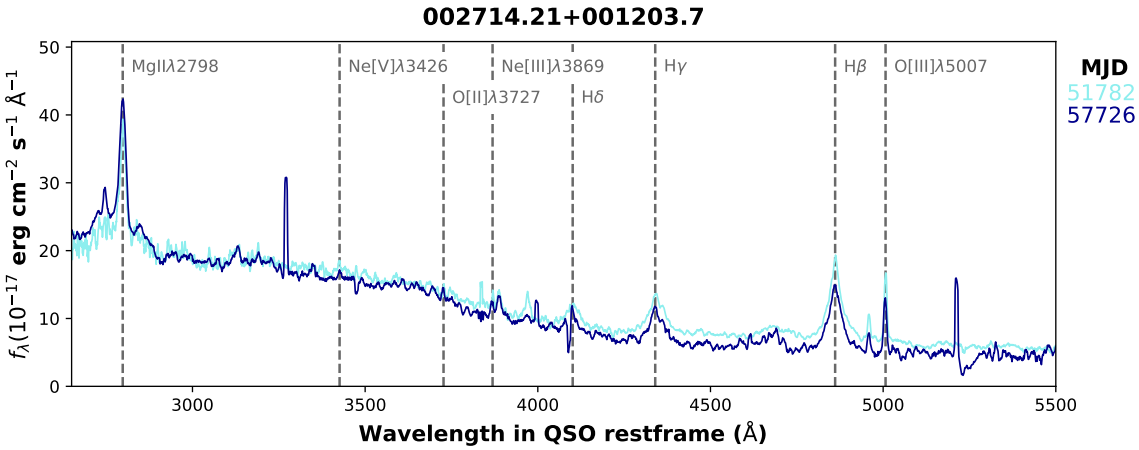
002714.21+001203.7
MgIIλ2798
Ne[V]λ3426
Ne[III]λ3869
Hγ
Hβ
O[III]λ5007
O[II]λ3727
Hδ
MJD
51782
57726
$f_\lambda(10^{-17}$ erg cm^{-2} s^{-1} Å^{-1})
Wavelength in QSO restframe (Å)

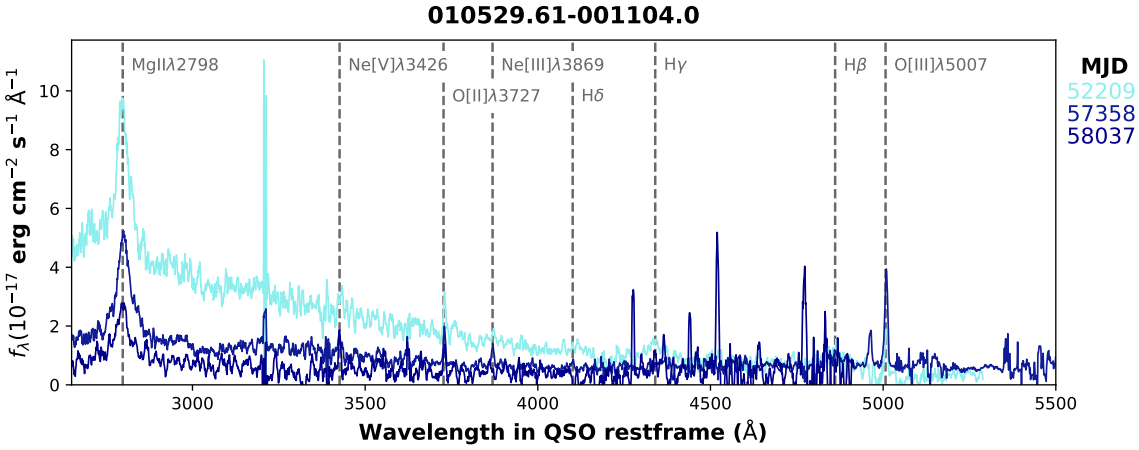
010529.61-001104.0
MgIIλ2798
Ne[V]λ3426
Ne[III]λ3869
Hγ
Hβ
O[III]λ5007
O[II]λ3727
Hδ
MJD
52209
57358
58037
$f_\lambda(10^{-17}$ erg cm^{-2} s^{-1} Å^{-1})
Wavelength in QSO restframe (Å)

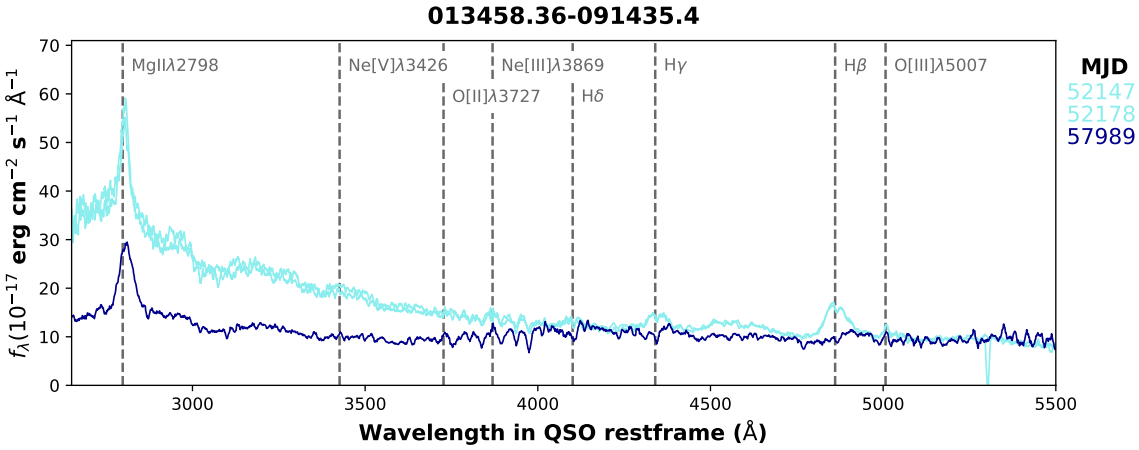
013458.36-091435.4
MgIIλ2798
Ne[V]λ3426
Ne[III]λ3869
Hγ
Hβ
O[III]λ5007
O[II]λ3727
Hδ
MJD
52147
52178
57989
$f_\lambda(10^{-17}$ erg cm^{-2} s^{-1} Å^{-1})
Wavelength in QSO restframe (Å)

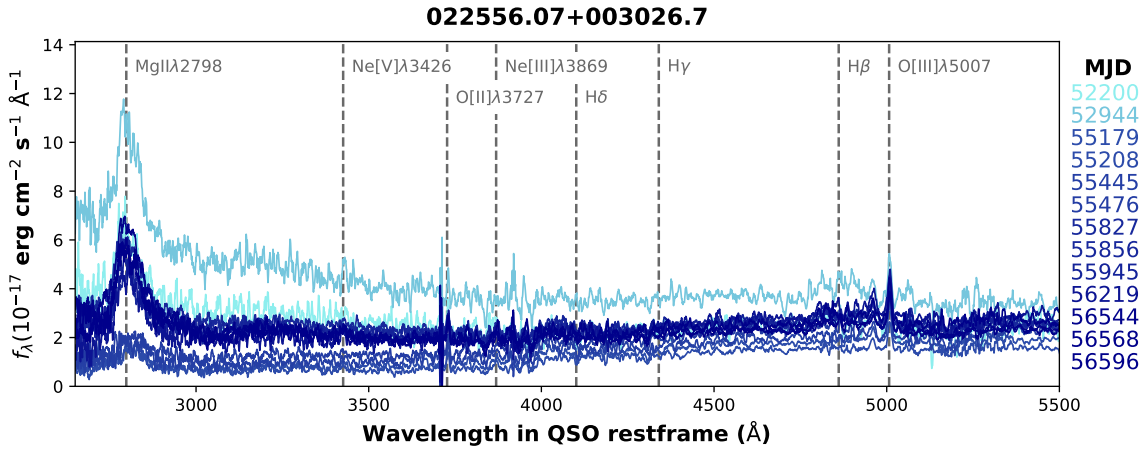
022556.07+003026.7
MgIIλ2798
Ne[V]λ3426
Ne[III]λ3869
Hγ
Hβ
O[III]λ5007
O[II]λ3727
Hδ
MJD
52200
52944
55179
55208
55445
55476
55827
55856
55945
56219
56544
56568
56596
$f_\lambda(10^{-17}$ erg cm^{-2} s^{-1} Å^{-1})
Wavelength in QSO restframe (Å)

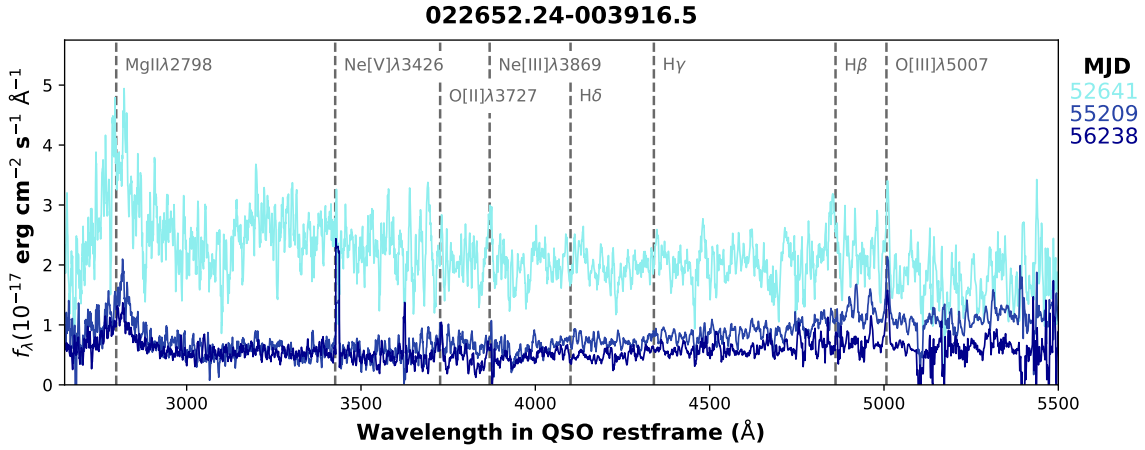
022652.24-003916.5
MgIIλ2798
Ne[V]λ3426
Ne[III]λ3869
Hγ
Hβ
O[III]λ5007
O[II]λ3727
Hδ
MJD
52641
55209
56238
$f_\lambda(10^{-17}$ erg cm^{-2} s^{-1} Å^{-1})
Wavelength in QSO restframe (Å)

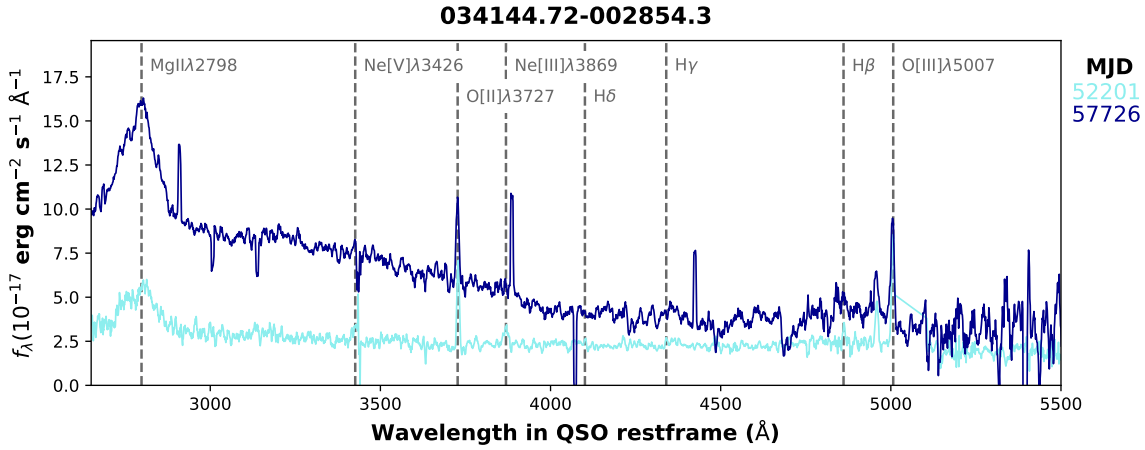
034144.72-002854.3
MgIIλ2798
Ne[V]λ3426
Ne[III]λ3869
Hγ
Hβ
O[III]λ5007
O[II]λ3727
Hδ
MJD
52201
57726
$f_\lambda(10^{-17}$ erg cm^{-2} s^{-1} Å^{-1})
Wavelength in QSO restframe (Å)

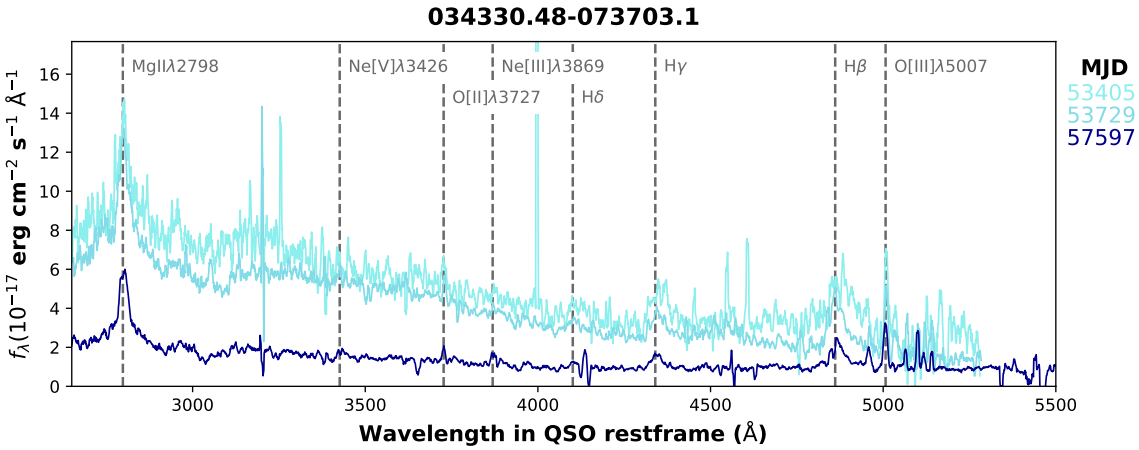
034330.48-073703.1
MgIIλ2798
Ne[V]λ3426
Ne[III]λ3869
Hγ
Hβ
O[III]λ5007
O[II]λ3727
Hδ
MJD
53405
53729
57597
$f_\lambda(10^{-17}$ erg cm^{-2} s^{-1} Å^{-1}
Wavelength in QSO restframe (Å)

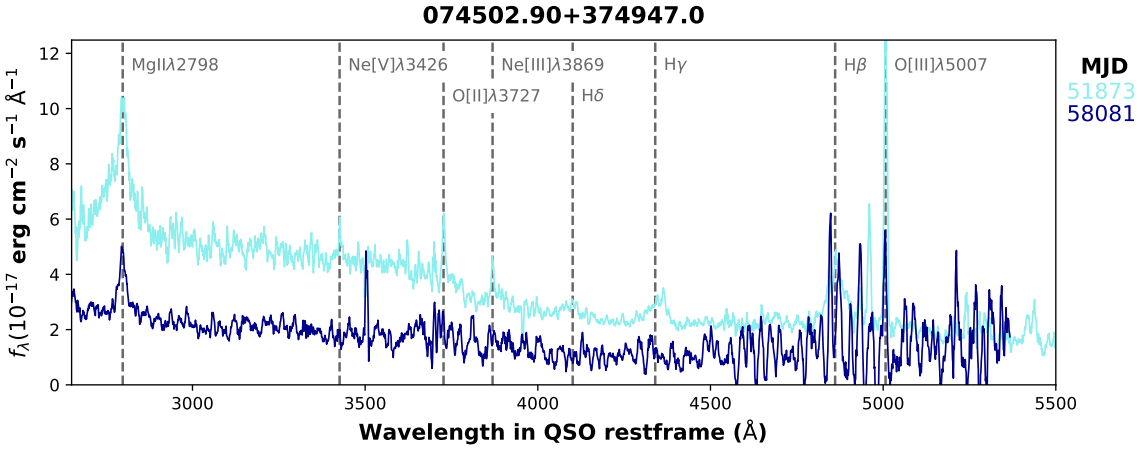
074502.90+374947.0
MgIIλ2798
Ne[V]λ3426
Ne[III]λ3869
Hγ
Hβ
O[III]λ5007
O[II]λ3727
Hδ
MJD
51873
58081
$f_\lambda(10^{-17}$ erg cm^{-2} s^{-1} Å^{-1}
Wavelength in QSO restframe (Å)

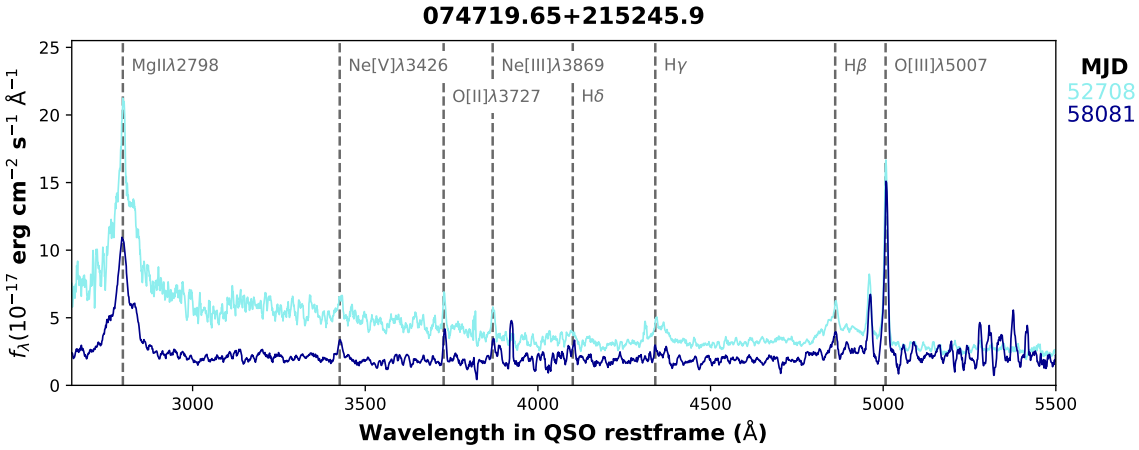
074719.65+215245.9
MgIIλ2798
Ne[V]λ3426
Ne[III]λ3869
Hγ
Hβ
O[III]λ5007
O[II]λ3727
Hδ
MJD
52708
58081
$f_\lambda(10^{-17}$ erg cm^{-2} s^{-1} Å^{-1}
Wavelength in QSO restframe (Å)

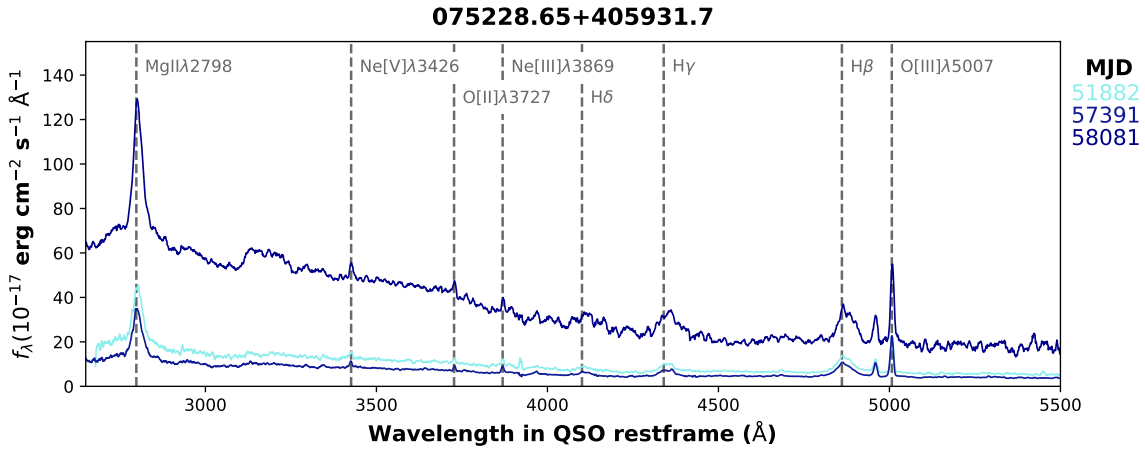
075228.65+405931.7
MgIIλ2798
Ne[V]λ3426
Ne[III]λ3869
Hγ
Hβ
O[III]λ5007
O[II]λ3727
Hδ
MJD
51882
57391
58081
$f_\lambda(10^{-17}$ erg cm^{-2} s^{-1} Å^{-1}
Wavelength in QSO restframe (Å)

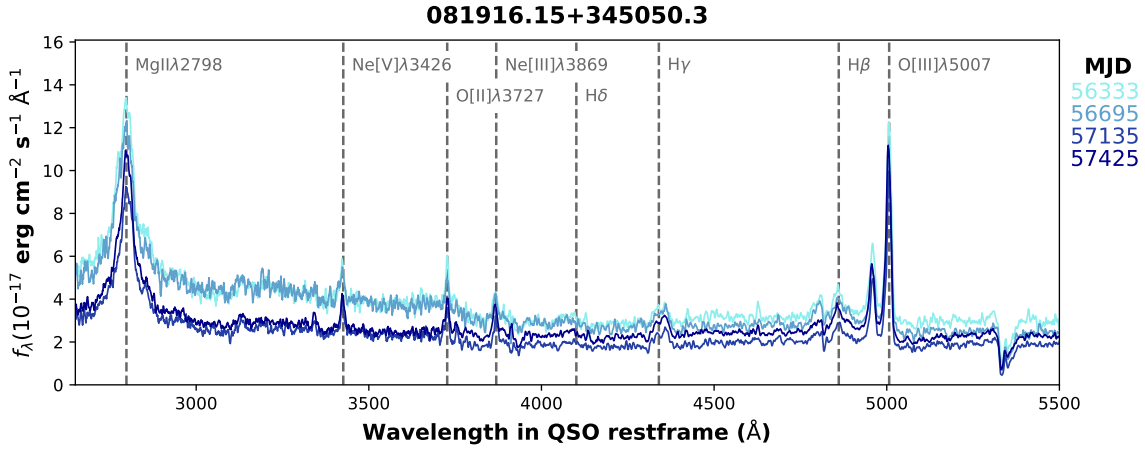
081916.15+345050.3
MgIIλ2798
Ne[V]λ3426
Ne[III]λ3869
Hγ
Hβ
O[III]λ5007
O[II]λ3727
Hδ
MJD
56333
56695
57135
57425
$f_\lambda(10^{-17}$ erg cm^{-2} s^{-1} Å^{-1}
Wavelength in QSO restframe (Å)

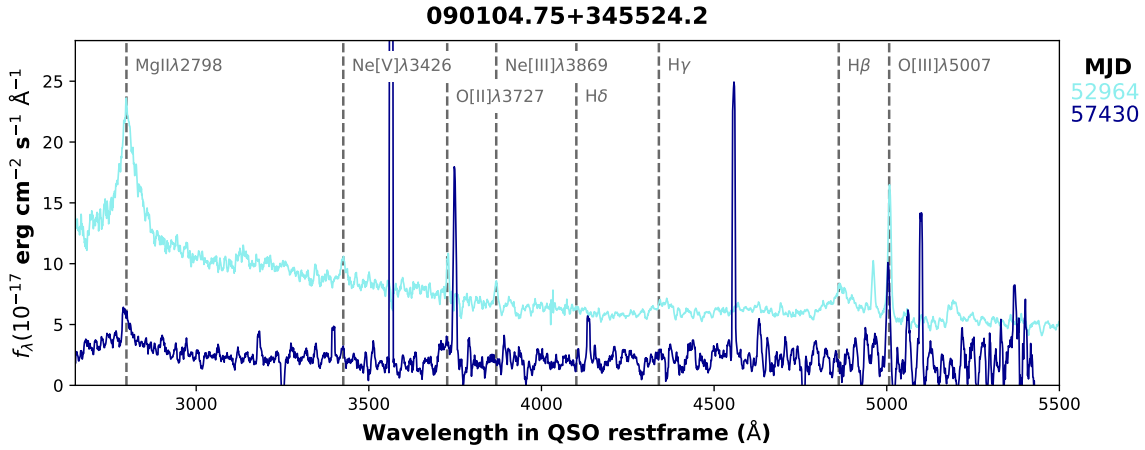
090104.75+345524.2
MgIIλ2798
Ne[V]λ3426
Ne[III]λ3869
Hγ
Hβ
O[III]λ5007
O[II]λ3727
Hδ
MJD
52964
57430
$f_\lambda(10^{-17}$ erg cm^{-2} s^{-1} Å^{-1}
Wavelength in QSO restframe (Å)

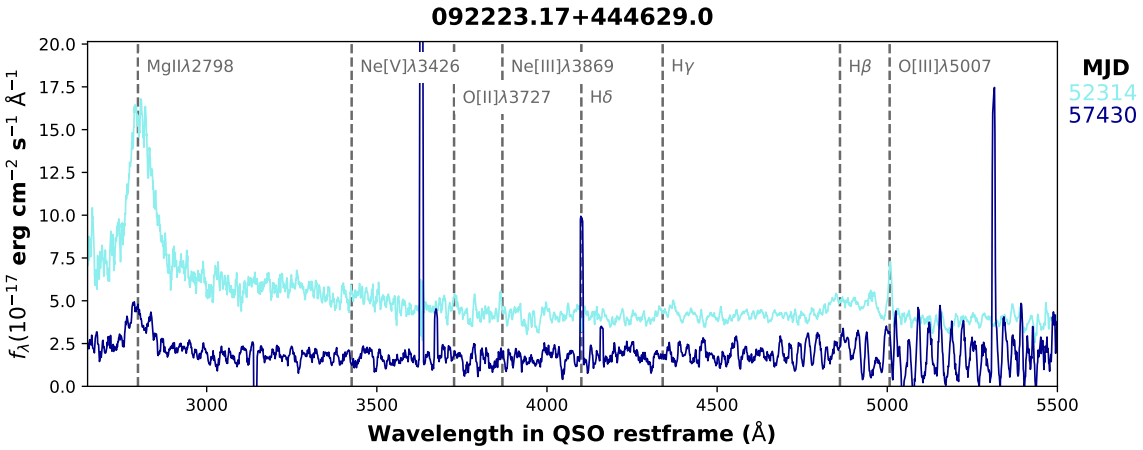
092223.17+444629.0
MgIIλ2798
Ne[V]λ3426
Ne[III]λ3869
Hγ
Hβ
O[III]λ5007
O[II]λ3727
Hδ
MJD
52314
57430
$f_\lambda(10^{-17}$ erg cm^{-2} s^{-1} Å^{-1}
Wavelength in QSO restframe (Å)

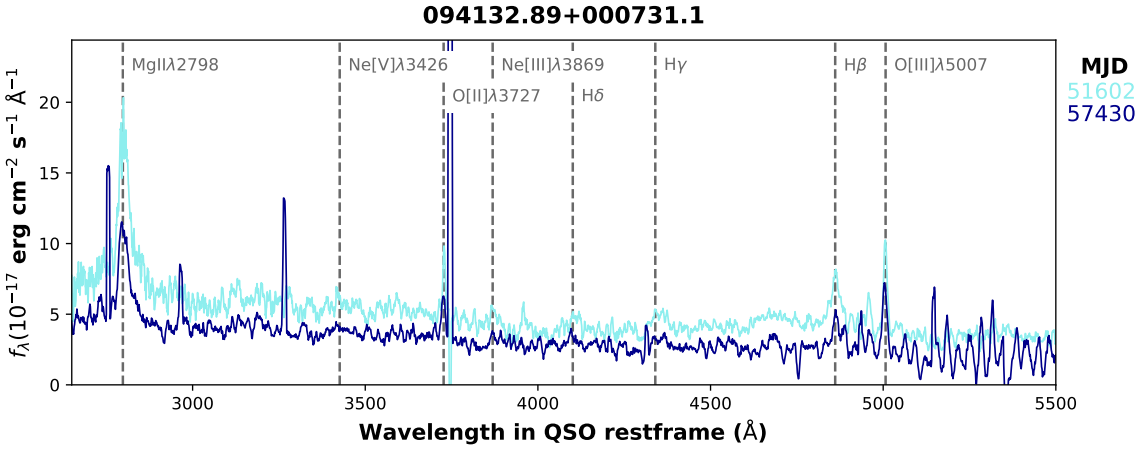
094132.89+000731.1
MgIIλ2798
Ne[V]λ3426
Ne[III]λ3869
Hγ
Hβ
O[III]λ5007
O[II]λ3727
Hδ
MJD
51602
57430
$f_\lambda(10^{-17}$ erg cm^{-2} s^{-1} Å^{-1}
Wavelength in QSO restframe (Å)

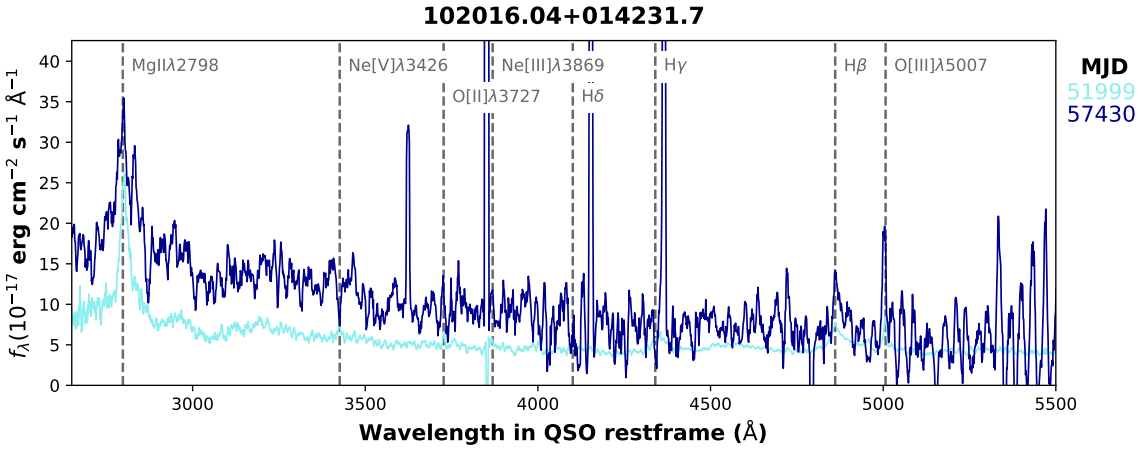
102016.04+014231.7
MgIIλ2798
Ne[V]λ3426
Ne[III]λ3869
Hγ
Hβ
O[III]λ5007
O[II]λ3727
Hδ
MJD
51999
57430
$f_\lambda(10^{-17}$ erg cm^{-2} s^{-1} Å^{-1}
Wavelength in QSO restframe (Å)

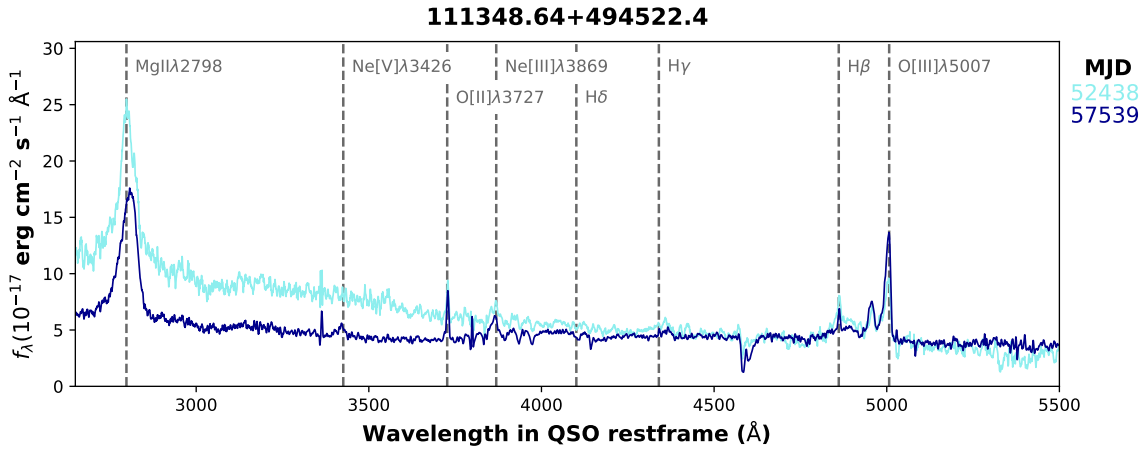
111348.64+494522.4
MgIIλ2798
Ne[V]λ3426
O[II]λ3727
Ne[III]λ3869
Hδ
Hγ
Hβ
O[III]λ5007
MJD
52438
57539
$f_\lambda(10^{-17}$ erg cm^{-2} s^{-1} Å^{-1}
Wavelength in QSO restframe (Å)

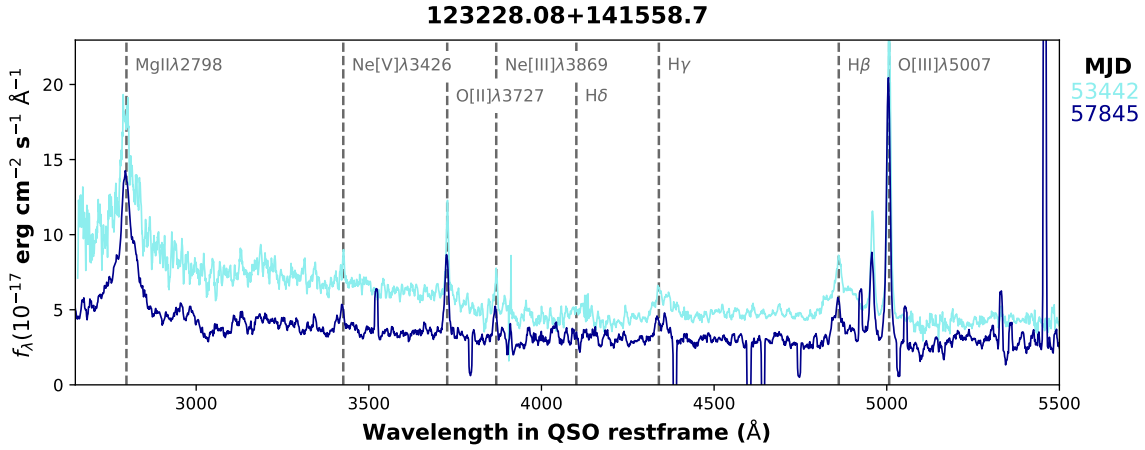
123228.08+141558.7
MgIIλ2798
Ne[V]λ3426
O[II]λ3727
Ne[III]λ3869
Hδ
Hγ
Hβ
O[III]λ5007
MJD
53442
57845
$f_\lambda(10^{-17}$ erg cm^{-2} s^{-1} Å^{-1}
Wavelength in QSO restframe (Å)

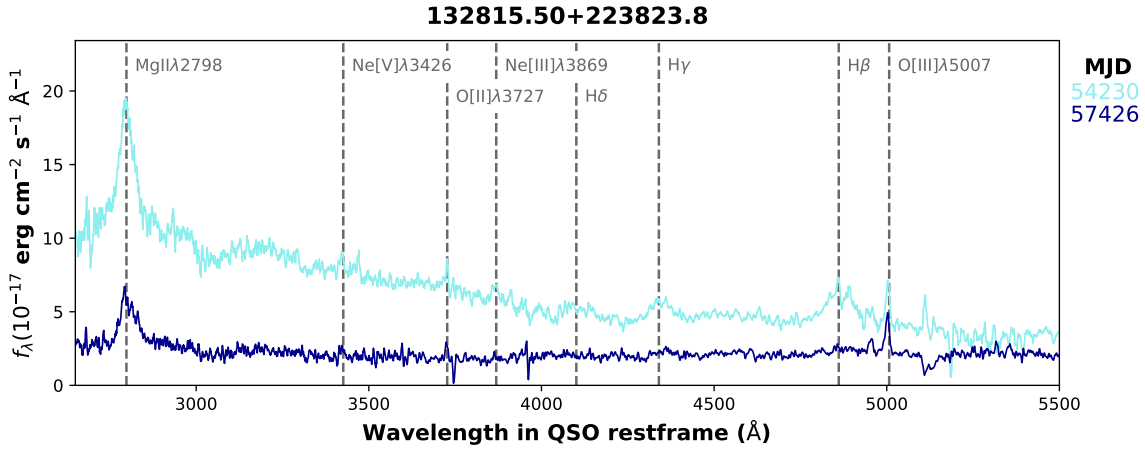
132815.50+223823.8
MgIIλ2798
Ne[V]λ3426
O[II]λ3727
Ne[III]λ3869
Hδ
Hγ
Hβ
O[III]λ5007
MJD
54230
57426
$f_\lambda(10^{-17}$ erg cm^{-2} s^{-1} Å^{-1}
Wavelength in QSO restframe (Å)

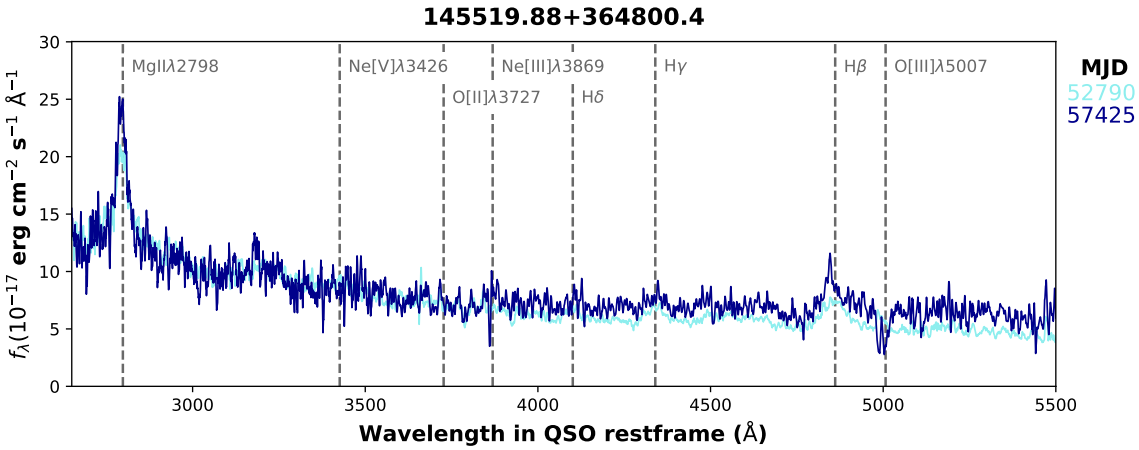
145519.88+364800.4
MgIIλ2798
Ne[V]λ3426
Ne[III]λ3869
Hγ
Hβ
O[III]λ5007
O[II]λ3727
Hδ
MJD
52790
57425
$f_\lambda(10^{-17}$ erg cm^{-2} s^{-1} Å^{-1}
Wavelength in QSO restframe (Å)

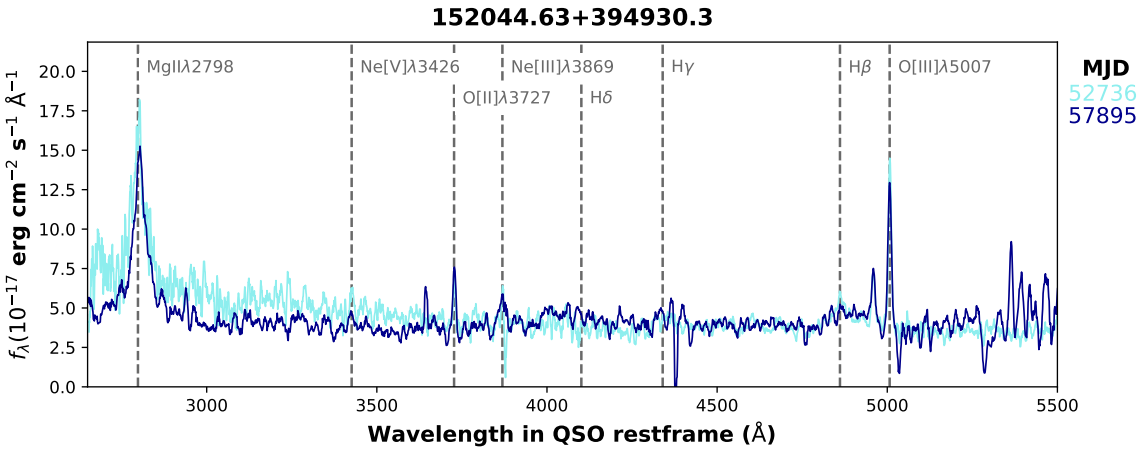
152044.63+394930.3
MgIIλ2798
Ne[V]λ3426
Ne[III]λ3869
Hγ
Hβ
O[III]λ5007
O[II]λ3727
Hδ
MJD
52736
57895
$f_\lambda(10^{-17}$ erg cm^{-2} s^{-1} Å^{-1}
Wavelength in QSO restframe (Å)

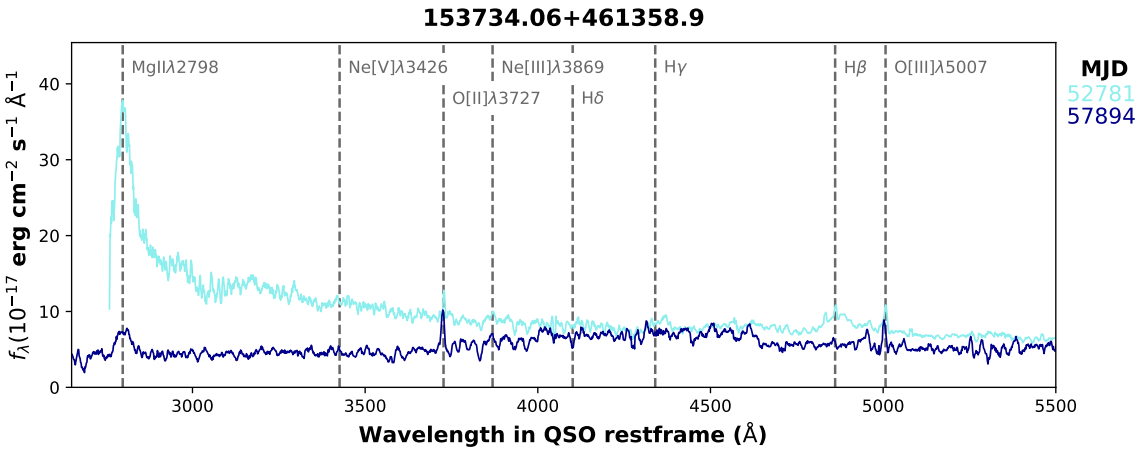
153734.06+461358.9
MgIIλ2798
Ne[V]λ3426
Ne[III]λ3869
Hγ
Hβ
O[III]λ5007
O[II]λ3727
Hδ
MJD
52781
57894
$f_\lambda(10^{-17}$ erg cm^{-2} s^{-1} Å^{-1}
Wavelength in QSO restframe (Å)

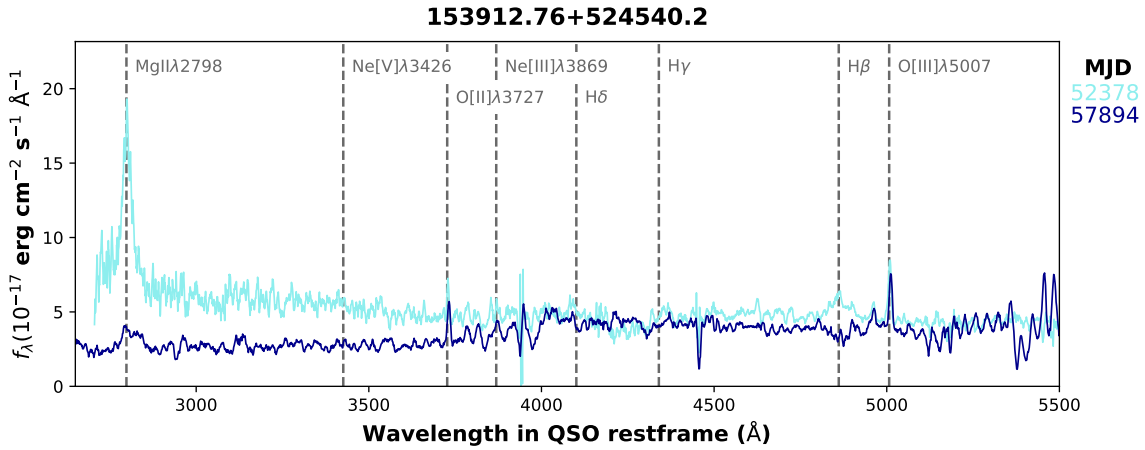
153912.76+524540.2
MgIIλ2798
Ne[V]λ3426
Ne[III]λ3869
Hγ
Hβ
O[III]λ5007
O[II]λ3727
Hδ
MJD
52378
57894
$f_\lambda(10^{-17}$ erg cm^{-2} s^{-1} Å^{-1}
Wavelength in QSO restframe (Å)

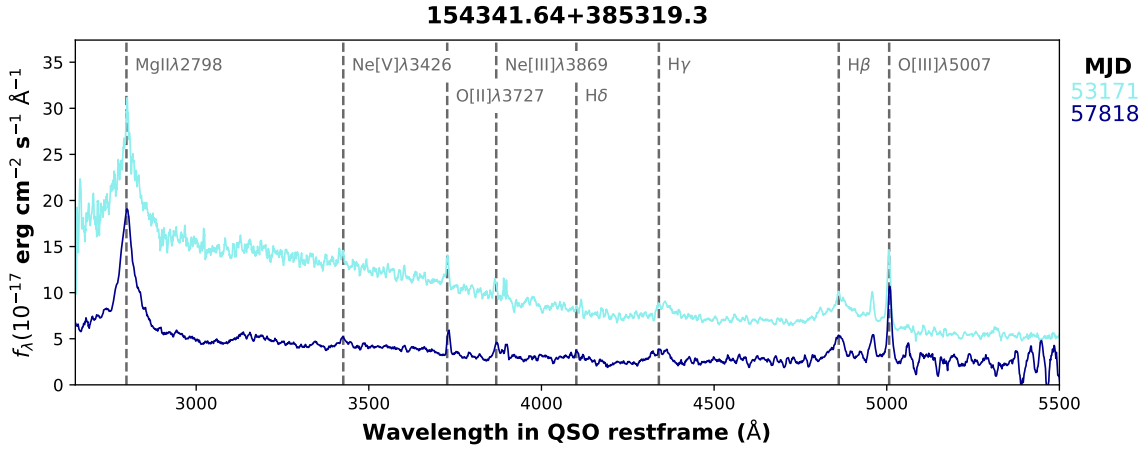
154341.64+385319.3
MgIIλ2798
Ne[V]λ3426
Ne[III]λ3869
Hγ
Hβ
O[III]λ5007
O[II]λ3727
Hδ
MJD
53171
57818
$f_\lambda(10^{-17}$ erg cm^{-2} s^{-1} Å^{-1}
Wavelength in QSO restframe (Å)

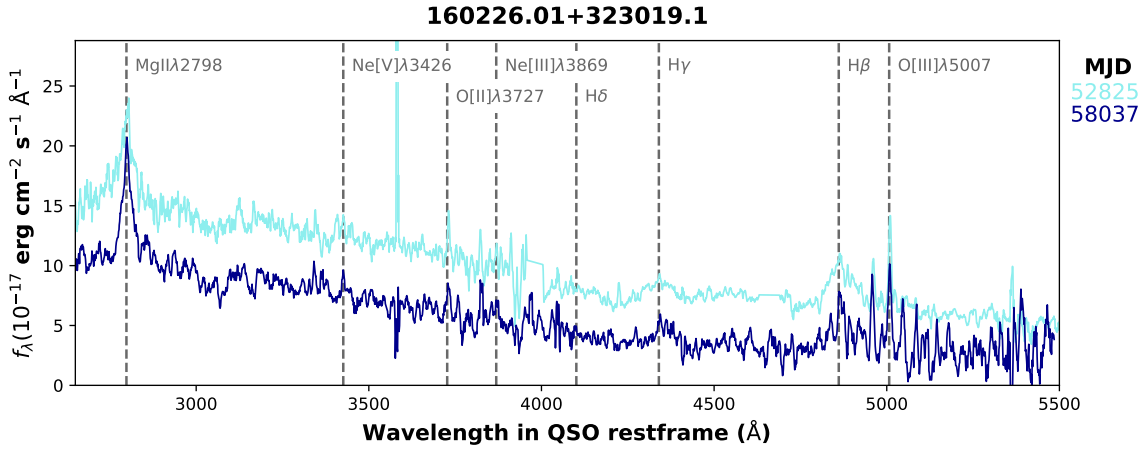
160226.01+323019.1
MgIIλ2798
Ne[V]λ3426
Ne[III]λ3869
Hγ
Hβ
O[III]λ5007
O[II]λ3727
Hδ
MJD
52825
58037
$f_\lambda(10^{-17}$ erg cm^{-2} s^{-1} Å^{-1}
Wavelength in QSO restframe (Å)

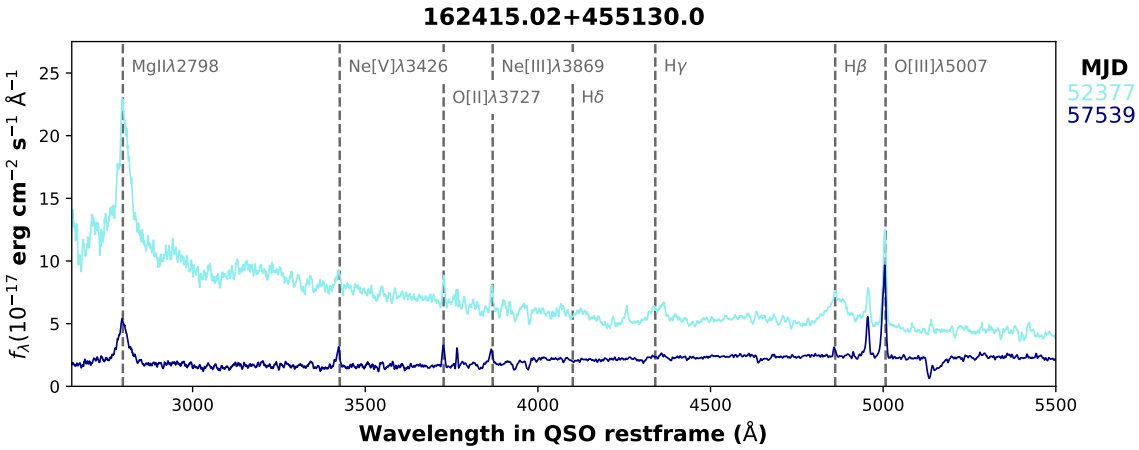
162415.02+455130.0
MgIIλ2798
Ne[V]λ3426
Ne[III]λ3869
Hγ
Hβ
O[III]λ5007
O[II]λ3727
Hδ
MJD
52377
57539
$f_\lambda(10^{-17}$ erg cm^{-2} s^{-1} Å^{-1}
Wavelength in QSO restframe (Å)

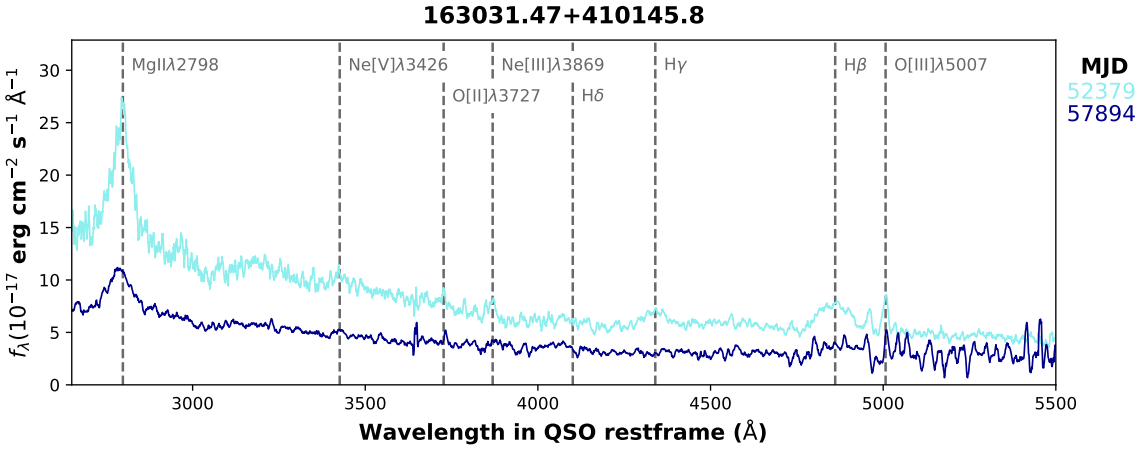
163031.47+410145.8
MgIIλ2798
Ne[V]λ3426
Ne[III]λ3869
Hγ
Hβ
O[III]λ5007
O[II]λ3727
Hδ
MJD
52379
57894
$f_\lambda(10^{-17}$ erg cm^{-2} s^{-1} Å^{-1}
Wavelength in QSO restframe (Å)

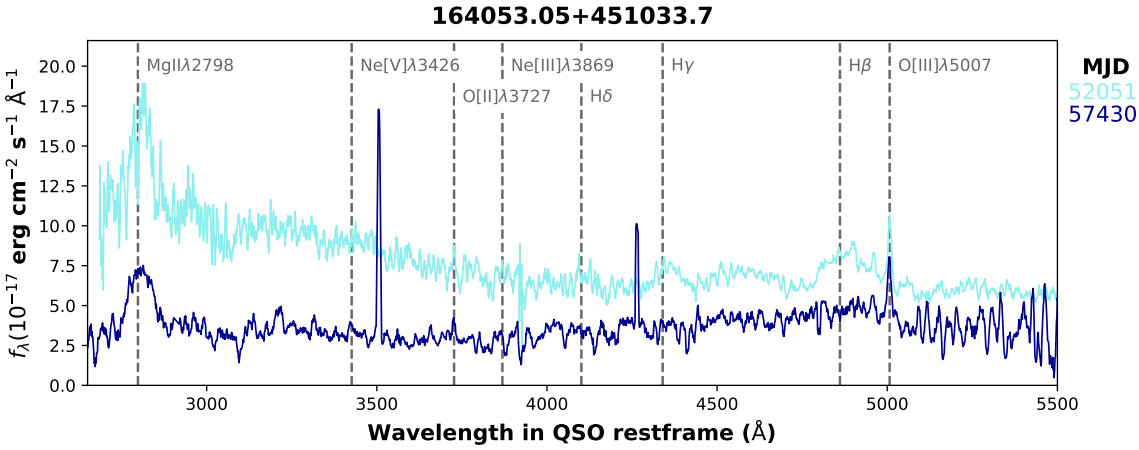
164053.05+451033.7
MgIIλ2798
Ne[V]λ3426
Ne[III]λ3869
Hγ
Hβ
O[III]λ5007
O[II]λ3727
Hδ
MJD
52051
57430
$f_\lambda(10^{-17}$ erg cm^{-2} s^{-1} Å^{-1}
Wavelength in QSO restframe (Å)

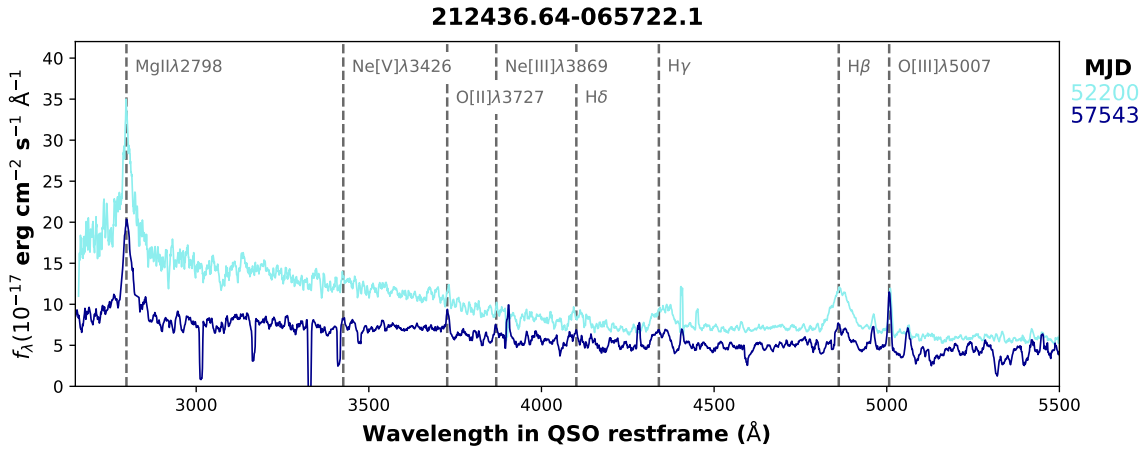
212436.64-065722.1
MgIIλ2798
Ne[V]λ3426
Ne[III]λ3869
Hγ
Hβ
O[III]λ5007
O[II]λ3727
Hδ
MJD
52200
57543
$f_\lambda(10^{-17}$ erg cm^{-2} s^{-1} Å^{-1}
Wavelength in QSO restframe (Å)

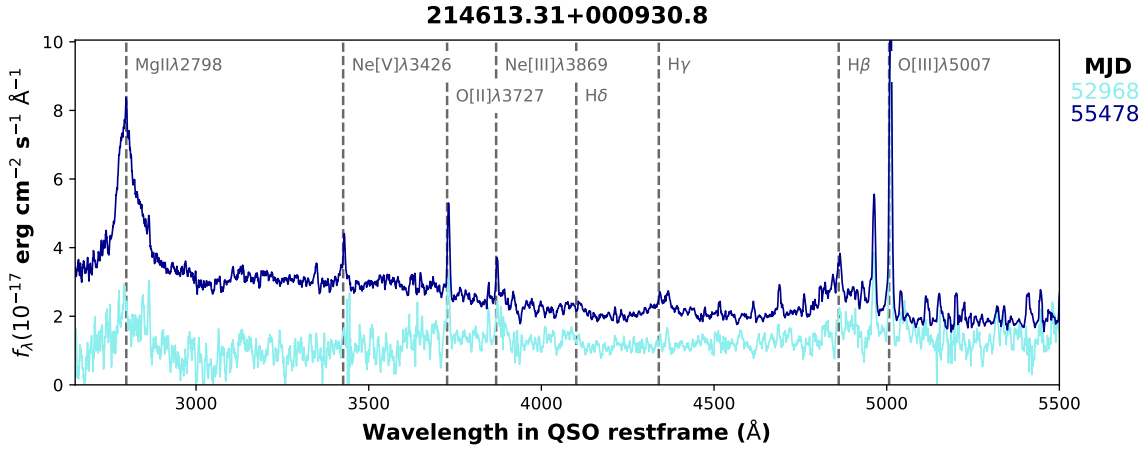
214613.31+000930.8
MgIIλ2798
Ne[V]λ3426
Ne[III]λ3869
Hγ
Hβ
O[III]λ5007
O[II]λ3727
Hδ
MJD
52968
55478
$f_\lambda(10^{-17}$ erg cm^{-2} s^{-1} Å^{-1}
Wavelength in QSO restframe (Å)

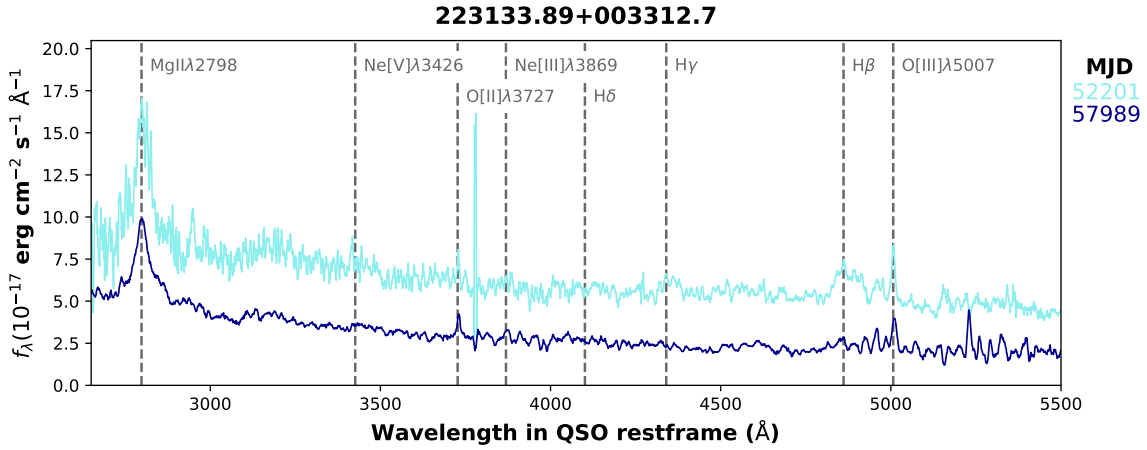
223133.89+003312.7
MgIIλ2798
Ne[V]λ3426
Ne[III]λ3869
Hγ
Hβ
O[III]λ5007
O[II]λ3727
Hδ
MJD
52201
57989
$f_\lambda(10^{-17}$ erg cm^{-2} s^{-1} Å^{-1}
Wavelength in QSO restframe (Å)

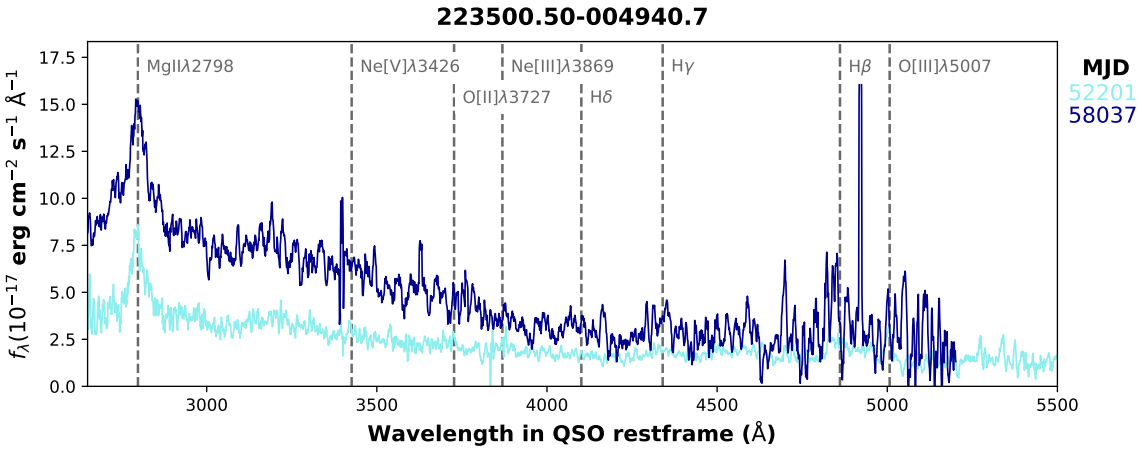
223500.50-004940.7
MgIIλ2798
Ne[V]λ3426
Ne[III]λ3869
Hγ
Hβ
O[III]λ5007
O[II]λ3727
Hδ
MJD
52201
58037
$f_\lambda(10^{-17}$ erg cm^{-2} s^{-1} Å^{-1}
Wavelength in QSO restframe (Å)

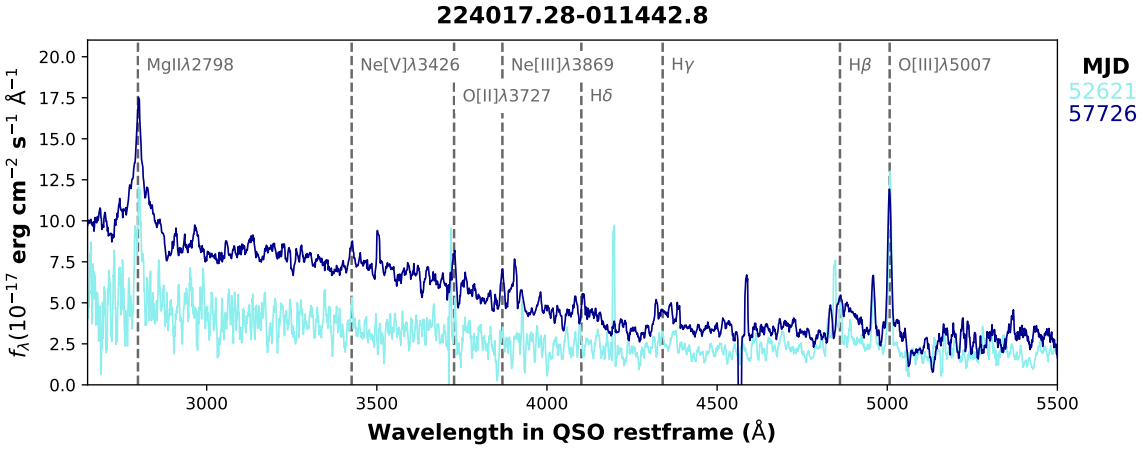
224017.28-011442.8
MgIIλ2798
Ne[V]λ3426
Ne[III]λ3869
Hγ
Hβ
O[III]λ5007
O[II]λ3727
Hδ
MJD
52621
57726
$f_\lambda(10^{-17}$ erg cm^{-2} s^{-1} Å^{-1}
Wavelength in QSO restframe (Å)

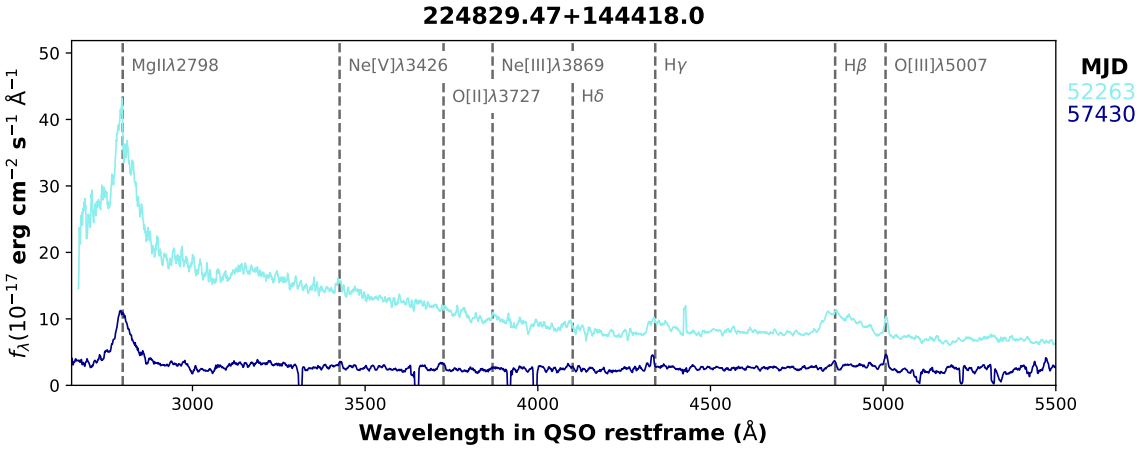
224829.47+144418.0
MgIIλ2798
Ne[V]λ3426
Ne[III]λ3869
Hγ
Hβ
O[III]λ5007
O[II]λ3727
Hδ
MJD
52263
57430
$f_\lambda(10^{-17}$ erg cm^{-2} s^{-1} Å^{-1}
Wavelength in QSO restframe (Å)

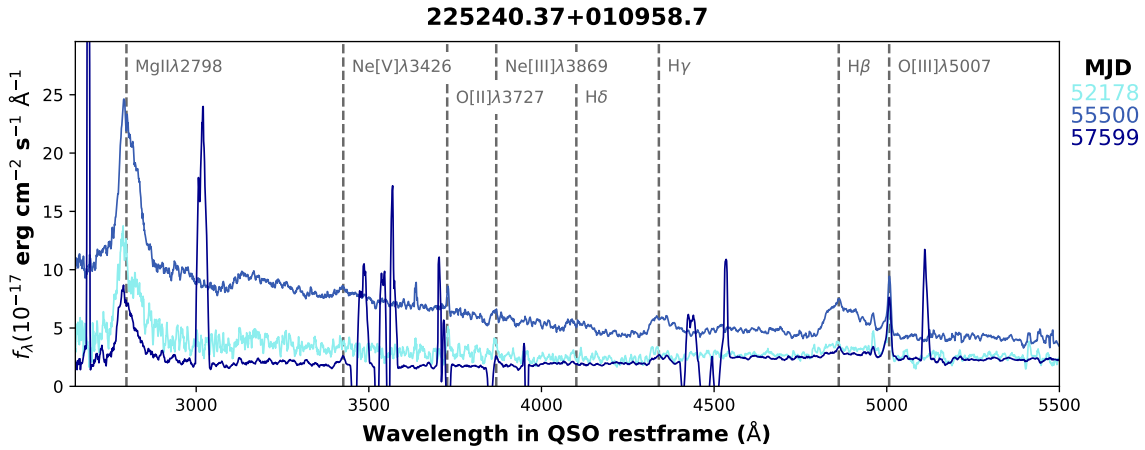
225240.37+010958.7
MgIIλ2798
Ne[V]λ3426
Ne[III]λ3869
Hγ
Hβ
O[III]λ5007
O[II]λ3727
Hδ
MJD
52178
55500
57599
$f_\lambda(10^{-17}$ erg cm^{-2} s^{-1} Å^{-1}
Wavelength in QSO restframe (Å)

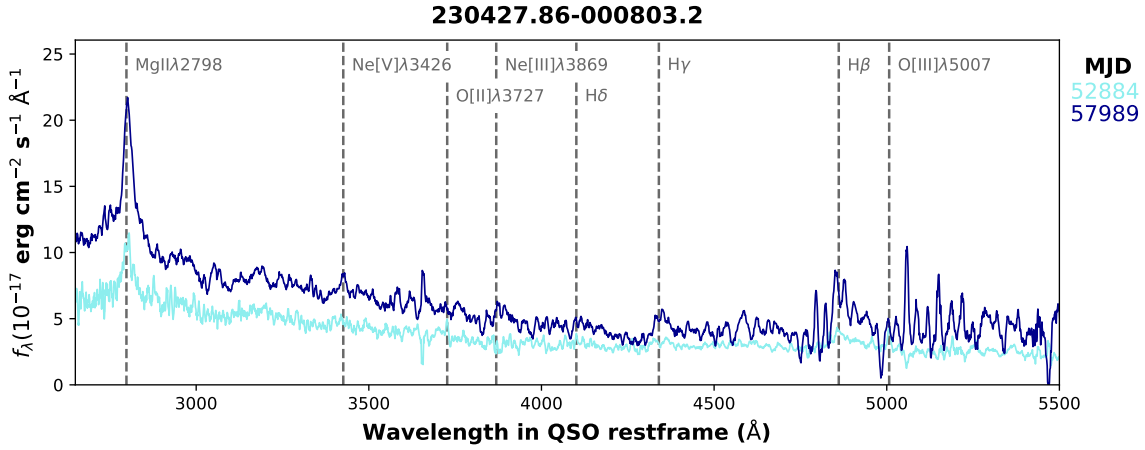
230427.86-000803.2
MgIIλ2798
Ne[V]λ3426
Ne[III]λ3869
Hγ
Hβ
O[III]λ5007
O[II]λ3727
Hδ
MJD
52884
57989
$f_\lambda(10^{-17}$ erg cm^{-2} s^{-1} Å^{-1}
Wavelength in QSO restframe (Å)

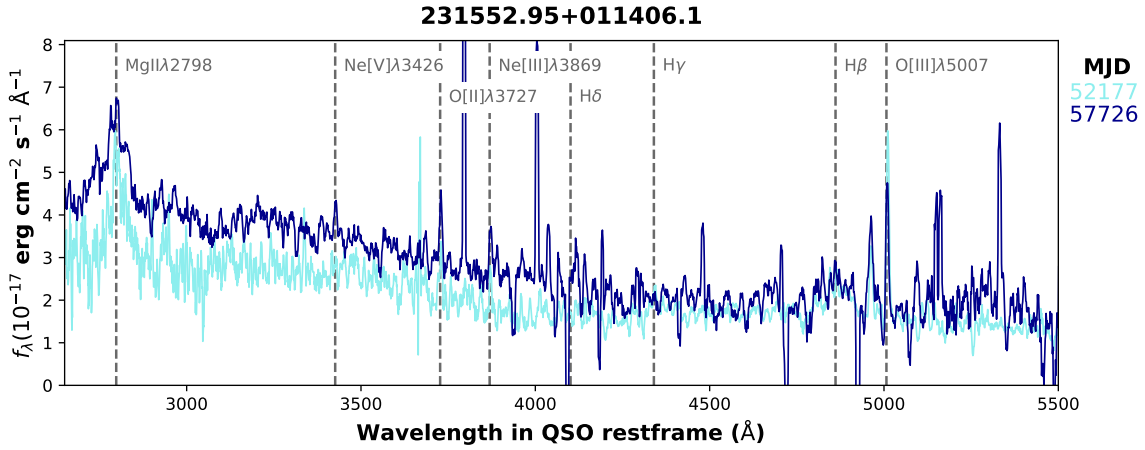
231552.95+011406.1
MgIIλ2798
Ne[V]λ3426
Ne[III]λ3869
Hγ
Hβ
O[III]λ5007
O[II]λ3727
Hδ
MJD
52177
57726
$f_\lambda(10^{-17}$ erg cm^{-2} s^{-1} Å^{-1}
Wavelength in QSO restframe (Å)

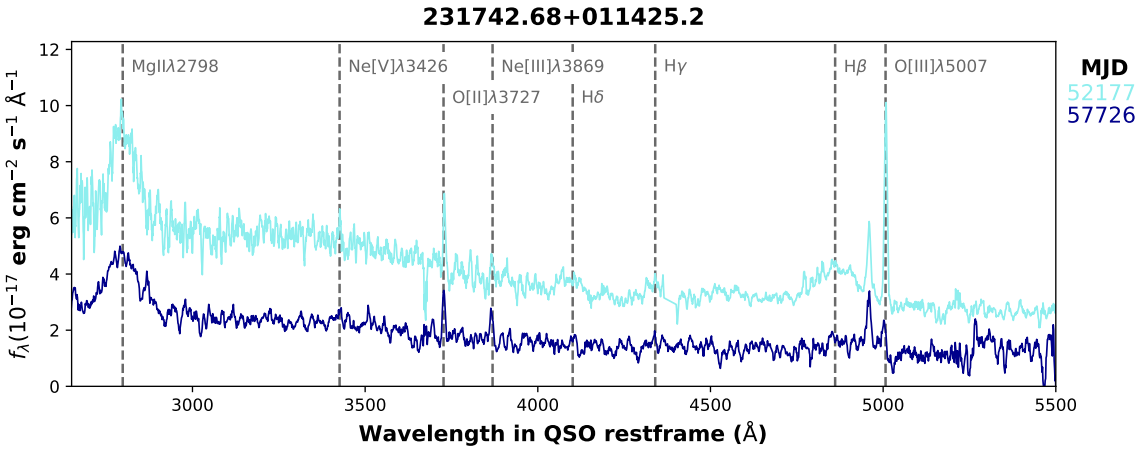
231742.68+011425.2
MgIIλ2798
Ne[V]λ3426
Ne[III]λ3869
Hγ
Hβ
O[III]λ5007
O[II]λ3727
Hδ
MJD
52177
57726
$f_\lambda(10^{-17}$ erg cm^{-2} s^{-1} Å^{-1}
Wavelength in QSO restframe (Å)

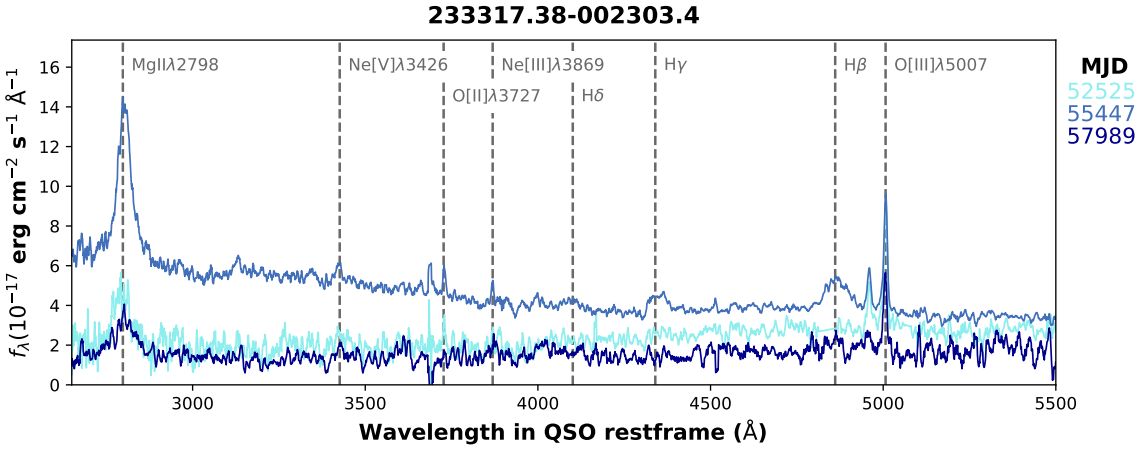
233317.38-002303.4
MgIIλ2798
Ne[V]λ3426
Ne[III]λ3869
Hγ
Hβ
O[III]λ5007
O[II]λ3727
Hδ
MJD
52525
55447
57989
$f_\lambda(10^{-17}$ erg cm^{-2} s^{-1} Å^{-1}
Wavelength in QSO restframe (Å)

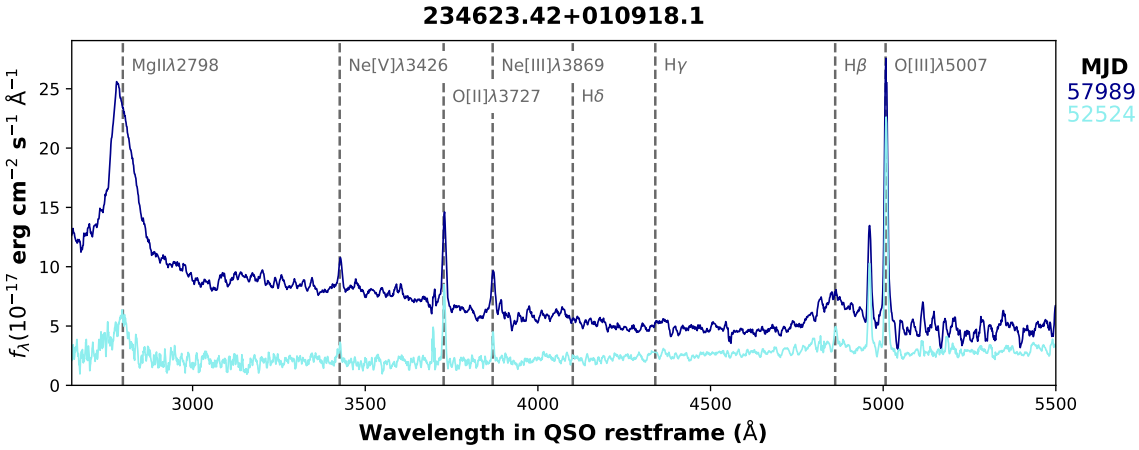
234623.42+010918.1
MgIIλ2798
Ne[V]λ3426
Ne[III]λ3869
Hγ
Hβ
O[III]λ5007
O[II]λ3727
Hδ
MJD
57989
52524
$f_\lambda(10^{-17}$ erg cm^{-2} s^{-1} Å^{-1}
Wavelength in QSO restframe (Å)

Bibliography

Abolfathi B., et al., 2018, The Astrophysical Journal Supplement, 235, 42

Ahn C. P., et al. 2013, VizieR Online Data Catalog, p. V/139

Angel J. R. P., Hilliard R. L., Weymann R. J., 1979, in Weekes T. C., ed., SAO Special Report Vol. 385, The MMT and the Future of Ground-Based Astronomy. p. 87

Antonucci R., 1993, ARA&A, 31, 473

Antonucci R., 2012, Astronomical and Astrophysical Transactions, 27, 557

Antonucci R. R. J., Miller J. S., 1985, ApJ, 297, 621

Aretxaga I., et al., 1999, ApJ, 519, L123

Baker J. G., Menzel D. H., 1938, ApJ, 88, 52

Balbus S. A., Hawley J. F., 1991, ApJ, 376, 214

Baldwin J. A., 1977, ApJ, 214, 679

Baldwin J., Burke W., Gaskell C., Wampler E., 1978, Nature, 273, 431

Baldwin J. A., Phillips M. M., Terlevich R., 1981, PASP, 93, 5

Baldwin J., Ferland G., Korista K., Verner D., 1995, The Astrophysical Journal Letters, 455, L119

Barth A. J., et al., 2015, ApJS, 217, 26

Baskin A., Laor A., 2018, MNRAS, 474, 1970

Baskin A., Laor A., Stern J., 2014a, MNRAS, 438, 604

Baskin A., Laor A., Stern J., 2014b, MNRAS, 445, 3025

Bassett B., Hlozek R., 2010, Baryon acoustic oscillations. p. 246

Bentz M. C., et al., 2010, ApJ, 716, 993

Bentz M. C., et al., 2013, ApJ, 767, 149

Berman L., 1936, MNRAS, 96, 890

Bischoff K., Kollatschny W., 1999, Astronomy & Astrophysics, 345, 49

Blaes O., 2014, Space Sci. Rev., 183, 21

Blanchard P. K., et al., 2017, ApJ, 843, 106

Blandford R. D., McKee C. F., 1982, The Astrophysical Journal, 255, 419

Boller T., Balestra I., Kollatschny W., 2007, A&A, 465, 87

Bolton A. S., et al., 2012, The Astronomical Journal, 144, 144

Boroson T. A., Green R. F., 1992, ApJS, 80, 109

Bruce A., 2018, PhD thesis, Universiry of Edinburgh

Bruce A., et al., 2017, MNRAS, 467, 1259

Bruhweiler F., Verner E., 2008, ApJ, 675, 83

Cackett E. M., et al., 2015, ApJ, 810, 86

Cackett E. M., et al., 2018, ApJ, 857, 53

Capellupo D. M., et al., 2015, MNRAS, 446, 3427

Cardelli J. A., Clayton G. C., Mathis J. S., 1989, ApJ, 345, 245

Chiang J., Murray N., 1996, ApJ, 466, 704

Clavel J., et al., 1991, ApJ, 366, 64

Cohen R. D., et al., 1986, ApJ, 311, 135
Collin-Souffrin S., Dumnont S., Joly M., Pequignot D., 1986, A&A, 166, 27
Condon J. J., 1992, ARA&A, 30, 575
Condon J. J., et al., 1998, AJ, 115, 1693
Czerny B., Hryniewicz K., 2011, A&A, 525, L8
Czerny B., Naddaf M.-H., 2018, preprint, p. arXiv:1811.04326
De Rosa G., et al., 2015, ApJ, 806, 128
Denney K. D., et al., 2014, ApJ, 796, 134
Devereux N., 2018, MNRAS, 473, 2930
Dexter J., Agol E., 2011, The Astrophysical Journal Letters, 727, L24
Dexter J., Begelman M. C., 2019, MNRAS, 483, L17
Dietrich M., et al., 2002, The Astrophysical Journal, 581, 912
Dong X.-B., et al., 2009, ApJ, 703, L1
Drake A. J., et al., 2009, ApJ, 696, 870
Edge D. O., et al., 1959, Mem. RAS, 68, 37
Elitzur M., Ho L. C., 2009, ApJ, 701, L91
Elitzur M., Netzer H., 2016, Monty Notices of the Royal Astronomical Society, 459, 585
Elvis M., 2000, ApJ, 545, 63
Elvis M., 2017, ApJ, 847, 56
Elvis M., et al., 1994, Astrophysical Journal, Supplement Series, 95, 1
Eracleous M., Lewis K. T., Flohic H. M. L. G., 2009, New Astron. Rev., 53, 133
Event Horizon Telescope Collaboration et al., 2019, ApJ, 875, L6
Fabian A. C., 2012, ARA&A, 50, 455
Fabricant D., Cheimets P., Caldwell N., Geary J., 1998, Publications of the Astronomical Society of the Pacific, 110, 79
Fanaroff B. L., Riley J. M., 1974, MNRAS, 167, 31P
Ferland G. J., et al., 2013, Rev. Mex. Astron. Astrofis., 49, 137
Ferrarese L., Merritt D., 2000, ApJ, 539, L9
Ferrarese L., et al., 2001, ApJ, 555, L79
Fitzpatrick E. L., 1999, PASP, 111, 63
Fukugita M., et al., 1996, The Astronomical Journal, 111, 1748
Gandhi P., et al., 2009, A&A, 502, 457
Gardner E., Done C., 2017, MNRAS, 470, 3591
Gaskell C. M., 2009, New Astron. Rev., 53, 140
Gaskell C. M., 2017, MNRAS, 467, 226
Gaskell C., Goosmann R., Klimek E., 2008, Memorie della Societa Astronomica Italiana, 79, 1090
Gezari S., et al., 2017a, ApJ, 835, 144
Gezari S., Cenko S. B., Arcavi I., 2017b, ApJ, 851, L47
Gilli R., Comastri A., Hasinger G., 2007, A&A, 463, 79
Giustini M., Proga D., 2019, preprint, p. arXiv:1904.07341
Goad M. R., Korista K. T., 2014, MNRAS, 444, 43
Goad M. R., O'Brien P. T., Gondhalekar P. M., 1993, MNRAS, 263, 149
Goad M. R., Korista K. T., Ruff A. J., 2012, MNRAS, 426, 3086
Goad M. R., et al., 2019, MNRAS, 486, 5362

Goodrich R. W., 1995, ApJ, 440, 141
Graham M. J., et al., 2019, preprint, p. arXiv:1905.02262
Gravity Collaboration et al., 2018, Nature, 563, 657
Grier C. J., et al., 2013, ApJ, 764, 47
Grier C. J., et al., 2017, ApJ, 851, 21
Gunn J. E., et al., 2006, The Astronomical Journal, 131, 2332
Guo H., et al., 2016, ApJ, 826, 186
Guo H., et al., 2019, arXiv e-prints, p. arXiv:1907.06669 arXiv:1907.06669
Haardt F., Maraschi L., 1991, ApJ, 380, L51
Harris D. W., et al., 2016, AJ, 151, 155
Heckman T. M., Best P. N., 2014, ARA&A, 52, 589
Hines D. C., Wills B. J., 1993, ApJ, 415, 82
Ho L. C., 2008, ARA&A, 46, 475
Hryniewicz K., et al., 2014, A&A, 562, A34
Husemann B., et al., 2016, A&A, 593, L9
Hutchings J. B., Craven S. E., 1988, AJ, 95, 677
Hutsemékers D., et al., 2017, A&A, 604, L3
Jiang Y.-F., Stone J. M., Davis S. W., 2014, ApJ, 796, 106
Kaiser N., et al., 2010, in Ground-based and Airborne Telescopes III. p. 77330E
Kelly B. C., Bechtold J., Siemiginowska A., 2009, ApJ, 698, 895
Kembhavi A. K., Narlikar J. V., 1999, Quasars and Active Galactic Nuclei: An Introduction. Cambridge University Press
Khachikian E. E., Weedman D. W., 1971, Astrofizika, 7, 389
Kishimoto M., et al., 2008, Nature, 454, 492
Kokubo M., et al., 2014, ApJ, 783, 46
Kollatschny W., 2003a, A&A, 407, 461
Kollatschny W., 2003b, A&A, 412, L61
Kollatschny W., Bischoff K., 2002, A&A, 386, L19
Kollatschny W., et al., 2001, Astronomy & Astrophysics, 379, 125
Korista K. T., Goad M. R., 2000, ApJ, 536, 284
Korista K. T., Goad M. R., 2004, ApJ, 606, 749
Kormendy J., Freeman K. C., 1998, in American Astronomical Society Meeting Abstracts. p. 21.05
Kozłowski S., et al., 2010, The Astrophysical Journal, 708, 927
Krolik J., 1999, Active Galactic Nuclei. From the Central Black Hole to the Galactic Environment. Princeton
Kynoch D., et al., 2019, MNRAS, 485, 2573
LaMassa S., et al., 2015, The Astrophysical Journal, 800, 144
Lagos C. D. P., et al., 2011, MNRAS, 414, 2148
Landt H., et al., 2008, The Astrophysical Journal Supplement Series, 174, 282
Landt H., Ward M. J., Elvis M., Karovska M., 2014, MNRAS, 439, 1051
Lawrence A., 2012, Monthly Notices of the Royal Astronomical Society, 423, 451
Lawrence A., 2016, in Mickaelian A., Lawrence A., Magakian T., eds, Astronomical Society of the Pacific Conference Series Vol. 505, Astronomical Surveys and Big Data. p. 107
Lawrence A., 2018, Nature Astronomy, 2, 102

Lawrence A., 2019, Probability in Physics: An Introductory Guide. Springer
Lawrence A., Elvis M., 2010, The Astrophysical Journal, 714, 561
Lawrence A., et al., 2016, MNRAS, 463, 296
Lira P., et al., 2018, ApJ, 865, 56
MacAlpine G. M., 1972, ApJ, 175, 11
MacLeod C., et al., 2010, The Astrophysical Journal, 721, 1014
MacLeod C., et al., 2012, The Astrophysical Journal, 753, 106
MacLeod C., et al., 2016, The Monthly Notices of the Royal Astronomical Society, 457, 389
MacLeod C., Green P., Anderson S., 2019, The Astrophysical Journal
Madejski G., Sikora M., 2016, Annual Review of Astronomy and Astrophysics, 54, 725
Maiolino R., et al., 2010, A&A, 517, A47
Margala D., et al., 2016, The Astrophysical Journal, 831, 157
Matt G., Guainazzi M., Maiolino R., 2003, MNRAS, 342, 422
Matthews T. A., Sandage A. R., 1963, ApJ, 138, 30
Mattila S., et al., 2018, Science, 361, 482
Mayo J. H., Lawrence A., 2013, MNRAS, 434, 1593
McElroy R. E., et al., 2016, A&A, 593, L8
McHardy I. M., et al., 2014, MNRAS, 444, 1469
McLure R. J., Dunlop J. S., 2004, MNRAS, 352, 1390
McLure R. J., Jarvis M. J., 2002, MNRAS, 337, 109
Merloni A., 2016, in Haardt F., et al., eds, Lecture Notes in Physics, Berlin Springer Verlag Vol. 905, Lecture Notes in Physics, Berlin Springer Verlag. p. 101
Merloni A., et al., 2014, MNRAS, 437, 3550
Merloni A., et al., 2015, MNRAS, 452, 69
Metzroth K. G., Onken C. A., Peterson B. M., 2006, ApJ, 647, 901
Morgan C. W., Kochanek C. S., Morgan N. D., Falco E. E., 2010, ApJ, 712, 1129
Netzer H., 1980, ApJ, 236, 406
Netzer H., 2013, The Physics and Evolution of Active Galactic Nucltaei. Cambridge
Netzer H., 2015, Annual Review of Astronomy and Astrophysics, 53, 365
Netzer H., Laor A., 1993, ApJ, 404, L51
Netzer H., Marziani P., 2010, ApJ, 724, 318
Noda H., Done C., 2018, MNRAS, 480, 3898
Novikov I., Thorne K., 1973, in De Witt C., De Witt B., eds, Black Holes, Les Houches 1973. Gordon & Breach, New York
O'Brien P. T., Goad M. R., Gondhalekar P. M., 1995, MNRAS, 275, 1125
Oke J. B., 1963, Nature, 197, 1040
Osmer P., Shields J., 1999, in Ferland G., Baldwin J., eds, ASP Conference Series Vol. 162, Quasars and Cosmology. p. 235
Osterbrock D. E., 1977, ApJ, 215, 733
Osterbrock D., 1981, The Astrophysical Journal, 249, 462
Paltani S., Courvoisier T. J. L., 1994, A&A, 291, 74
Pancoast A., et al., 2014, MNRAS, 445, 3073
Pâris I., et al., 2012, Astronomy & Astrophysics, 548, A66
Pâris I., et al., 2014, Astronomy & Astrophysics, 563, A54
Pâris I., et al., 2018, Astronomy & Astrophysics, 613, A51

Peterson B., 1997, An Introduction to Active Galactic Nuclei. Cambridge
Peterson B., 2006, The Broad-Line Region in Active Galactic Nuclei. Springer Berlin Heidelberg, Berlin, Heidelberg, pp 77–100
Peterson B. M., 2008, New Astron. Rev., 52, 240
Peterson B. M., 2014, Space Sci. Rev., 183, 253
Peterson B. M., et al., 1998, ApJ, 501, 82
Peterson B. M., et al., 2000, ApJ, 542, 161
Planck Collaboration et al., 2016, A&A, 594, A13
Pringle J. E., Rees M. J., 1972, A&A, 21, 1
Proga D., Ostriker J., Kurosawa R., 2008, The Astrophysical Journal, 676, 101
Rakić N., et al., 2017, A&A, 603, A49
Ramos Almeida C., et al., 2016, MNRAS, 461, 1387
Reichert G. A., et al., 1994, ApJ, 425, 582
Richards G. T., et al., 2002, The Astronomical Journal, 123, 2945
Richards G. T., et al., 2006, ApJS, 166, 470
Richards G. T., et al., 2011, Astronomical Journal, 141, 167
Roig B., Blanton M. R., Ross N. P., 2014, ApJ, 781, 72
Roseboom I. G., et al., 2013, MNRAS, 429, 1494
Ross N. P., et al., 2018, MNRAS, 480, 4468
Ruan J. J., et al., 2016, ApJ, 826, 188
Ruan J. J., et al., 2019, in AAS/High Energy Astrophysics Division. AAS/High Energy Astrophysics Division. p. 106.44
Rumbaugh N., et al., 2018, ApJ, 854, 160
Runco J. N., et al., 2016, The Astrophysical Journal, 821, 33
Runnoe J. C., et al., 2016, 455, 1691
Schlafly E. F., Finkbeiner D. P., 2011, The Astrophysical Journal, 737, 103
Schlegel D. J., Finkbeiner D. P., Davis M., 1998, ApJ, 500, 525
Schmidt M., 1963, Nature, 197, 1040
Schmidt K. B., et al., 2012, ApJ, 744, 147
Schneider D. P., et al., 2010, The Astronomical Journal, 139, 2360
Seyfert C. K., 1943, ApJ, 97, 28
Shakura N. I., Sunyaev R. A., 1973, Astronomy & Astrophysics, 24, 337
Shang Z., et al., 2005, ApJ, 619, 41
Shapiro S. L., Lightman A. P., Eardley D. M., 1976, ApJ, 204, 187
Shappee B. J., et al., 2014, ApJ, 788, 48
Shen Y., Ho L. C., 2014, Nature, 513, 210
Shen Y., Liu X., 2012, ApJ, 753, 125
Shen Y., et al., 2011, The Astrophysical Journal Supplement, 194, 45
Shen Y., et al., 2016a, The Astrophysical Journal, 818, 30
Shen Y., et al., 2016b, ApJ, 818, 30
Shen Y., et al., 2016c, ApJ, 831, 7
Śniegowska M., Czerny B., 2019, preprint, p. arXiv:1904.06767
Stern J., Laor A., 2012, MNRAS, 426, 2703
Stern J., Laor A., Baskin A., 2014, MNRAS, 438, 901
Stern D., et al., 2018, ApJ, 864, 27

Storchi-Bergmann T., Baldwin J. A., Wilson A. S., 1993, ApJ, 410, L11
Stoughton C., et al., 2002, The Astronomical Journal, 123, 485
Sulentic J. W., Marziani P., Del Olmo A., Zamfir S., 2016, Ap&SS, 361, 55
Sun M., et al., 2015, The Astrophysical Journal, 811, 42
Sun M., et al., 2018, ApJ, 854, 128
Tadhunter C., 2016, Astronomische Nachrichten, 337, 159
Tadhunter C., et al., 2018, MNRAS, 478, 1558
Tody D., 1986, in Crawford D. L., ed., Proc. SPIEVol. 627, Instrumentation in astronomy VI. p. 733
Tohline J. E., Osterbrock D. E., 1976, ApJ, 210, L117
Tran H. D., 2003, ApJ, 583, 632
Trevese D., et al., 2007, A&A, 470, 491
Urry C., Padovani P., 1995, Publications of the Astronomical Society of the Pacific, 107, 803
Vanden Berk D. E., et al., 2001, AJ, 122, 549
Vanden Berk D. E., et al., 2004, ApJ, 601, 692
Véron-Cetty M. P., Joly M., Véron P., 2004, A&A, 417, 515
Vestergaard M., Wilkes B. J., 2001, the Astrophysical Journal Supplement, 134, 1
Wang S., et al., 2019, preprint, p. arXiv:1903.10015
Welsh B. Y., Wheatley J. M., Neil J. D., 2011, A&A, 527, A15
Winter L. M., Veilleux S., McKernan B., Kallman T. R., 2012, ApJ, 745, 107
Woo J.-H., 2008, AJ, 135, 1849
Wu J., et al., 2009, The Astrophysical Journal, 702, 767
Yang Q., et al., 2018, ApJ, 862, 109
Yang Q., et al., 2019, preprint, p. arXiv:1904.10912
Yuan F., Narayan R., 2014, ARA&A, 52, 529
Zhu D., Sun M., Wang T., 2017, ApJ, 843, 30
van Dokkum P. G., Bloom J., Tewes M., 2012, L.A.Cosmic: Laplacian Cosmic Ray Identification, Astrophysics Source Code Library, ascl:1207.005